CENTER FOR INFRASTRUCTURE ENGINEERING STUDIES

Steel-Free Hybrid Reinforcement System for Concrete

Bridge Decks

By

Dr. Abdeldjelil Belarbi

Huanzi Wang

UTC R52

Technical Report Documentation Page

1. Report No. UTC R52	2. Government Accession No.	3. Recipient's Catalog No.
4. Title and Subtitle Steel-Free Hybrid Reinforcement System for Concrete Bridge Decks		5. Report Date Dec 2004
		6. Performing Organization Code
7. Author/s Dr. Abdeldjelil Belarbi, Huanzi Wang		8. Performing Organization Report No. 00001140 OT052
9. Performing Organization Name and Address Center for Infrastructure Engineering Studies/UTC program University of Missouri - Rolla 223 Engineering Research Lab Rolla, MO 65409		10. Work Unit No. (TRAIS)
		11. Contract or Grant No. DTRS98-G-0021
12. Sponsoring Organization Name and Address U.S. Department of Transportation Research and Special Programs Administration 400 7th Street, SW Washington, DC 20590-0001		13. Type of Report and Period Covered Final
		14. Sponsoring Agency Code

15. Supplementary Notes

16. Abstract

A research project was initiated to develop a nonferrous hybrid reinforcement system for concrete bridge decks by using continuous fiberreinforcedpolymer
(FRP) rebars and discrete randomly distributed polypropylene fibers. This hybrid system may eliminate problems related to corrosion of steel reinforcement while providing requisite strength, stiffness, and desired ductility, which are shortcomings of FRP reinforcement system in reinforced concrete.
The test results showed that with the addition of fibers, structural performances of the system are improved. Although polypropylene fibers do not increase the ultimate bond strength, they provide enhanced ductile bond behavior. Also, with the addition of fibers, the flexural behaviors are improved with the increase of the ductility index µ by approximately 40%, as compared to the plain concrete beams. In addition, with the addition of polypropylene fibers, the durability of the system was improved. Furthermore, some design recommendations are proposed based on analytical models and test results.

17. Key Words Fiber Reinforced Polymer, Fiber-Reinforced-Concrete, Bond, Ductility, Durability	18. Distribution Statement No restrictions. This document is available to the public through the National Technical Information Service, Springfield, Virginia 22161.		
19. Security Classification (of this report) unclassified	20. Security Classification (of this page) unclassified	21. No. Of Pages	22. Price

Form DOT F 1700.7 (8-72)

ABSTRACT

New materials and design methods are being investigated for the design of bridge components to alleviate the current devastating corrosion problems. A research project was initiated at the University of Missouri (UM) and the Missouri Department of Transportation (MoDOT) to develop a nonferrous hybrid reinforcement system for concrete bridge decks by using continuous fiber-reinforced-polymer (FRP) rebars and discrete randomly distributed polypropylene fibers. This hybrid system may eliminate problems related to corrosion of steel reinforcement while providing requisite strength, stiffness, and desired ductility, which are shortcomings of FRP reinforcement system in reinforced concrete.

The overall study plan includes: (1) development of design procedures for an FRP/FRC hybrid reinforced bridge deck, (2) laboratory studies of static and fatigue bond performances and ductility characteristics of the system, (3) accelerated durability tests of the system, and (4) static and fatigue tests on full-scale hybrid reinforced composite bridge decks (this was conducted at University of Missouri – Columbia).

The test results showed that with the addition of fibers, structural performances of the system are improved. Although polypropylene fibers do not increase the ultimate bond strength, they provide enhanced ductile bond behavior. Also, with the addition of fibers, the flexural behaviors are improved with the increase of the ductility index μ by approximately 40%, as compared to the plain concrete beams. In addition, with the addition of polypropylene fibers, the durability of the system was improved. Furthermore, some design recommendations are proposed based on analytical models and test results.

ACKNOWLEDGMENTS

TABLE OF CONTENTS

LIST OF ILLUSTRATIONS

LIST OF TABLES

NOTATIONS

a	distance from the support to the point load applied, in.
A	effective tension area per bar, in.^{2}
A_f	area of rebars, in.^{2}
A_{split}	concrete splitting area, in.^{2}
b_e	effective beam width, in.
C	cover depth, in.
C_E	environmental reduction factor
d	distance from the extreme compression fiber to centroid of the tension reinforcement
d_b	diameter of rebar, in.
d_c	thickness of concrete cover measured from extreme tension fiber to the center of the closest layer of longitudinal bars
E_c	modulus of elasticity of concrete, psi
E_f	modulus of elasticity of FRP rebar, psi
E_t	total energy of the system, kips-in.
E_e	elastic energy, kips-in.
$E_{0.75Pu}$	energy corresponding at 75% of the ultimate load, kips-in.
F	friction force on deformation with unit area, psi
f_c'	concrete compressive strength, psi
f_{ct}	concrete splitting tensile strength, ksi
f_f	stress in the FRP reinforcement, ksi

f_{fu}	tensile strength of FRP bars, ksi
h_r	height of deformation, in.
I_e	effective moment of inertia of the section, in.^{4}
I_g	gross moment of inertia of the section, in.^{4}
k_b	coefficient that accounts for the degree of bond between the FRP bar and the surrounding concrete
L	span length, in.
l_d	embedment length, in.
l_{db}	basic development length, in.
l_e	effective splitting length, in.
M_a	moment applied to the section, kips-in.
M_{cr}	cracking moment including rebars' contribution, kips-in.
M_{cr-exp}	cracking moment measured from experiments, kips-in.
M_{DL}	moment induced by deal loads, kips-in.
M_{LL+I}	moment induced by live load and impact, kips-in.
M_u	ultimate flexural strength, kips-in.
$M_{\varepsilon=0.001}$	flexural strength at concrete strain of 0.001, kips-in.
n_i	number of cycles applied at a particular stress level
$N_{max,i}$	number of cycles which cause fatigue failure at a certain stress level
P	normal stress on deformation, psi
R	resultant stress of P and F, psi
R_r	radial component of R, psi
S	crack spacing

S_m	slip at peak bond strength, in.
S'_m	slip at second peak bond strength, in.
S_r	residual slip after fatigue loading, in.
T	pullout force, kips
u	bond strength (longitudinal component of R), psi
u'	bond strength at second peak, psi
$u_{0.002}$	bond strength at the slip of 0.002 in. at the free end, psi
$u_{0.01}$	bond strength at the slip of 0.01 in. at the loaded end, psi
u_{design}	design bond strength , psi
$u_{b,f}$	bond strength of FRP rebar to concrete, psi
$u_{b,s}$	bond strength of steel rebar to concrete, psi
u_{test}	bond strength based on test results, psi
$u_{theo.}$	theoretical bond strength, psi
w	crack width at tensile face of the beam, in.
V_f	volume fraction of fibers
α	rib angle
β	coefficient to converse crack width corresponding to the level of reinforcement to the tensile face of beam
β_d	modification factor for FRP reinforced beam
Δ_{mid}	mid-span deflection, in.
ε_{cu}	ultimate concrete strain
$\psi_{\varepsilon=0.001}$	curvature at concrete strain of 0.001
ψ_u	curvature at ultimate

γ adjustment factor for different embedment length

μ friction coefficient

μ_E ductility index

ρ_f reinforcing ratio

1. INTRODUCTION

1.1. BACKGROUND AND PROBLEM STATEMENT

There are approximately 592,000 bridges in the United States. Of these, approximately 78,000 are classified as structural deficient. Eighty thousand bridges are functionally obsolete (FHwA, 2003). These numbers indicate that in excess of 25 percent of the bridges listed in the National Bridge Inventory Databases are in need of repair or replacement. Steel corrosion is the primary reason for the structural deficiency of bridges. The annual direct cost of corrosion for highway bridges is estimated to be $8.3 billion. This consists of $3.8 billion to replace structurally deficient bridges over the next ten years, $2.0 billion for maintenance and cost of capital for concrete bridge decks, $2.0 billion for maintenance and cost of capital for concrete substructures (minus decks), and $0.5 billion for maintenance painting of steel bridges. Life-cycle analysis estimates indirect costs to the user due to traffic delays and lost productivity at more than ten times the direct cost of corrosion maintenance, repair, and rehabilitation. (www. CorrosionCost.com 2004).

Corrosion decay has been a continual challenge for bridge engineers. Corrosion is aggravated by the common usage of deicing salts in cold climate areas; e.g., many regions in North America. Several methods, such as epoxy coated rebars, synthetic membranes, or cathodic protection have been developed to mitigate the corrosion. However, each method has shown only limited success (Keesler and Power, 1988; Rasheeduzzafar et al., 1992).

Recently, a non-metallic material, fiber reinforced polymer (FRP), has been adopted in civil engineering as an alternative to the traditional steel rebar to overcome the corrosion problem. FRP materials offer many advantages over the conventional steel reinforcement, such as, corrosion-free, high tensile strength, light weight, ease of handling, and free of electromagnetism. However, due to their brittle behaviors and lower modulus of elasticity, they also induce unsatisfactory structural ductility and serviceability problems.

The use of fibers in reinforced concrete (RC) has resulted in an increase in concrete toughness, ductility, and freeze-thaw durability, as well as in an improved resistance to crack growth, plastic and drying shrinkage, impact loading, and fatigue loading (ACI 544.1R-96). It is proven to have notable benefits to RC structures, especially under service conditions.

The idea of combining corrosion-free FRP bars with fiber reinforced concrete (FRC) is appealing. It is believed that this kind of hybrid system may eliminate problems related to corrosion of steel reinforcement, while providing requisite strength, stiffness, and desired ductility, which are shortcomings of the plain concrete and FRP reinforcement system.

1.2. METHOD OF IMPLEMENTATION

Recently, the Missouri State Department of Transportation (MoDOT) sponsored a project to study the steel-free FRP/FRC hybrid system with the aim of developing more durable bridges. As part of this project, several tasks needed to be undertaken to fulfill this goal. The overall program can be summarized as follows:

(A) Review Current Procedures in the Design of Bridge Deck. The MoDOT and AASHTO procedures for the design of deck slabs in steel girder bridges were reviewed to understand the current approaches in the design of concrete decks. By taking into account the arching action in the deck, researchers (Campbell, Chitnuyanondh, and Batchelor, 1980; Batchelor and Kwun 1981; Bakht and Mufti, 1998) in Canada developed the steel-free bridge deck concept. The innovative Canadian approach was also studied. The above reviews were facilitate development of a set of preliminary design specifications for the new hybrid concrete bridge deck system that has the mechanical and service performance comparable to that of the conventional steel reinforced concrete decks.

(B) Laboratory Studies of Bond Performances. Perfect bond is essential for "reinforced concrete". Because it is a new material in civil engineering, research on bond between FRP rod and concrete is necessary. One of the key reasons is that there is a lack of standardization on the manufacture of FRP rods. Different surface treatments resulted in tremendously different bond behaviors (Ehsani et al., 1997; Kaza, 1999).

Three test methods are commonly used to study bond behaviors: namely, pullout bond test, splitting bond test, and flexural bond test. Different test methods provide different information on the bond behaviors. Pullout tests can clearly represent the concept of anchorage and is usually adopted to study the bond behavior between rebar and concrete. Although pullout tests cause concrete to be in compression and the testing bar to be in tension, a stress condition not exhibited in real structures, a reasonable correlation was found between structural performance and measures of performance in the pullout test (Cairns and Abdullah, 1992). Splitting bond tests can be used to study the

splitting bond behavior under different cover thicknesses. The effect of the transverse reinforcement on bond behavior can be avoided when properly designed. Splitting bond tests can simulate the stress field of real structures to some extent; it can simulate the shear stress field but not the stress gradient induced by bending. Flexural bond tests have the advantage of representing actual stress fields in real beams and the cover effects on bond. However, it requires considerable confining reinforcement to avoid a shear failure, and so bond splitting failures are unlikely (Cairns and Plizzari, 2003). All three study methods were investigated and compared with each other. The flexural bond test was conducted by the University of Missouri – Columbia (UMC) and is not reported in this report.

(C) **Laboratory Studies of Ductility Characteristics.** Ductility is a design requirement in most civil engineering structures and is mandated by most design codes. In RC structures, ductility is defined as the ratio of post yield deformation to yield deformation. For properly reinforced and dimensioned members, RC member will exhibit good ductile behavior Due to the linear-stain-stress relation of FRP bars, traditional definition of ductility cannot be applied to the structures reinforced with FRP reinforcement. Two approaches, i.e., energy-based approach and deformation-based approach, have been developed and successfully used (Naaman and Jeong, 1995; Jaeger et al., 1995)**.** With the addition of fibers, the toughness of concrete will be greatly increased. Thus, a significant increase in the energy absorption of the entire system is expected.

(D) **Accelerated Durability Tests of the Hybrid System.** Composite materials offer many advantages such as corrosion resistance, and their use in bridge decks have

become more technically attractive and economically viable. However, long-term

performances have to be clearly understood before it can be applied in the field with

confidence.

Much research has been done on the durability issue regarding individual FRP

components, but there is a paucity of literature on the durability of FRP and concrete

system. The durability mechanism depends more on the interrelation between the

materials than on the individual component's property. In addition, the mechanical

properties of a hybrid material system may deteriorate much faster than that suggested by

the property degradation rates of the individual components making up the hybrid system

(Schutte, 2004). The FRP/FRC hybrid system is new; research on durability

characteristics of this hybrid system has not been found in open literature. Thus,

accelerated durability tests on the FRP/FRC system are necessary. Specimens were

subjected to cycles of freeze-thaw and high temperature while in contact with salt water.

Bond characteristics and flexural performance were evaluated, and results were compared

to those without environmental effects.

(E) Static and Fatigue Tests on Full-Scale Hybrid Reinforced Composite

Bridge Decks. Several full-scale hybrid reinforced slabs were designed and tested using

the results developed in the previous study. This task was performed by the UMC, but is

not reported in this report.

1.3. RESEARCH SIGNIFICANCE

New materials and design methods are being investigated for the design of

bridges to eliminate the current corrosion problems. A research project was initiated at

the University of Missouri to develop a nonferrous hybrid reinforcement system for

concrete bridge decks using FRP rebars and discrete randomly distributed polypropylene

fibers. This study will provide new insights for bridge engineers and researchers.

1.4. PREVIOUS RESEARCH ON STEEL-FREE BRIDGE

The steel-free design concept in concrete bridge decks is not new. Considering the

arching action in the decks between supports, Canadian researchers have developed a

system that realizes the idea of steel-free. The steel-free concrete bridge deck system

utilized transverse steel straps welded to the top flange of each girder. The straps

prevented the outward movement of the girders, as shown in Figure 1.1. After the

cracking of the concrete, the concrete slab sustained loads through an arching action that

is enabled by compressive membrane forces in the concrete. The polypropylene fibers

were added to the concrete to control the plastic shrinkage cracking of the deck. To

guarantee the composite action between the concrete slab and the steel girder, shear studs

were used. Table 1.1 lists the steel-free bridges constructed in Canada (Bakht and Mufti,

1998).
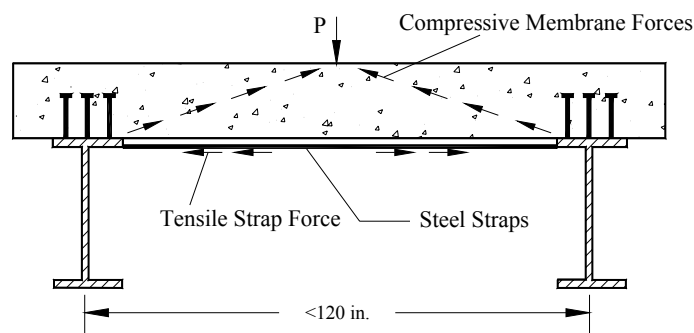
**Figure 1.1. Typical Cross Section of Steel-Free Concrete Bridge Deck
(Bakht and Mufti, 1998)**

Table 1.1. Summary of Canadian Steel-Free Bridges (Bakht and Mufti, 1998)

Bridge	Girder Spacing	Slab Thickness	Features
Slamon River (1995)	Steel Plate 8.86 ft	8 in.	-first steel-free deck slab in new construction -transverse confinement by welded steel straps -barrier wall loads taken to girders -6% more expensive than conventional slab
Chatham (1996)	Steel Plate 6.89 ft	7 in.	-first steel-free deck slab used in rehabilitation -transverse confinement by welded steel straps -CFRP for transverse negative bending -first barrier wall with double-headed tension bars and GFRP grid -significantly more expensive than conventional slab
Crowchild Trail (1997)	Steel Plate 6.56 ft	7.4 in.	-transverse confinement by studded straps -GFRP for transverse negative moments -first steel-free deck slab in continuous-span bridge -selected in competitive bidding against conventional slab
Waterloo Creek (1998)	Precast Concrete 9.18 ft	7.6 in.	-first steel-free deck slab on precast concrete girders -transverse confinement by studded straps -nearly the same cost as conventional slab
Lindquist (1998)	steel plate 11.48 ft	6 in.	-first steel-free precast panel -transverse confinement with studded straps embedded in precast panel -recorded girder spacing to minimum thickness ratio, being 23.3 -30% cheaper than conventional panel

In recent years, there has been a great deal of activity in use of FRP reinforcement in the concrete bridge decks in the United States. A convenient database has been developed by the United States Department of Transportation's Federal Highway Administration (FHwA, 2003) to provide information on the projects in United States using FRP reinforcement in concrete bridge decks.

The first FRP rebar reinforced bridge deck constructed across Buffalo Creek in McKinleyville, West Virginia, is worthy of note. The McKinleyville Bridge was a 177-ft long, three-span, continuous structure accommodating two lanes of traffic. The design of the FRP reinforced concrete deck was based on a design method developed at the Constructed Facility Center at West Virginia University. The design method is similar to the procedures for the highway bridges working stress design of transversely reinforced concrete decks, as described in the American Association of State Highway Transportation Officials' Standard Specifications. The design required a deck thickness of 9 in. and #4 FRP rebars as the main transverse reinforcement of a 6-in spacing. The main reinforcement was tied to #3 FRP bars for distribution reinforcement, also at 6 in. spacing. The clean covers for top and bottom reinforcements were 1 ½ in. and 1in, respectively.

The Sierrita de la Cruz Creek Bridge in Potter County, Texas, had two of its seven spans redecked with an FRP cast-in-place reinforced concrete deck slab, where the top mat was made of GFRP bars (#6 at 5.5 in. center to center in both directions), and the bottom mat was made of epoxy-coated steel rebars (Bradberry, 2001). The composite deck slab also had stay-in-place forms made of concrete precast panels reinforced with epoxy-coated steel rebars at the bottom.

More recently, a new FRP reinforced bridge deck was built inWaupum, Wisconsin. The uniqueness of this bridge was the combination of three different FRP materials. The FRP reinforcing system was made up of three different components: a stay-in-place FRP pultruded deck panel, standard FRP rebars, and a bi-directional FRP pultruded grid panel, as shown in Figure 1.2 (Berg et al., 2004). The deck was 8 in. thick with 1.5 in. of cover at the top. The deck panels served as the bottom tensile

reinforcement for the deck in the transverse direction. Standard FRP rods served as the temperature and shrinkage reinforcement. The grid served as the top reinforcement of the concrete deck.
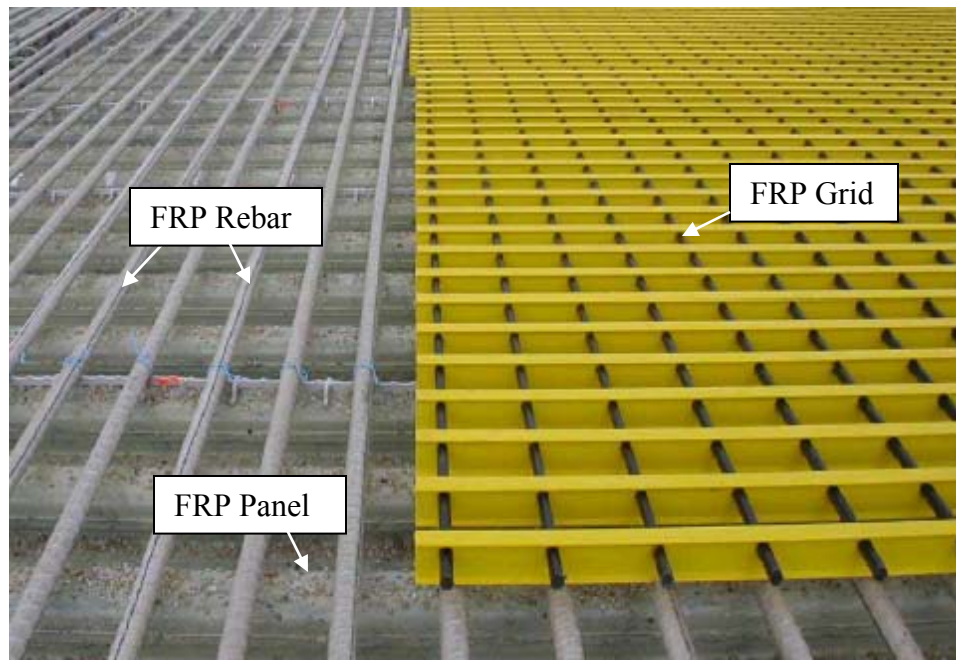
Figure 1.2. FRP Panels, FRP Rebars and FRP Grid Used in Wisconsin

1.5. OUTLINE OF THE REPORT

Chapter 2 gives background information of the bridge design procedures, including the AASHTO Standard Specifications, AASHTO LRFD and MoDOT Design Approach.

Chapter 3 provides the details of the experimental program, including the experimental variables, testing specimens, testing matrix, and test setup and procedures.

Chapter 4 to Chapter 6 cover the bond characteristics, flexural behavior, and the durability performance of this hybrid system. The test specimens, test setup, test procedures, test results, and some theoretical derivations are presented.

Chapter 7 presented the design recommendations for the FRP/FRC hybrid concrete bridge deck.

Chapter 8 contains all the conclusions that were obtained based on the test results and theoretical analysis. Furthermore, some recommendations for the future study are also provided.

2. BACKGROUND

2.1. GENERAL

The proposed FRP/FRC hybrid reinforcement system is a novel approach for bridge deck application. Neither field application nor research has been found in the open literature. To facilitate development of the design procedures for the new deck system that has mechanical and service performance comparable to that of conventional steel reinforced concrete decks, the current AASHTO and MoDOT design procedure in the deck slabs of steel girder bridges were reviewed.

2.2. AASHTO AND MODOT DECK SLAB DESIGN PRCEDURES

Decks are the platform of a roadway extending horizontally over a crossing. Decks have many functions. In addition to provide the riding surface for vehicular traffic, they also serve several structural purposes. The bridge deck distributes the vehicular wheel loads to the girders, which are the primary load-carrying members on a bridge superstructure. And the deck is often composite with the main girders and, thus, helps to increase the flexural strength and torsional rigidity of the bridge. For most new bridges, cast-in-place concrete bridge decks are chosen as the most appropriate deck type. Typically, these types of decks are designed as a transverse beam supported by the main longitudinal girders. While cast-in-place concrete decks designed as transverse beams have been the standard for decades, bridge deck type and design is continuing to evolve.

2.2.1. Loads Relative to Deck Slab Design. From the construction stage through its service life, the bridge deck must sustain various loads. The bridge engineer must take

into account a wide variety of loads which vary based on duration (permanent or temporary), deformation (concrete creep, thermal expansion, etc.), and effect (shear, bending, compression, torsion, etc.).

- **Permanent Loads**

    (a) Dead Load. The dead load on a deck slab is the aggregate weight of all elements. This includes the deck, wearing surface, stay-in-place forms, sidewalks and railings, parapets, signing, and utilities.

    (b) Superimposed Dead Load. Superimposed dead loads are those loads added onto the deck after it has cured. From the list of elements mentioned previously, the designer should treat items such as sidewalks, railings, parapets, signing, utilities and the wearing surface independently.

- **Temporary Loads**

    (a) Vehicle Live Load. To help designers accurately model the live load on a structure, hypothetical design vehicles based on truck loading, such as HS20, were developed by AASHTO.

    (b) Impact. In order to account for the dynamic effects of the loading of a moving vehicle onto a structure, an impact factor is used as a multiplier for certain structural elements.

    (c) Construction Loads. During the construction period, large stresses in the structural members may be induced. It is the engineers' responsibility to consider this effect.

- **Deformation and Response Loads**

(a) **Shrinkage.** Shrinkage is the natural change in volume of concrete that occurs over time. While recommended methods of optimal curing will reduce shrinkage effects, reinforcement is added perpendicular to the main reinforcement to account for tensile stresses induced by shrinkage.

(b) **Thermal Forces.** The effects of thermal forces on a structure are significant and should not be underestimated by the designer. In general, thermal forces are caused by fluctuations in temperature. Reinforcements are required on the top of the deck and also in the negative regions for continuous joint-free decks to withstand the tensile stresses induced by temperature change.

2.2.2. Detail Design Procedures. AASHTO Standard Specifications, MoDOT Bridge Manual, and AASHTO LRFD design procedures for a typical girder bridge deck are discussed in detail in the following sections.

2.2.2.1. AASHTO standard specifications. The American Association of State Highway and Transportation Officials (AASHTO) has published design specifications for many decades. These specifications, adopted throughout the United States, have been updated periodically. AASHTO's 17th Edition, Standard Specifications for Highway Bridges, published in 2002, is the latest specification.

STEP 1: Choose the general parameters

Some general design parameters have to be decided first, such as (1) slab thickness; (2) girder spacing; (3) girder type; (4) reinforced steel; (5) concrete strength; and (6) future wearing surface (FWS).

STEP 2: Compute the effective span length

CASE A: slab on two supports:

The effective span length is decided as follows when slab on two supports:

S = the Distance Center to Center of Supports & S ≤ Clear Span +Slab Thickness

(AASHTO 3.24.1.1)

CASE B*: slab supported on steel stringers over more than two supports

The effective span length is as follows when slab on more than two supports:

S = Distance between Edges of Top Flange + ½ Top Flange Width

(AASHTO 3.24.1.2 (b))

STEP 3: Compute moment due to dead load

(a) <u>Dead Load:</u>

Dead load consists of the following:

(1) slab; (2) FWS; (3) barrier curb; (4) media; (5) railing; (6) pedestrian curb and fence

(b) <u>Moment calculation:</u>

CASE A: simple spans:

The moment induced is:

$$M_{DL} = \frac{WS^2}{8},$$

CASE B: slabs continuous over more than 2 supports:

The moment induced is:

$$M_{DL} = \frac{WS^2}{10},$$

where W = dead load

S = effective span length

(AASHTO does not give specific dead load moment equations. This is the generally accepted expression).

CASE C: cantilever slabs:

Compute the moments induced by different loads and add them together.

STEP 4: Compute moment due to live load + impact

<u>(A) Interior spans.</u>

(1) Calculate the moment induced by live load, M_{LL}

Moment induced by live load is computed as follows:

CASE A: Main reinforcement perpendicular to traffic

    (a) simple span

$$M_{LL}=(\frac{S+2}{32})P \qquad\qquad\qquad (AASHTO\ 3.24.3.1)$$

    (b) slabs continuous over more than two supports

$$M_{LL}=0.8(\frac{S+2}{32})P \qquad\qquad\qquad (AASHTO\ 3.24.3.1)$$

where   P = Live load

    = 12,000lb for H15 & HS15 loading or

    = 16,000lb for H20 & HS20 loading

    CASE B: Main reinforcement parallel to traffic

      (a) simple span

        HS20 loading:

        Spans up to and including 50 feet: LLM = 900S foot-pounds;

        Spans 50 feet to 100 feet: LLM =1,000 (1.30S-20.0) foot-pounds.

        HS15 loading:

Use ¾ of the values obtained from the formulas for HS 20 loading.

(b) slabs continuous over more than two supports

Moments in continuous spans shall be determined by suitable analysis using the truck or appropriate lane loading.

(AASHTO 3.24.3.2)

(2) Compute the moment induced by live load and impact, M_{LL+I}

Moment induced by the live load and impact is computed as follows:

$M_{LL+I} = M_{LL} \times I$

where: I = Impact coefficient

$$= \frac{50}{L+125} \leq 0.3 \qquad\qquad \textit{(AASHTO 3.8.2.1)}$$

L = Length in feet of the portion of the span that is loaded to produce the maximum stress in the member.

(B) Cantilever Spans

(a) Truck Loads

The moment induced by the truck load is computed as follows:

CASE A: Reinforcement perpendicular to traffic

$M_{LL} = P \times X/E \qquad$ (foot-pounds)

where: P = Wheel load

E = the effective length of slab resisting post loadings

= 0.8X+3.75

X = the distance in feet from load to point of support

(AASHTO 3.24.5.1.1)

CASE B: reinforcement parallel to traffic

$M_{LL} = P{\times}X/E$

where: $E = 0.35X+3.2{\leq}7.0$ feet

(b) Railing Loads

$M_{LL} = Py/E$

where: P = Highway design loading=10kips

Y = moment arm

E = 0.8X+3.75 feet, where no parapet is used

= 0.8X+5.0 feet, where a parapet is used

X = the distance is feet from the center of the post to the point under

investigation

* Railing and wheel loads shall not be applied simultaneously.

STEP 5: Compute factored bending moment

The factored bending moment can be expressed as follows:

$M_u = 1.3(M_{DL}+1.67M_{LL+I})$

$M_u \geq 1.2M_{cr}$ (This requirement may be waived if the area of reinforcement

provided at a section is at least one-third greater than that required

by analysis based on the loading combinations)

STEP 6: Protection against Corrosion

The minimum cover for the slab in inches is shown in Table 2.1.

STEP 7: Compute the Main Reinforcement

The main reinforcement needed is computed based on the following equations:

$$\phi M_n = A_S f_y (d - \frac{a}{2})$$

Table 2.1. Minimum Cover (inches)   *(AASHTO 8.22)*

	Concrete deck slabs in mild climate	Concrete deck slabs which have no protective corrosion protection and are frequently exposed to deicing salts
Top Reinforcement	2	2.5
Bottom reinforcement	1	1

$$a = A_s f_y / (0.85 f'_c b) \qquad\qquad \textit{(AASHTO 8.16.3.2.1)}$$

$$\rho_s \leq 0.75 \rho_b \qquad\qquad \textit{(AASHTO 8.16.3.1.1)}$$

$$\rho_b = \frac{0.85 \beta_1 f'_c}{f_y} (\frac{87,000}{87,000 + f_y}) \qquad\qquad \textit{(AASHTO 8.16.3.2.2)}$$

All the above equations can be derived based on the normal assumptions used in the RC members, as shown in Figure 2.1.

STEP 8: Compute distribution steel in bottom of slab

To provide for the lateral distribution of the concentrated live loads, reinforcement shall be placed transverse to the main steel reinforcement in the bottom of the slabs except culvert or bridge slabs where the depth of fill over the slab exceeds 2 feet.

(AASHTO 3.24.10.1)

Figure 2.1. Stress-Stain Diagram

(a) for main reinforcement parallel to traffic

$$\text{Percentage} = \frac{100}{\sqrt{S}} \leq 50\%$$

(b) for main reinforcement perpendicular to traffic

$$\text{Percentage} = \frac{220}{\sqrt{S}} \leq 67\%$$

where S = the effective span length in feet   *(AASHTO 3.24.10.2)*

STEP 9: Shrinkage & temperature reinforcement

Reinforcement for shrinkage & temperature stresses shall be provided near exposed surfaces of slabs not otherwise reinforced.

$A_s \geq 1/8$ in.^{2}/ft in each direction

Spacing $\leq 3h_{slab}$

≤ 18 in.   *(AASHTO 8.20)*

STEP 10: Negative moment reinforcement over supports

In the negative regions of continuous spans, the minimum longitudinal reinforcement, including the longitudinal distribution reinforcement, must equal or exceed 1 percent of the cross sectional area of the concrete slab. Two-thirds of this required reinforcement is to be placed in the top layer of the slab within the effective width. *(AASHTO 10.38.4.3)*

STEP 11: Check serviceability

The crack width should be limited during the service conditions. Because of the scatter in crack widths, AASHTO or MoDOT do not limit crack width, but rather limits the magnitude of the term:

$$Z = f_s \sqrt[3]{d_c A}$$

Based on this method, the allowable stress in the reinforcement is limited as follows:

(a) compute f_s at service load

$$f_s = \frac{M}{A_s j d};$$

(b) compute allowable $f_{s,allow}$

$$f_{s,allow} = \frac{Z}{(d_c A)^{1/3}} \leq 0.6 f_y \qquad\qquad \textit{(AASHTO 8.16.8.4)}$$

where A=effective tension area, in square inches, of concrete surrounding the flexural tension reinforcement and having the same centroid as that reinforcement, divided by the number of bars or wires. When the flexural reinforcement consists of several bar or wire sizes, the number of bars or wires shall be computed as the total area of reinforcement

divided by the largest bar or wire used. For calculation purposes, the thickness of clear

concrete cover used to compute A should not be greater than 2 inches.

d_c = distance measured from extreme tension fibre to center of the closest bar or

wire in inches. For calculation purposes, the thickness of the clear concrete cover used to

compute d_c should not be taken greater than 2 inches.

$Z \leq 170$kips/in for members in moderate exposure conditions

≤ 130kips/in for members in severe exposure conditions

(c) check

$f_s \leq f_{s,allow}$

2.2.2.2. MoDOT bridge manual. The MoDOT Bridge Manual, developed for

the design of bridges in the state of Missouri, builds on and references the latest

AASHTO Standard specifications. It has more restricted conditions on design than

AASHTO LFD. Load Factor Design methods for all bridges (both steel and concrete) are

used.

STEP 1: Choose the general parameters

First of all, some general design parameters have to be decided.

(1) slab thickness: cast-in-place concrete slab with conventional forming with

thickness of 8.5 in.; or 3 in. prestressed concrete panels with 5-1/2 in. minimum cast-in-

place concrete.

(2) concrete strength is recommended equal to 4000 psi, and the stress at service

is 1600 psi.

(3) reinforcing steel is equal to 60,000 psi.

(4) modular ratio of elasticity between concrete and reinforcement is 8.

(5) future wearing surface (F.W.S) is 3 in. thick and is equal to35 lb/ft^2.

(6) girder type & spacing should be decided case by case.

(BM Sec 3.30.1.2-1; 3.30.1.2-2)

STEP 2: Compute the effective span length

The effective span length is decided as follows:

CASE A: slab on two supports:

S = the Distance Center to Center of Supports & S ≤ Clear Span +Slab Thickness

CASE B: slab supported on steel stringers over more than two supports

S = distance between Edges of Top Flange + ½ Top Flange Width

(AASHTO 3.24.1; BM Sec3.30.1.2-1)

STEP 3: Moment over Interior Support

(a) compute moment due to dead load

CASE A: Simple spans:

$$M_{DL} = \frac{WS^2}{8},$$

CASE B: slabs continuous over more than 4 supports:

$$M_{DL} = -0.100WS^2$$

CASE C: slabs continuous over more than 5 supports:

$$M_{DL} = -0.107WS^2,$$

where W = dead load

S = effective span length

(BM Sec 3.30.1.2-1)

(b) compute moment due to live load

The moment due to the live load can be computed by two cases as follows:

CASE A: main reinforcement perpendicular to traffic

(1) simple span

The moment is decided as:

$$M_{LL} = (\frac{S+2}{32})p$$

(2) slabs continuous over more than two supports

The moment is decided as:

$$M_{LL} = 0.8(\frac{S+2}{32})p$$

where   P = Live load

    = 12,000lb for H15 & HS15 loading or

    = 16,000lb for H20 & HS20 loading

(AASHTO 3.24.3, BM Sec 3.30.1.2-1)

CASE B: main reinforcement parallel to traffic

(1) simple span

HS20 loading:

Spans up to and including 50 feet LLM = 900S foot-pounds;

Spans 50 feet to 100 feet: LLM = 1,000 (1.30S×20.0) foot-pounds.

HS15 loading:

Use ¾ of the values obtained from the formulas for HS20 loading.

(2)   slabs continuous over more than two supports

Moments in continuous spans shall be determined by suitable analysis

using the truck or appropriate lane loading.

(AASHTO 3.24.3.2)

(c) compute moment due to live load + impact

The moment is decided as:

$M_{LL+I} = M_{LL} \times I$

where I = Impact coefficient

$$= \frac{50}{L+125} \leq 0.3 \qquad\qquad\qquad \textbf{\textit{(AASHTO 3.8.2.1)}}$$

L = Length in feet of the portion of the span that is loaded to produce the

maximum stress in the member.

STEP 4: Cantilever moment

(a) compute moment due to dead load

Moment induced by dead load can be expressed as follows:

Dead load Moment =Moment due to slab, future wearing surface (F.W.S) and

safety barrier curb (S.B.C.)

(b) compute moment due to live load + impact

Wheel Loads

The moment due to the wheel load can be computed as the following two cases:

> ***CASE A:*** reinforcement perpendicular to traffic

> > The moment due to live load and impact is:

> > $M_{LL+I} = P \times X/E$

> > where: P = wheel load (apply impact factor)

> > E = the effective length of slab resisting post loadings

> > = 0.8x+3.75

> > X = the distance in feet from load to point of support

CASE B: reinforcement parallel to traffic

The moment due to live load and impact is:

$M_{LL+I} = P \times X/E$

Where: $E = 0.35X + 3.2 \leq 7.0$ feet   *(AASHTO 3.24.5.1.2)*

Collision Loads

The moment due to the collision load can be computed as the follows:

$M_{COLL} = \dfrac{Py}{E}$

where: $P = 10$ kips (collision force)

$y = $ Moment arm (curb height + 0.5 slab thickness)

$E = 0.8X + 5.0$

where: $X = $ Dist. from C.G. of S.B.C. to support

Find the greater of the two (wheel load & collision load) for design load

$M_u = 1.3(M_{DL} + 1.67M_{LL+I})$

(BM Sec 3.30.1.2-1)

STEP 5: Determine the design moment

Use the bigger one of the cantilever moment and the interior moment as the design moment.

STEP 6: Protective against Corrosion

3 inches clear cover preferred minimum for cast-in-place, 2-3/4 inches clear cover preferred minimum for prestressed panels to accommodate No.8 bars over supports and 2-1/2 inches clear cover absolute minimum by AASHTO 8.22.1.

(BM Sec 3.30.1.2-1A)

STEP 7: Determine the top transverse reinforcement

By the normal design equations for the reinforced members, the transverse reinforcement can be decided as follows:

(1) $\phi M_n = A_S f_y (d - \dfrac{a}{2})$

$a = A_s f_y / (0.85 f_c' b)$

(AASHTO 8.16.3)

(2) Check ρ_{max} & ρ_{min}

$\rho_{max} = 0.75 \rho_b$

$= 0.75[\dfrac{0.85 \beta_1 f_c'}{f_y}(\dfrac{87,000}{87,000 + f_y})]$

(AASHTO 8.16.3)

The minimum reinforcement shall provide:

$\rho_{min} = 1.67(\dfrac{h}{d})^2 \dfrac{\sqrt{f_c'}}{f_y}$

STEP 8: Bottom transverse reinforcement

For design of the bottom transverse reinforcement, the following applied:

(a) Assume the positive moment is the same as the negative moment

(b) Remove 1.0 inch of wearing surface from the effective depth.

Note: When using prestressed panels, P/S panels replace the bottom transverse reinforcement.

(BM Sec. 3.30.1.2-1)

STEP 9: Longitudinal distribution reinforcement

Distribution reinforcements include the reinforcements for shrinkage and temperature and over the supports, as shown in Figure 2.2.

(a)   Top of Slab

Use # 5 bars at 15 in. spacing for temperature distribution, as shown in Figure 2.2.

(BM Sec. 3.30.1.2-1A)

(b) Bottom of Slab

The distribution reinforcement at the bottom is decided as follows and shown in Figure 2.2.
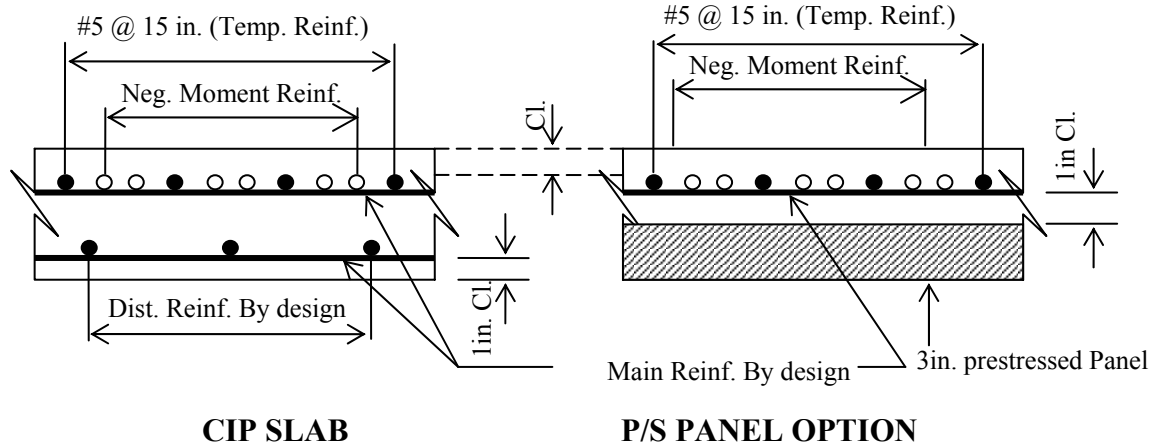
Figure 2.2.   Distribution Reinforcement (Gupta, 2001)
Note: cl.=Clear Cover
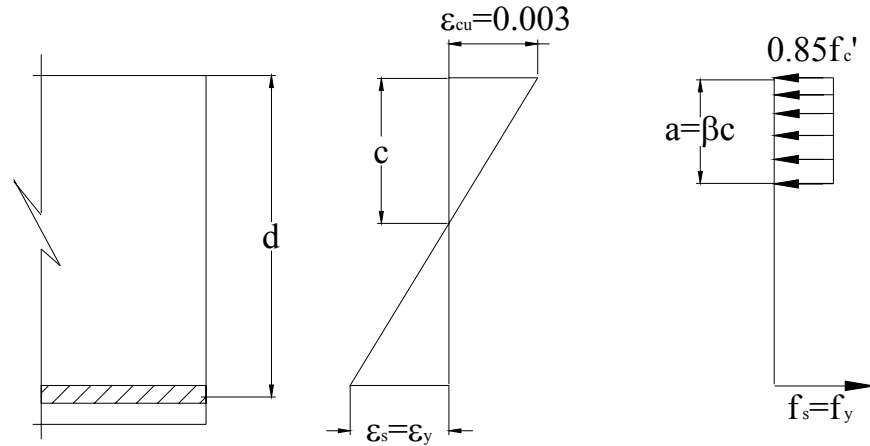
(1). For main reinforcement parallel to traffic

$$\text{Percentage} = \frac{100}{\sqrt{s}} \leq 50\%$$

(2). For main reinforcement perpendicular to traffic

$$\text{Percentage} = \frac{220}{\sqrt{s}} \leq 67\%$$

where S = the effective span length in feet

(AASHTO 3.24.10)

STEP 10: Negative moment reinforcement over supports

For slabs on steel girder, add #6 bars at 5 in. between #5 bars.

(AASHTO 10.38.4)

STEP 11: Serviceability Requirement

The same method is adopted as AASHTO to control the crack width.

(1) Allowable Stress

$$f_{s,allow} = \frac{Z}{(d_c \times A)^{1/3}} \leq 0.6 f_y$$

where: Z=130 k/in.

d_c = Distance from extreme tension fiber to center of closest bar (concrete cover shall not be taken greater than 2)

A = Effective tension area of concrete

= $2d_c S$

S = Bar spacing center to center

(2) Actual Stress

$$f_s = \frac{M_w}{A_s \times j \times d};$$

where: M_w =Service load moment;

A_s =Area of steel;

j=moment arm coefficient

$$k = \sqrt{(n\rho)^2 + 2n\rho} - n\rho;$$

$$\rho = \frac{A_s}{bd};$$

b= Effective width;

d= Effective depth;

(3) Check   *(BM Sec. 3.30.1.2-1A)*

$f_s \leq f_{s,allow}$

2.2.2.3. AASHTO LRFD. AASHTO LRFD Bridge Design Specifications, first published in 1994, is based on load resistance factors and employs the load and resistance factor design (LRFD) methodology. The factors have been developed from the theory of reliability based on current statical knowledge of loads and structural performance.

STEP 1: Determine the deck thickness

$$t_{deck} = \frac{S+10}{30}.$$

Where S = the girder spacing. The minimum required deck thickness, excluding provisions for grinding, grooving, and sacrificial surface is t_{deck} = 7.0 in.

(LRFD Table 2.5.2.6.3-1, LRFD 9.7.1.1)

STEP 2: Compute the effective length

STEP 3: Determine unfactored dead loads

For simplicity, the deck will be designed as a one-foot wide one way slab. Therefore, all loads will be determined on a per foot width.

STEP 4: Determine unfactored live loads

a) Wheel load:

Truck axle load = 32 kips/axle

The axle load of 32 kips is distributed equally such that each wheel load is 16 kips.

(LRFD 4.6.2.1, 3.6.1.3.3, 3.6.1.2.2)

b) Calculate the number of live load lanes

Generally, the number of design lanes should be determined by taking the integer part of the ratio w/12.0, where w is the clear roadway width in FT between curbs and/or barriers.

(LRFD 3.6.1.1.1)

c) Determine the wheel load distribution

The width of the primary strip is listed in Table 2.2.

Table 2.2. Width of the Primary Strip

Type of Deck	Direction of Primary Strip Relative Traffic	Width of Primary Strip (in)
Concrete: • Cast-in-place	Overhang Either Parallel or Perpendicular	45.0 + 10.0x +M: 26.0 + 6.6s -M: 48.0 + 3.0s
• Cast-in-place with stay-in-place concrete formwork	Either Parallel or Perpendicular	+M: 26.0 + 6.6s -M: 48.0 + 3.0s
• Precast, post-tensioned	Either Parallel or Perpendicular	+M: 26.0 + 6.6s -M: 48.0 + 3.0s

(LRFD 4.6.2.1, Table 4.6.2.3-1, 4.6.2.1.3)

d) Determine the live loads on one foot strip:

The unfactored wheel loads placed on a one foot strip based on the width of the strips, that is, 16 kips/w, where w = the width of primary strip.

STEP 5: Determine the wheel load location to maximize the live-load

moment

Apply the unfactored loads to a continuous one-foot-wide beam spanning across the girders and find the maximum moment value.

The design section for negative moments may be taken as follows: one-quarter the flange width from the centerline of support for steel beam.

(LRFD 4.6.2.1.6)

STEP 6: Determine the load factors

The factored load can be decided as follows:

$$Q = \eta \sum \gamma_i q_i$$

where Q = factored load

η = load modifier

γ = load factor

q = unfactored loads

(LRFD 1.3.2.1, 3.4.1)

(a) Load modifier

The load modifier, η, used in the above equation can be calculated as follows:

$\eta = \eta_D \eta_R \eta_i > 0.95$

where for strength limit state

$\eta_D = 1.05$ for non-ductile components and connections

$= 0.95$ for ductile components and connections

$\eta_R = 1.05$ for non-redundant members

$= 0.95$ for redundant members

For other limit state

$\eta_D = \eta_R = 1.0$

$\eta_i \geq 1.05$ if a bridge is deemed of operational importance

$\eta_i \geq 0.95$ otherwise

(LRFD 1.3.3, 1.3.4, 1.3.5)

(b) Load factor

Load factors are listed in Table 2.3.

Table 2.3. Load Factors

	Maximum Load Factor	Minimum Load Factor
Slab and barrier rail	$\gamma_{DCmax} = 1.25$	$\gamma_{DCmin} = 0.90$
Future wearing surface	$\gamma_{Dwmax} = 1.50$	$\gamma_{Dwmin} = 0.65$

$\gamma_{LL} = 1.75$

$\gamma_{IM} = 1.75$ (Strength-1 Load Combination)

(LRFD Table 3.4.1-1, Table 3.4.1-2, 3.4.1, 3.3.2)

(c) Multiple presence factor

$m_{1lane} = 1.20$, $m_{2lane} = 1.00$, $m_{3lane} = 0.85$, $m_{>3lane} = 0.65$

(LRFD Table 3.6.1.1.2-1)

(d) Dynamic load allowance

$IM = 0.33$

(LRFD 3.6.1.2, 3.6.2)

STEP 7: Calculate the factored moments

$$M_u = \eta[\gamma_{DC}(M_{DD}) + \gamma_{DC}(M_{DB}) + \gamma_{Dw}(M_{DW}) + (m)(1 + IM)(\gamma_{LL})(M_{LL})$$

As specified in *LRFD 4.6.2.1.1*, the entire width of the deck should be designed for these maximum moments.

STEP 8: Determine the slab reinforcement detailing requirements

(a) Determine the top deck reinforcement cover

The top deck requires a minimum cover of 2 in. over the top mat reinforcement (when exposing to deicing salt, 2.5 in.), unless environment conditions at the site require additional cover. This cover does not include additional concrete placed on the deck for sacrificial purposes, grooving, or grinding.

The cover of the bottom of the cast-in-place slabs is 1.0 in. for steel bar up to No. 11 and 2.0 in. for No. 14 to No. 18.

(LRFD Table 5.12.3-1)

(b) Determine deck reinforcement spacing requirements

$S \leq 1.5 \times t$ (t = thickness of slab) and S <18 in.

The minimum spacing of reinforcement is determined by *LRFD 5.10.3.1* and is dependent on the bar size chosen and aggregate size.

(LRFD 5.10.3.2)

(c) Determine distribution reinforcement requirements

Reinforcement is needed in the bottom of the slab in the direction of the girders in order to distribute the deck loads to the primary deck slab reinforcement.

Reinforcement should be placed in the secondary direction in the bottom of the slabs as a percentage of the primary reinforcement for positive moment as follows:

- For primary reinforcement parallel to traffic:

  $100/\sqrt{S} \leq 50\%$

- For primary reinforcement perpendicular to traffic:

$$220/\sqrt{S} \le 67\%$$

where S = the effective span length taken as equal to the effective length specified in Article 9.7.2.3 (in unit of foot)

(LRFD 9.7.3.2)

(d) Determine the minimum top slab reinforcement parallel to the girders

Reinforcement for shrinkage and temperature stresses should be provided near surfaces of concrete exposed to daily temperature changes and in structural mass concrete.

The top slab reinforcement should be a minimum as required for shrinkage and temperature of $0.11A_g/f_y$. And it should not be spaced farther than either 3.0 times the slab thickness or 18 inches.

(LRFD 5.10.8.2)

STEP 9: Check serviceability

The same method is adopted as previous design procedures.

$$f_{sa} = \frac{Z}{(d_c A)^{1/3}} \le 0.6f_y$$

where A = effective tension area, in square inches, of concrete surrounding the flexural tension reinforcement and having the same centroid as that reinforcement, divided by the number of bars or wires. When the flexural reinforcement consists of several bar or wire sizes, the number of bars or wires shall be computed as the total area of reinforcement divided by the largest bar or wire used. For calculation purposes, the thickness of the clear concrete cover used to compute A should not be taken greater than 2 inches.

d_c = distance measured from extreme tension fibre to center of the closest bar or wire in inches. For calculation purposes, the thickness of the clear concrete cover used to compute d_c shall not be taken greater than 2 inches.

$Z \leq 170$kips/in. for members in moderate exposure conditions, which corresponding to the limitation of crack width of 0.016 in.

≤ 130kips/in. for members in severe exposure conditions, which corresponding to the limitation of crack width of 0.013 in.

(LRFD 5.7.3.4)

2.2.3. Summary of the Design Procedures. A summary of the design procedures of the typical girder bridge deck is shown in Table 2.4.

Table 2.4. Bridge Deck Design Procedures

AASHTO Standard Spec.	AASHTO LRFD	MODOT	NOTES
Step1: Choose general parameters	Step1: Choose general parameters	Step1: Choose general parameters	**AASHTO**: $\dfrac{S+10}{30}\,ft$; **MoDOT**: 8.5 in. for C.I.P
Step 2: Compute effective span length	Step 2: Compute effective span length	Step 2: Compute effective span length	
Step 3: Compute moment due to dead load	Step 3: Determine unfactored dead load	Step 3: Determine moment over interior support	**1. LFD**: $M_{LL}=\dfrac{S+2}{32}P$; **LRFD**: Based on structural analysis. Loads are applied to a continuous 1-ft-wide beam spanning across the girder. Wheel load= 16 kips/W, where W is the width of primary strip.
Step 4: Compute moment due to live load + impact	Step 4: Determine unfactored live load	Step 4: Determine cantilever moment	
Step 5: Compute factored bending moments	Step 5: Calculate unfactored moments	Step 5: Determine design moments	**2. LFD**: $I=\dfrac{50}{L+125}\le 0.3$; **LRFD**: IM=0.33
	Step 6: Determine the load factors		**3. LFD**: M_u= 1.3(M_{DL}+1.67M_{LL+I}); **LRFD**:
	Step 7: Calculate factored moments		$M_u = \eta[\gamma_{DC}(M_{DD})+\gamma_{DC}(M_{DB})$ $+\gamma_{Dw}(M_{DW})+(m)(1+IM)(\gamma_{LL})(M_{LL})$
Step 6~10: Determine reinforcement in details (main reinforcement, bottom distribution reinforcement, shrinkage and temperature reinforcement, reinforcement over supports	Step 8: Determine reinforcement in details	Step 6~10: Determine reinforcement in details	**1.Temperature reinforcement:** **AASHTO**: $A_s \ge 1/8$ $Spacing \le 3slab \le 18"$ **MODOT**: #5 @ 15" **2.Reinforcement over support:** **AASHTO**: $A_s \ge 0.01A_g$ **MODOT**: #6 @ 5" between # 5 bars **3. Cover** **AASHTO**: 2.5" for exposing to deicing salts. **MODOT**: 3" for C.I.P
Step 11: Check serviceability	Step 9: Check serviceability	Step 11: Check serviceability	

3. EXPERIMENTAL PROGRAM

3.1. DETAILS OF THE EXPERIMENTAL PROGRAM

In this research program, the structural performances of the steel-free hybrid reinforcing system will be extensively investigated. The overall experimental study plan includes (1) laboratory studies of static and fatigue bond performances between FRP and FRC hybrid system; (2) laboratory studies of static and fatigue flexural characteristics for this hybrid system; (3) accelerated durability tests of the hybrid system; and (4) static and fatigue tests on full-scale hybrid reinforced composite bridge decks.

3.1.1. Studies of Bond Characteristics. Bond is essential for reinforced concrete structures. Three test methods are commonly used to study the bond characteristics: namely, pullout test, splitting bond test, and flexural beam test. These test methods provide information to bond behaviors. The pullout test can clearly represent the concept of anchorage and is usually adopted to study the bond behavior between rebar and concrete. Although the pullout test puts concrete in compression and the reinforcing bar in tension, a stress condition that is not representative of a RC beam or a bridge deck, a reasonable correlation was found between structural performance and measures of performance in the pullout test (Cairns and Abdullah, 1995). The splitting bond test can be used to study the splitting bond behavior under different cover thicknesses. The effect of the transverse reinforcement on bond behavior can be avoided when properly designed. The splitting bond test can simulate the stress field of real structures to some extent. The flexural beam test has the advantage of representing an actual stress field in real beams and slabs and the cover effects on bond. However, it requires considerable confining

reinforcement to avoid a shear failure, and so bond splitting failures may not occur (Cairns and Plizzari, 2003). In this testing program, all three types of bond tests were investigated and their results were compared.

3.1.1.1. Bond study by pullout test method. Test specimens, test setup, and test procedures are discussed in the following sections.

3.1.1.1.1. <u>Pullout test specimens.</u> A total of 45 pullout specimens were studied. The experimental variables included FRP rebar type (CFRP vs. GFRP), FRP rebar size (#4 vs. #8), concrete with or without polypropylene fibers, embedment length, and the loading conditions (monotonic vs. fatigue). Specimens were divided into 15 groups, as shown in Table 3.1.

The notation for specimens is as follows: the first character ("P" or "F") indicates the plain concrete or FRC; the second character ("C" or "G") indicates the rebar type, CFRP or GFRP; the third character (#4 or #8) is the bar size in US designation; the fourth character ("05" or "10") refers to the embedment length in the bar diameter d_b; the last character ("M" or "F") represents monotonic or fatigue loading.

Test specimens were designed according to RILEM recommendations (International Union of Laboratories and Experts in Construction Materials, Systems and Structures) with a 5 d_b embedment length (some with 10 d_b to study the effect of different embedment lengths), which was generally assumed to be able to represent local bond behavior. FRP rods were embedded in concrete to a predetermined length, l_d, in the concrete block. PVC pipe was used as a bond breaker at the first $5d_b$ length to minimize the bottom plate's restraint effect on the FRP rebar and to eliminate any undesirable confinement that may affect bond characteristics. More details are shown in Figure 3.1.

Table 3.1. Details of Pullout Specimen

Loading Conditions	Specimen I.D.	Materials	V_f (%)	l_d/d_b
Plain Monotonic	PC405M	#4 CFRP	0	5
	PG405M	#4 GFRP	0	5
	PG805M	#8 GFRP	0	5
FRC Monotonic	FC405M	#4 CFRP	0.5	5
	FC410M		0.5	10
	FG405M	#4 GFRP	0.5	5
	FG410M		0.5	10
	FG805M	#8 GFRP	0.5	5
	FG803M		0.5	3
Plain Fatigue	PC405F	#4 CFRP	0	5
	PG405F	#4 GFRP	0	5
	PG805F	#8 GFRP	0	5
FRC Fatigue	FC405F	#4 CFRP	0.5	5
	FG405F	#4 GFRP	0.5	5
	FG805F	#8 GFRP	0.5	5

Note: Each testing group has three test specimens.

3.1.1.1.2. Test setup and procedures. In the following sections, the test setup and procedures for the static bond and fatigue bond are presented.

(A) Static pullout bond test. The pullout tests were conducted in an MTS 880 machine. The test was run through close-loop displacement control using an external LVDT 2 (Linear Variable Differential Transformer) as a feedback device (see Figure 3.1). Because the FRP rods were weak in the transverse direction, special anchorages were used to protect the rebar from crushing. The free end of the FRP rebar was embedded in a steel pipe using an expansive grout as an interface. The pullout was then performed by pulling the steel pipe at one end, with the concrete block being encased in the steel reaction frame, as shown in Figure 3.1. The rebar's slip relative to the concrete was computed from measurements of both LVDTs placed at both ends of the rebar, as shown
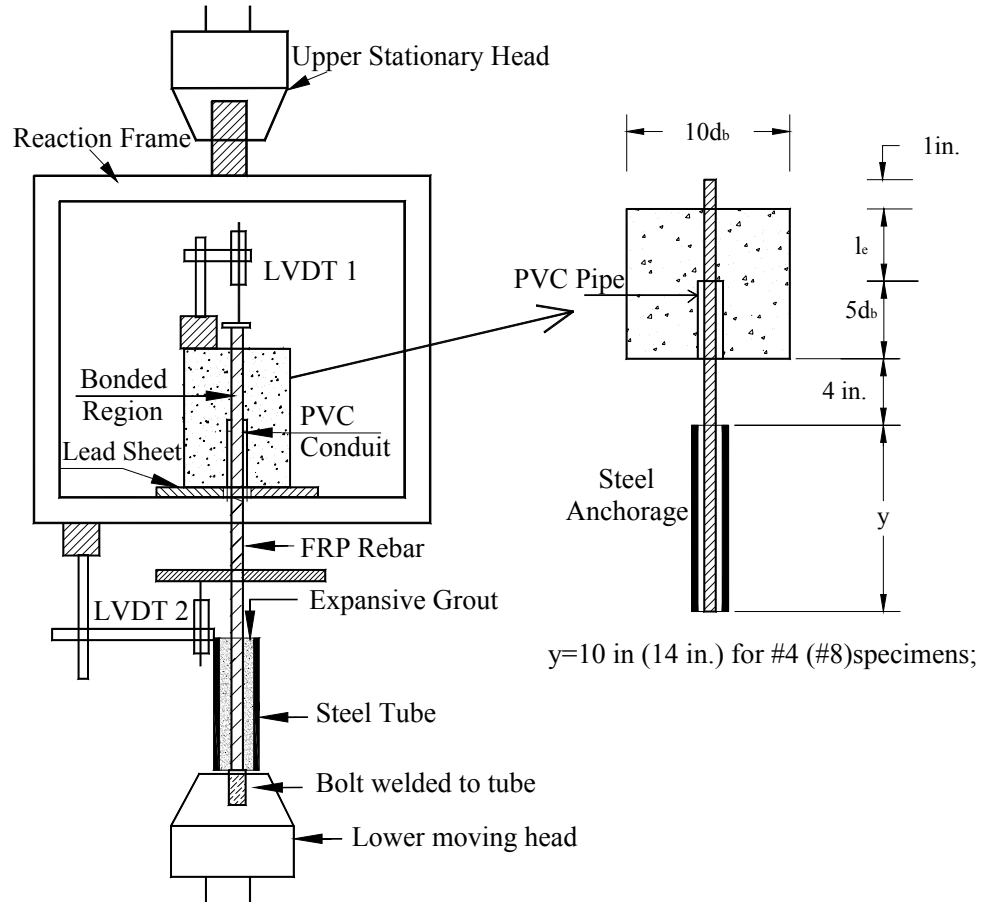
Figure 3.1. Pullout Test Specimen and Test Setup

in Figure 3.1. To minimize the eccentricity effect, lead sheets were placed between the concrete block and the reaction frame.

The pullout tests were monotonic by increasing the slip at 0.03 in/min rate. All measurements, including pullout load and displacements (slips), were recorded by a computer-controlled data acquisition system at the rate of 2 data/sec.

(B) Fatigue pullout bond tests. Fatigue tests were conducted under load control. A 5 Hz sinusoidal pattern of load cycles was used. Measurements, such as pullout load, slips at loaded end and slips at free end, were measured at 1, 10, 100, 1000, 10,000,

100,000, 500,000, and 1,000,000 cycles to study the residual slip development and progressive bond stiffness degradation. To eliminate the possible errors resulting from recording at high frequency, the loading frequency rate was reduced to 0.1 Hz. After reaching the maximum cycles of 1 million, the surviving specimens were subjected to monotonic pullout tests to failure.

- **Stress Range.** To simulate the real bridge loading conditions, a statistical analysis was conducted based on the MoDOT Bridge Design Manual (2001). A value of $\frac{M_{DL}}{M_u} = 5\%$ to 15%, $\frac{M_{DL} + M_{LL+I}}{M_u} = 45\%$ to 55% was calculated for the typical steel reinforced bridge deck. To avoid premature fatigue fracture of the FRP rebar before bond failure, the fatigue strength of the FRP rebar, which was much lower than its static strength, was also taken into account. ACI 440 recommends $0.20f_{fu}$ for GFRP and $0.55f_{fu}$ for CFRP, respectively. Based on the above considerations, a stress range of 10% to 60% ultimate bond strength was selected for #4 GFRP and #4 CFRP and 0% to 40% for #8 GFRP.

- **Frequency of Loading.** The actual rate of fatigue loading on a highway bridge has been reported as 0.5 to 1.0Hz, depending on the traffic (Demers, 1998; Mays and Tilly, 1982). Considerable heat is generated at high loading frequencies, and it reduces the fatigue life (Admi et al., 2000). Frequencies of fatigue loading under 4 or 5 Hz have been reported to produce negligible internal heating in glass FRP composites (Demers, 1998). To allow tests to be completed within a reasonable amount of time, a conservative frequency rate of 5Hz was chosen. At the rate of 5Hz, it took up to 3 days to run one test.

3.1.1.2. Bond Study by splitting test method. In the following sections, the test specimens, test setup, and the test procedures are discussed.

3.1.1.2.1. Splitting bond test specimens. A total of 24 specimens were investigated for the splitting bond tests. The experimental variables included FRP rebar size (#4 or #8), concrete cover depth, and concrete with or without polypropylene fibers.

The notation for the specimens is as follows: the first character (#4 or. #8) is the bar size in English designation; the second character ("P" or "F") indicates the plain concrete or FRC; the third character ("C" or "G") indicates the rebar type, CFRP or GFRP; the last character ("1" or "3") refers to the clear cover depth in the bar diameter, d_b. Specimens were divided into 12 groups, as shown in Table 3.2.

Table 3.2. Beam End Specimen Details

Specimen I.D.	Rebars	Embedment length l_d (in.)	Volume fraction V_f (%)	Cover C (in.)
4PG1	#4GFRP	$10d_b=5$	0	$1d_b=0.5$
4PG3		$10d_b=5$	0	$3d_b=1.5$
4FG1		$10d_b=5$	0.5	$1d_b=0.5$
4FG3		$10d_b=5$	0.5	$3d_b=1.5$
4PC1	#4CFRP	$10d_b=5$	0	$1d_b=0.5$
4PC3		$10d_b=5$	0	$3d_b=1.5$
4FC1		$10d_b=5$	0.5	$1d_b=0.5$
4FC3		$10d_b=5$	0.5	$3d_b=1.5$
8PG1	#8GFRP	$10d_b=10$	0	$1d_b=1$
8PG3		$10d_b=10$	0	$3d_b=3$
8FG1		$10d_b=10$	0.5	$1d_b=1$
8FG3		$10d_b=10$	0.5	$3d_b=3$

Note: Each testing group has two test specimens.

Specimens were designed based on ASTM A944 specifications. No. 4 specimens

consisted of #4 CFRP and #4 GFRP with dimensions of 9 in.×14 in.×24 in. No. 8

specimens consisted of No. 8 GFRP with dimensions of 9 in.×17 in.×24 in. Two PVC

pipes were used to cover the two ends of the testing rebar as bond breakers so as to adjust

the test embedment length to 10 d_b, as shown in Figure 3.2. Four closed stirrups were

used to increase shear strength of the No. 8 GFRP specimens. The stirrups were oriented

parallelly, rather than perpendicularly, to the side of specimens to eliminate their effect

on a splitting bond failure. This kind of specimen is thought to be especially good for

testing bond strength in bridge deck systems, where no stirrups are usually used. Steel

bars were also used as auxiliary flexural reinforcement (two No. 4 steel bars were used in

#4 specimens and two No. 6 steel bars for No. 8 specimens) to increase the flexural

capacity of the specimens, so that the failure of the specimens would be controlled by

bond. The specimens also contained two No. 5 steel rebars to ease fabrication and testing.

3.1.1.2.2. <u>Test setup and procedures.</u> Specimens were tested in a test setup, as

shown in Figure 3.3. A special steel frame with an opening at the front face was

fabricated. It was fixed to a steel beam, which was tied down to the laboratory floor. Due

to the weakness of the FRP in the transverse direction, an anchorage was developed at the

loaded end to protect the rebar from being crushed directly. The loaded-end of the rebar

was inserted through the opening of the steel frame, a hydraulic jack, a load cell, and a

spacer steel plate. The anchor served as part of the reaction frame to resist the pullout

load applied by the hydraulic jack and also to transfer the pullout load to the rebar. The

load cell was sandwiched between the hydraulic jack and the steel pipe, and it was used

to measure the pullout load. Relative slips between the rebar and concrete were measured

Figure 3.2. Beam End Specimen Details

(1) Units are in inches.

(2) Stirrups are used only in #8 specimens; for No.4 specimens, no additional stirrups are provided.
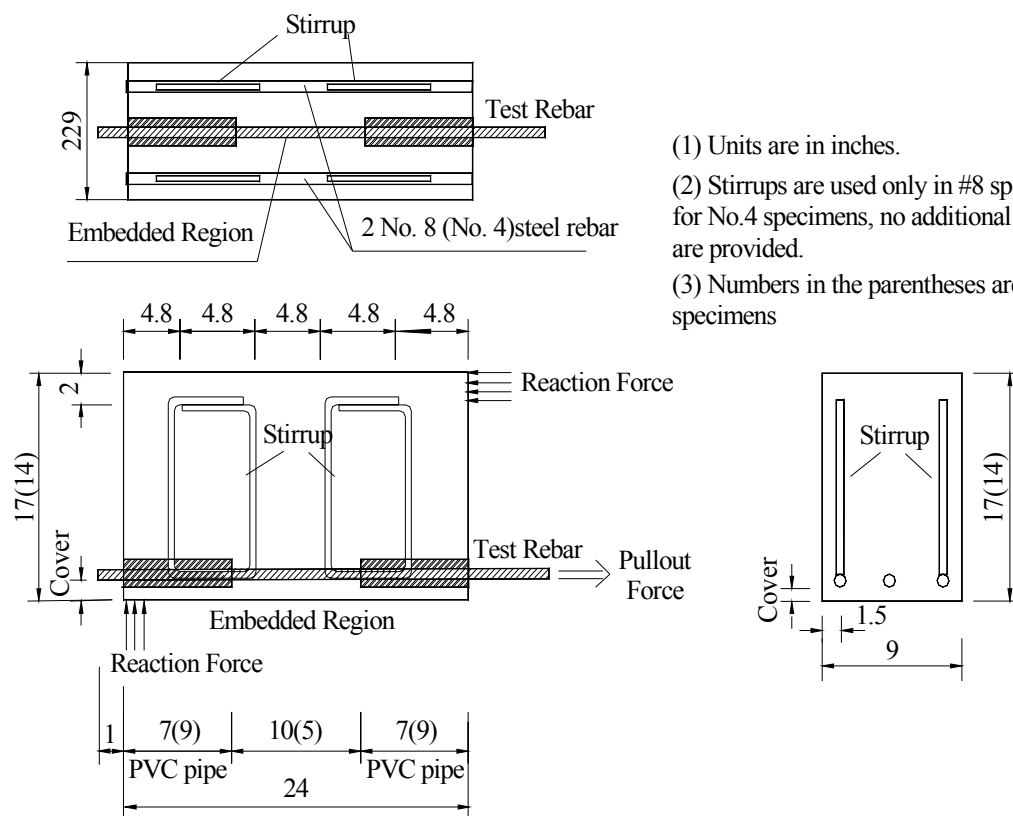
(3) Numbers in the parentheses are for No.4 specimens

by LVDTs attached to both ends of the rebar. All measurements, including the pullout load and displacements (slips), were recorded by a computer-controlled data acquisition system at the rate of 2 data/sec. This testing scheme successfully solved the grip problem induced by the weak characteristics of the FRP rebar in the transverse direction. It also simplified the test setup compared to the recommendations by the ASTM A-944 specifications.

3.1.2. Studies of Ductility Characteristics. In this study, several issues regarding flexural behaviors were addressed, including mid-span deflection, curvature, crack width, crack distribution, and relative slip of the longitudinal rebar to the concrete.
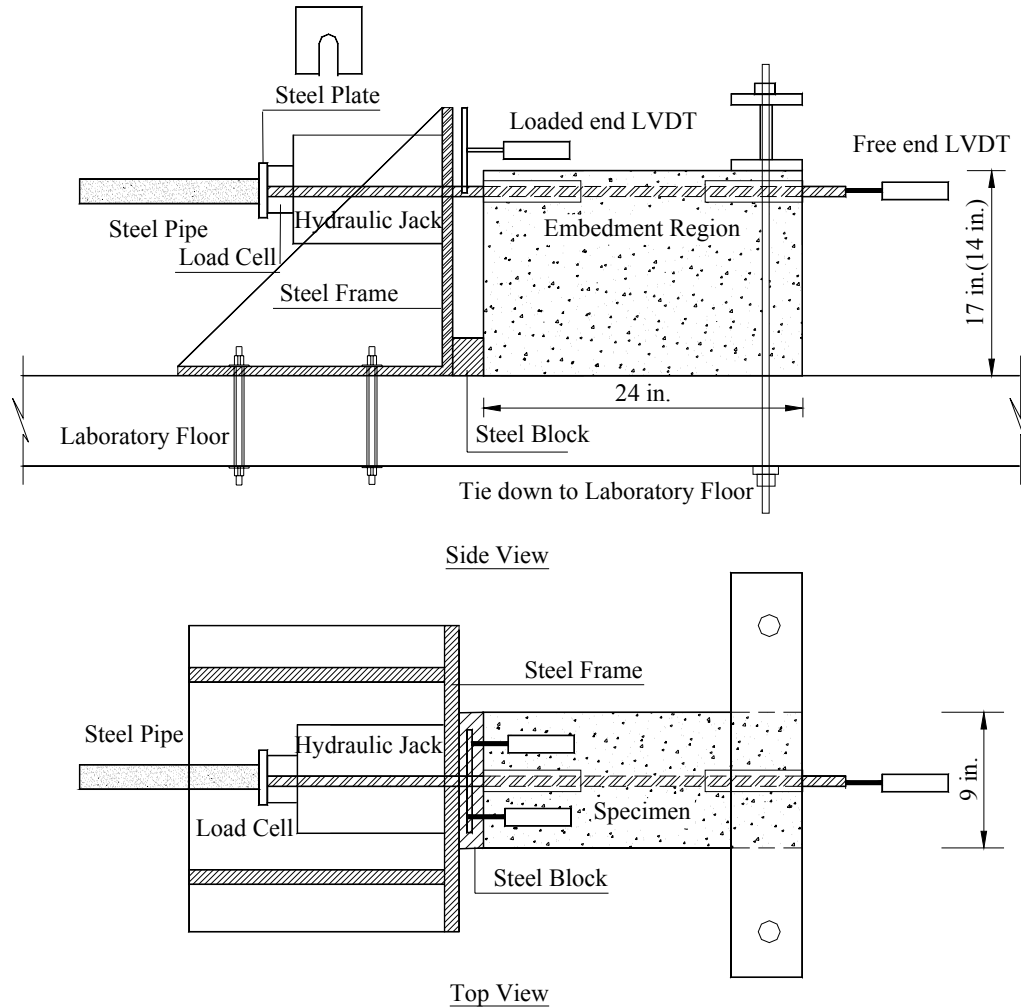
Figure 3.3. Test Setup of Beam End Tests

Also, the energy absorption capacity of this hybrid system was studied by loading/unloading at load level of 45% and 90% of its ultimate capacity. The residual deflection and crack width caused by the loading/unloading cycles were also discussed.

A total of 12 beams making 6 testing groups was investigated. Each testing group was composed of two similar beams, one subjected to monotonic loading and the other to repeated loading/unloading. The experimental variables included FRP rebar size (#4 vs. #8), rebar type (GFRP vs. CFRP), and Plain concrete vs. FRC.

3.1.2.1. Test specimens. The beams were 7 in. wide, 9 in. high, and 72 in. long. To avoid shear failure, traditional #3 steel U-shape stirrups with a spacing of 89 mm were used as shear reinforcement at both ends of the beams. To minimize the confining effect of the shear reinforcement on the flexural behaviors, no stirrups were used in the testing regions (pure bending regions). A concrete clear cover of 1.5 in. was used for all the beams. All beams were designed to fail by concrete crushing, as recommended by the current ACI 440. This was accomplished by using a reinforcement ratio greater than the balanced reinforcement ratio ρ_b. Specimen details are shown in Figure 3.4.
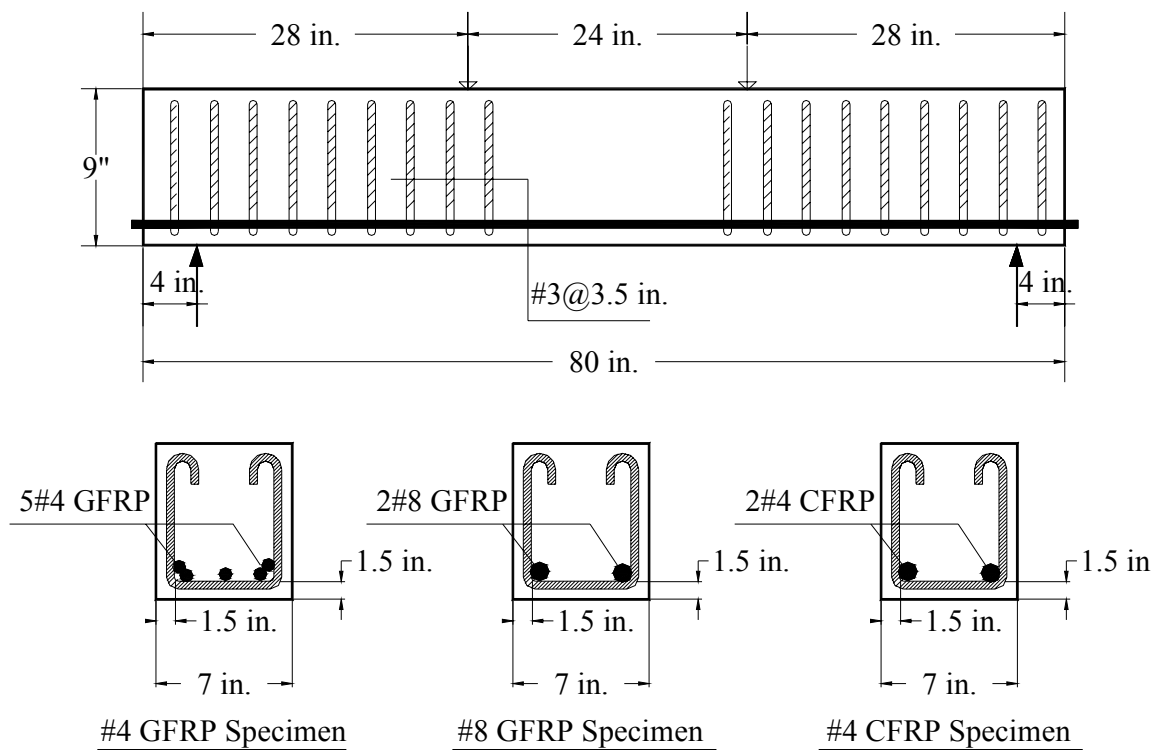
Figure 3.4. Beam Specimen Details

The notation for the specimen's identification is as follows: the first character "V"
means the unweathered specimens without being subjected to accelerated environmental
conditioning (this notation is for the convenience of the Section 5); the second character,
"P" or "F", indicates the plain concrete or FRC; the third character, "4" or "8", is the
rebar size in English designation used as reinforcement; the fourth character, "C" or "G",
indicates the rebar type, CFRP or GFRP, and the last character represents the first beam
or the second beam in the testing group. Details of the specimens are shown in Table 3.3.

Table 3.3. Flexural Beam Test Matrix

I.D.	f'c (psi)	A_f (in^2)	ρ_f / ρ_{fb}	V_f (%)
VP4G-1	7000	5#4=1.12	3.51	0
VP4G-2	7000	5#4=1.12	3.51	0
VP8 G-1	7000	2#8=1.67	3.6	0
VP8G-2	7000	2#8=1.67	3.6	0
VP4C-1	7000	2#4=0.34	3.16	0
VP4C-2	7000	2#4=0.34	3.16	0
VF4G-1	4400	5#4=1.12	4.71	0.5
VF4G-2	4400	5#4=1.12	4.71	0.5
VF8 G-1	4400	2#8=1.67	4.83	0.5
VF8G-2	4400	2#8=1.67	4.83	0.5
VF4C-1	4400	2#4=0.34	4.24	0.5
VF4C-2	4400	2#4=0.34	4.24	0.5

3.1.2.2. Test setup and procedures. Beams were subjected to a four-point
flexural testing, as shown in Figure 3.5. Beams were instrumented with three LVDTs in
the testing region (pure bending region) to monitor the mid-span deflection and determine
curvature. FRP rebars were instrumented with strain gauges to measure rebar deformation.

Two LVDTs were mounted at the top surface of the beam to record the compressive

concrete strain. In the testing region, Demac gages were bonded to the beam surface, 38

mm above the bottom (the same level as the longitudinal rebars) to measure the crack

widths. A microscope was also used to measure the crack width at the rebar location.

Another two LVDTs were mounted at the ends of the beam to record the relative slips

between the longitudinal rebar and the concrete (the longitudinal rebars were protruded

about 10 mm from the ends). Load was applied in increments by hydraulic jack and

measured with a load cell. Three increments were taken up to the initiation of cracking

and ten increments up to failure. At the end of each load increment, the load was held

constant, crack patterns were photographed, and near mid-span crack widths were

recorded.
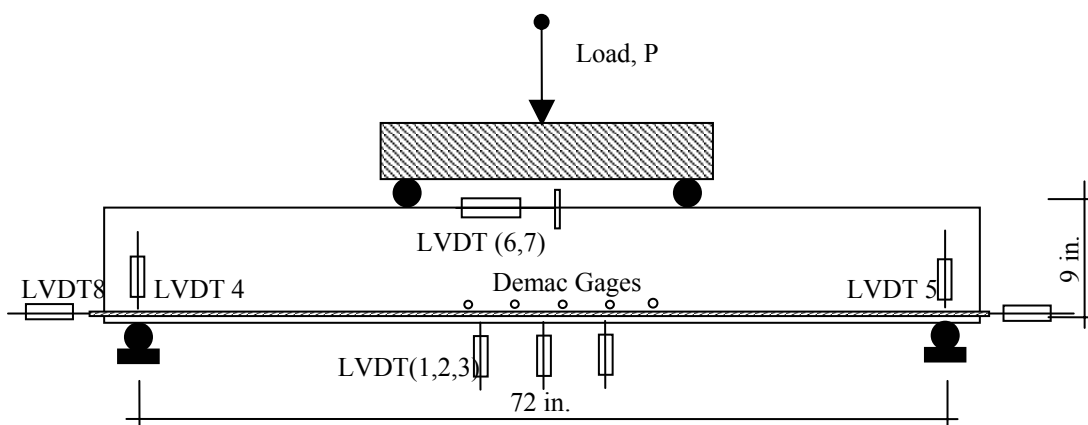
Figure 3.5. Flexural Beam Test Setup

Each testing parameter was investigated using two identical specimens, as shown

in Table 3.3. One beam was loaded monotonically to failure. The other beam was

subjected to loading/unloading cycles at 40% and 80% of its capacity to evaluate the residual deflection, residual crack width, as well as the energy absorption capacity.

3.1.3. Studies of Durability Characteristics. Composite materials offer many advantages, such as corrosion resistance, and their use in bridge decks has become more technically attractive and economically viable. However, long-term performances have to be investigated and clearly understood with confidence before its application in the field.

3.1.3.1. Test specimens. Details of the bond specimens and the beam specimens are presented in the following sections.

3.1.3.1.1. Bond specimens. Dimensions of test specimens were the same as the specimens described in Chapter 3.1.1.

Chemical agents will attack the reinforcing materials as well as the bond between the concrete and the reinforcing materials. In RC structures, cracks exist under service conditions. The degradation effect is expected to be more pronounced at locations where cracks exist. As shown in Figure 3.6, bond stress distribution along half of the crack spacing in the beam specimen is similar to that in the pullout bond specimen. Because the portion between the cracks is not directly in contact with solution, to better simulate the real situations, the portion at the loaded end of the bond specimens was directly exposed to salt water, while the portion at the free end was coated with water-proof epoxy to protect it from direct attack from salt water, as shown in Figure 3.7. Since the epoxy could induce unwanted mechanical anchorages and change the bond behavior when the rebar was pulled out, all the epoxy that stuck to the rebar was removed after the environmental conditioning.
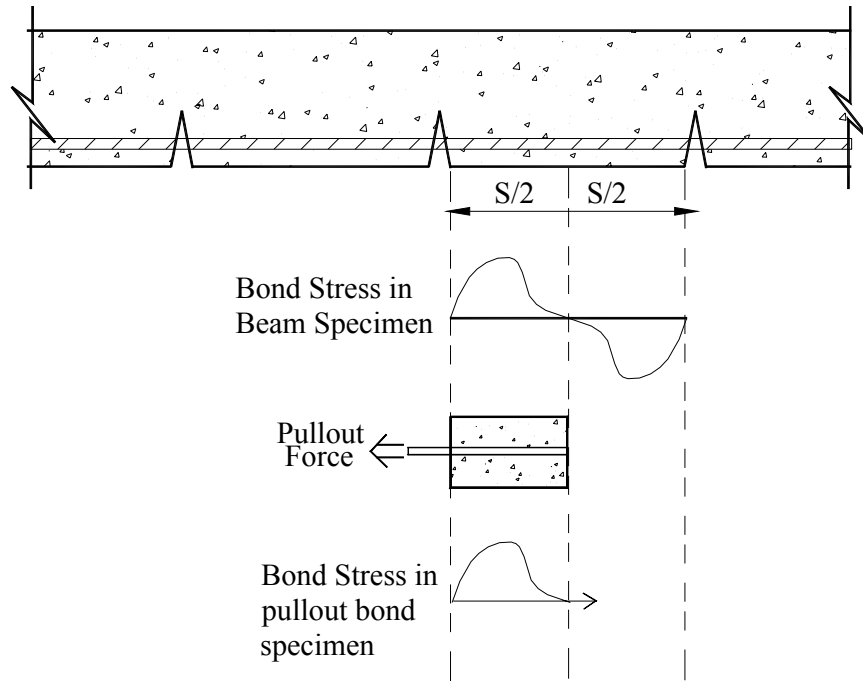
Figure 3.6. Bond Stress Distribution in Beam Specimen and Pullout Specimen
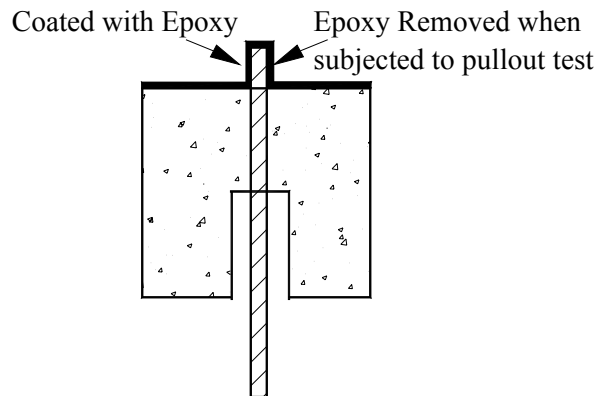
Figure 3.7. Pullout Specimens Coated with Epoxy at Free End

The notation for specimens is as follows: the first character, "V" or "D", indicates

the unweathered specimen or durability specimen; the second character, "P" or "F",

indicates the plain concrete or FRC, the third character (#4 vs. #8) is the bar size in US

designation, and the fourth character, "C" or "G", indicates the rebar type, CFRP or

GFRP. The test matrix of the bond specimens is shown in Table 3.4.

Table 3.4. Durability Bond Test Matrix

Specimen I.D.	Number of Specimens	f'c (psi)	V_f (%)	l_d/d_b
VP4C	3	6,900	0	5
VP4G	3	6,900	0	5
VP8G	3	6,900	0	5
VF4C	3	5,360	0.5	5
VF4G	3	5,360	0.5	5
VF8G	3	5,360	0.5	5
DP4C	3	6,900	0	5
DP4G	3	6,900	0	5
DP8G	3	6,900	0	5
DF4C	3	5,360	0.5	5
DF4G	3	5,360	0.5	5
DF8G	3	5,360	0.5	5

3.1.3.1.2. Beam specimens. The dimensions of the beams specimens were the

same as the beams described in Chapter 3.1.2.

As mentioned previously, cracks usually exist in the concrete structures under

service conditions. Cracked structures will be much more susceptible to environmental

attack than the intact ones. To represent realistic conditions, three artificial cracks for

each beam were fabricated, as shown in Figure 3.8. Those cracks were 0.024 in. wide (a

limitation of 0.020 in. for exterior exposure by ACI 440), 1.5 in. deep (cracks reaching

the rebars) and 8 in. in spacing. This was accomplished by putting 0.024 in. thick and 1.5

in. wide stainless steel sheets underneath the longitudinal rebars before casting the

concrete. Once the concrete had hardened, the steel plates were pulled out. Artificial

seams were thus created to simulate the concrete cracks.
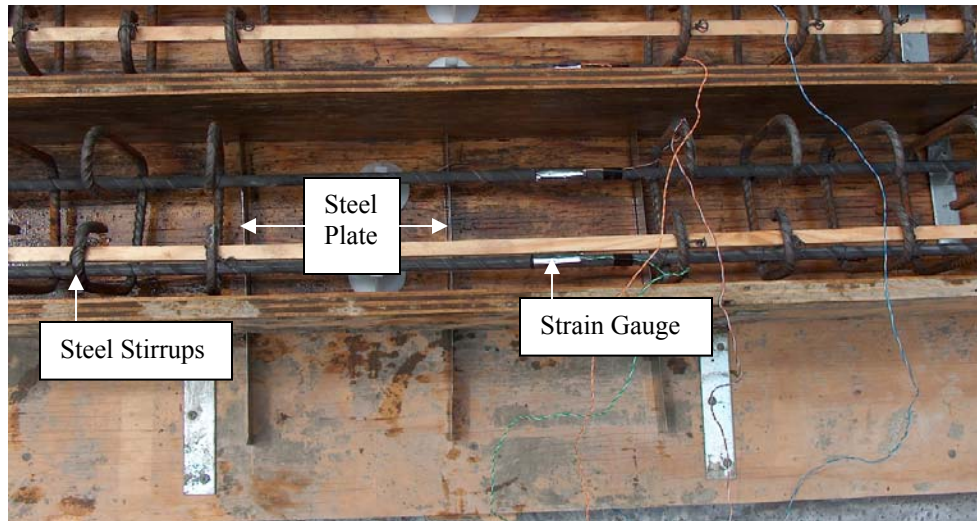
Figure 3.8. Artificial Cracks Created by Steel Plate

The notation for the specimens is as follows: the first character, "V" or "D",

indicates the unweathered specimens or durability specimens; the second character, "P"

or "F", indicates the plain concrete or FRC; the third character, "4" or "8", is the rebar

diameter in US designation; the fourth character, "C" or "G", indicates the rebar type,

CFRP or GFRP. The test matrix of the beam specimens is shown in Table 3.5.

3.1.3.2. Test setup and procedures. In the following sections, details about the

test setup and procedures are presented.

3.1.3.2.1. Bond tests. The bond test procedures are the same as those of the

pullout bond test described in Chapter 3.1.1.

Table 3.5. Durability Beam Test Matrix

Specimen I.D.	Number of Specimens	f_c' (psi)	A_f (in²)	ρ_f / ρ_{fb}	V_f (%)
VP4G	2	6900	5#4=1.12	3.51	0
VP8 G	2	6900	2#8=1.67	3.6	0
VP4C	2	6900	2#4=0.34	3.16	0
VF4G	2	4400	5#4=1.12	4.71	0.5
VF8 G	2	4400	2#8=1.67	4.83	0.5
VF4C	2	4400	2#4=0.34	4.24	0.5
DP4G	2	6900	5#4=1.12	3.51	0
DP8 G	2	6900	2#8=1.67	3.6	0
DP4C	2	6900	2#4=0.34	3.16	0
DF4G	2	4400	5#4=1.12	4.71	0.5
DF8 G	2	4400	2#8=1.67	4.83	0.5
DF4C	2	4400	2#4=0.34	4.24	0.5

3.1.3.2.2 Beam tests. The beam test procedures are the same as those of the flexural beam test described in Chpater 3.1.2.

3.1.3.2.3. Environmental conditioning. The internal temperature of the concrete was not the same as the air temperature in the chamber. It is important that the interface at the FRP/concrete reaches the targeted temperature, i.e., the internal temperature below 32°F during the freezing period and above 32°F during the thawing period. Thermocouples were embedded in two 4 in. × 8 in. concrete cylinders, one in air, the other one in water, to monitor the core temperature inside the concrete. Several preliminary freeze-thaw cycles were conducted to determine the appropriate air temperature and cycle time. It was found that a 9-hour cycle, consisting of a 6-hour freezing regime and 3-hour thawing regime, was adequate to obtain the freezing and thawing conditions in the core of the specimens. A computer data acquisition system was used to monitor the temperature change of the air, inside the concrete cylinder in air, and inside the concrete cylinder submerged in water. Temperatures were recorded at three-

minute intervals. The temperature variation during the freeze-thaw cycle is shown in

Figure 3.9. One can see that the temperature in the concrete specimens changed the

temperature at a much slower rate than the temperature in the air. However, the

temperature in the concrete specimen can reach the targeted temperature, with about three

hours in the thawing region and about six hours in the freezing region during each cycle.
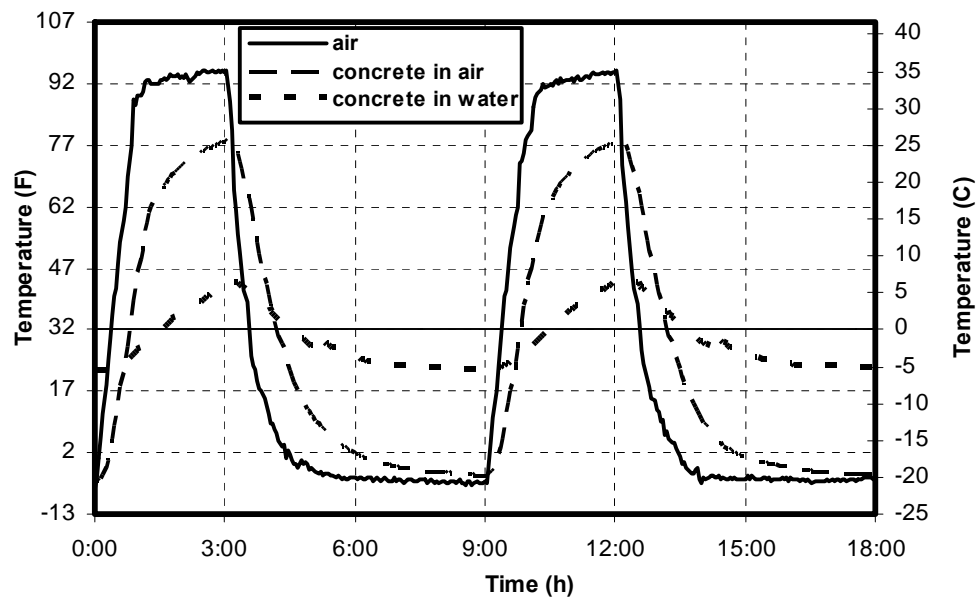
Figure 3.9. Cycle of Freezing-and-Thawing

The glass transition temperatures, T_g, for FRP materials were considered in

deciding the high temperature magnitude. FRP materials should not be used at

temperatures above their glass transition temperatures, T_g. The glass transition

temperatures for vinyl ester and polyester resin are 200^0F and 170^0F, respectively. Also,

after considering the temperature in the US Mid-West region, it was decided that the high

temperature cycle ranged from 95^0F to 140^0F.

As shown in Figure 3.10, a combined environmental cycle consisted of 20 freeze-thaw cycles and 20 high temperature cycles. The same cycles were iterated 10 times. Thus, a total of 200 freeze-thaw cycles and 200 high temperature cycles were conducted during the study program to simulate the seasonal weather changes. Compared to the long-term average temperature data on Missouri, the determined environmental cycles were far more severe than the average temperature so that the worst-case scenario and the accelerated test were possible.

3.1.3.2.4. Preparation of de-icing solution. In this study, a solution of sodium chloride (NaCl), 5% by weight, was selected to simulate the de-icing salt solution. Bond specimens were submerged into the salt solution in two large tanks. Also, due to the large dimensions of beam specimens, the effects of de-icing salt on flexural performance were investigated by the ponding test (ASTM C 1543-02). The beams were placed upside down in the environmental chamber to allow the surface with cracks to face up. Using a silicone sealant, polystyrene strips were bonded to the top surfaces of the beams to form dikes to retain the salt solution. Inspection was made to check the water level by every two days. The beams were kept moist by adding additional fresh solution. At the end of the environmental conditioning, no solid salt was observed left on the surface of the beams, which meant that the concentration of salt solution did not vary significantly. It seems that the leakage of the salt solution between the dike and the beam surface may be the main reason for the reduction of the salt solution.

It took approximately 100 days to complete the 10 combined environmental cycles. Figure 3.11 shows the specimens in the environmental chamber. One can see the salt solution was retained in the dike on the top of the beams, which have three artificial
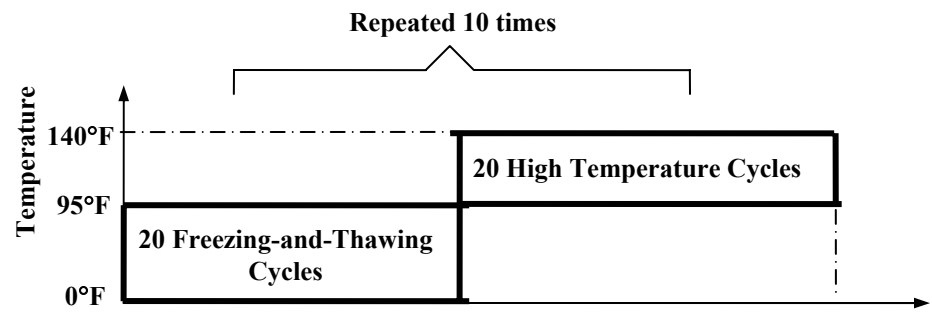
(a) Combined Environmental Cycle
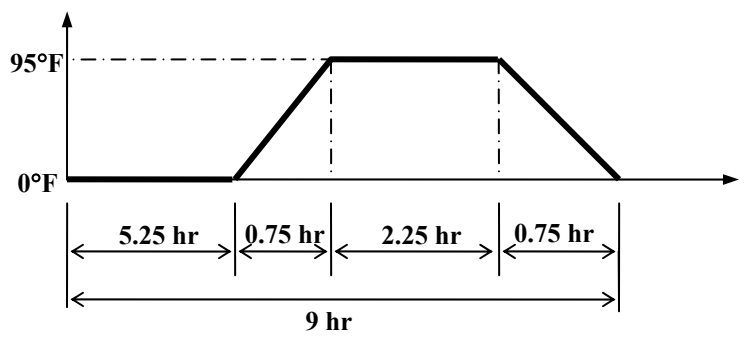
(b) Freezing-and-Thawing Cycle
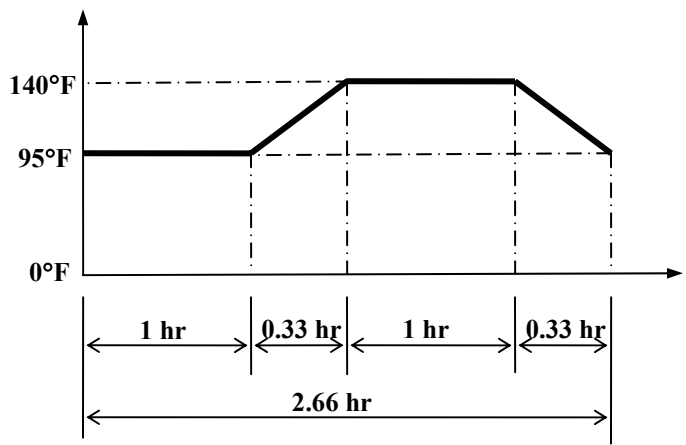
(c) High Temperature Cycle

Figure 3.10. Combined Environmental Cycles used in this Study

cracks. After the environmental conditioning, specimens were removed from the chamber and allowed to dry for one week before testing.
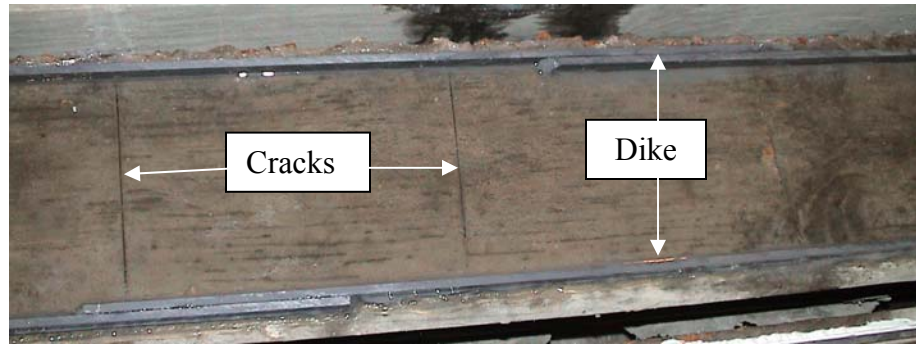
(a) Photo Showing Artificial Cracks on the Surface of Beams
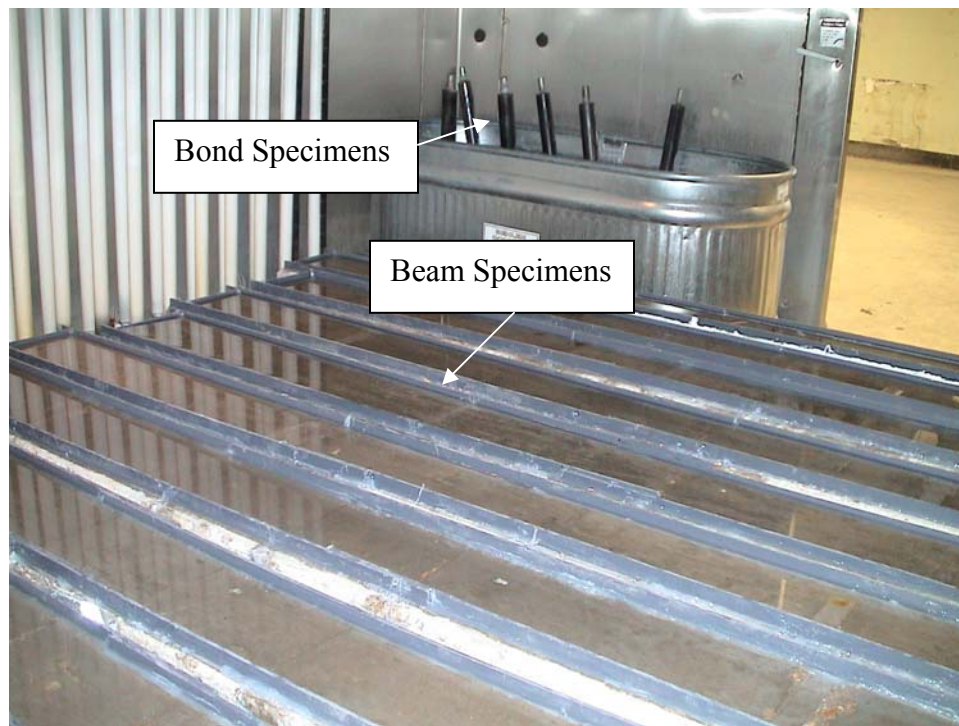
(b) Bond Specimens and Beam Specimens Placed in the Chamber

Figure 3.11. Photograph of Specimens in the Environmental Chamber

3.2. MATERIALS

3.2.1. FRP Rods. Three types of commonly used FRP rods were adopted in this study: namely the #8 GFRP, #4 GFRP, and #4 carbon fiber reinforced polymer (CFRP), as shown in Figure 3.12. The surface of the GFRP rods is tightly wrapped with a helical fiber strand to create indentations along the rebar, and sand particles are added to the surface to enhance its bonding strength. For the #4 GFRP, the pitch of the fiber strand is about 1 in., and the angle between the strands to the longitudinal direction β is 60 degrees. For the #8 GFRP, the pitch of the fiber strand is 0.87 in. and β is 75 degrees, as shown in Figure 3.13. The deformation angles α are 2 degrees and 5 degrees for #4 GFRP and #8 GFRP, respectively. The surface of the CFRP is very smooth, as shown in Figure 3.12. The resin used was epoxy modified vinyl ester, based on the information provided by the manufacturer. The mechanical properties of FRP rods as reported by their manufacturer are summarized in Table 3.6.

#8 GFRP

#4 GFRP

#4 CFRP

Figure 3.12. FRP Rods Used in this Study
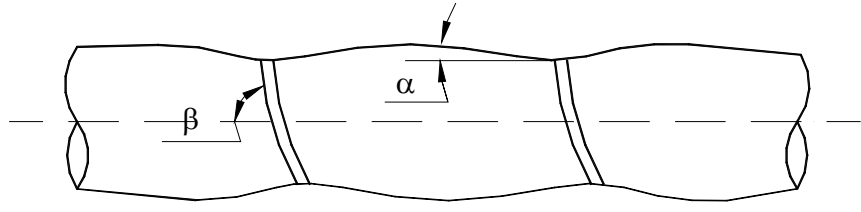
Figure 3.13. Deformation of GFRP Rebar

Table 3.6. Mechanical Properties of FRP Rods

	#4 CFRP	#4 GFRP	#8 GFRP
Tensile Strength (ksi)	300	100	80
Elastic Modulus (ksi)	18,000	5,920	5,920

3.2.2. Polypropylene Fiber. Currently, many fiber types are commercially available including steel, glass, synthetic, and natural fibers. To fulfill the completely steel-free concept, polypropylene fiber was used in this study. The fibers are fibrillated and commercially available in 2.25 in. length, as shown in Figure 3.14.
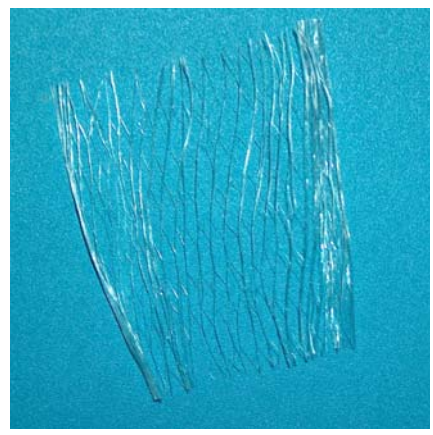
Figure 3.14. Polypropylene Fibers Used in this Study

3.2.3. Concrete. The concrete mix used in this study is based on an existing MoDOT mix design, as shown in Table 3.7. For practical application, the volume fraction of fiber (V_f) of 0.5% was used to make the FRC take the benefits from the fibers, while ensuring good workability of the concrete. It should be noted that the purpose of this study was to qualitatively investigate the benefits gained from the fibers to the FRP reinforcing system. The different volume fractions' effect was not a variable to be investigated in this study. Several concrete batches were made at different time for different tests. The compression strengths and the air content of concrete and FRC on the day of testing were measured and listed in the Table 3.8.

Table 3.7. Concrete Mix Design

	Portland Cement Type I (lb/yard^3)	Water (lb/yard^3)	Fly ash (Class C) (lb/yard^3)	Sand (lb/yard^3)	Coarse Aggregate (Limestone) (lb/yard^3)	Air Entraining Agent (oz)
Plain Concrete	625	200	200	1,300	1,720	8
FRC	620	209	110	1,140	1,820	7

Table 3.8. Concrete Properties

		Pullout Bond Test	Splitting Bond Test	Flexural Beam Test	Durability Bond	Durability Beam
Plain Concrete	Compressive Strength (psi)	7,400	5,660	6,900	6,900	6,900
	Air Content	4.5%	4.1%	4.9%	4.9%	4.9%
FRC	Compressive Strength (psi)	5,360	3,479	4,400	5,360	4,400
	Air Content	6%	8.5%	5.8%	6%	5.8%

4. STATIC AND FATIGUE BOND TEST RESULTS

4.1 INTRODUCTION

It is generally understood that the three primary mechanisms of bond behaviors result from chemical adhesion, mechanical interlock, and friction resistance. Each component contributes to the overall bond performance in varying degrees depending on the type of rebar. Typical bond mechanisms for the deformed rebars are shown in Figure 4.1 (Hamad, 1995).
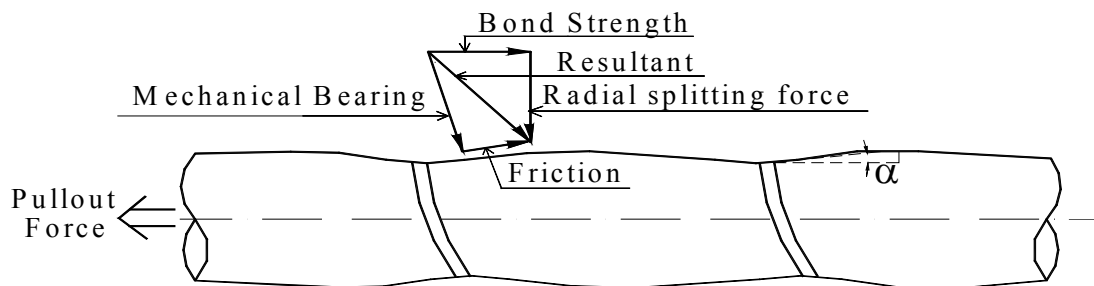
Figure 4.1 Bond Mechanisms for Deformed GFRP Rebar (Hamad, 1995)

Based on its overall performance, bond can be divided into two categories, the average bond and the local bond, as shown in Figure 4.2. The average bond is the average bond over a specific length of embedment, and its value is generally varied with the embedment length. The local bond is an inherent property of the rebar and the concrete. It is independent of the embedment length and is determined by its constitutions (the concrete and the rebar) and the interaction between the constitutions.
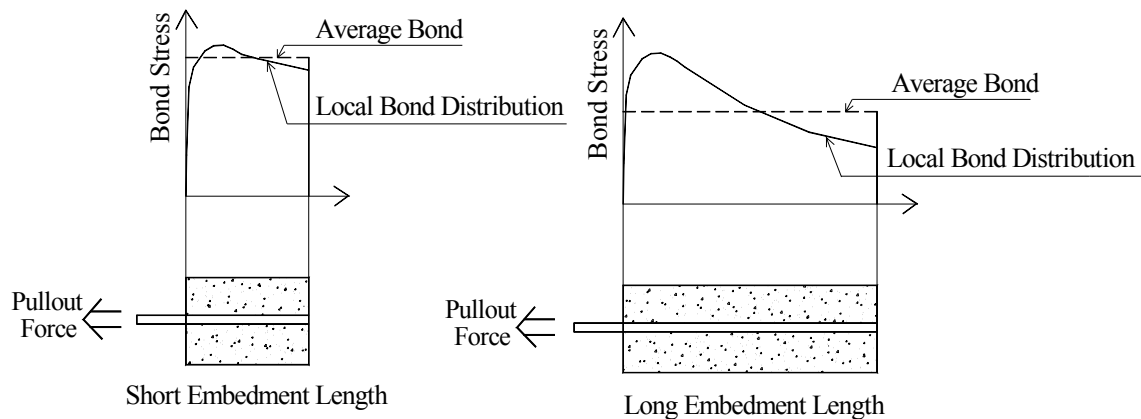
Figure 4.2. Average Bond and Local Bond

Considerable studies have been conducted on the bond behavior of the Glass Fiber Reinforced Polymer (GFRP) rebar in plain concrete. Different types of the FRP rebars have quite different bond characteristics, which are strongly dependent on the mechanical and physical properties of external layer of FRP rods (Ehsani et al., 1997; Kaza, 1999). On the other hand, because no accepted manufacturing standards for FRP are available, bond research is far from satisfactory. For the deformed GFRP rebar having similar surface to rebar GFRP, as shown in Figure 3.9, the bond strength is equivalent to or larger than those of ordinary deformed steel (Cosenza et al., 1997; Kaza, 1999). Research also showed that for some smooth surface rebars, the bond strength can be as low as 145 psi (Nanni at al., 1995), which is about 10% of that of steel. As for Carbon Fiber Reinforced Polymer (CFRP) rebar, relatively fewer experimental data are available in the literatures. Four types of CFRP rods were tested by Malvar et al. (2003) and they found that when there was sufficient surface deformation, 1,160 psi or more of bond strength could be reached.

Compared to relatively rich materials on monotonic bond tests, literatures on fatigue bond tests are very limited and the testing results are also controversial. Test results by Katz (2000) indicated that there was a reduction in the bond strength after cyclic loading, while Bakis et al. (1998) found that the bond strength in cyclically loaded beams increased as compared to the bond strength in the monotonic tests.

Fibers may improve the properties of concrete, although there is no strong opinion on the effect on the strength (ACI 544, 1996). As a consequence, with the addition of fibers, bond performance will change due to the alteration of the concrete properties. Bond between the traditional steel bars and the FRC was investigated by several researchers and the test results indicated the addition of fibers significantly improved the post-peak bond behavior. However, no agreement was reached on its effect on bond strength. As for bond behavior of the FRP bars embedded in the FRC, open literature does not provide any published information.

Three test methods are commonly used to study bond behaviors: namely, pullout test, splitting bond test, and flexural beam test. These test methods provide different information to the bond behaviors. Pullout tests can clearly represent the concept of anchorage and is usually adopted to study the bond behavior between rebar and concrete. Although pullout tests cause concrete to be in compression and the testing bar to be in tension, a stress condition not exhibiting in real structures, a reasonable correlation was found between structural performance and measures of performance in the pullout test (Cairns and Abdullah, 1995). Splitting bond tests can be used to study the splitting bond behavior under different cover thicknesses. The transverse reinforcement's effect on bond behavior can be avoided when properly designed. Splitting bond tests can simulate the

stress field of real structures to some extent; it can simulate the shear stress field but not the stress gradient induced by bending. Flexural beam tests have the advantage to represent actual stress fields in real beams and the cover effects on the bond. But, it requires considerable confining reinforcement to avoid a shear failure and so bond splitting failures are unlikely (Cairns and Plizzari, 2003). In this program, all three types of tests were investigated and compared. In this Chapter, bond characteristics, studied by pullout test method and splitting bond test method, are presented.

4.2. PULLOUT BOND TEST RESULTS

4.2.1. Test Results and Discussions. The average bond strength was calculated as the pullout force over the embedded area of the rebar. The slip at the loaded end was calculated as the the value of LVDT2 minus the elastic deformation of the FRP rebar between the bond zone and the location of LVDT2. It should be mentioned that the deformation of the steel frame was very small, less than 1% of the slip (approximately 0.0015 in. when the pullout load equals to 45 kips), which the total slip was larger than 0.30 in., thus it was ignored for simplicity. When the bond strength of specimens was compared with different concrete strengths, f_c', bond strength was normalized based on the square root of f_c', which is adopted in the current ACI 318-02.

4.2.1.1. Monotonic pullout tests. The monotonic test results are listed in Table 4.1. Most of the test results were repeatable with small variations for the same testing group. In the case of PG405M and FG405M, there was a combination of both pullout and splitting failure modes. Since the slip at failure was very different for different failure modes, the coefficients of variance for slip in these two groups were large.

Table 4.1. Summary of Static Pullout Bond Test Results

Specimen I.D.	Bond Strength First (Second)Peak $u/\sqrt{f_c'}$ ($u'/\sqrt{f_c'}$) (psi/$\sqrt{psi}$)		Slip at First (Second)Peak $S_m(S_m')$ (in.)		0.002 in. Bond Strength $u_{0.05}/\sqrt{f_c'}$ (psi/$\sqrt{psi}$)		Mode[1]
	Average	COV (%)	Average	COV (%)	Average	COV (%)	
PC405M	11.40 (15.24)	6.01 (5.33)	0.03 (0.69)	9.77 (4.42)	11.52	7.49	P
PG405M	32.88	7.80	0.36	40.57	15.12	6.95	S/P
PG805M	30.6	2.95	0.34	9.31	11.88	5.09	S
FC405M	14.04 (13.20)	14.20 (1.54)	0.04 (0.67)	11.11 (9.57)	13.92	13.57	P
FC410M	16.68 (15.12)	14.26 (3.97)	0.07 (0.66)	3.68 (16.92)	16.32	13.14	P
FG405M	31.92	5.16	0.41	23.22	17.64	23.38	S/P
FG410M	28.2	4.44	0.37	16.23	24.36	4.53	S
FG805M	26.04	7.25	0.54	6.21	13.08	12.13	P
FG803M	29.28	5.92	0.48	6.52	13.20	12.26	P

Note (1): P=Pullout failure; S=Splitting failure;
(2): Two peak values were observed only in CFRP specimens, refer to Figure 3.4; The numbers in the parenthesis are the vales at the second peak;
(3): Values are the average of three duplicate specimens;

- **Effect of Rebar Surface Conditions.** Due to their significant surface differences, bond behavior of the GFRP and the CFRP are not the same, as shown in Figure 4.3. The bond strength of the GFRP was about twice as much as that of the CFRP. The bond failure of the CFRP was controlled by the rebar pullout, providing more ductile behavior.

(a) Bond-slip behavior of CFRP. During the pullout of the CFRP rebars, the surface of the rebar was severely rubbed and the resin was scratched off (see Figure 4.4). The surface of the CFRP used in this study was very smooth. As a result, a very low
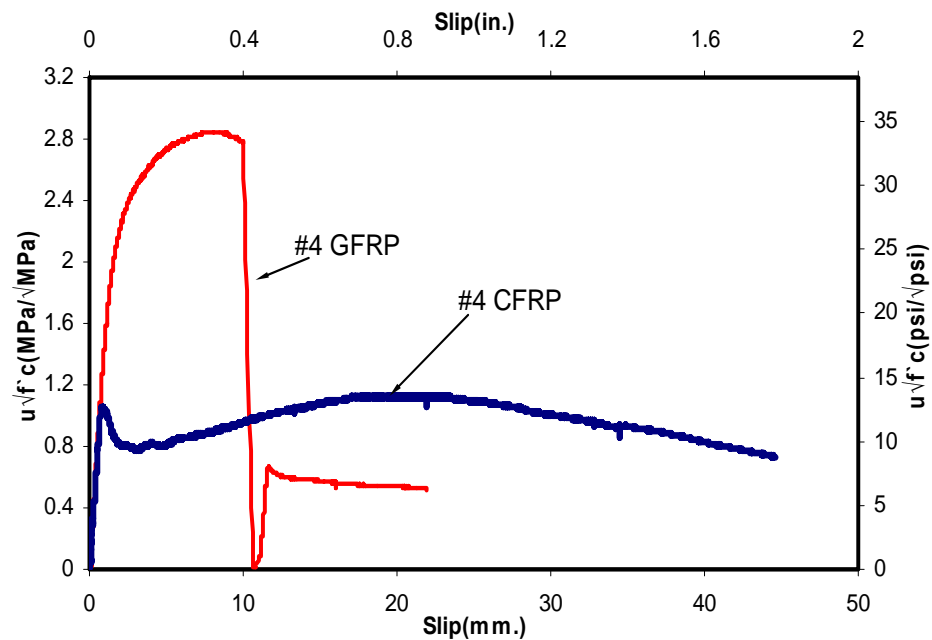
(a) Bond-slip Relationship of GFRP and CFRP in FRC Specimens
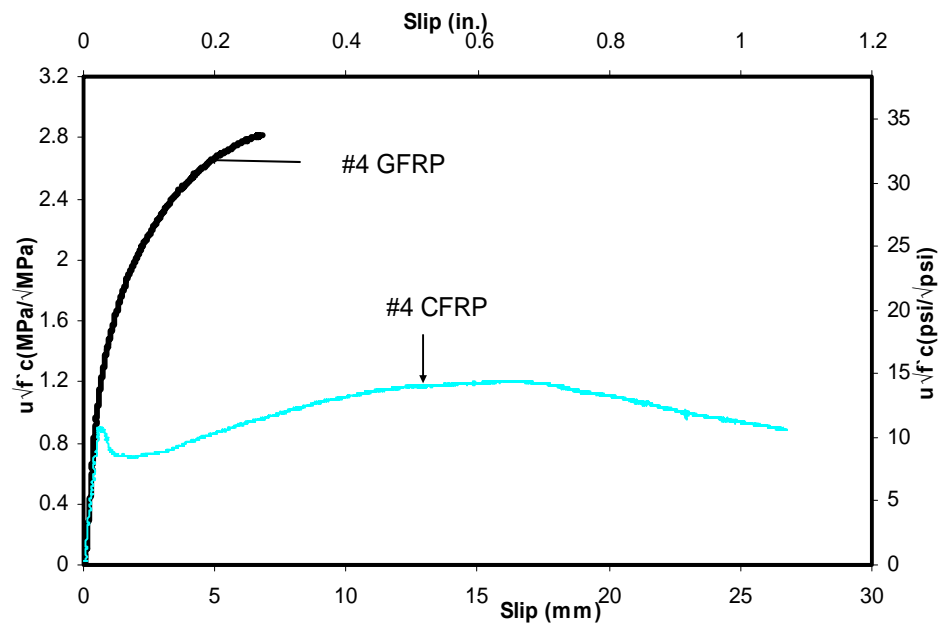
(b) Bond-slip Relationship of GFRP and CFRP in Plain Concrete Specimens

Figure 4.3. Bond-slip Relationship of GFRP and CFRP

(a) CFRP Rebar   **(b) GFRP Rebar**
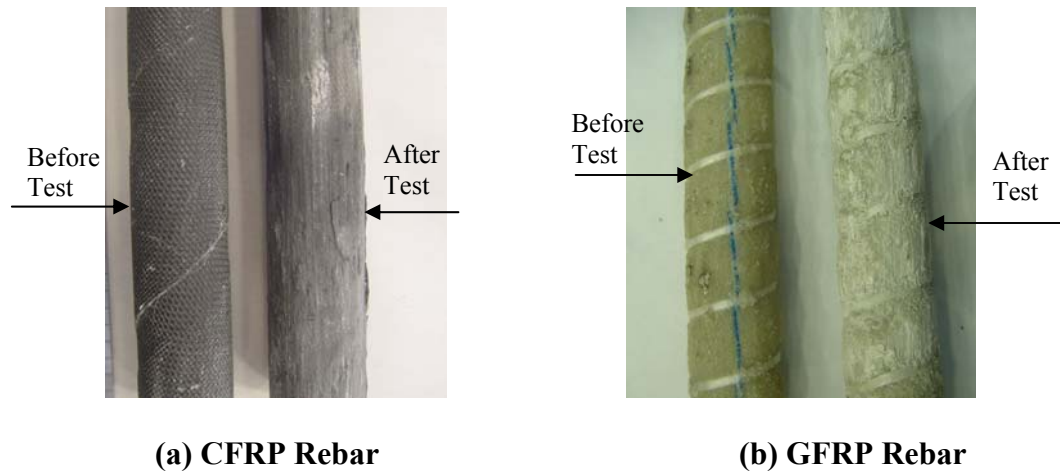
Figure 4.4. Surface Conditions of Various Rebar Before and After Loading

mechanical bearing force can be expected. Thus, for the CFRP rebar, the mechanical

bearing can be neglected. Load-slip response for the CFRP can be roughly divided into

four phases, as shown in Figure 4.5.
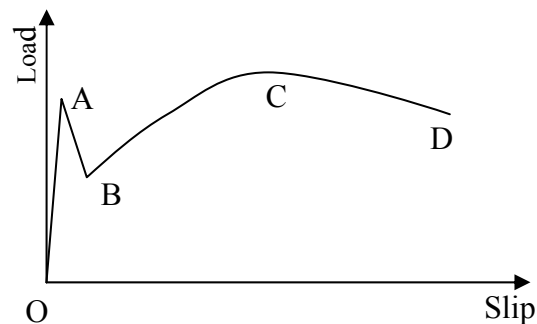
Figure 4.5. Idealized Load-Slip Curve for CFRP Rebar Embedded in Concrete

Phase I (as described in Figure 4.5 in portion O~A): At Phase I, the chemical

bond and friction force resisted pullout force together, which resulted in a very high bond

stiffness.

Point A (refer to Figure 4.5): Chemical bond was broken at the loaded end first and then extended to the free end. The peak value of chemical adhesion was reached at Point A. After this point, chemical bond was completely lost along the whole rebar.

Phase II (as described in Figure 4.5 in portion A~B): After the chemical bond was broken, only the friction component was present. The total resisting force provided only by the friction decreased suddenly. Because the tests were controlled by the slip at the loaded end, the slip between the rebar and concrete continued increasing constantly. As a result, the pullout load had to be reduced to maintain the increasing rate of the slip. When the pullout load dropped to Point B, a new equilibrium was reached. The chemical bond component can be calculated by the difference of the bond strength at Point A and Point B *minus* the increase of the friction bond component from Point A to Point B. For the CFRP rebar used in this study, the chemical bond strength was 150 to 200 psi. Chemical cohesion between deformed steel bars and concrete was reported, ranging from 150 to 300 psi by Choi et al. (2002).

Phase III (as described in Figure 4.5 in portion B~C): As the slip continued to increase, friction force increased accordingly, and the load-slip curve went up again. Due to the loss of chemical bond, the curve B~C was much flatter than O~A. At this phase, microcracks occurred and propagated.

Point C (refer to Figure 4.5): At Point C, friction reached its maximum value.

Phase IV (as described in Figure 4.5 in portion C~D): With the increasing of slip, more and more microcracks developed. It caused the confinement from concrete to rebar to reduce. Thus, the friction force between rebar and concrete also decreased. The load-slip curve was softened.

Based on the bond-slip curve, two peak bond values were observed for each specimen. (1) In Phase I, chemical adhesion and friction resistance dominated bond behavior. The first peak occurred when maximum local chemical bond stress spread to the free end. (2) In phase II, friction force dominated the bond behavior. The second peak value occurred when friction force reached its maximum.

(b) Bond-slip behavior of GFRP.   At failure, the surface of the GFRP rebar was damaged, and resin was rubbed off from the rebar surface. Some small pieces of resin scale were noticed in the concrete, and helical fiber strands were broken in several specimens. However, the overall shape of the rebar remained intact. The deformation created by the helical fiber strand could still be seen, which suggested that the deformation was not transversely crushed or sheared off by the bearing force from the concrete. In other words, the resin acted as a good cover to protect the glass fibers, as shown in Figure 4.4b. Previous work carried out by other researchers (Katz, 1999; Chaallal and Benmokrane, 1993) showed that the shearing of the rib is the main reason for the bond failure in the deformed FRP bars. This kind of failure phenomenon was not observed in this study. That may be due to the different surface characteristics of the FRP rebar. In the studies conducted by Katz et al. and Chaallal and Benmokrane, the ratio of the projected area that was normal to the bar axis to the shearing area of the rib was much smaller than that of the rebar used in this study, as shown in Figure 4.6.

Consequently, when the bearing forces on the projected deformation are the same (i.e., deformation heights, h_r, are the same), the rebar as shown in Figure 4.6b will induce much larger shearing stresses on the rib. Thus, it is easier for the rib to be sheared off. In other words, rib deformation like Figure 4.6a is more desirable to prevent such shearing

off failure. This factor is more important for the FRP rebar than it is for the traditional

steel rebar, since the ribs of the FRP rebar are made of resin, which is much weaker in

shear-resisting capacity. At this point, the bond is strongly relative to the FRP

manufacturer.

(a) Deformation pattern of GFRP used in this study

(b) FRP with other deformed patterns
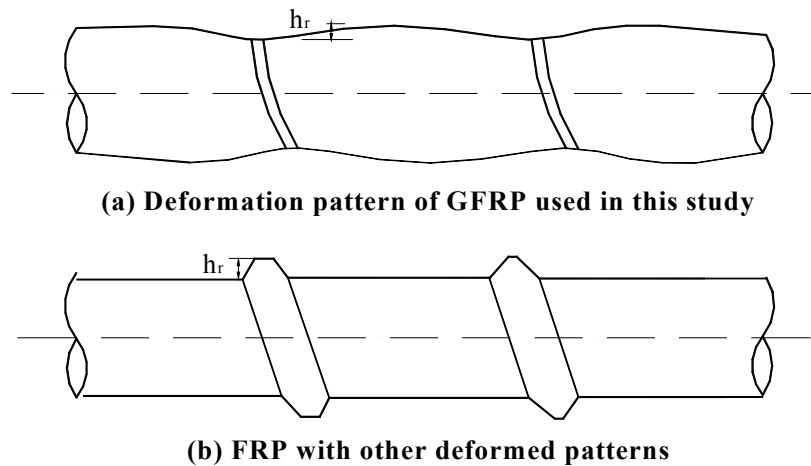
Figure 4.6. Different Deformation Patterns of FRP Rebars

Chemical bond played a much less important role for the GFRP specimens than

for the CFRP specimens. It was the mechanical bearing and friction force that dominated

the bond behavior. Due to the GFRP's relatively rough surface, internal cracks (crack

unnoticeable at concrete surface) were created, even at a very low load level. It was

thought that chemical adhesion had been lost at these portions (Goto, 1971). Since the

CFRP had a very smooth surface, no internal cracks, or very few, were formed at the

initial loading. Chemical cohesion was almost intact until the relative slip between the

rebar and concrete was too large, and then it was broken abruptly.

- **Embedment Length Effect.** Similar to the traditional steel rebar, bond stresses along the FRP rebar are also nonlinearly distributed along the embedded portion (Benmokrane et al., 1996). The bond mechanisms for the CFRP and GFRP bars in this study were different, therefore, the embedment length effect on bond strength was also different.

(a) GFRP: As mentioned earlier, mechanical bearing dominated the bond. The bond stresses were nonlinearly distributed along the embedment portion. High bond stresses concentrated at the portions near the loaded end, and the bond stresses decrease sharply toward the free end. In the case of the longer embedment length, a relatively smaller portion of the embedded area had large bond stress. Consequently, the average bond strength with a longer embedment length would have a lower value, as shown in Figure 4.7. Also, the slope of the bond-slip curve of the specimens with shorter embedment length was steeper than that of the specimens with longer embedment length. That was due to the fact that the higher bond stress concentrated near the loaded end and lower bond stress developed far away the loaded end. Thus, when the average bond stress was calculated based on the pullout load divided over the whole embedment length, the specimens with longer embedment would have lower bond stiffness.

(b) CFRP: As mentioned previously, all the bond strength came from friction resistance at ultimate (the second peak). The friction resistance was a function of the friction coefficient and normal pressure on the rebar. Obviously, the friction coefficient was the same along the rebar. Also, the normal pressure was the same along the embedment portion, except that the portions near the ends had lower values due to less confinement at the ends. As a result, the bond stress distribution was almost uniformly
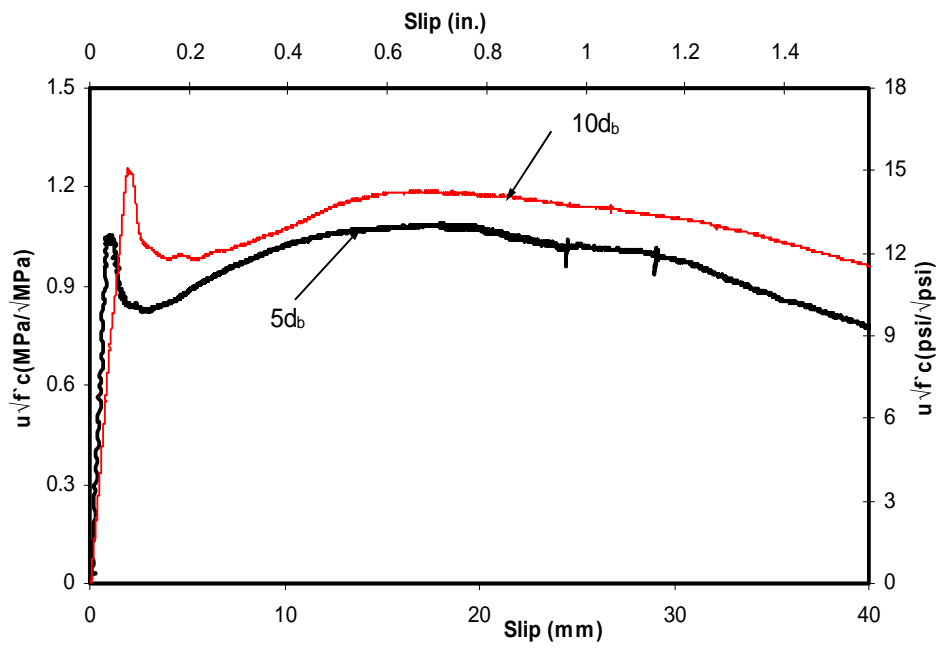
(a) Bond-Slip Relationship of #4 CFRP
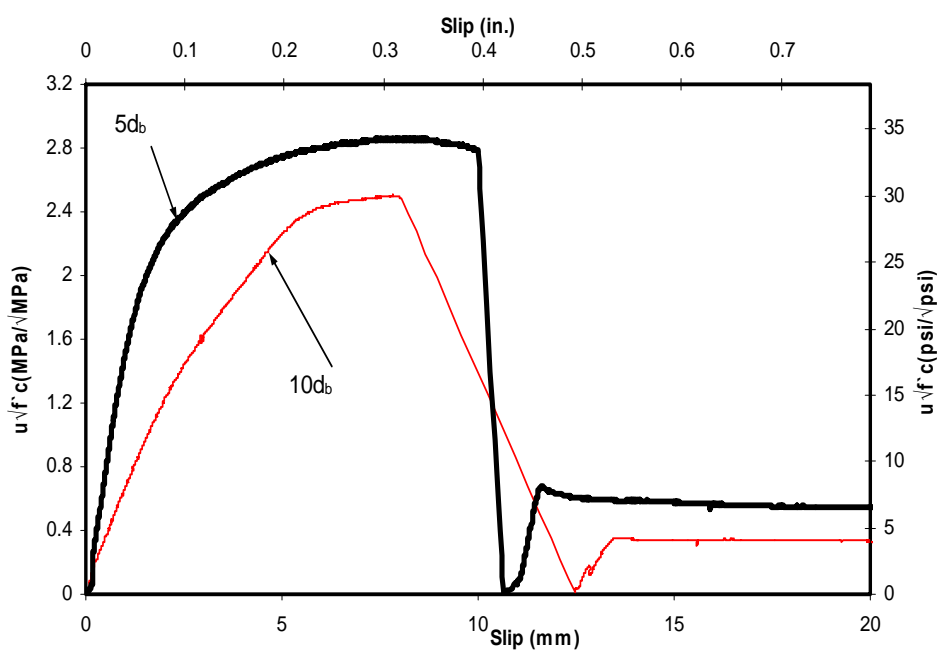
(b) Bond-Slip Relationship of #4 GFRP

**Figure 4.7. Embedment Length Effect on Bond-Slip Behavior
of Various CFRP and GFRP Rebars**
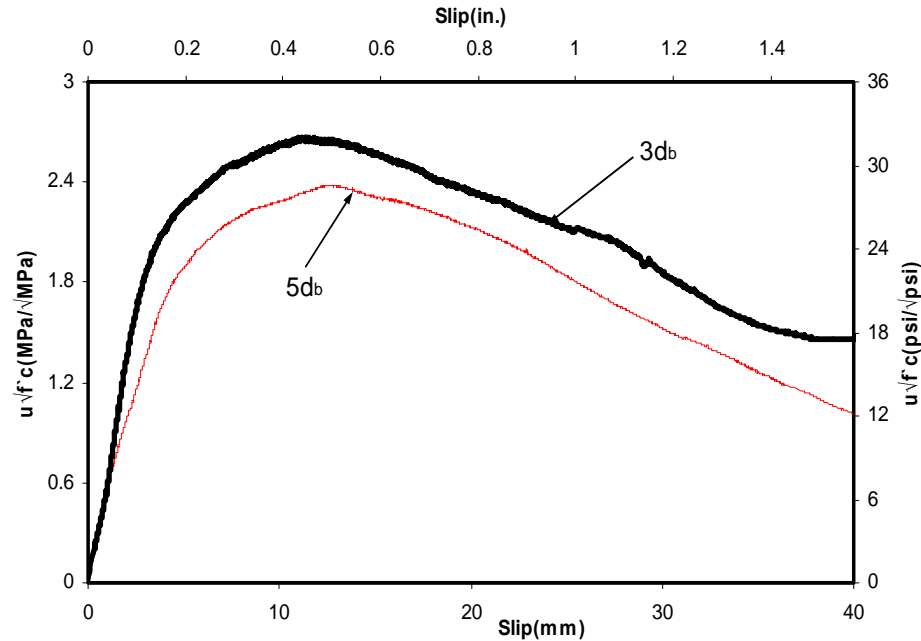
(c) Bond-Slip Relationship of #8 GFRP

**Figure 4.7. Embedment Length Effect on Bond-Slip Behavior
of Various CFRP and GFRP Rebars (Cont.)**

distributed along the embedment length. The average bond strength over the whole

embedment length would not decrease with the increasing of the embedment length. It

could even get a higher value due to the relative small portion of rebar near the ends. A

14% increase of the bond strength was observed in this study, when the embedment

length increased from 5 d_b to 10 d_b, as shown in Figure 4.7a.

- **Diameter Effect.** As shown in Figure 4.8, the bond strengths of the #4

specimen were about 8% and 23% higher than the #8 embedded in the plain concrete and

the FRC, respectively. One explanation is that the possibility of defect (voids created by

concrete bleeding—Tighiouart et al., 1998) is higher for a larger rebar, a phenomenon

similar to the size effect on the behavior of various brittle materials. Another possible

explanation is the Poisson effect; as there is elongation in the longitudinal direction, the
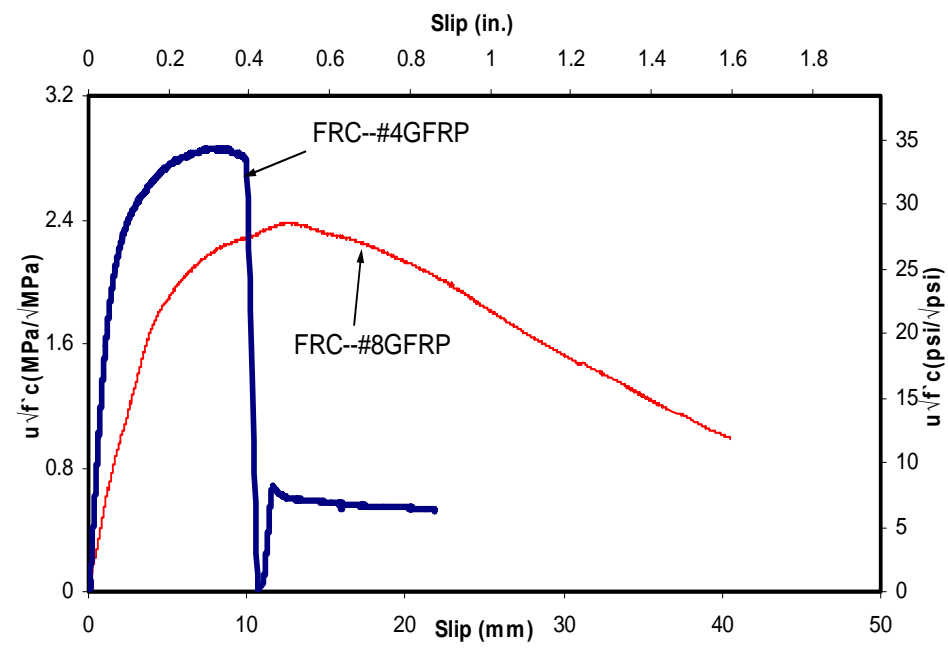
(a) Fiber Reinforced Concrete
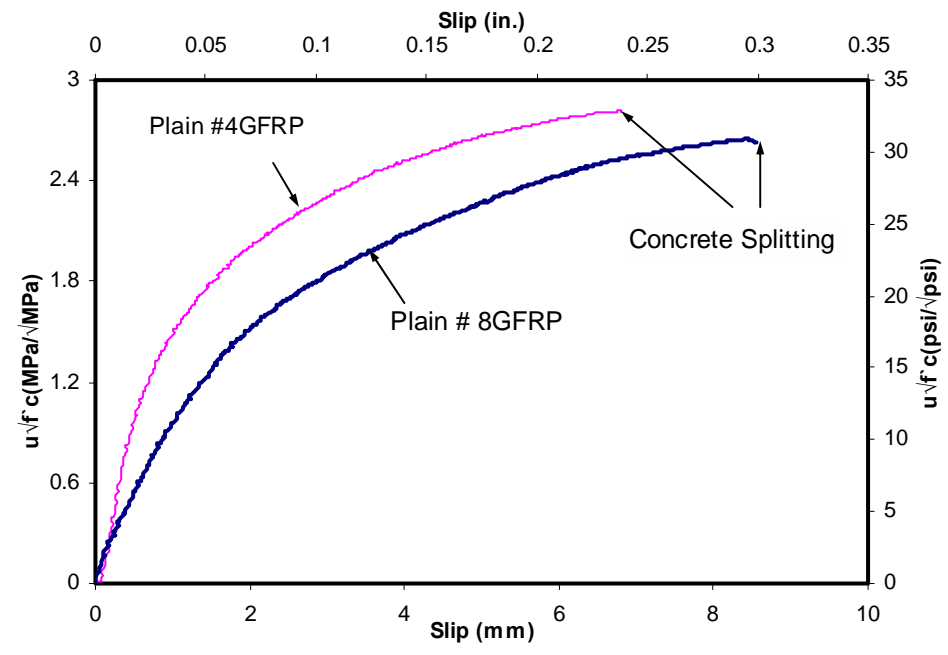
(b) Plain Concrete

Figure 4.8. Diameter Effect on Bond-Slip Behavior

transverse direction tends to contract. Consequently, the confinement from the concrete to the rebar will be reduced to some extent. This effect is more significant for a larger rebar; thus, a rebar with a bigger diameter will have smaller bond strength.

- **Effect of Polypropylene Fibers**

(a) The ultimate bond strength slightly decreased with the addition of the polypropylene fibers. The reduction ranged from 3% to 16% (see Table 4.1 and Figure 4.9).
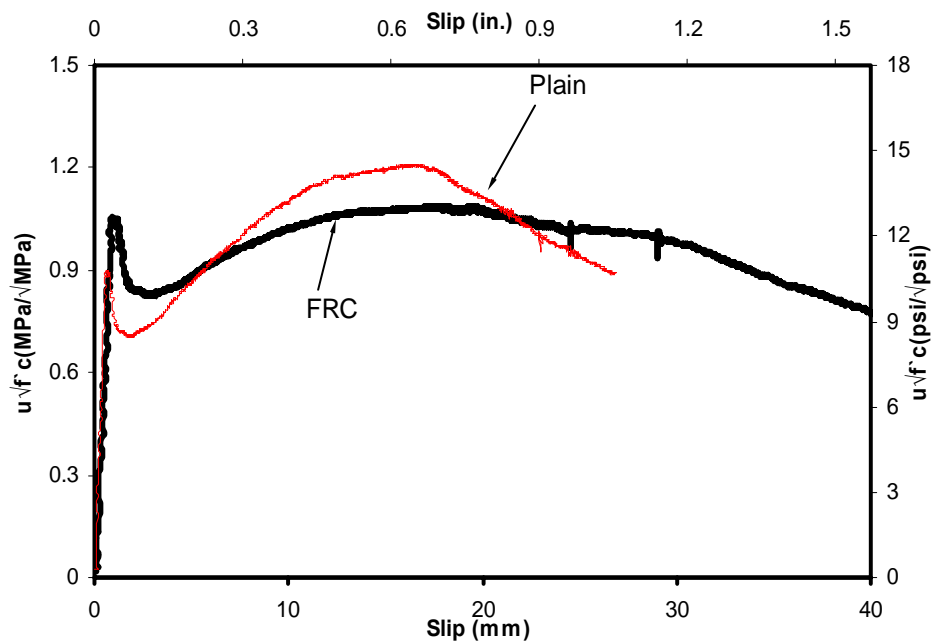
(a) Bond-Slip Relationship of #4 CFRP

Figure 4.9. Polypropylene Fibers' Effect on Bond-Slip Behavior of CFRP and GFRP Rebars
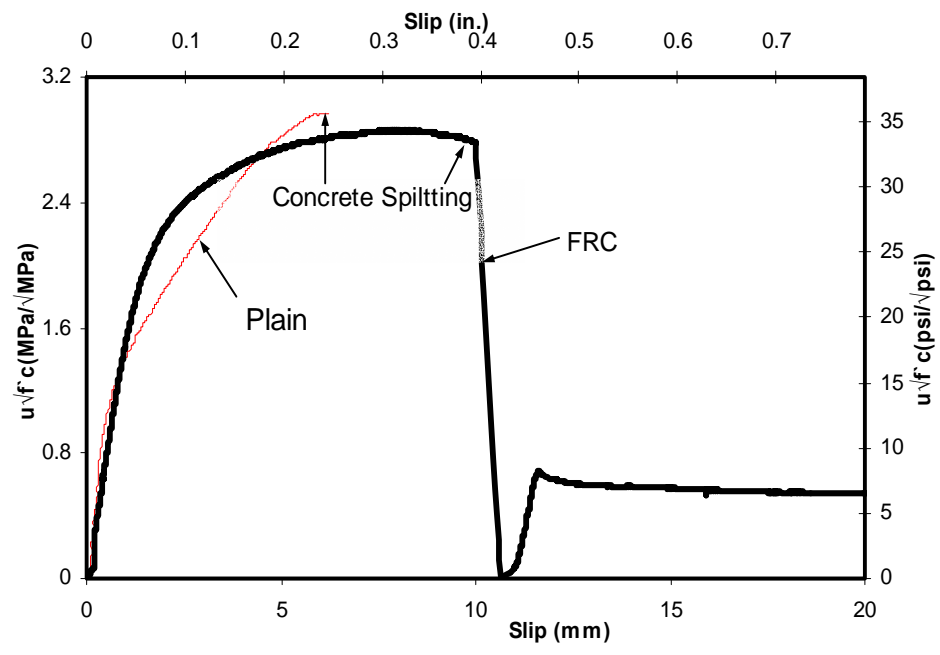
(b) Bond-Slip Relationship of #4 GFRP
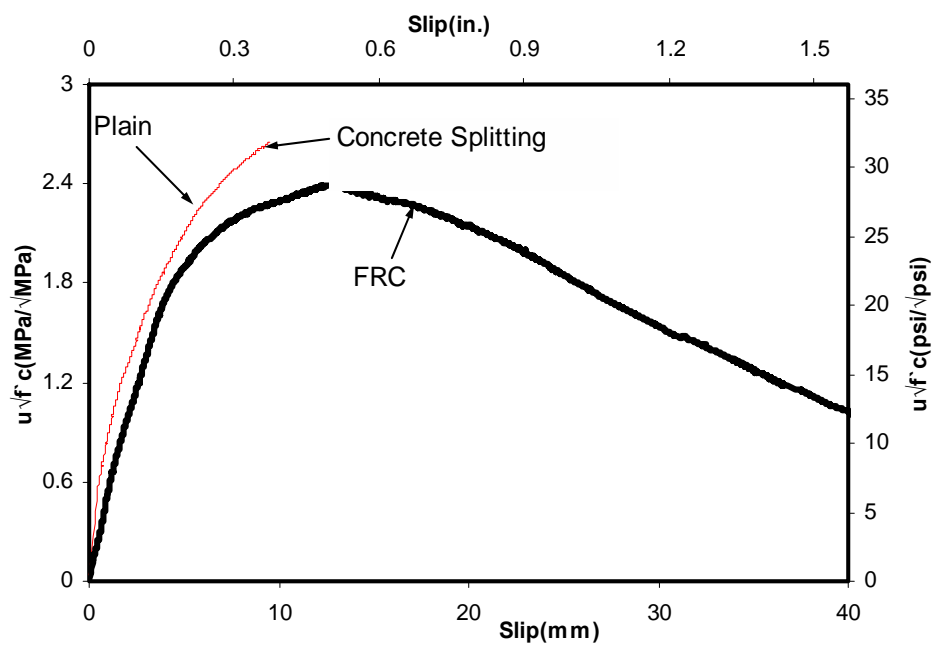
(c) Bond-Slip Relationship of #8 GFRP

Figure 4.9. Polypropylene Fibers' Effect on Bond-Slip Behavior of CFRP and GFRP Rebars (Cont.)

(b) The slip corresponding to the ultimate bond strength increased significantly with the addition of fibers for the GFRP specimens and less for the CFRP specimens. As discussed previously, in the case of the GFRP, internal microcracks were created due to the mechanical bearing; however, fewer internal cracks existed in the case of CFRP, due to its negligible mechanical bearing. Only when the microcracks developed could the polypropylene fibers functioned effectively to limit the opening of microcracks and thus decreased the rate of microcracks propagation. Since many more microcracks existed in the GFRP specimens, the contribution from the polypropylene fibers was more noticeable.

(c) The addition of fibers changed the failure mode; most specimens that failed in concrete splitting changed to pullout failure.

(d) When specimens failed in splitting, the failure for the plain concrete specimens was much more brittle than that of the FRC specimens. As shown in Figure 4.10, the plain concrete specimens usually failed by breaking the concrete into several pieces; while, in the case of the FRC specimens, splitting cracks developed along the splitting plane. With the presence of the polypropylene fibers, the specimens were held together and remained integrated.

Figure 4.10. Failure for FRC and Plain Concrete Specimens

4.2.1.2. Fatigue pullout tests. Fatigue loading will produce a progressive deterioration of bond caused by the propagation of microcracks and the progress of micro-crushing of concrete in front of the irregularity of the rebar surface (ACI 408-99). The damage accumulation can be observed by measuring the relative slip between the concrete and the rebar.

- **General Observations.** Different results were drawn for different specimens when they were subjected to the fatigue loading. The #4 CFRP and the #8 GFRP specimens withstood one million cycle fatigue loading, while, the #4 GFRP specimens failed because the concrete split prematurely. It should be noted that ranges of fatigue loading were 10% to 60%, 10% to 60%, and 0% to 40% of their ultimate monotonic bond strengths for #4 CFRP, #4 GFRP, and #8 GFRP specimens, respectively.

Because the #4 GFRP and the #8 GFRP had similar surface conditions and bond mechanisms, we may regard that their fatigue bond behaviors were also the same. Based on the limited test data, 10% to 60% and 0% to 40% can be conservatively considered as the fatigue bond limit to sustain one million cycle loading for the CFRP and the GFRP, respectively.

- **Residual Slip Accumulation.** The commonly accepted hypothesis to determine the damage accumulation due to fatigue loading is the Miner's hypothesis. According to the rule, failure occurs if $\sum \dfrac{n_i}{N_{max,i}} = 1$, where n_i is the number of cycles applied at a particular stress level, and $N_{max,i}$ is the number of cycles which cause fatigue failure at that same stress level. Test results have shown that this hypothesis is only partly suitable for FRP fatigue bond behavior.

As shown in Figure 4.11, the residual slips accumulated gradually with the increasing number of cycles, but the rate of increase was not constant. Micro-voids between rebar and concrete existed at the time of the specimen fabrication; i.e., rebar was not in full contact with the concrete. When the specimens were subjected to fatigue loading, some of the micro-voids would be gradually closed. At the beginning, relatively large amounts of voids existed; thus, the residual slips were easier to develop. After a certain number of fatigue cycles, most of the voids were closed and the system became stabilized. At that point, the accumulation rate of the residual slip slowed down. Figure 4.11 shows slip vs. cycle-number curve can be roughly divided into two phases. The first approximately 10,000 cycles may be regarded as the first phase. The rest of the curve is the second phase. During the first phase, the fatigue damage accumulated much faster than it did in the second phase. After the first phase, the slip increased linearly with a much lower rate.

- **Fatigue Loading Effect on Residual Bond-Slip Behavior**

(1) Fatigue Loading Effect on Bond Stiffness. Fatigue loading can increase bond stiffness (Figure 4.12). This was reported by Gylltoft et al. (1982) based on a study on steel bars embedded in the plain concrete. As mentioned previously, the rebar and concrete were not in full contact because of the micro-voids. After the specimen had been subjected to fatigue loading, some of the voids were closed, resulting in a larger contacting area. Another reason may be that the rebar surface became rougher after being subjected to the fatigue loading, and the friction resistance increased consequently.

(2) Fatigue Loading Effect on Ultimate Bond Strength. The fatigue loading may increase the ultimate bond strength to some extent, as shown in Figure 4.12 and
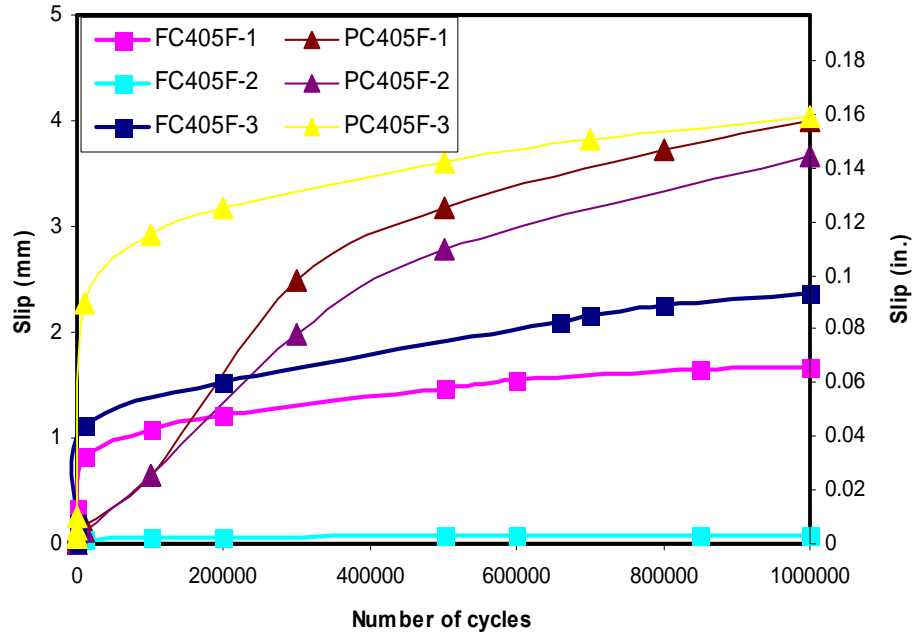
(a) Residual Slips vs. Cycle Numbers of #4 CFRP
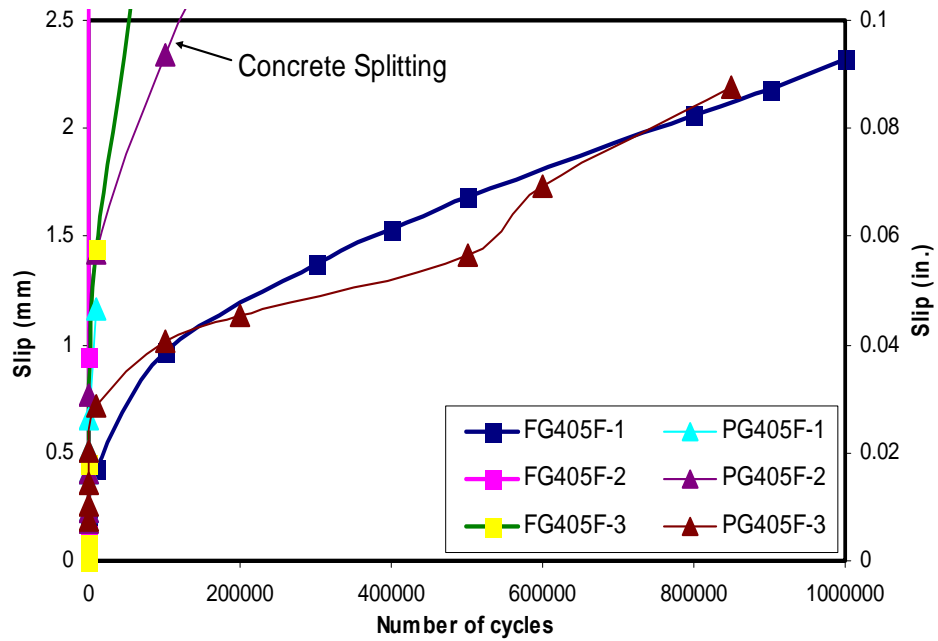
(b) Residual Slips vs. Cycle Numbers of #4 GFRP

Figure 4.11. Residual Slips versus Cycle Numbers of Various FRP Rebars
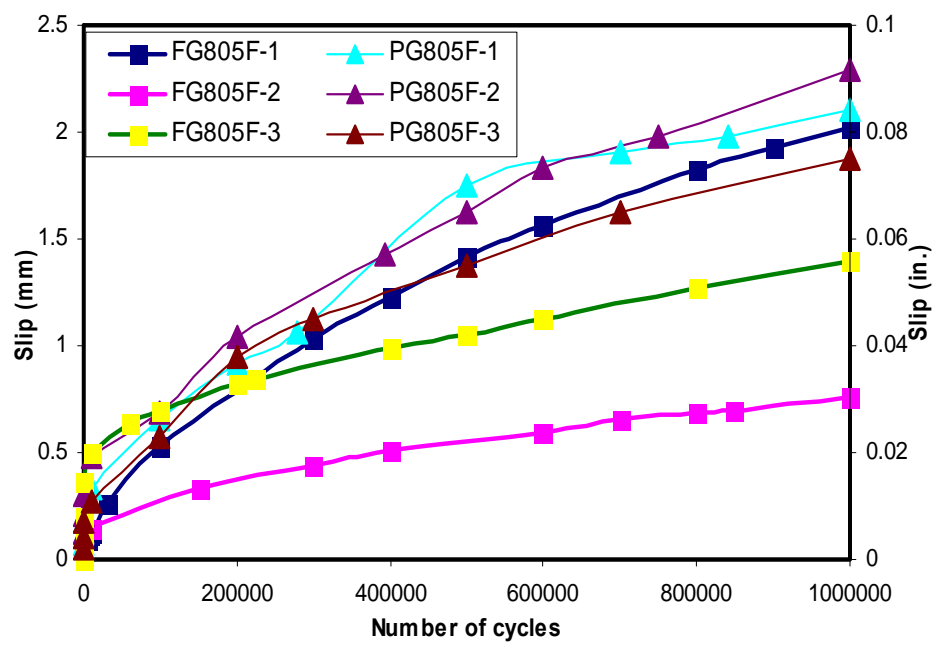
(c) Residual Slips vs. Cycle Numbers of #8 GFRP

Figure 4.11. Residual Slips versus Cycle Numbers of Various FRP Rebars (Cont.)
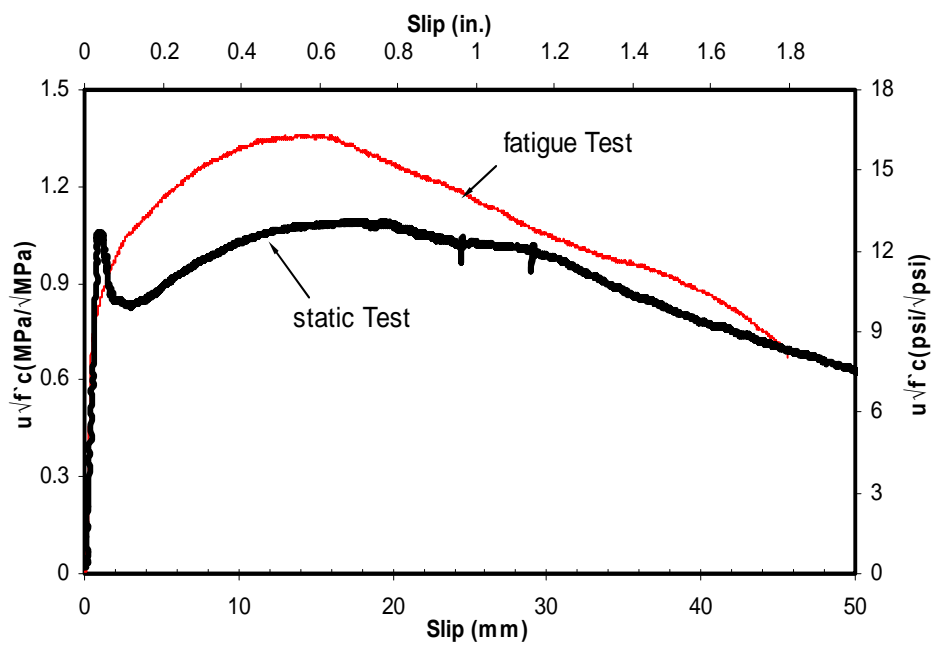
(a) Bond-Slip Relationship of #4 CFRP

Figure 4.12. Residual Bond-Slip Response Before and After Fatigue Loading
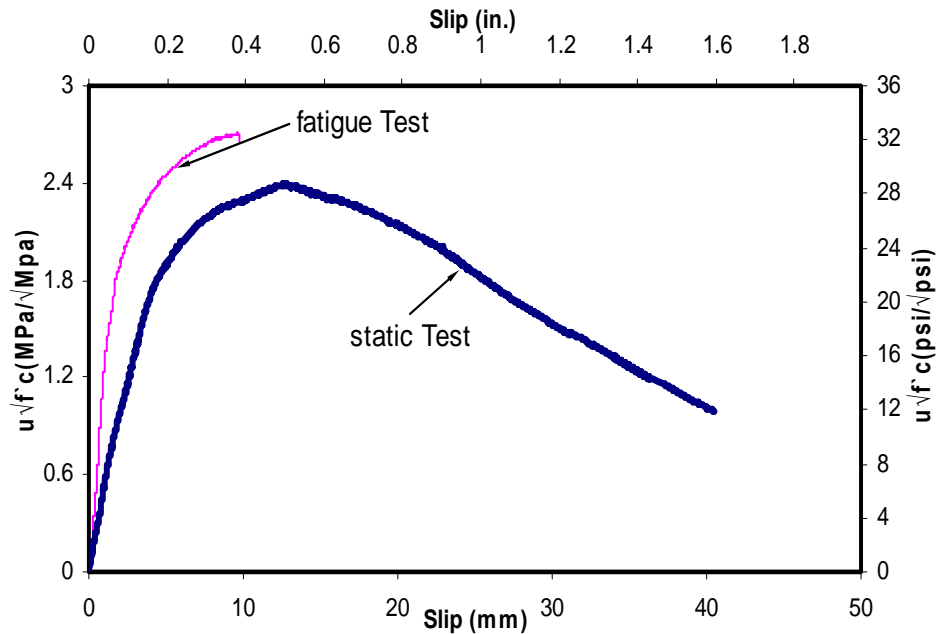
(b) Bond-Slip Relationship of #8 GFRP

Figure 4.12. Residual Bond-Slip Response Before and After Fatigue Loading (Cont.)

Table 4.2. The reasons are that fatigue loadings cause the micro-voids close up and result in more contact area.

    (3) Accumulated Slip's Effect on Load-Slip Behavior. Specimens that did not fail during the fatigue tests were subjected to the monotonic pullout tests. When compared to the specimens without fatigue loading, the slip, S_m, of the post-fatigue specimens decreased. Interestingly, when adding the slip, S_m, and residual slip, S_r, due to the fatigue loading (see Table 4.2), the sum of the slip would be very close to that of the specimen without fatigue loading, S_m. This may be due to the slip, to a large extent, had already occurred during the fatigue loading. Also, the total slip is an inherent property between the rebar and the concrete and has little relationship with the loading history. A similar phenomenon was observed for

Table 4.2. Fatigue Bond Tests Results

I.D.	Post-fatigue Specimens					Specimens without fatigue loading	
	Bond strength $u/\sqrt{f_c'}$ ($psi/\sqrt{psi}$)	Slip[1] S_m (in.)	Residual slip due to fatigue[2] S_r (in.)	S_m+S_r (1)+(2)		Average Bond Strength $u/\sqrt{f_c'}$ ($psi/\sqrt{psi}$)	Average Slip S_m (in.)
PC405F	15.12	0.50	0.16	0.66			
	15.24 15.6	0.44	0.16	0.60	0.64	15.24	0.69
	16.56	0.51	0.14	0.65			
PG805F	35.52	0.23	0.08	0.31			
	35.4 36	0.16	0.09	0.26	0.32	30.6	0.34
	36.96	0.30	0.08	0.38			
FC405F	13.8	0.60	0.07	0.67			
	13.2 14.4	0.66	0.00	0.67	0.67	13.2	0.67
	16.32	0.57	0.09	0.66			
FG805F	27.84	0.43	0.08	0.51			
	32.28 29.52	0.38	0.03	0.41	0.45	26.04	0.54
	35.52	0.36	0.06	0.42			

Note: (1) PG405F and FG405F specimens did not sustain 1 million cycles and are not listed

(2) Unlike the static tests, fatigue test results are more scattering. Thus, individual test results are also listed

the steel rebar embedded in plain concrete (Rehm and Eligehausen, 1979; Clark and Johnston, 1983).

(4) Fatigue Loading Effect on Failure Mode. The load-slip behavior became more brittle after being subjected to fatigue loading, and the fatigue loading could even change the failure mode. Two of the three FG805F specimens failed by the concrete splitting, while all the specimens FG805M failed in the rebar pullout. The fatigue loading did not change the failure mode of the CFRP specimens.

- **Effect of Polypropylene Fibers.** Polypropylene fibers could effectively decrease the rate of microcracks propagation, which was manifested by the fatigue bond tests.

(1) Residual Slip. With the addition of polypropylene fibers, the residual slip due to fatigue loading decreased (see Figure 4.13). The test results were scattered, a characteristic well known in fatigue tests. However, it was clear that the progressive rate of the residual slip was noticeably reduced with the addition of fibers.

(2) Degradation of Bond Stiffness. With the addition of polypropylene fibers, the degradation rate of bond stiffness due to the fatigue loading decreased (see Figure 4.13). For CFRP specimens without fibers, the bond stiffness reduction ranged from 0% to 35%. However, for CFRP specimens after adding fibers, no bond stiffness degradation was observed. For GFRP specimens without fibers, the bond stiffness reduction ranged from 20% to 30%. However, for GFRP specimens after adding fibers, the reduction range was reduced to 5% to15%. Similar observations were made by Gopalaratnam et al. (2004) based on their flexural bond tests.

4.2.2. Prediction of Ultimate Bond Strength. Bond of GFRP to concrete is controlled by the following internal mechanisms: chemical bond, friction resistance, and mechanical bearing of the GFRP rod against the concrete. When large slip exists, friction and mechanical bearing are considered to be the primary means of stress transfer.

Based on the test results, slippage between the FRP rebar and the concrete was very large at failure (more than 0.4 in. at the loaded end and 0.1 in. at the free end). Thus it is safe to conclude that all the chemical adhesion has already been destroyed; that is, all the bond strength consisted only of friction and mechanical bearing.
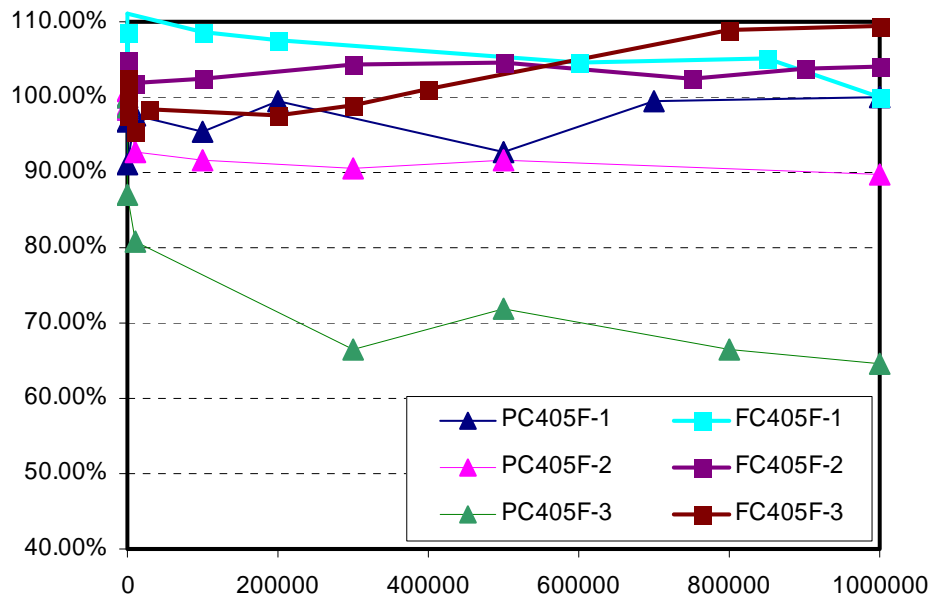
(a) Bond Stiffness Degradation Rate of #4 CFRP
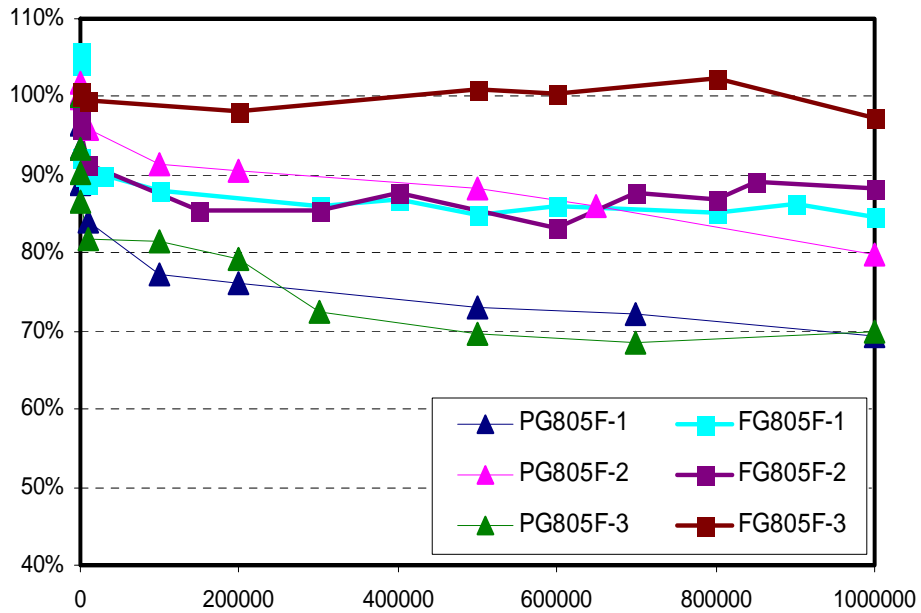
(b) Bond Stiffness Degradation Rate of #8 GFRP

Figure 4.13. Bond Stiffness Degradation Rate

Through mechanical analysis (Figure 4.14), the summation of longitudinal

component, u, is equal to the total pullout force. Thus, $\pi d_b l_d u = T$ will result in:

$$u = \frac{T}{\pi d_b l_d} \text{ psi} \tag{4.1}$$

$$R_r = \frac{u}{\tan(\alpha + \arctan \mu)} = \frac{T}{\pi d_b l_d \ \tan(\alpha + \arctan \mu)} \text{ psi} \tag{4.2}$$
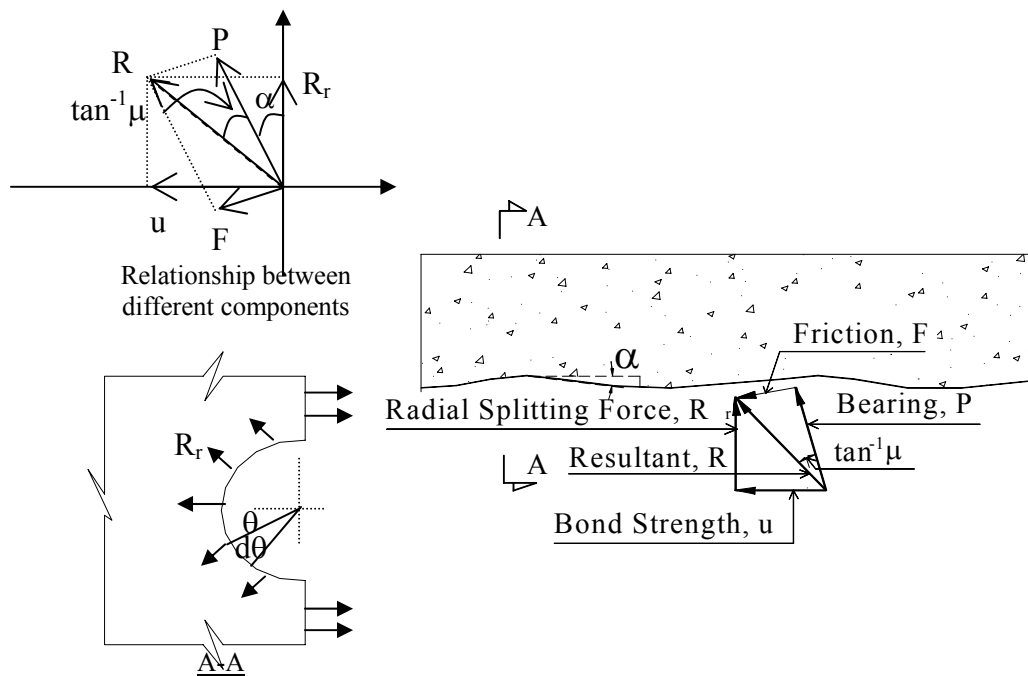
Figure 4.14. Relationship between Bond Strength and Splitting Force

The splitting force is caused by radial component, R_r. For simplification, it is

assumed that the concrete is split into one half, and the force is evaluated as follows:

$$F_{split} = \int_{-\frac{\pi}{2}}^{\frac{\pi}{2}} R_r l_d \frac{d_b}{2} \cos \theta d\theta = \frac{T(1 - \mu \tan \alpha)}{\pi(\mu + \tan \alpha)} \text{ lbs} \tag{4.3}$$

where P is normal bearing force on deformation with unit area,

F is friction force on deformation with unit area,

R is resultant of P and F,

R_r is radial component of R,

u is longitudinal component of R=bond strength,

T is pullout force,

μ is friction coefficient, and

α is rib angle.

The pullout force is then expressed by:

$$T = \frac{\pi(\mu + \tan \alpha)}{1 - \mu \tan \alpha} \times F_{split} \qquad (4.4)$$

It is assumed that the splitting tensile strength is reached and uniformly distributed along the splitting plane at the ultimate stage because of the plasticity of the concrete. Therefore,

$$F_{split} = f_{ct} A_{split} \text{ lbs} \qquad (4.5)$$

Substituting Equation 4.5 into Equation 4.4 results in

$$T = \frac{\pi(\mu + \tan \alpha)}{1 - \mu \tan \alpha} \times f_{ct} A_{split} \text{ lbs}$$

Finally, the bond strength, u, is expressed by:

$$u = \frac{T}{\pi d_b l_d} = f_{ct} \frac{\mu + \tan \alpha}{1 - \mu \tan \alpha} \frac{A_{split}}{d_b l_d} \text{ psi} \qquad (4.6)$$

where A_{split} is the concrete splitting area, and f_{ct} is the splitting tensile strength. f_{ct} has been related to $\sqrt{f_c'}$ in many publications. According to Carrasquillo et al. (1981), f_{ct} is approximated by $f_{ct} = 6.8(f_c')^{0.5}$ in psi and $f_{ct} = 0.56(f_c')^{0.5}$ in MPa. It is assumed that the

tensile strength will not be changed with the addition of a small amount of polypropylene

fibers.

Based on results reported in Table 4.3, by assuming µ equals 0.45, predictions of

the bond strength correlated well with the test results.

Table 4.3. Comparison of Bond Strength between Prediction and Experiment

f_c' (psi)	d_b (in.)	α degree	u_{test} (psi)	µ=0.4		µ=0.45		µ=0.5	
				U_{theo} (psi)	$\frac{u_{test}}{u_{theo}}$	$u_{pred.}$ (psi)	$\frac{u_{test}}{u_{theo}}$	$u_{theo.}$ (psi)	$\frac{u_{test}}{u_{theo}}$
7,400	0.5	2	2,850	2,263	1.25	2,524	1.12	2,785	1.02
7,400	1	5	2,644	2,553	1.04	2,814	0.94	3,075	0.86
5,360	0.5	2	2,352	1,929	1.22	2,146	1.09	2,379	0.99
5,360	0.5	2	2,070	1,929	1.07	2,146	0.96	2,379	0.87

Equation 4.6 shows good correlation for bond strength controlled by concrete

splitting. In this study, it is assumed that deformation of the FRP bar is strong enough to

prevent itself from being sheared off. This assumption is generally valid in normal

strength concrete, especially for the rebar with deformations with small angles to the

longitudinal direction, like the GFRP used in this study. The FRP rebar with steep

deformations (as shown in Figure 4.6b) will produce larger shear stresses on the ribs,

even when they have the same projected rib areas (i.e. the same h_r), and thus, the ribs are

easier to be sheared off. When the bond behavior is governed by the rib shear strength

other than concrete splitting, Equation.4.6 is no longer valid.

4.2.3. Basic Development Length. The application of the ultimate bond strength

data to real design is not appropriate because of the excessive slip occurring in these

specimens at large loads. Too much slip will result in untolerated crack widths. Although the FRP rebars were relatively inert to environmental exposure, the slip may cause some other problems, e.g., aesthetics. For traditional steel reinforced structures, ACI 318-02 requires a maximum crack width of 0.016 in. for interior exposure and 0.013 in. for exterior exposure. ACI 440 recommends crack limitation for FRP structures to be 0.020 in. and 0.028 in. for exterior and interior exposure, respectively. From a designer's point of view, Mathey and Watstein (1961) suggested that bond stress corresponding to 0.01 in. slippage of loaded end or 0.002 in. of free end for steel reinforced structures can be defined as critical bond stress. The criterion of 0.01 in. slippage at loaded-end was decided based on half of the crack width limitation. In a study conducted by Ferguson et al. (1965), the researchers discovered that the loaded-end slip of the pullout specimens was larger than that of the beam specimens because flexural cracks in beam specimens tended to distribute the slip in several places along the beam. Also, since there is relatively low elastic modulus of FRP materials (GFRP is about 1/5 that of steel, CFRP is about 2/3 that of steel), greater elongation along the embedded rebar will be produced and lead to larger loaded-end slip. Thus, 0.01 in. slippage at the loaded-end of pullout specimens as design criterion is too conservative. To keep it comparable to limits imposed on steel rebar, bond strength corresponding to 0.002 in. slippage at the free-end is recommended as designing bond strength.

For the FRP rebar, the basic development length, l_{db}, is defined as the minimum embedment length required to develop fracture tensile strength, f_{fu}, of the FRP rebar. Based on the equilibrium equation, $l_{db}\pi d_b u = A_f f_{fu}$ results in:

$$l_{db} = \frac{A_f f_{fu}}{\pi d_b u} \text{ in.} \qquad (4.7)$$

Referring to ACI 318-02, the development length of the rebar is expressed as follows:

$$l_d = \frac{f_{fu}}{K\sqrt{f_c'}} d_b \text{ in.}$$ (4.8)

Equating (4.7) to (4.8) gives an expression to the coefficient $K = \frac{4u}{\sqrt{f_c'}}$

where A_f = area of the FRP bar in in.^{2};

f_{fu} = ultimate strength of FRP bar in psi,

f_c' = concrete strength, psi.

d_b = diameter of FRP rebar in in., and

u = bond strength in psi.

A statistical analysis was performed on the design bond strength. Assuming the test results were distributed as Student t distribution, the bond strength with 95% confidence was computed as $\overline{u} - t \frac{s}{\sqrt{n}}$, where t is t distribution quantity, and is equal to 2.353 for 95% confidence in the case of three specimens; $\overline{u}$ is the average bond strength; s is the standard derivation; n is the number of the test specimens, in this study $n = 3$. Thus, a coefficient $K = 42$ was obtained. As mentioned previously, specimens after fatigue loading have higher bond stiffness and capacity. Thus, this equation can also be safely used in the fatigue loading situations.

If adjusting the development length to the AASHTO format, the equation used for development length is:

$$l_{db} = 0.05 \frac{A_f f_{fu}}{\sqrt{f_c'}} \text{ in.}$$ (4.9)

where A_f = area of the FRP rebar, in^2.

A K value of 0.04 is adopted by AASHTO for the steel reinforcement. Based on this study, the development length for the FRP bars is recommended to be 25% larger than that of the steel bar.

4.3. SPLITTING BOND TEST RESULTS

4.3.1. Test Results and Discussions. In the following sections, the observations from the tests and several parameters that would influence the bond characteristics will be discussed. These parameters included the fiber effect by volume fraction (V_f), cover effect (C_b), and rebar diameter (d_b).

The average bond strength is calculated as the pullout force over the embedded area of the rebar. When comparing the bond strength of specimens with different concrete strengths, f_c', bond strength was normalized by dividing by the square root of f_c', which is adopted in the current AASHTO Code.

Cracks, if any, initiated from the loaded end and propagated to the free end. Following this, some cracks derivated from the longitudinal direction to the transverse direction. Crack patterns observed on the outside of the specimens are shown in Figure 4.15 and listed in Table 4.4.

After failure, concrete covers were removed from the specimens to allow inspection of the surface conditions of the rebars after testing. No major differences were observed between the FRC specimens and the plain concrete specimens. The following are some of the observations (see Figure 4.16):
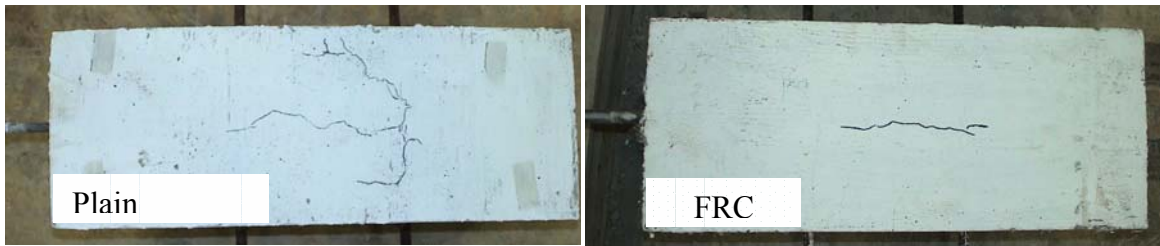
(a) Crack patterns of #4 CFRP with 1 d_b cover in plain concrete and FRC
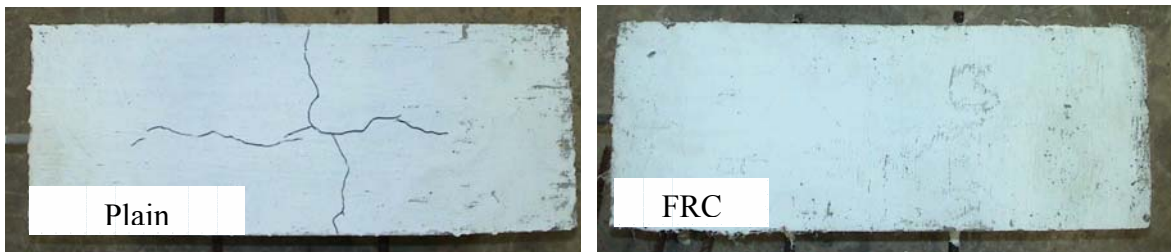
(b) Crack patterns of #4 CFRP with 3 d_b cover in plain concrete and FRC

(c) Crack patterns of #4 GFRP with 1 d_b cover in plain concrete and FRC
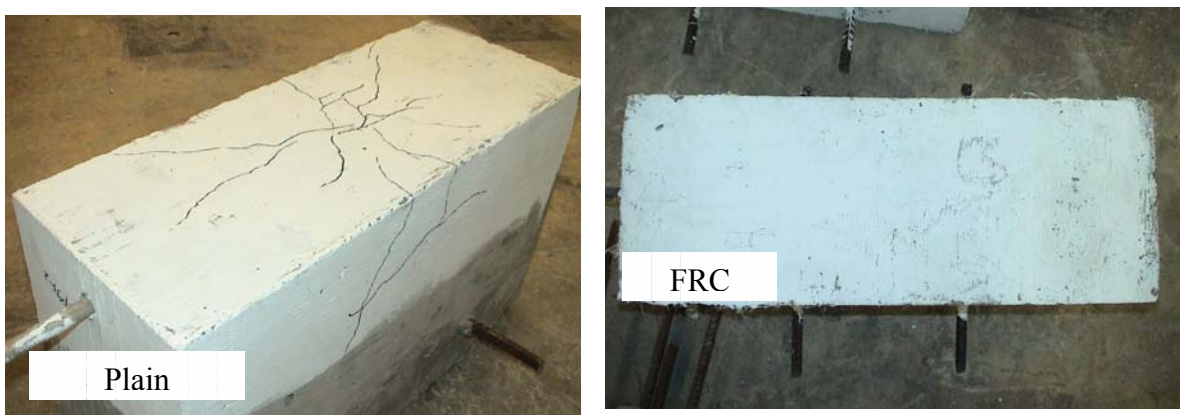
(d) Crack patterns of #4 GFRP with 3 d_b cover in plain concrete and FRC

Figure 4.15. Crack Patterns for Various Specimens Showing Effect of C_b and V_f
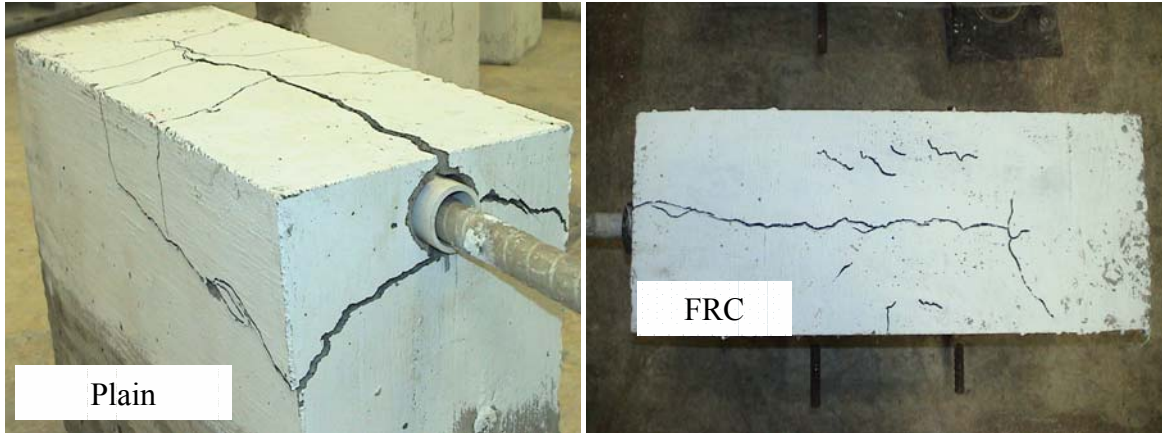
(e) Crack patterns of #8 GFRP with 1 d_b cover in plain concrete and FRC
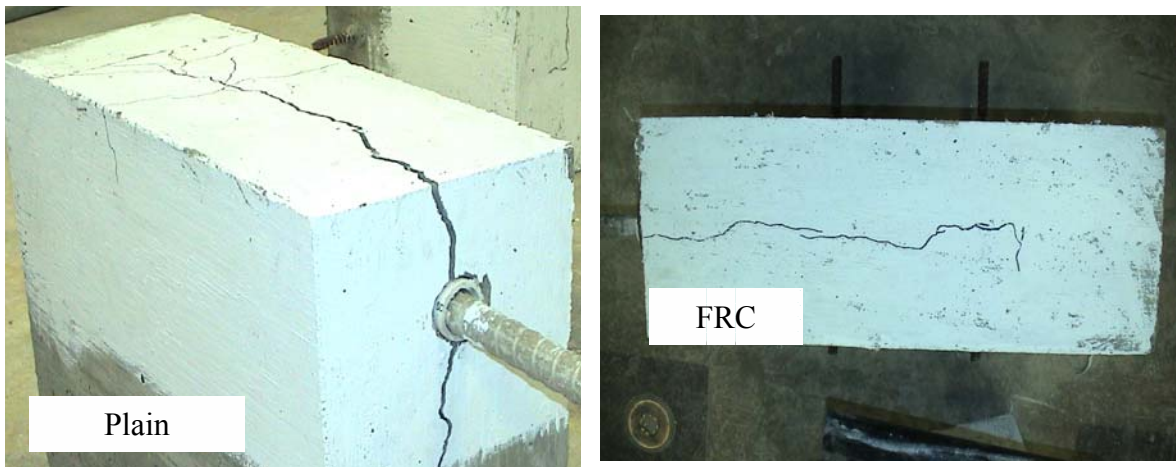
(f) Crack patterns of #8 GFRP with 3 d_b cover in plain concrete and FRC

**Figure 4.15. Crack Patterns for Various Specimens Showing
Effect of C_b and V_f (Cont.)**

In the GFRP specimens, some resin of the rebar was scratched off the rebar surface and remained attached to the concrete. The indentation shape of the GFRP rebar was not changed, showing that the transverse direction of the rebar could sustain the bearing compression force. Traces of concrete were observed on the rebar surface, which revealed a good chemical bond between the rebar and the concrete.

Table 4.4. Description of Test Results

I.D.	Failure Mode	Splitting Crack Width	Descriptions
4PC1	Splitting	0.001 in.	One longitudinal crack along the embedment portion developed first, and then the concrete cover at the embedment portion spalled.
4PC3	Splitting	0.007 in.	One longitudinal crack along the embedment portion developed and extended toward the front face but did not reach the front face. Transverse flexural cracks were also observed.
4PG1	Splitting	0.035 in.	Concrete cover spalled at the embedment portion. No cracks at side faces were observed.
4PG3	Splitting	0.011 in.	Longitudinal splitting crack developed and extended toward the front face but did not reach the front face. Transverse flexural cracks were observed. Cracks at side faces developed at the embedment portion. No cracks at the front face were observed.
8PG1	Splitting	0.2 in.	One big crack went through from front face to the free end, accompanied by several transverse cracks induced by bending. Two big cracks were also observed at the front face. They extended along the side faces and finally connected with the longitudinal crack at the surface, splitting the concrete into several pieces.
8PG3	Splitting	0.25 in.	One big crack went through from front face to the free end and extended down to the bottom at the front face; it almost splitted the concrete into halves. Several transverse cracks also were observed.
4FC1	Splitting	0.001 in.	One crack developed and was limited to the embedment region.
4FC3	Pullout	N/A	
4FG1	Splitting	0.003 in.	One crack developed and was limited to the embedment region.
4FG3	Pullout	N/A	
8FG1	Splitting	0.015 in.	One longitudinal crack developed at the embedment portion, extended to the front face, and then went down to the rebar.
8FG3	Splitting	0.009 in.	One longitudinal crack developed at the embedment portion, extended to the front face, and then went down to the rebar.

Note: (1) See Figure 4.15 for crack Patterns.
     (2) Results and descriptions are based on two duplicate specimens.
     (3) Splitting crack width was measured by microscope.
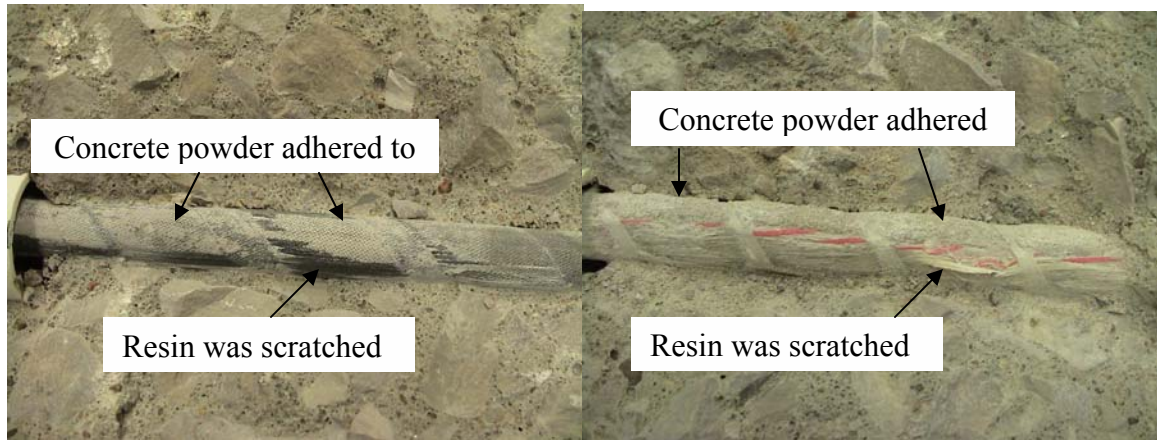
Figure 4.16. Surface Condition of Various FRP Rebars after Testing

In the CFRP specimens, some resin was scratched off the rebar surface and remained glued to the concrete surface. Traces of concrete were observed on the rebar surface, which revealed a good chemical bond between the rebar and the concrete.

4.3.1.1. Fiber effect on bond characteristics. In the following sections, the fibers' effects on the bond characteristics, in terms of crack patterns and bond slip response, are discussed.

(a) Splitting Crack Patterns

The following are some of the different observations regarding the crack patterns between the plain concrete specimens and the FRC specimens.

All the plain concrete specimens failed by concrete splitting. Most of the FRC specimens failed also by concrete splitting, except for the #4 CFRP and #4 GFRP specimens with 3 d_b cover, which failed by rebar pullout. The width of the splitting cracks was smaller in the case of the FRC specimens, which revealed that the fibers could effectively restrict the development of cracks. Concrete spalling was observed in several plain concrete specimens, but it did not occur in the FRC specimens. Since concrete spalling is a sign of

more severe damage of concrete cover, one can see that with the addition of fibers, the damage is less severe compared to the plain concrete specimen. When specimens failed by concrete splitting, the FRC specimens failed in a much more ductile fashion.

(b) Bond-Slip Response

The bond-slip curve could roughly be divided into two portions, the ascending portion and descending portion. The fibers showed some effects on the overall bond-slip curves.

In the ascending portion (as shown in Figure 4.17), the plain concrete and FRC specimens did not show any significant difference. At the initial loading stage, the bond-slip curves increased linearly. Since no splitting cracks were developed, the bond
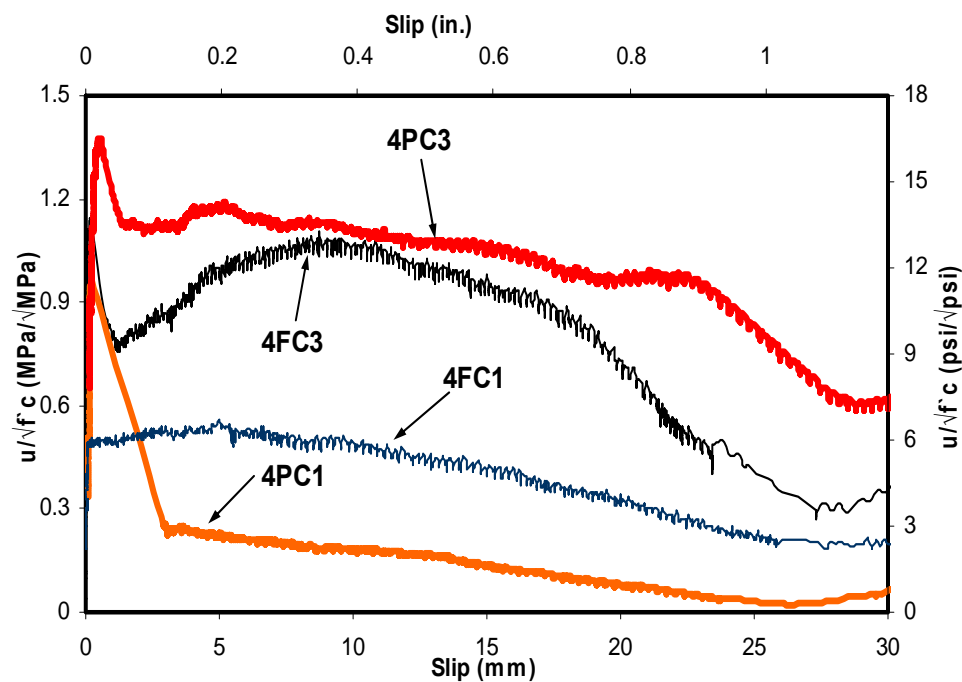
(a) Bond-Slip Relationships of #4 CFRP

Figure 4.17. Bond-Slip Relationship of Various Rebars in Plain Concrete and FRC
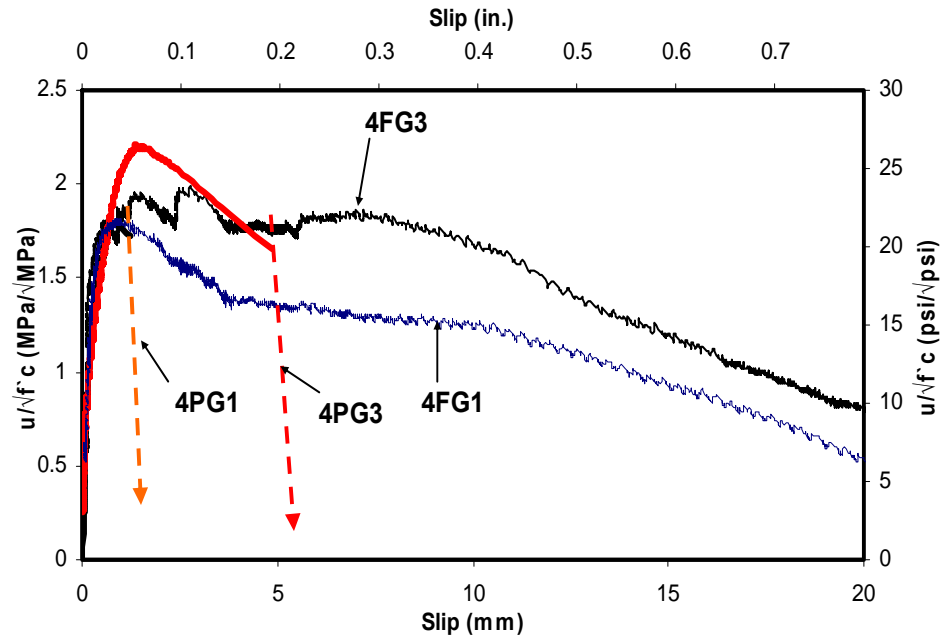
(b) Bond-Slip Relationship of #4 GFRP
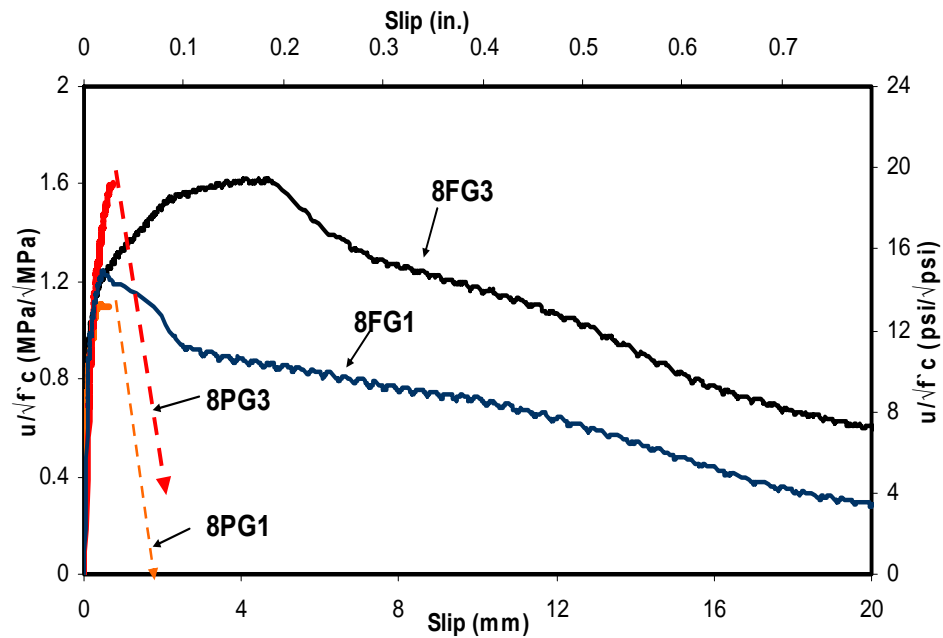
(c) Bond-Slip Relationship of #8 GFRP

Figure 4.17. Bond-Slip Relationship of Various Rebars in Plain Concrete and FRC (Cont.)

stiffness was quite high. At about 50% to 80% of the ultimate capacity, the splitting micro-cracks developed. The stiffness of the bond-slip curve decreased accordingly.

In the descending portion, the confinement from the concrete to rebar decreased with the propagation of the splitting cracks. Consequently, the pullout loads dropped. In the descending portion (as shown in Figure 4.17), significant differences were observed between the plain concrete specimens and the FRC specimens. In the plain concrete, after reaching its capacity, the load dropped suddenly to zero. However, in the FRC, after reaching the peak, with the presence of fibers, which limited the propagation of splitting cracks, the confinement force from the concrete was still relatively significant. Therefore, the bond-slip curve dropped gently and maintained at more than 70% of its capacity, even at the slip of 0.4 in.

4.3.1.2. Cover effect on bond characteristics. The bond strength increased with the increase of the clear cover depth. The increasing rates differed for the different specimens, as shown in Figure 4.17 and Table 4.5. Before the bond reached the peak, the bond-slip curves for specimens with 1 d_b and 3 d_b were almost identical. Specimens with 1 d_b cover always failed with less capacity and smaller slips.

4.3.1.3. Diameter effect on bond characteristics. The smaller diameter rebar had higher bond capacity, similar to the behavior of the traditional steel rebar, as shown in Table 4.5.

4.3.2. Theoretical Prediction of Bond Strength. The theory used in pullout specimens should also be valid in beam end specimens since the bond mechanism is similar. However, the definition of the effective splitting area, A_{split}, is necessary before the direct application of Equation 4.6.

Table 4.5. Test Results of Beam End Tests

I.D.	Ultimate Bond Strength u (psi)	Ultimate Bond Strength[*] $u/\sqrt{f_c'}$ $(psi/\sqrt{psi})$	Loaded-End Slip at Peak (in.)	Free-End Slip at Peak (in.)	Design Bond Strength u_{design} (psi)	95% of Design Strength (psi)
4PC1	943	12.48	0.011	0.001	904	863
4PC3	1,318	17.52	0.018	0.002	1,025	962
4FC1	357	6.00	0.003	0.004	454	428
4FC3	880	14.88	0.009	0.001	1,107	995
4PG1	1,607	21.24	0.038	0.002	1,072	1,012
4PG3	2,055	27.24	0.052	0.010	1,089	982
4FG1	1,279	21.60	0.037	0.011	1,146	1,054
4FG3	1,388	23.40	0.215	0.202	1,398	1,387
8PG1	969	12.84	0.020	0.002	844	696
8PG3	1,436	19.08	0.026	0.001	957	848
8FG1	893	15.12	0.019	0.002	976	964
8FG3	1,179	19.92	0.162	0.132	975	954

(1) Numbers are the average values for two testing specimens.
(2) The asterisk indicates the bond strength normalized to square root of concrete strength.

Several models have been developed for the bond strength prediction of the traditional steel rebar. In these models, an assumption is commonly used: concrete within the cylinder or square (the largest square or circle that can be drawn within the beam section around the rebar, as shown in Figure 4.18) is regarded as the effective portion to prevent the beam from splitting. In other words, the contribution from the portion outside the cylinder or square is ignored (Kemp, 1986). This theory does not consider the beam-width effect on bond strength. Two beams, as shown in Figure 4.18, should have the same bond strength based on that theory, since they have the same area of concrete to resist the beam from splitting. However, research showed that the width of the beam could influence the bond strength and that wider beams resulted in higher bond strength
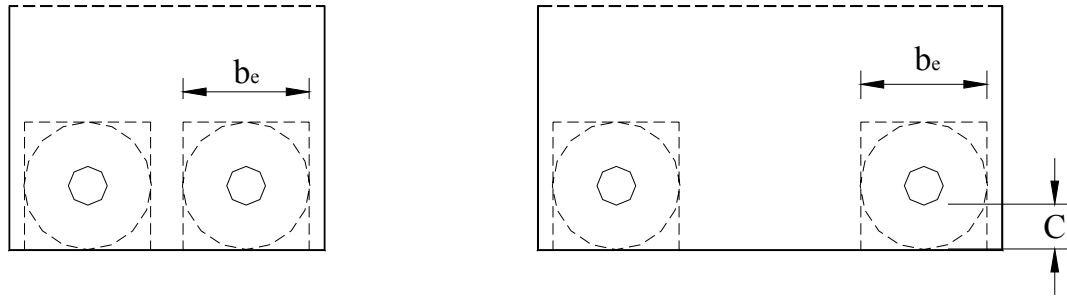
Figure 4.18. Previous Definition of Contribution from Concrete

(Chinn et al., 1955; Ferguson and Thompson, 1962). This phenomenon reveals that concrete outside the circle or square has a noticeable effect on bond strength and cannot be ignored. Wider beams have more concrete to prevent beams from splitting. In other words, the effective splitting area increases with the increasing of the beam width. Apparently, it is the effective beam width rather than the total beam width that influences the bond strength.

Based on the above explanation, schematic pullout specimens (rectangular concrete blocks surrounded by dash lines with an area of $b_e \times (l_e + d_b + C)$, as shown in Figure 4.19), are used to represent the beam to describe its bond mechanism. Thus, the approach used in the pullout specimens can be applied to the beam situation. The effective splitting area, as shown in Figure 4.19b, is taken as

$$A_{split} = (l_e + C)l_d \text{ in.}^2 \tag{4.10}$$

where l_e is the effective splitting length, and l_e is a function of effective beam width. In this analysis, l_e is assumed to be equal to $b_e/3$ in this study and b_e is the effective beam width, from center to center of the rebar spacing or from the edge of the beam to the center of the rebar spacing;
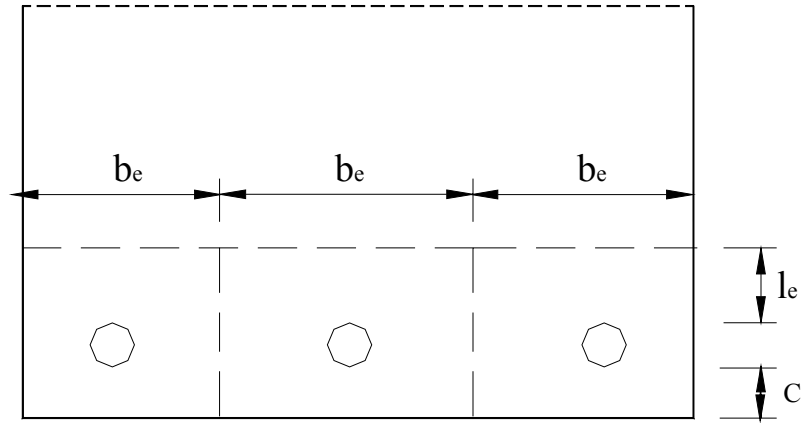
(a) Schematic pullout specimens in a beam
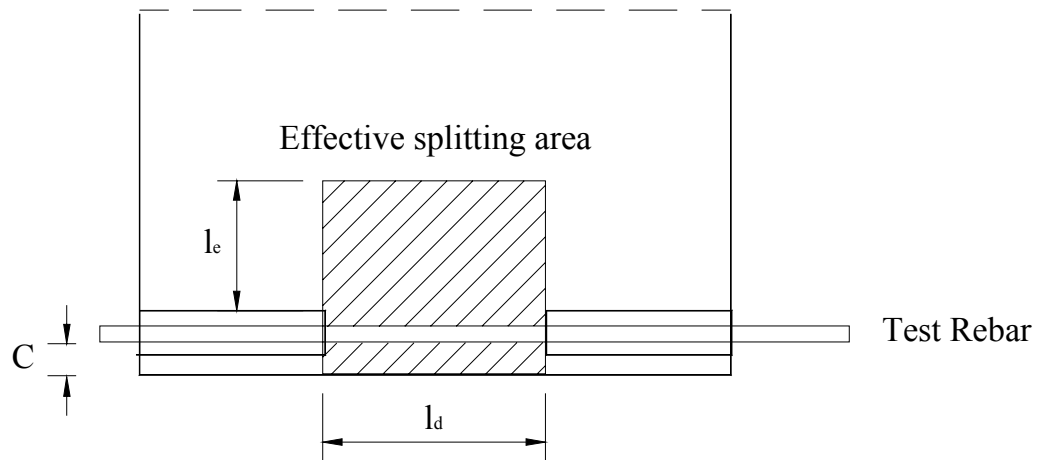
(b) The effective splitting area (hatched area)

Figure 4.19. Definition of Splitting Area for Beam End Specimen

Substituting Equation 4.9 into Equation 4.6 and taking $l_e=b_e/3$ results in:

$$u = \frac{(3C+b_e)}{3d_b} \times \frac{\mu+\tan\alpha}{1-\mu\tan\alpha} f_{ct} \;\; \text{psi}$$

(4.11)

To test the correlation of Equation 4.10, a comparison was made between test results and predictions, as shown in Table 4.6. Since Equation 4.10 is based on the assumption that the specimen fails in concrete splitting, only specimens that failed in this mode were included. As shown in Table 4.6, the predictions of Equation 4.10 are close to the test results but are consistently lower by about 10% than those of the test results. Bond strength is highly dependent on the embedment length as well. Specimens with longer embedment length usually result in lower average bond strength. To account for this, an adjustment factor, γ, is added to reflect the embedment length. Thus, Equation 4.10 becomes

$$u = \frac{(3C + b_e)}{3d_b} \times \frac{\mu + \tan \alpha}{1 - \mu \tan \alpha} \gamma f_{ct} \quad \text{psi} \tag{4.12}$$

in which γ is a function of embedment length, based on the current test results, where $l_d = 10 d_b$, γ can be taken as 0.9. Further study is needed to look into various embedment lengths and other situations, such as the effect of different fiber volume fraction.

Table 4.6. Comparison of Bond Strength between Prediction and Experiment

Specimen I.D.	f'c (psi)	C/d$_b$	d$_b$ (in.)	b$_e$ (in.)	α degree	u$_{test}$ (psi)	u$_{theo}$ (psi) Eq. (9)	$\frac{u_{test}}{u_{theo}}$
4PG1	5656	1	0.5	9	2	1588	1743	0.91
4PG3	5656	3	0.5	9	2	2055	2241	0.92
8PG1	5656	1	1	9	5	969	1131	0.86
8PG3	5656	3	1	9	5	1436	1697	0.85
4FG1	3480	1	0.5	9	2	1279	1368	0.94
8FG1	3480	1	1	9	5	893	888	1.01
8FG3	3480	3	1	9	5	1179	1331	0.89
Average								0.91
COV								0.05

4.3.3. Basic Development Length. By adopting the same methodology used in the pullout tests, a similar expression based on the test data from splitting bond test was developed for the basic development length for the FRP rebars embedded in FRC.

Based on the test data from a total of 24 specimens (The #4 CFRP with 1 d_b cover was not considered, which had much lower bond strength value when compared to the other cases. This may be due to the ill vibration during fabrication of the specimen.), a statistical analysis with 95% confidence was conducted (the method is the same as that conducted in pullout bond test). The following expression was obtained

$$l_{db} = \frac{f_{fu} d_b}{37\sqrt{f_c'}} \text{ in.}$$ (4.13)

Also, by adjusting the format to the AASHTO, the development length can be computed as the following expression:

$$l_{db} = 0.056 \frac{A_f f_{fu}}{\sqrt{f_c'}} \text{ in.}$$ (4.14)

As mentioned previously, a K value of 0.04 is adopted by AASHTO for the steel reinforcement. Based on this study, the development length for the FRP bars is recommended to be 40% larger than that of the steel bar.

The development length derived based on the beam tests are slightly larger (approximately 10%) than that obtained from the pullout bond test. As we discussed previously, the pullout bond specimen is under compression in the case of pullout bond tests, which will induce confinement effect on the bond and result in larger bond strength. Consequently, the development length computed by the pullout test method is smaller. Since the stress condition in beam end specimens are closer to the real conditions,

Equation 4.13 or 4.14 is recommended as the equation to calculate the development length for FRP reinforcement.

ACI 440 recommendations for the development length is:

$$l_{db} = \frac{f_{fu} d_b}{2700} \text{ in.}$$
(4.15)

By assuming the concrete strength of 5000 psi, one can see that the development length computed by Equation 4.15 is very close to ACI 440 recommendation.

4.4. CONCLUDING REMARKS

Bond characteristics were investigated by two different methods; i.e., the pullout bond test and the splitting bond test. Fibers, bar surface, diameter, embedment length, cover depth, and fatigue loading's effect on bond characteristics were investigated. The following concluding remarks could be made:

- With the addition of fibers, the bond-slip relationship significantly improved in the post-peak region, while little change was observed for the pre-peak behavior. The FRC specimens failed in a more ductile fashion with a smooth descending portion. A large portion of the load could be held, even at large slip. The plain concrete specimens failed in a very brittle fashion. Once it reached the peak value, the load dropped suddenly to zero.

- Different bond mechanisms were observed for the CFRP and the GFRP specimens due to their different surface treatments. Bond strength of the GFRP specimen was about twice as much as that of the CFRP. The GFRP specimen failed by concrete splitting; while the bond failure of the CFRP specimen initiated by the rebar pullout, providing more ductile behavior;

- Fatigue loading, within a working stress range, was shown to increase the bond stiffness and the bond strength, while causing the bond behavior to be more brittle and often change the failure mode from rebar pullout to concrete splitting.

- The large amount of slip between the rebar and concrete has occurred during the fatigue loading. Therefore, the total slip, including the residual slip due to fatigue loading, could be regarded as an inherent property for bond behavior between the rebar and the concrete, and it has little relationship with the loading history.

- Polypropylene fibers can effectively decrease the rate of bond degradation due to the fatigue loading.

- Based on analytical derivation and experimental calibration, an equation was proposed to predict the bond strength for the FRP bars embedded in FRC failed by concrete splitting.

- Bond value corresponding to 0.002 in. at the free-end slip or 0.01 in. at the loaded end was recommended as the designing bond strength in previous studies (Mathey and Watstein, 1961). Based on this criteria, an equation for the basic development length of the FRP rebar in the FRC was proposed.

5. FLEXURAL DUCTILITY TEST RESULTS

5.1. INTRODUCTION

Ductility is a structural design requirement in most design codes. In steel RC structures, ductility is defined as the ratio of post-yield deformation to yield deformation which usually comes from steel. Ductile structural members offer many benefits for the structures. The most important aspect is that for the ductile structures, there will be a warning before failure; while little or no warning can be observed before failure for the brittle structures. Due to the linear-strain-stress relationship of the FRP bars, the traditional definition of ductility cannot be applied to the structures reinforced with FRP reinforcement. Several methods, such as the energy based method and the deformation based method, have been proposed to calculate the ductility index for FRP reinforced structures (Naaman and Jeong, 1995, and Jaeger et al., 1995).

Due to the linear elastic behavior of the FRP bars, the flexural behavior of FRP reinforced beams exhibits no ductility as defined in the steel reinforced structures. A great deal of effort has been made to improve and define the ductility of the beams reinforced with FRP rebars. To date, there are three approaches; one approach is to use the hybrid FRP rebars; that is, pseudo-ductile materials are fabricated by combining two or more different FRP reinforcing materials to simulate the elastic-plastic behavior of the steel rebars. Harris, Somboonsong, and Ko (1998) tested beams reinforced with the hybrid FRP reinforcing bars and they found that the ductility index of those beams can be close to that of the beams reinforced with steel. This method has shown some success in the research studies but has resulted in limited practical applications because of the

complicated and costly manufacturing process of the hybrid rebars. Another approach to realize the ductility of the FRP reinforced members is through the progressive failure of bond and the combination of rebars with different mechanical properties (Gopalaratnam, 2005). The third approach is to improve the property of concrete. ACI 440 recommends the FRP reinforced structure be over-reinforced and designed so that the beams fail by concrete crushing rather than by rebar rupture. Thus, the ductility of the system is strongly dependent on the concrete properties. Alsayed and Alhozaimy (1999) found that with the addition of 1% steel fibers, the ductility index could be increased as much as 100%. Li and Wang (2002) reported that the GFRP rebars reinforced with engineered cementitious composite material showed much better flexural behaviors. The ductility was also found to be significantly improved.

This chapter presents research result on the flexural behavior of concrete beams reinforced with FRP rebars and concrete containing polypropylene fibers. The different behaviors of plain concrete beams and FRC beams are also discussed.

5.2. TEST RESULTS AND DISCUSSIONS

This Chapter provides a summary of the overall flexural behavior of the FRP/FRC hybrid system in terms of crack distribution, load-deflection response, relative slip between the rebar and concrete, cyclic loading effect on flexural behavior, and strain distribution in concrete and reinforcement. Comparison between FRP/Plain concrete system and FRP/FRC system is also discussed.

5.2.1. Crack Distribution. Figures 5.1 to 5.3 show the typical crack patterns for the FRP reinforced beams at moderate (40% M_u) and high (80% M_u) load levels to
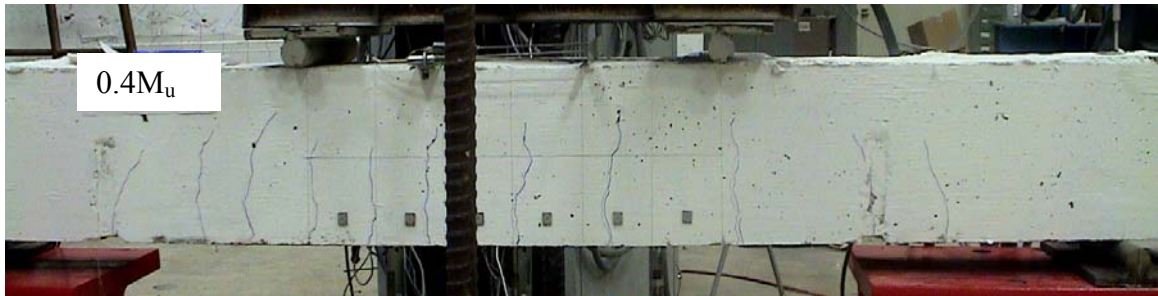
(a) VF4C (FRC Beams)
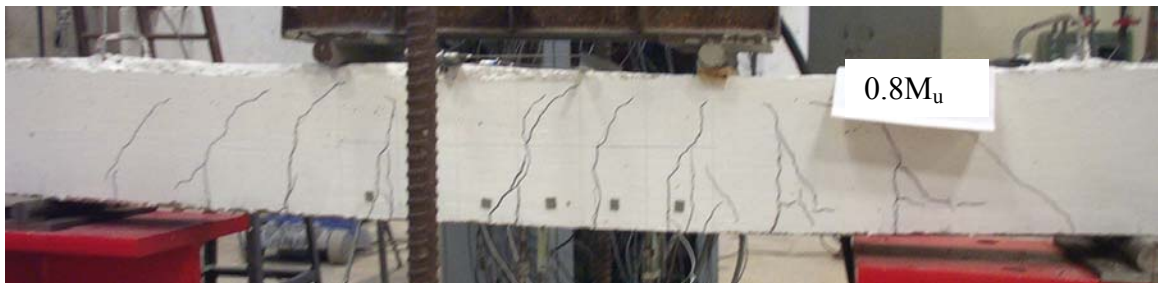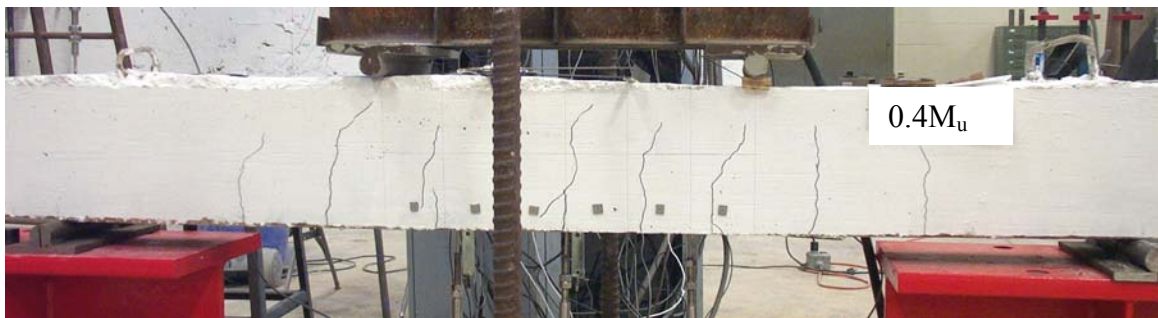
(b)VP4C (Plain Concrete Beams)

Figure 5.1. Crack Patterns for #4 CFRP Beams
at Moderate and High Level Loading

0.4M$_u$

0.8M$_u$

(b) VF4G (FRC Beams)

0.4M$_u$

0.8M$_u$
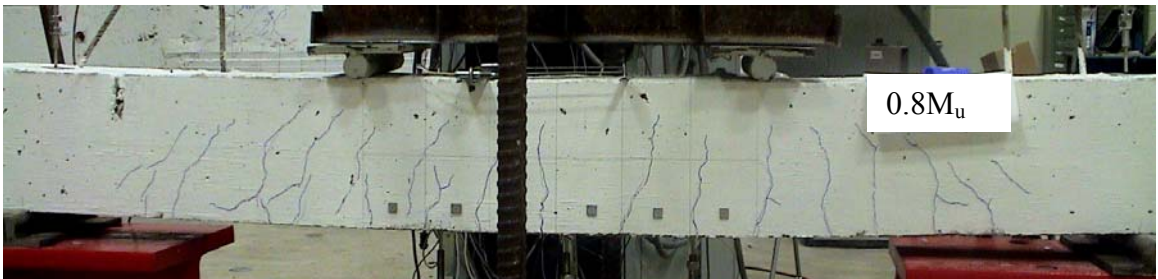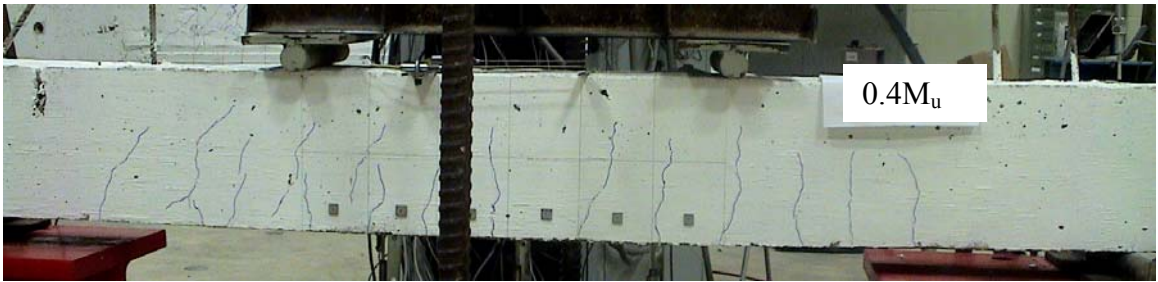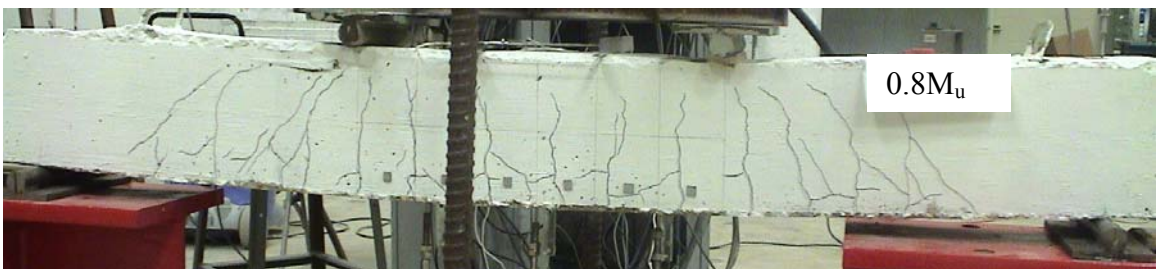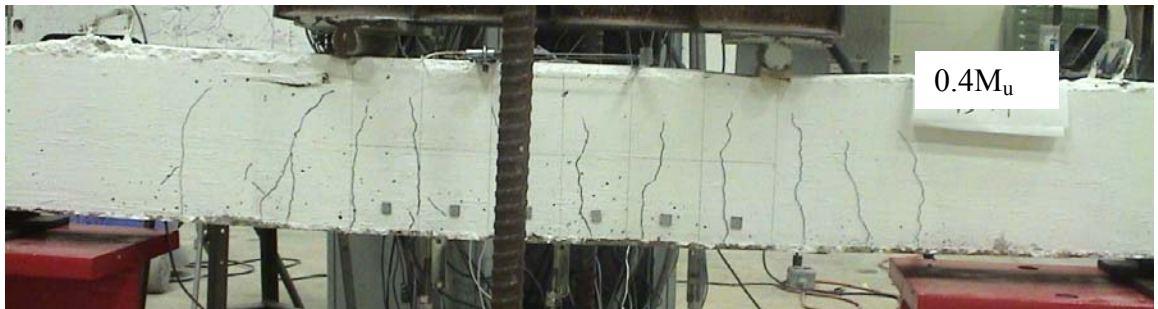
(b) VP4G (Plain Concrete Beams)

**Figure 5.2. Crack Patterns for #4 GFRP Beams
at Moderate and High Level Loading**

0.4M$_u$

0.8M$_u$

(a) VF8G (FRC Beams)

0.4M$_u$

0.8M$_u$
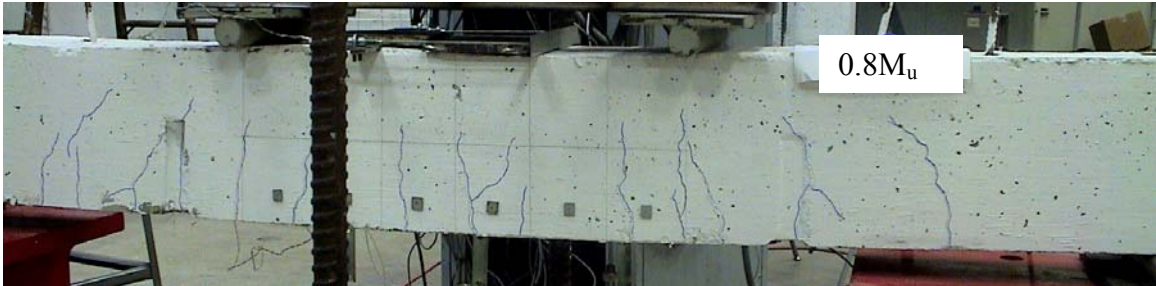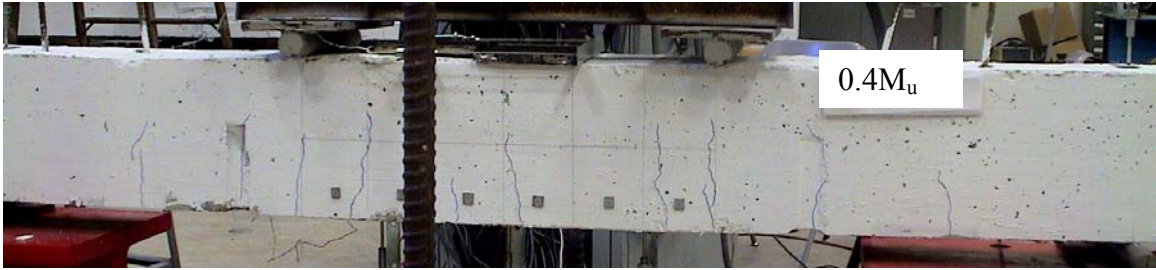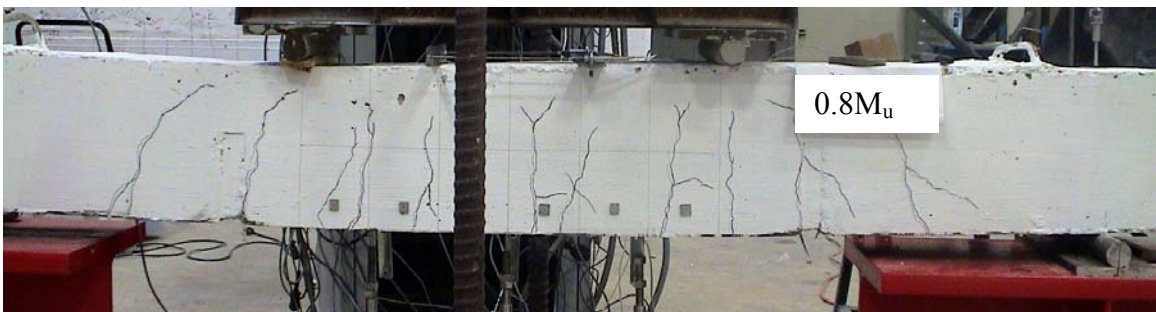
(b) VP8G (Plain Concrete Beams)

**Figure 5.3. Crack Patterns for #8 GFRP FRC Beams
at Moderate and High Level Loading**

investigate the crack distribution at different load level. Like traditional steel rebar reinforced beams, vertical flexural cracks developed first at the pure bending regions. Then, the inclined shear cracks were induced with the increase of load.

- **Cracking Moment.** Theoretical and experimental values for cracking moments are given in Table 5.1. As shown in Table 5.1, the experimental values were close to the theoretical values but were consistently lower by about 20% than those of the theoretical predictions. Also, as expected, the cracking moment was not affected by the addition of 0.5% of polypropylene fibers. This was because the elongation at break of the polypropylene fiber is three orders of magnitude greater than the ultimate tensile strain of the concrete due to the low elastic modulus (500 to 700 ksi). Hence, the concrete would crack long before the fiber strength was approached.

- **Crack Spacing.** Table 5.2 shows the average crack spacing at 40% and 80% of the flexural capacity. With the increase of load, crack spacing slightly decreased. Interestingly, by comparing the crack spacing between the plain concrete beams and the FRC beams, the crack spacing was virtually the same at 80% of ultimate load, while the crack spacing of the FRC beams was about 20% smaller than that of plain concrete at a moderate service load (about 40% of ultimate load).

Studies suggest that the flexural cracking can be closely approximated by the behavior of a concrete prism surrounding the main reinforcement and having the same centroid. Cracks initiate when the tensile stress in the concrete exceeds the tensile strength of concrete, f_t'. When this occurs, all the force in the prism is transferred to the rebar. Away from the crack, the concrete stress is gradually built up through the bond stress between the rebar and the concrete. When the stresses in the concrete are large

enough and exceed the tensile strength of concrete f_t', a new crack forms. The above

mechanism is demonstrated in Figure 5.4.

Table 5.1. Cracking Moment and Average Crack Spacing

Specimen I.D.	M_{cr} (kips-in.)	$M_{cr\text{-}exp}$ (kips-in.)	$\dfrac{M_{cr}}{M_{cr-exp}}$
VP4C-1	60.0	53.1	1.13
VP4C-2		48.3	1.24
VP4G-1	60.0	54.3	1.10
VP4G-2		48.3	1.24
VP8G-1	60.4	48.1	1.26
VP8G-2		48.3	1.25
Average		50.1	1.20
VF4C-1	47.7	42.3	1.13
VF4C-2		42.3	1.13
VF4G-1	47.7	40.3	1.18
VF4G-2		44.0	1.08
VF8G-1	48.1	36.3	1.33
VF8G-2		36.7	1.31
Average		40.3	1.19

Note: the self weight of beams have been included in calculating the experimental cracking moments.

Table 5.2. Average Crack Spacing

Specimen I.D.	Crack Spacing, S_m, at 40%M_u (in.)	Crack Spacing, S_m, at 80%M_u (in.)	$\dfrac{S_{FRC}}{S_{plain}}$ at 40%M_u	$\dfrac{S_{FRC}}{S_{plain}}$ at 80%M_u	ACI-440 (in.)	CEB-FIP Code (in.)
VP4C	6.00	4.55	N/A	N/A	7.30	4.50
VP4G	5.28	3.58	N/A	N/A	5.40	3.75
VP8G	6.00	4.23	N/A	N/A	8.02	4.24
VF4C	4.60	4.20	0.77	0.93	7.30	4.50
VF4G	4.00	3.43	0.76	0.96	5.40	3.75
VF8G	4.80	4.40	0.8	1.04	8.02	4.24

First Crack

Formation of First Crack

Uniform concrete stress
transfered by fibers

First Crack

Formation of First Crack

Distribution
before formation
of second
crack

Bond Stess

Stess in Concrete

f'_t

Bond Stress

Contribution from
bond stress

Stess in Concrete

f'_t

Contribution from
bridging of fibers

First Crack   Second Crack

S_1

First Crack   Second Crack

Fiber Bridging

S_2

(a) Crack Formation in Plain Concrete Beam   (b) Crack Formation in FRC Beam

**Figure 5.4. Mechanism of Crack Formation in Plain Concrete Beams
and FRC Beams**

With the addition of fibers, the mechanism of crack formation is slightly changed,

as shown in Figure 5.4. Some tensile loads can be transferred across the cracks by the

bridging of fibers. Thereby, the stress in the concrete comes from not only the bond stress,

but the bridging of fibers as well. With the contribution from the fibers, less bond stress is

needed to reach the same cracking stress. Consequently, the spacing of crack is smaller in

the FRC beams than in the plain concrete beams ($S_2 < S_1$ as shown in Figure 5.4).

At the high level of load, due to inadequate bond between the fibers and concrete,

fibers are pulled out and the contribution from the bridging of fibers is diminished.

- **Compared with the Predictions by CEB-FIP Code.** The CEB-FIP Code

expression for the average crack width for the steel reinforced concrete is in the following

manner:

$$S_m = 2(c + \frac{s}{10}) + k_1 k_2 \frac{d_b}{\rho_{ef}} \text{ in.} \tag{5.1}$$

where c = clear concrete cover

s = maximum spacing between longitudinal reinforcing bars but shall not be taken greater than 15 d_b

d_b = bar diameter

$\rho_{ef} = A_s / A_{cef}$

A_s = area of steel considered to be effectively bonded to the concrete

A_{cef} = area of effective embedment zone of the concrete

k_1 = 0.4 for deformed bars; and 0.8 for plain bars

k_2 = coefficient to account for stain gradient

The same method is adopted for the FRP reinforced beams and compared to the test data. As shown in Table 5.2, the prediction values underestimate the crack spacing at the service load (40% of the ultimate), especially in the case of the plain concrete beams.

- **Compared with the Prediction by ACI 440.** Based on the current ACI 440 recommends for the crack width of the FRP reinforced member, the following equations can be derived to calculate the crack spacing:

$$w = 2200 k_b \sqrt[3]{d_c A} \text{ in.} \tag{5.2}$$

where w = the crack width at tensile face of the beam,

A = the effective tension area per bar,

d_c = the thickness of concrete cover measured from extreme tension fiber to the center of the closest layer of longitudinal bars, and

k_b = the coefficient that accounts for the degree of bond between the FRP bar and the surrounding concrete. ACI suggests 1.2 for deformed FRP bars if k_b is not experimentally known.

As shown in Table 5.2, the ACI predictions overestimate the crack spacing for both plain concrete beams and FRC beams when k_b is equal to 1.2.

- **Crack Width.** During the tests, crack widths were measured by the distance changes between the Demac gages. Figures 5.5 to 5.7 show the relationships between the crack width and the applied moment. In the following section, several currently available models to predict the crack width are discussed and compared with test results.
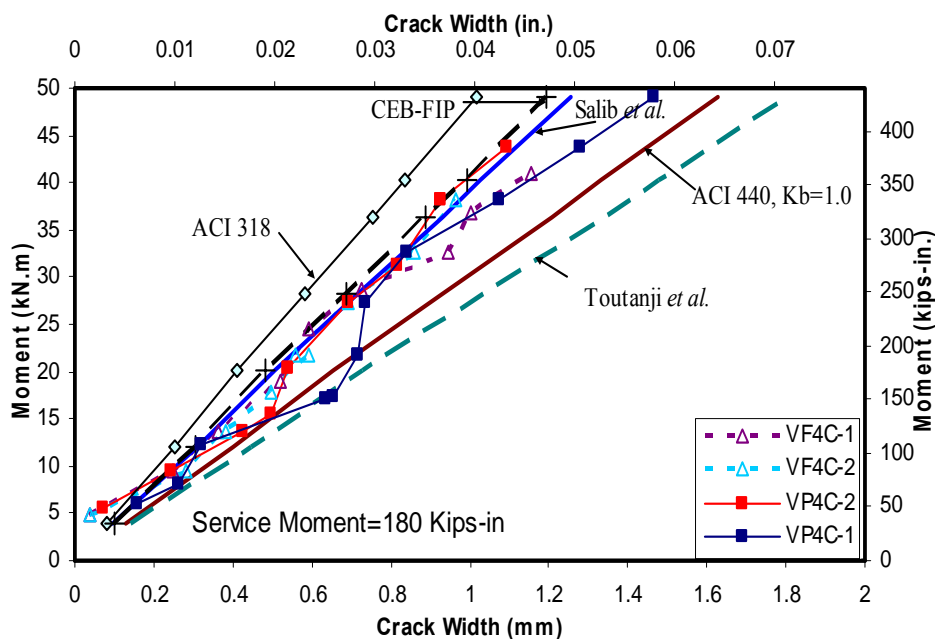
Figure 5.5. Crack Width versus Applied Moment of #4 CFRP Beams
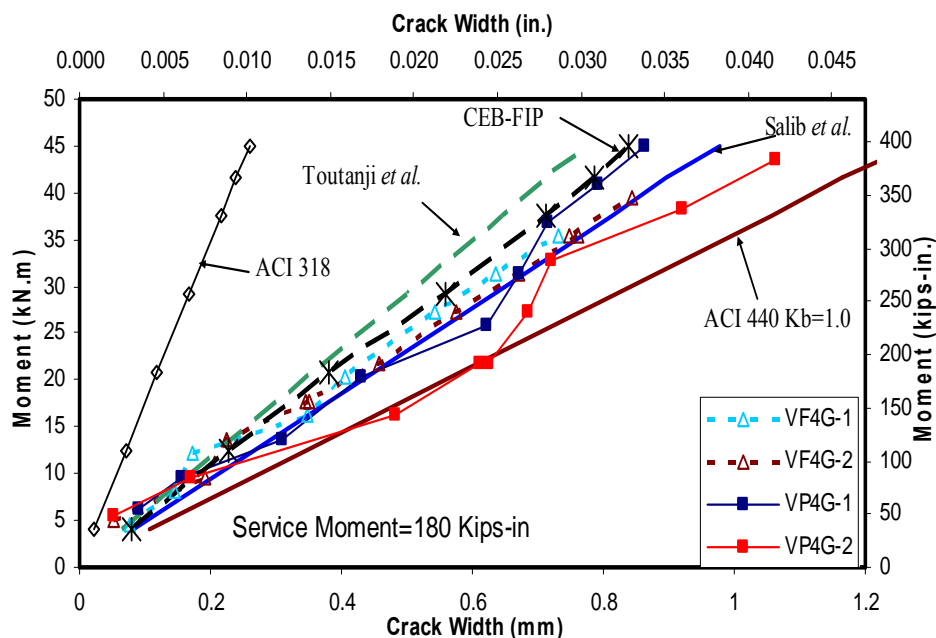
Figure 5.6. Crack Width versus Applied Moment of #4 GFRP Beams
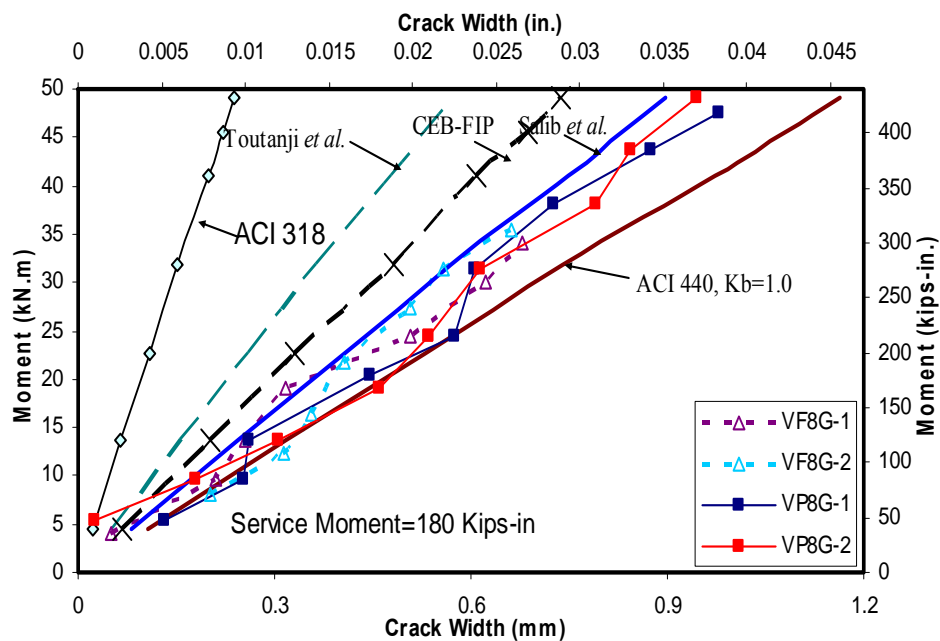
Figure 5.7. Crack Width versus Applied Moment of #8 GFRP Beams

Based on the well-known Gergely-Lutz (1973) equation, ACI 440 recommends the equation to calculate the crack width of FRP reinforced member as follows:

$$w = \frac{2200}{E_f} k_b \beta f_f \sqrt[3]{d_c A} \text{ in.}$$

(5.3)

where w = the crack width at tensile face of the beam,

A = the effective tension area per bar,

d_c = the thickness of concrete cover measured from extreme tension fiber to the center of the closest layer of longitudinal bars,

f_f = the stress in the FRP reinforcement,

β = the coefficient to converse crack width corresponding to the level of reinforcement to the tensile face of beam, and

k_b = the coefficient that accounts for the degree of bond between the FRP bar and the surrounding concrete. It was reported that k_b ranges from 0.71 to 1.83 for different types of GFRP bars (Gao et al., 1998). ACI 440 does not give a mathematical relationship between k_b and the bond strength. And it suggests 1.2 for deformed FRP bars if k_b is not experimentally known.

Toutanji and Saafi (2000) reported that the crack width was a function of the reinforcement ratio. They proposed the following equation to predict the crack width:

$$w = \frac{200}{E_f \sqrt{\rho_f}} \beta f_f \sqrt[3]{d_c A} \text{ in.}$$

(5.4)

where ρ_f is the reinforcing ratio.

Based on the equivalent beam concept, Salib and Abdel-Sayed (2004) proposed the following equation:

$$w = 0.076 \times 10^{-3} \times \{(E_s / E_f)(u_{b,s} / u_{b,f})^{2/3}\} \times \beta f_f \sqrt[3]{d_c A} \text{ in.}$$

(5.5)

By substitute E_s=29000 ksi; thus

$$w = \left(\frac{2200}{E_f} \times (2/3) \sqrt{\frac{u_{b,s}}{u_{b,f}}} \right) \times \beta f_f \sqrt[3]{d_c A} \text{ in.} \qquad (5.6)$$

where $u_{b,s}$ and $u_{b,f}$ are the bond strengths of steel rebar and FRP rebar, respectively.

In Equation 5.6, the values of $u_{b,f}$ and $u_{b,f}$ need to be evaluated and decided upon.

For traditional steel rebar, according to ACI 318-02, $l_d = \frac{f_y d_b}{25\sqrt{f_c'}}$ (neglecting the adjusting

coefficients) and based on the definition of the development length,

$$\pi d_b l_d u_{b,s} = f_y A_s \qquad (5.7)$$

One gets: $u_{b,s} = 6.25\sqrt{f_c'}$ psi.

For FRP rebar used in this study, based on the previous study (Belarbi and Wang,

2005), $u_{b,f} = 9.25\sqrt{f_c'}$. Based on these approximate values, Equation 5.5 become

$$w = \frac{1700}{E_f} \beta f_f \sqrt[3]{d_c A} \text{ in.} \qquad (5.8)$$

The crack width can also be derived based on the crack spacing. Concrete can

sustain very small tensile stain due to stress before it cracks. After cracking, the tensile

side of the beam elongates by widening of the cracks and by formation of new cracks.

Ignoring the small elastic stain in the concrete between the cracks, the crack width can

also be expressed as follows:

$$w = \varepsilon_f S_m \text{ in.} \qquad (5.9)$$

Substitute Equation 5.1 into 5.9, result in

$$w = \varepsilon_f \left\{ 2(c + \frac{s}{10}) + k_1 k_2 \frac{d_b}{\rho_{ef}} \right\} \text{ in.} \qquad (5.10)$$

As shown in Figures 5.5 through 5.7, the Salib et al. model gives reasonable predictions of the crack width for both plain concrete beams and FRC beams. For the Toutanji et al. model, the prediction values show poor correlation with the experimental results. When for low reinforcing ratios, (for the CFRP beams, ρ=0.67%), the model overestimates the crack width. Vice versa, for high reinforcing ratios (#4 GFRP beams, ρ=2.2%, and #8 GFRP beams, ρ=3.3%), the model underestimates the crack width. Therefore, it may be concluded that it is the bond characteristics rather than the reinforcing ratio that affect the crack width.

The predictions based on current ACI 440 equations were also compared with the test results. The accuracy of the equation largely depends on the value of k_b. Even when selecting k_b =1.0, one can see that the predictions are still conservative. Similar observations were made by El-Salakawy and Benmokrane (2004).

Compared to the test results, the predictions based on the CEB-FIP Code underestimated the crack width, especially in the case of #8 GFRP. As shown in Table 5.2, the prediction by Equation 5.1 underestimate the crack spacing at the service load, thus, the predicted crack width will be underestimated.

- **Fiber Effect on Crack Width.** With the addition of fibers, the crack widths were slightly decreased at the same load level, especially at the service load, as shown in Figures 5.5 through 5.7.

As shown in Table 5.3, the crack widths were smaller in the case of FRC beams as compared to plain concrete beams at the service load. As discussed earlier, the crack spacing was decreased at the service load due to the contribution from the fibers. Since

the crack width is proportionally related to the crack spacing, the crack width is expected

to be smaller in the FRC beams at the service load.

**Table 5.3. Comparison of Crack Width between Plain Concrete
Beams and FRC Beams at Service Load**

Specimen I.D.	VP4C	VP4G	VP8G	VF4C	VF4G	VF8G
Crack Width (in.)	0.024	0.019	0.018	0.021	0.016	0.014
% decrease relative to respective plain concrete	N/A	N/A	N/A	10%	16%	20%

Note: the values are average of two beams.

5.2.2. Load-Deflection Response. Figures 5.8 and 5.9 show the typical

experimental moment-deflection curves for the plain concrete beams and the FRC beams

reinforced with different types of FRP rebars. With the increasing of moment, cracks

occurred in the testing region when the moment exceeded the cracking moment, M_{cr}.

Consequently, the flexural stiffness of the beams was significantly reduced and the

curves were greatly softened. As expected, due to the linear-elastic behaviors of the FRP

rebars, the FRP reinforced beams showed no yielding. The curves went up almost

linearly until the crushing of concrete.

- **Fiber Effect on Moment-Deflection Curves.** In order to compare the

flexural behaviors between plain concrete beams and FRC beams, all the load-deflection

curves of the plain concrete beams were normalized, based on the following rules: 1)

moment was divided by a coefficient C_M, defined as $C_M = \frac{M_{ACI-plain}}{M_{ACI-FRC}}$, where $M_{ACI\text{-}plain}$ and

$M_{ACI\text{-}FRC}$ are theoretical ultimate capacities computed based on ACI 440 for beams with
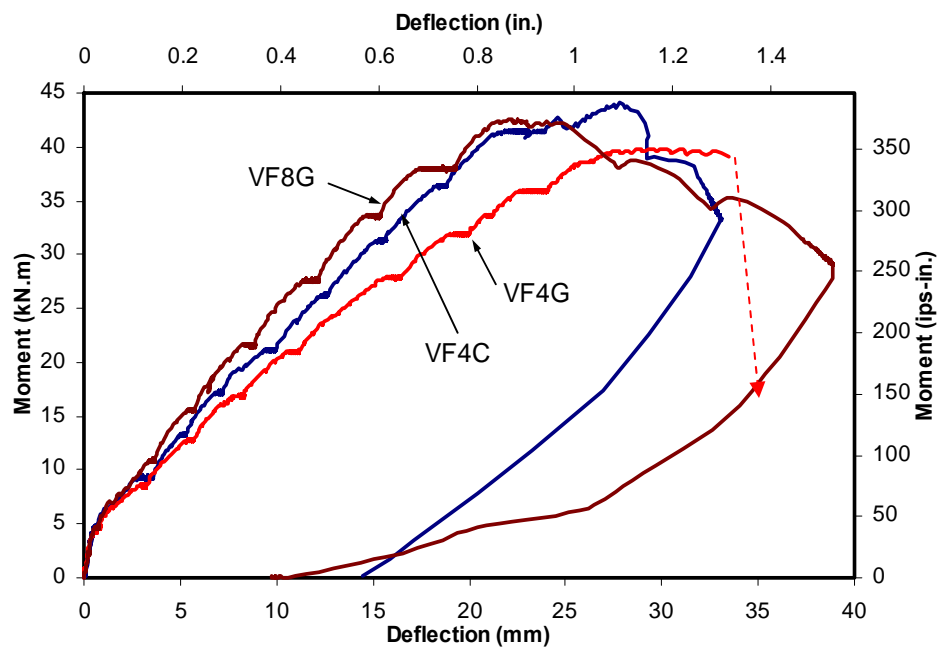
Figure 5.8. Moment-Deflection Relationship for FRC Beams
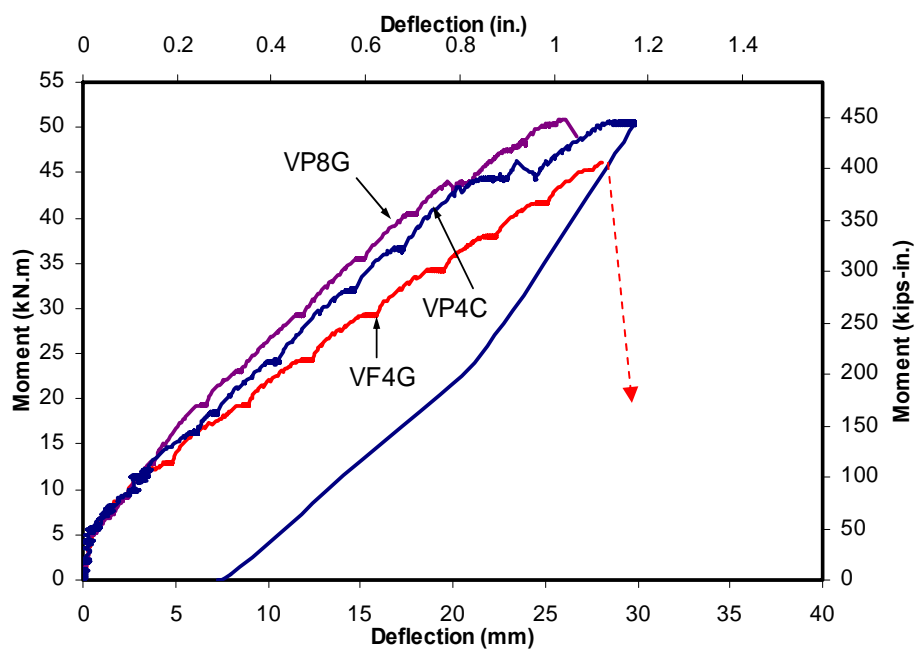
Figure 5.9. Moment-Deflection Relationship for Plain Concrete Beams

**Table 5.4. Comparison of Flexural Strength and Deflection between
FRC Beams and Plain Concrete Beams**

Specimen I.D. (1)	Ultimate Moment (kips-in.) (2)		Ultimate Deflection (in.) (3)		Ultimate Moment (kips-in.) (4)		Ultimate Deflection (in.) (5)		$\dfrac{M_{FRC}}{M_{Plain}}$ (6)	$\dfrac{\Delta_{FRC}}{\Delta_{Plain}}$ (7)
VP4C-1	457	450	1.19	1.18	375	369	1.03	1.02	N/A	N/A
VP4C-2	442		1.17		362		1.00			
VP4G-1	405	413	1.03	1.03	330	336	0.94	0.94	N/A	N/A
VP4G-2	420		1.02		342		0.93			
VP8G-1	448	449	0.96	0.96	360	360	0.87	0.87	N/A	N/A
VP8G-2	449		0.95		360		0.86			
VF4C-1	415	402	1.20	1.15	415	402	1.20	1.15	1.09	1.13
VF4C-2	388		1.10		388		1.10			
VF4G-1	350	356	1.19	1.19	350	356	1.19	1.19	1.06	1.27
VF4G-2	362		1.19		362		1.19			
VF8G-1	371	366	0.95	0.91	371	366	0.95	0.91	1.02	1.05
VF8G-2	361		0.87		361		0.87			

Note: Columns (4) and (5) are the normalized values of Column (3) and (4); Columns (6) and (7) are the ratios of moment or deflection between the FRC beams to those of the plain concrete beams after normalizations.

concrete strengths equal to the plain concrete beams and the FRC beams using the same

approach, respectively; 2) deflection was divided by a coefficient C_D, defined as

$C_D = \dfrac{\Delta_{ACI-plain}}{\Delta_{ACI-FRC}}$, where $\Delta_{ACI-plain}$ and $\Delta_{ACI-FRC}$ are theoretical deflection based on ACI 440

for beam with concrete strengths equal to the plain concrete beams and FRC beams at the

service load (40% of the ultimate load), respectively.

As shown in Table 5.4 and Figures 5.10 through 5.12, with the addition of fibers,

the ultimate moments and deflections were increased. The plain concrete beams failed in

a more brittle manner. Once it reached the capacity, the concrete was crushed and the
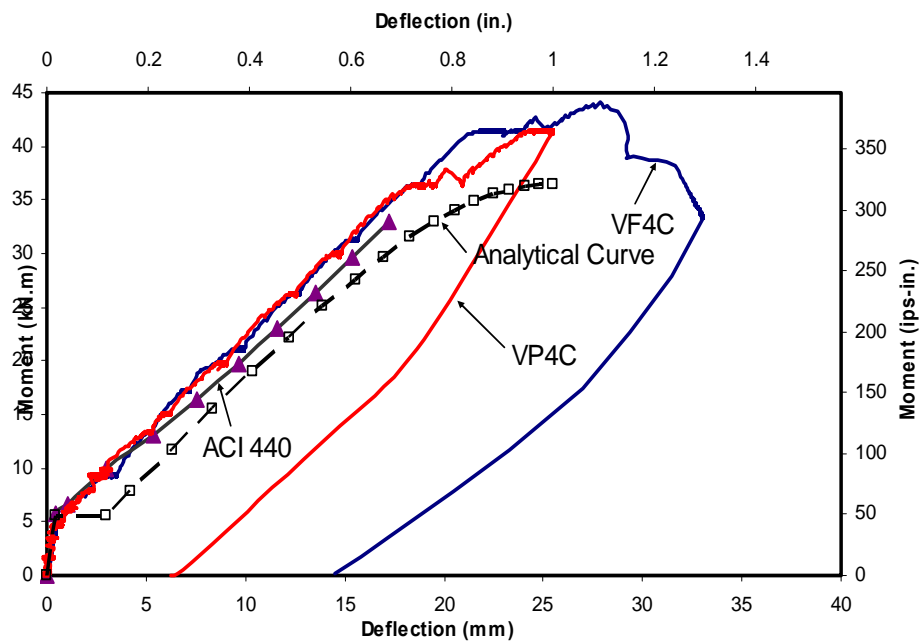
Figure 5.10. Moment-Deflection Relationship for #4 CFRP with/without Fibers
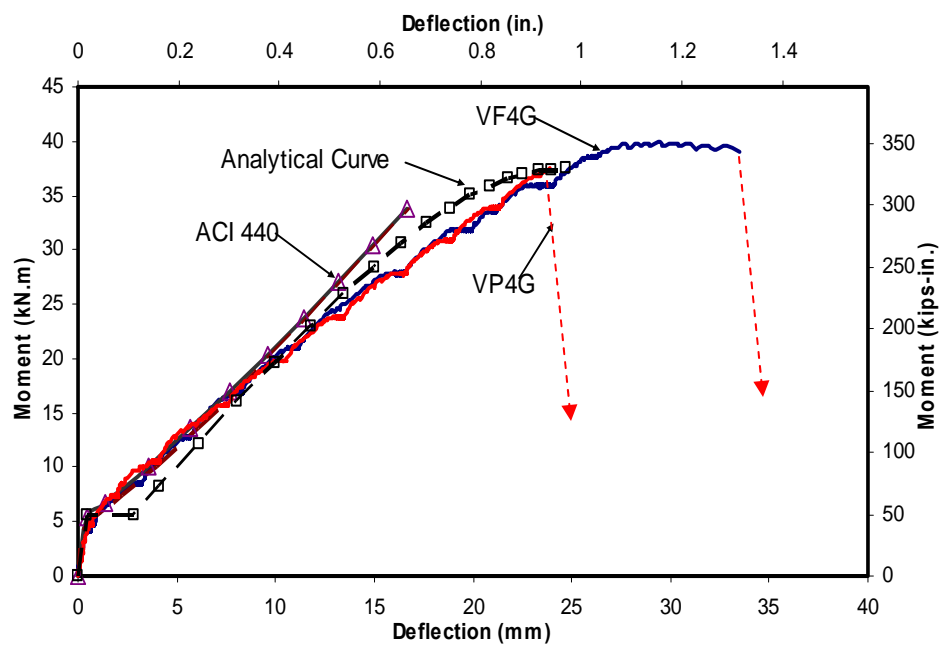
Figure 5.11. Moment-Deflection Relationship for #4 GFRP with/without Fibers
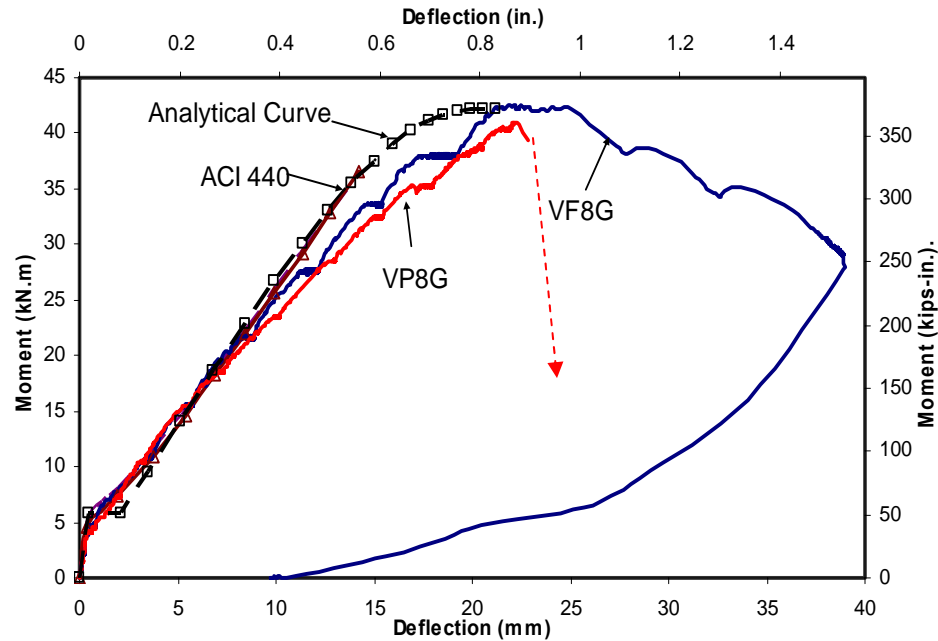
Figure 5.12. Moment-Deflection Relationship for #8 GFRP with/without Fibers

load dropped suddenly and violently. FRC beams failed in a more ductile way as the load

dropped more gently and smoothly.

Theoretical Correlation. Deflection at mid-span for a simply supported beam of

total length L and subjected to a four-point flexural test is given as

$$\Delta_{mid} = \frac{Pa}{24E_cI_e}(3L^2 - 4a^2) + \frac{Ph^2a}{10GI_e} \text{ (in.)} \tag{5.11}$$

The first term on the right is from the flexural component, and the second term is

from the shear component. In this study, testing beams had a span-depth ratio of 2.67.

Based on calculation, it was found that the shear component was about 3% of the flexural

component. It was, therefore, neglected for simplicity. Thus, Equation 5.11 becomes

$$\Delta_{mid} = \frac{Pa}{24E_cI_e}(3L^2 - 4a^2) \text{ in.} \tag{5.12}$$

ACI 440 recommends the following expressions to calculate the effective moment of inertia I_e:

$$I_e = I_g \text{ when } M_a \leq M_{cr};$$

$$I_e = \left(\frac{M_{cr}}{M_a}\right)^3 \beta_d I_g + \left[1 - \left(\frac{M_{cr}}{M_a}\right)^3\right] I_{cr} \leq I_g \text{ when } M_a > M_{cr} \qquad (5.13)$$

where $\beta_d = \alpha_b\left[\dfrac{E_f}{E_s} + 1\right]$, and ACI 440 recommends taking the value of $\alpha_b = 0.5$ for all the

FRP bar type. $\qquad (5.14)$

As shown in Figures 5.10 to 5.12, ACI 440 equations predict the moment-deflection response fairly well, especially at the service stage. Thus, the equations recommended by the current ACI 440 would be used for the design purpose for both plain concrete beams and FRC beams.

A more refined analysis was also conducted to compare the theoretical and experimental results. The theoretical moment-deflection curves were obtained based on the double integration of a theoretical moment-curvature relationship, in which the Thorenfeldt model was used to represent the stress-strain relationship of the concrete, as shown in the following equation:

$$f_c = \frac{n(\varepsilon_c / \varepsilon_c')f_c'}{n - 1 + (\varepsilon_c / \varepsilon_c')^{nk}} \qquad (5.15)$$

Based on the information provided by Collins and Mitchell (1991), $n = 2.6$, $k = 1.16$, $\varepsilon_c' = 0.00198$ was adopted in this study when the concrete strength is equal to 4,400 psi in the Thorenfeldt model. The above coefficients were derived based on experimental study on normal-weight concrete. Because the concrete in this study was also normal-

weight concrete, it is assumed that the above predictions can reasonably predict the stress-strain relationship of the concrete used in this study. The implementation of the double integration of the theoretical moment-curvature relationship was based on the conjugate beam method. The analytical curve was interrupted at $\varepsilon_c = 0.0045$. As shown in Figure 5.10 to 5.12, the theoretical curves show good match with the experimental results.

5.2.3. Relative Slip between Longitudinal Rebar and Concrete at Ends. No relative slip was observed for any test specimens during the test program. That means that the development lengths as designed based on the previous bond study (Belarbi and Wang, 2005) were adequate for the FRP bars to develop the required forces.

5.2.4. Loading/Unloading Effect on the Flexural Behaviors. No significant differences were observed before and after loading and unloading cycles in the crack width, crack distribution, and deflection. Also, the flexural stiffness did not change after cyclic loading, as shown in Figures 5.13 to 5.14.

5.2.5. Strains in Reinforcement and Concrete. Figures 5.15 to 5.17 present the measured mid-span strains in reinforcement and in concrete versus the applied moment. It can be seen that after cracking, the strains in the reinforcement increased almost linearly up to failure. Because all test beams failed in concrete crushing rather than FRP reinforcement rupture, the maximum measured strains in the reinforcement were less than the ultimate tensile strains. In beams reinforced with #4 CFRP, #4 GFRP, and #8 GFRP, the maximum measured strains were 12,000; 12,000; and 8,000 microstrains, respectively; while the ultimate strains were 16,700; 16,900; and 13,500 microstrains, respectively.

The differences of the moment-strain curves between the plain concrete beams and the FRC beams were significant. In the plain concrete beams, once reaching the
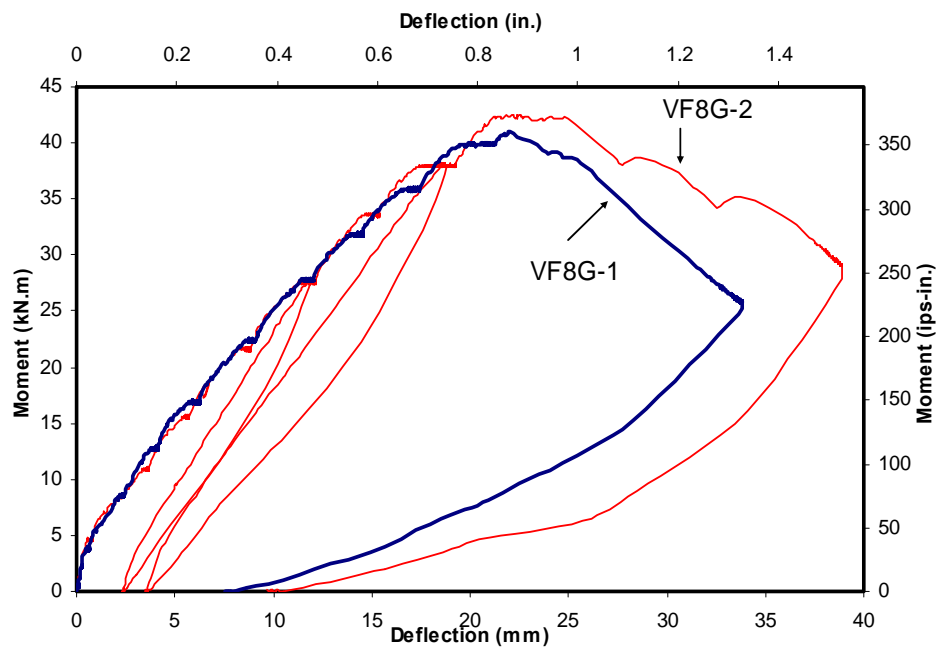
Figure 5.13. Typical Loading/unloading Cycle's Effect on FRC Beams
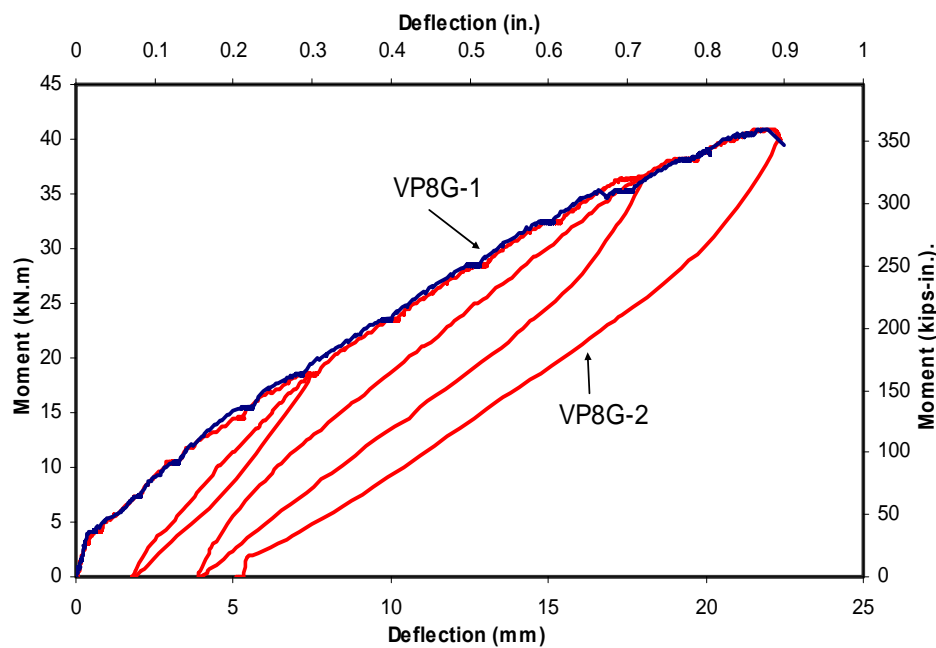
Figure 5.14. Typical Loading/unloading Cycle's Effect on Plain Concrete Beams
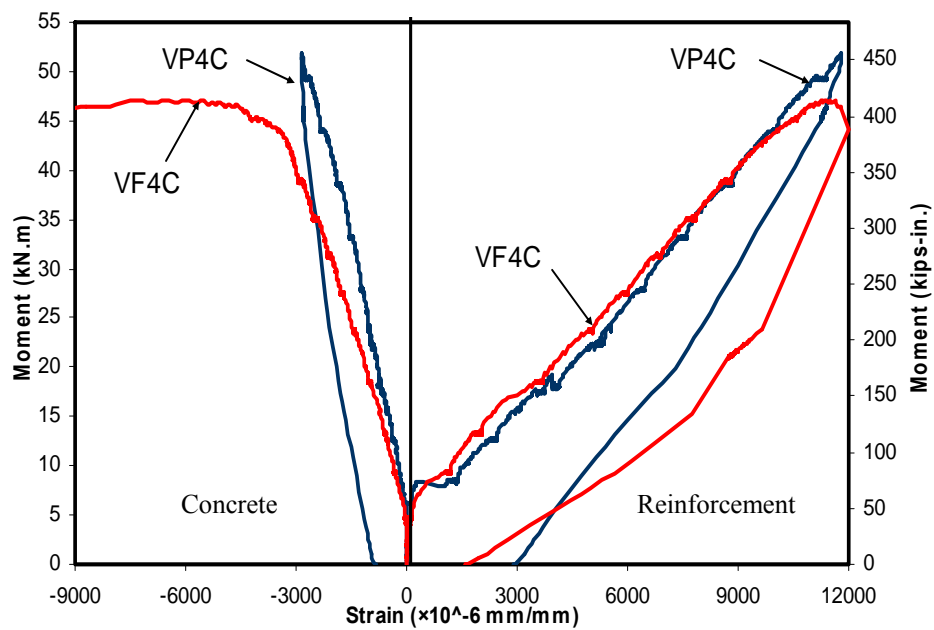
Figure 5.15. Typical Strain Distributions of #4 CFRP Beams
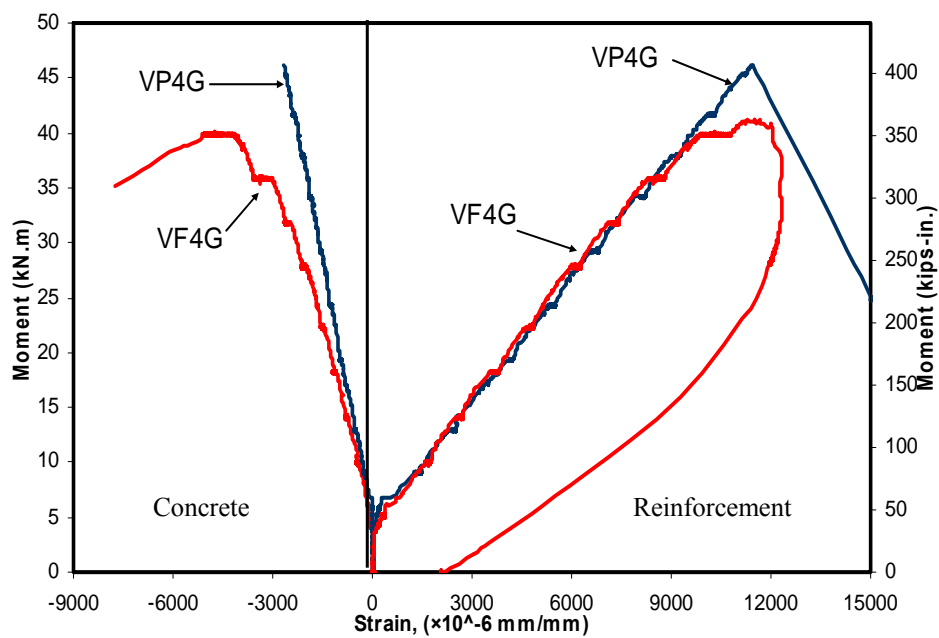
Figure 5.16. Typical Strain Distributions of #4 GFRP Beams
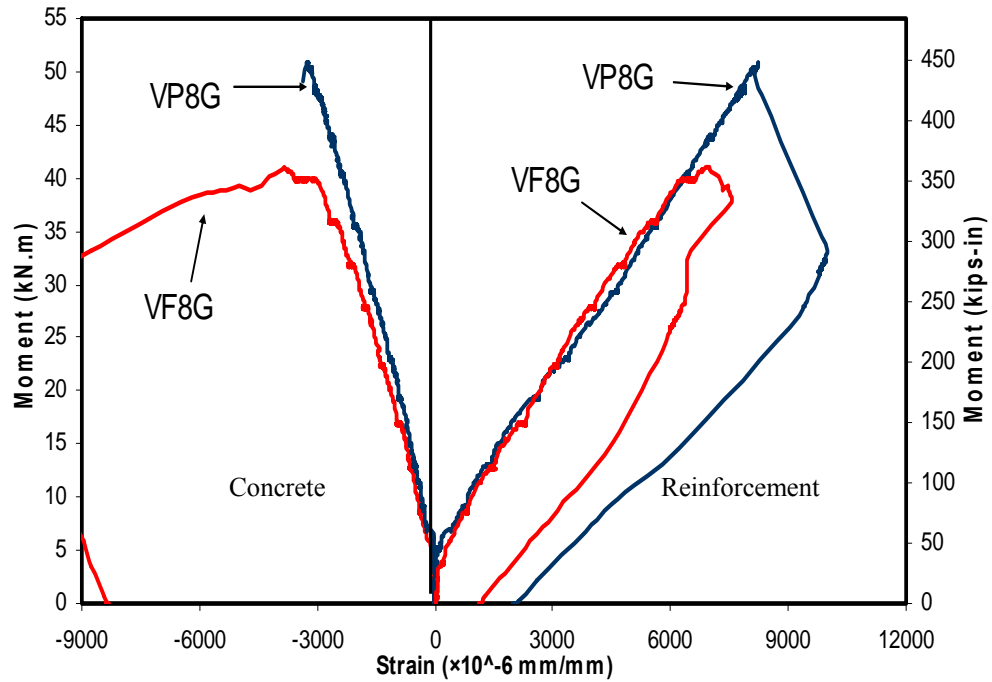
Figure 5.17. Typical Strain Distributions of #8 GFRP Beams

ultimate, concrete failed by crushing, and strains in the reinforcement dropped suddenly.

However, in the FRC beams, when beams reached the ultimate, concrete was held

together and the strains in the concrete and strains in the reinforcement kept increasing

gradually. Furthermore, with the addition of fibers, the ultimate strain for the concrete

was increased. In plain concrete beams, the measured ultimate concrete strains ranged

from 2,700 microstrains to 3,300 microstrains with an average of 2,950 microstrains. In

the FRC beams, the measured ultimate concrete strains ranged from 4,000 microstrains to

5,000 microstrains with an average of 4,500 microstrains.

5.3. PREDICTIONS OF THE ULTIMATE FLEXURAL CAPACITY

As shown in Table 3.5, the reinforcing ratio, ρ_f, for all the beams were greater than the balanced ratio, ρ_{bf}, which is defined as follows:

$$\rho_{bf} = \alpha_1 \beta_1 \left(\frac{f_c'}{f_{fu}} \right) \left(\frac{\varepsilon_{cu}}{\varepsilon_{cu} + \varepsilon_{fu}} \right) \tag{5.15}$$

where ε_{cu}=0.003 as defined by ACI 318-02.

As expected, all the beams failed in concrete crushing. Figure 5.18 shows the typical failure mode.

Figure 5.18. Typical Failure Mode

Predictions by the ACI 440 equations were based on the following assumptions:

(1) Plane sections remain plane; that is, the concrete and the reinforcement strain values are proportional to their distance from the neutral axis.

(2) The tensile strength of the concrete is ignored.

(3) A parabolic stress distribution in the concrete was utilized, and the stress block factors, α_1 and β_1, as defined in ACI 318, were adopted.

(4) The ultimate concrete compressive strain ε_{cu} is 0.003. ε_{cu} =0.0035 were also

computed for comparison in this study.

(5) There is perfect bond between the reinforcement and the concrete.

ACI 440 recommends the following equations to predict the flexural strength:

$$M_n = \rho_f f_f \left(1 - 0.59 \frac{\rho_f f_f}{f_c'}\right) bd^2 \text{ kips-in.} \tag{5.16}$$

$$f_f = \left(\sqrt{\frac{\left(E_f \varepsilon_{cu}\right)^2}{4} + \frac{0.85\beta_1 f_c'}{\rho_f} E_f \varepsilon_{cu}} - 0.5 E_f \varepsilon_{cu}\right) \leq f_{fu} \text{ psi} \tag{5.17}$$

There are two possible ways by which fibers can increase the flexural strength: one is that the fibers function as auxiliary reinforcement to carry some tensile stresses; the other way is that the fibers can improve the concrete properties. In this study, contribution of fibers in tensile strength was neglected since

(1) Compared to the steel fibers, the tensile strength of polypropylene fibers is low: less than 1/3 of the tensile strength of the steel fibers.

(2) Due to the low elastic modulus of polypropylene fiber (500 to 700 ksi), the elongation at break is three orders of magnitude greater than the tensile strain at failure of the concrete. Hence, the concrete will crack long before the fiber strength is approached.

Thus, the most likely contribution from the fibers to increase the flexural strength is to improve the concrete properties. As shown in Figure 5.19, ultimate concrete strain measured for FRC beams in this study is larger than the value recommended by ACI. In this study, a value of 0.0035 is used. As shown in Table 5.5, the theoretical predictions agree well with the test results. As discussed earlier, the concrete strains of the FRC

beams at failure were greater than 0.0035. For the design of the FRC beams, it is suggested that ε_{cu} to be equal to 0.0035, with a comparable safety factor of $\varepsilon_{cu} = 0.003$ for the plain concrete beams.
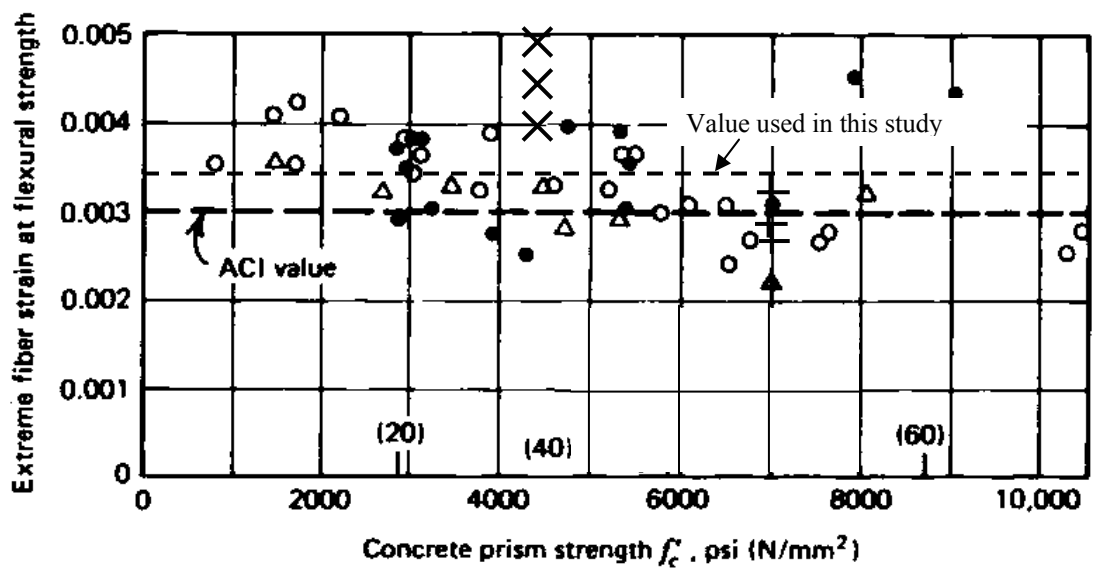
Figure 5.19. Comparison of Ultimate Strain of Concrete of ACI Value and Test Results in this Study (Courtesy of Park and Paulay)
Note: × is the values of FRC measured in this study; + is the values of plain concrete measured in this study.

5.4. DUCTILITY EVALUATION

As mentioned earlier, since the traditional definition of ductility can not be applied to the structures reinforced with FRP reinforcement, there is a need for developing a new approach and a set of ductility indices to both quantitatively and qualitatively evaluate the FRP reinforced members.

Table 5.5. Predictions of Ultimate Capacities

Specimen I.D.	$M_{exp.}$ (kips-in.)	M_{ACI} (kips-in) ε_{cu}=0.003	$\dfrac{M_{ACI}}{M_{exp.}}$	M^{*}_{ACI} (kips-in.) ε_{cu}=0.0035	$\dfrac{M^{*}_{ACI}}{M_{exp.}}$
VP4C	450	355	0.79	377	0.84
VP4G	413	367	0.89	388	0.94
VP8G	449	401	0.89	423	0.94
Average			**0.86**		**0.91**
VF4C	402	290	0.72	306	0.76
VF4G	356	298	0.84	314	0.88
VF8G	366	322	0.88	338	0.92
Average			**0.81**		**0.86**

Note: M_{ACI} and M^{*}_{ACI} is the prediction of moment capacity based on ACI equations. And the ultimate strain assumed to be 0.003 for M_{ACI} and 0.0035 for M^{*}_{ACI}, respectively;

The calculations of ductility index related to the FRP reinforced members have been widely studied. Two approaches have been in the literature proposed to address this problem.

5.4.1. Energy Based Approach. Based on the definition of the energy based approach, ductility can be defined ability to absorb the energy and can be expressed as the ratio between the total energy and the elastic energy, as shown in Figure 5.20.

Naaman and Jeong (1995) proposed the following equation to compute the ductility index, μ_E:

$$\mu_E = \frac{1}{2}\left(\frac{E_t}{E_e}+1\right) \text{ kips-in.} \tag{5.18}$$

where E_t is the total energy computed as the area under the load deflection curve; and E_e is the elastic energy. The elastic energy can be computed as the area of the triangle formed at failure load by the line having the weighted average slope of the two initial straight lines of the load deflection curve, as shown in Figure 5.20.
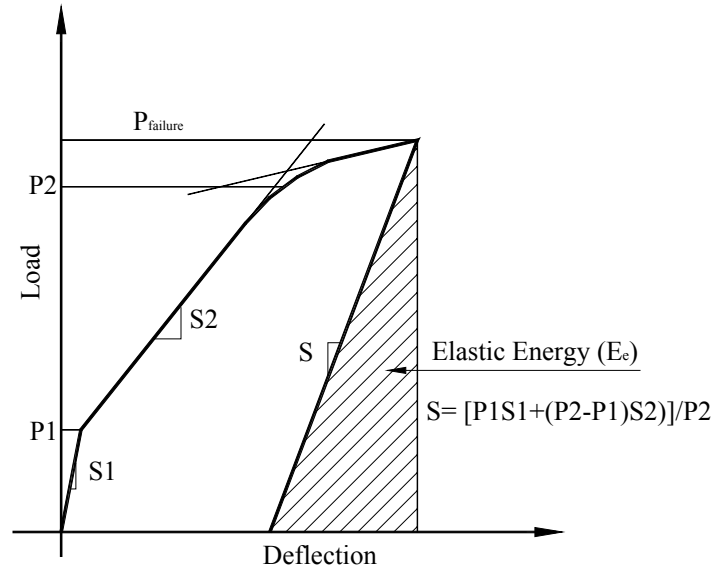
Figure 5.20. New Definition of Ductility Index (Naaman and Jeong, 1995)

5.4.2. Deformation Based Approach. The deformation based approach was first introduced by Jaeger et al. (1995). It takes into account the strength effect as well as the deflection (or curvature) effect on the ductility. Both the strength factor C_s and the deflection factor C_d (or curvature factor C_c) are defined as the ratio of moment or deflection (or curvature) values at ultimate to the values corresponding to the concrete compressive strain of 0.001. The strain of 0.001 is considered the beginning of inelastic deformation of concrete.

$$\mu_E = C_s \times C_d \text{ or } \mu_E = C_s \times C_c \tag{5.19}$$

$$C_s = \frac{M_u}{M_{\varepsilon=0.001}} \tag{5.20}$$

$$C_d = \frac{\Delta_u}{\Delta_{\varepsilon=0.001}} \tag{5.21}$$

$$C_c = \frac{\psi_u}{\psi_{\varepsilon=0.001}} \tag{5.22}$$

Thus, the ductility is reflected by its deformability margin between the ultimate stage and the service stage.

In the following sections, ductility indices based on both approaches, that is deformation based approach and energy based approach, are computed and compared.

5.4.3. Ductility Index Computed by the Energy Based Method. As shown in Figure 5.20, the definition of elastic slope is dependent on the selections of P1, P2, S1, and S2. Also, the experimental moment-deflection curves, as shown in Figures 5.8 and 5.9, were hard to be idealized into three portions with three distinct slopes and it could induce some subjective errors if the curves are artificially divided. In this study, the elastic slopes were decided by the slopes of loading/unloading cycles during the tests rather than using the theoretical predictions proposed by Naaman and Jerong (1994). The ductility indices computed are shown in Table 5.6.

5.4.4. Ductility Index Computed by the Deformation Based Method. Theriault and Benmokrane (1998) found that the ductility indices computed by the curvature factor demonstrated more consistent in comparison to those computed by deflection factor. Therefore, the curvature factor is adopted in this study. Figures 5.21 to 5.23 show the typical moment-curvature relationship of the testing beams. The ductility indices are computed and shown in Table 5.7.

5.4.5. Ductility Index. As shown in Tables 5.6 and 5.7, the ductility indices computed by the two methods are quite different. The effect from the addition of fibers on the ductility indices is much more pronounced when calculated based on the Jaeger method.
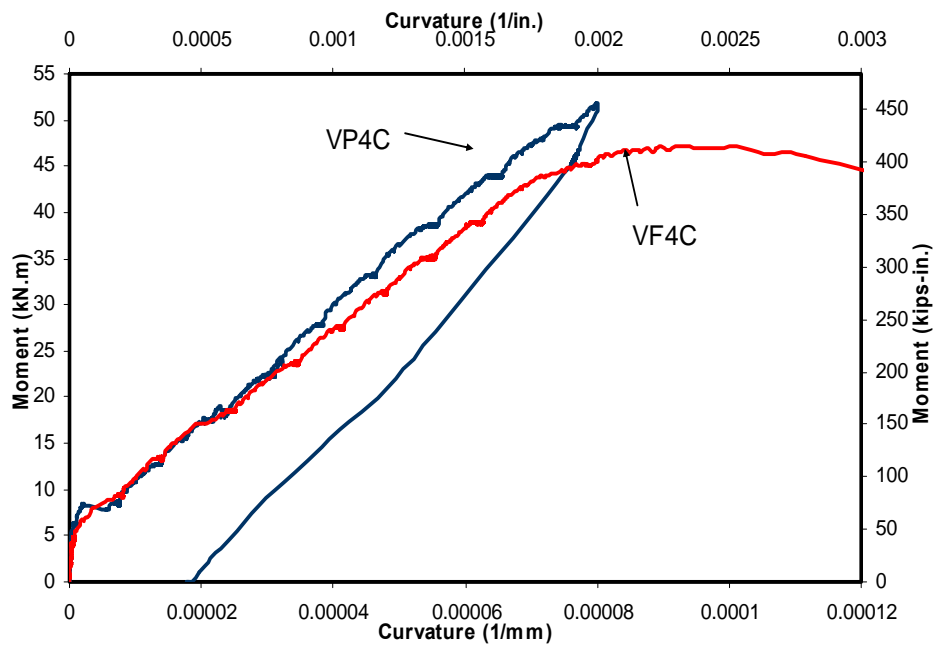
Figure 5.21. Typical Moment Curvature Relationship for #4 CFRP Beams
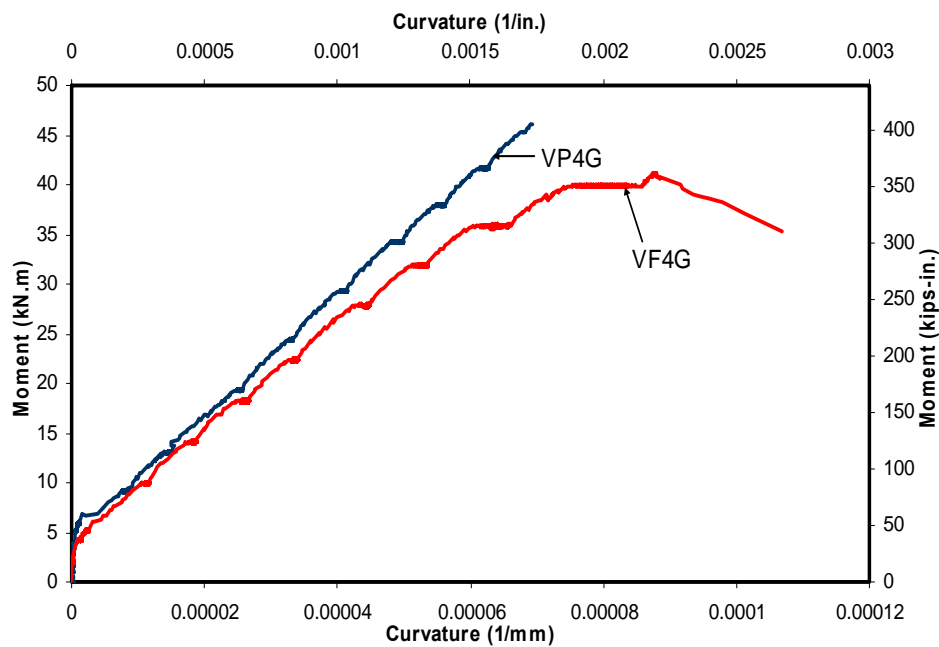
Figure 5.22. Typical Moment Curvature Relationship for #4 GFRP Beams
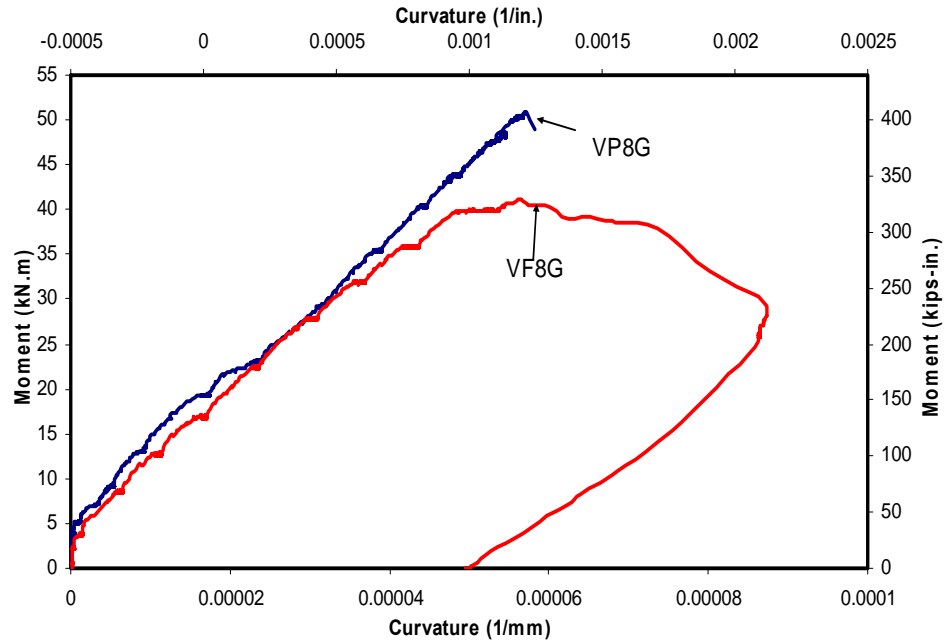
Figure 5.23. Typical Moment Curvature Relationship for #8 GFRP Beams

Table 5.6. Ductility Index by Energy Based Method (Naaman and Jeong, 1995)

Specimen I.D.	E_t (kips-in.)	E_e (kips-in)	μ_E	$\dfrac{\mu_{E-FRC}}{\mu_{E-Plain}}$
VP4C	27.83	14.58	1.45	1
VP4G	22.17	13.92	1.30	1
VP8G	23.00	12.00	1.46	1
VF4C	24.33	11.50	1.56	1.07
VF4G	22.08	11.33	1.48	1.14
VF8G	18.25	9.08	1.50	1.03
Average				1.08

Table 5.7. Ductility Index by Deformation Based Method (Jaeger, 1995)

Specimen I.D.	$M_{\varepsilon=0.001}$ (kips-in.)	$\psi_{\varepsilon=0.001}$ (1/in.)	M_u (kips-in.)	ψ_u (1/in.)	μ_E	$\dfrac{\mu_{E-FRC}}{\mu_{E-Plain}}$
VP4C	202	7.82×10^{-4}	450	19.46×10^{-4}	5.50	1
VP4G	177	6.66×10^{-4}	405	17.63×10^{-4}	6.05	1
VP8G	190	4.96×10^{-4}	449	14.73×10^{-4}	7.04	1
VF4C	163	6.15×10^{-4}	402	20.78×10^{-4}	8.35	1.52
VF4G	153	5.74×10^{-4}	356	22.10×10^{-4}	8.94	1.48
VF8G	157	4.45×10^{-4}	366	14.40×10^{-4}	7.56	1.08
Average						1.36

A schematic load-deflection curve for a certain material reinforced beam, as shown in Figure 5.24, is created to explain the different results by the two methods. With the addition of fibers, the load capacity and deflection are increased from P1 to P2 and Δ1 to Δ2 proportionally.

Although there are different ways to calculate the ductility index, ductility can be defined as the ability to absorb the inelastic energy without losing its load capacity. Higher inelastic energy absorption of the same system means higher ductility. Obviously, from this standpoint, the addition of fibers significantly improves the system's ductility. However, based on the prediction of Naaman and Jerong's ductility index, the ductility is the same before and after the addition of fibers. Because the ratios of $\dfrac{E_t}{E_e}$ are the same, μ_E is not changed. The reason is although the absorption of the inelastic energy with the addition of fibers increases, the absorption of the elastic energy is also increased
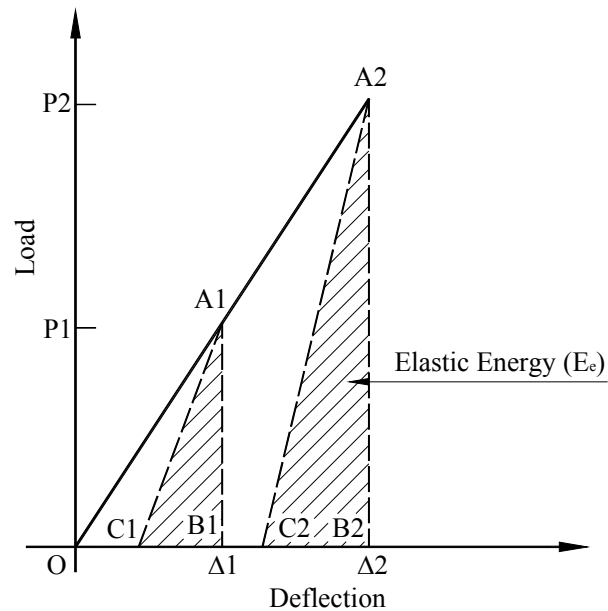
Figure 5.24. Schematic Load-Deflection Relationship

proportionally. Thus, the index μ_E remains constant in this example. From this standpoint, the ductility index proposed by Naaman and Jerong cannot efficiently take into account the benefits gained from the increase of the ultimate moment capacity and the accompanying increase of the deflection with the addition of fibers. The ductility index based on the Jaeger approach is more reasonable. It not only considers factors resulting from the load capacity, but it also considers the deformation effect on the ductility. The ductility increases approximately 40% with the addition of fibers, based on the Jaeger approach. Also, all the ductility indices, as calculated by the Jaeger method, were found to be above the lower limit of 4 recommended by Jaeger and the Canadian Highway Bridge Design Code. Both the plain concrete beams and the FRC beams can, therefore, be considered acceptable for design in terms of ductility requirement.

5.5. CONCLUDING REMARKS

A research program was initiated to investigate the feasibility of steel-free hybrid reinforcement system for concrete bridge decks by combining FRP reinforcement with the polypropylene fiber reinforced concrete. From the flexural study covered in this paper, the following conclusions can be drawn:

- The deflection predicted by the current ACI 440 guidelines yield results consistent with experimental results, especially at the service load stage, and could be used for both the plain concrete beams and the FRC beams.

- The model proposed by Salib et al. (2004) yields reasonable predictions of the crack width for both the plain concrete beams and the FRC beams. The predictions by the ACI 440 were found to be conservative.

- The addition of fibers reduced the crack widths at the service load in the case of FRC beams as compared to plain concrete beams.

- The compression concrete strain measured at the compression fiber of the FRC beams was larger than that of the plain concrete beams. It ranged from 4,000 microstrains to 5,500 microstrains, with an average of 4,500 microstrains for the FRC beams, while concrete strains, ranging from 2,700 microstrains to 3,300 microstrains, with an average of 2,950 microstrains, were measured for the plain concrete beams.

- With the addition of polypropylene fibers, the ductility indices increased by approximately 40% based on deformation based approach, which takes into account the strength effect as well as the deflection (or curvature) effect on determining the ductility. In addition, both plain concrete beams and FRC beams

provided an adequate deformability level, as described by Jaeger. Moreover, FRC

made it slightly more ductile, based on the new definition of ductility for the FRP

reinforced beam.

6. ACCELERATED DURABILITY TEST RESULTS

6.1. INTRODUCTION

Many studies have been carried out on the durability of individual FRP components, but literature concerning durability of the FRP and the concrete as a system, in terms of durability of bond and durability of flexural behavior, is sparse. The durability mechanism depends more on the inter-relation between the materials than on an individual component's property. In addition, the mechanical properties of a hybrid material system may deteriorate much faster than that suggested by the property degradation rates of the individual components making up the hybrid system (Schutte, 1994). The FRP/FRC hybrid system is a novel approach, and research on the durability characteristics of this hybrid system is paucity with limited information in open literature. Thus, accelerated durability tests on the FRP/FRC system are necessary.

Limited research has been conducted on the durability characteristics of the FRP and the plain concrete system, in terms of the bond and the flexural behavior after being subjected to the long-term environmental conditioning. Katz et al. (1999) observed a reduction of 80 to 90% in the bond strength as the temperature increased from 68^0F to 482^0F. In addition, a reduction of the bond stiffness was observed as the temperature increased. Mashima and Iwamoto (1993) noted that the bond strengths for both glass and carbon FRP seemed not to be reduced up to 300 cycles of freezing-and-thawing. Bank et al. (1998) studied the bond degradation by submerging the specimens that were made of different types of FRP rebars in tap water at $176 \,^0$F for up to 84 days. They found a good relation between material degradation and the bond degradation. Al-Dulaijan et al. (2001)

investigated the effect of the environmental pre-conditioning on the bond of the FRP reinforcement to concrete. The FRP rebars were exposed to three types of solution, ammonia, acetic acid, and water at 176 ^{0}F for 28 days, before the rebars were embedded into concrete. They reported that the lugged rods had significantly reduced bond strength due to the degradation of the resin or the fiber/resin interface. On the other hand, little difference was observed for the smooth rods.

As for the durability of beam tests as a system, very limited information was found in the published literature. Laoubi et al. (2002) observed that the change in the overall behavior, in terms of deflection, ultimate capacity, and mode of failure, for the tested beams (both under-reinforced and over-reinforced) after 200 freezing-and-thawing cycles was insignificant. Approximately 10% reduction in the ultimate strength was observed by Tannous and Saadatmanesh (1998) in their tests of under-reinforced beams submerged in de-icing solutions for two years. Sen et al. (1993, 1999) investigated FRP pretensioned beams under tidal/thermal cycles. They found that fiberglass strands were unsuitable for pretensioning application in a marine environment. The CFRP beams showed good durability, although degradation in both bond and flexural strength was observed.

Based on the limited information discussed above, it is still not clear whether the bond or flexural behavior degrades, or to what extent, after being subjected to various environmental agents. Furthermore, most of the studies mentioned previously on the FRP and concrete system concentrate on certain specific applications and do not reflect the environmental conditions to which bridge decks would be subjected in the US Mid-West region, where bridge decks are oftentimes subjected to freezing-and-thawing cycles while

exposed to de-icing salts. Therefore, further study is needed to investigate the durability characteristics of the whole system.

6.2. PROBLEM STATEMENT

Composite materials, as well as the whole reinforcing system, will degrade by the attack from various environmental agents. The environmental agents that have potential effects on the long-term structural behaviors of this FRP/FRC hybrid system are discussed as follows:

- **Thermal Effect**

The thermal parameters of steel reinforcement and concrete are very close, as shown in Table 6.1. Thus, there is little or no interaction between the steel rebar and concrete due to the thermal effect on RC structure. Unlike the traditional RC structures, the CTE (coefficient of thermal expansion) between fibers and concrete is different. Furthermore, the resin materials used to bind the fibers have very large CTE in comparison to concrete. A significant interaction can occur with the temperature variation, which may affect the interactive properties between the two materials. To study the thermal effect on the FRP/FRC system, temperatures were varied from -4 ^{o}F to 140 ^{o}F in this study to investigate the thermal effect on the system.

- **Freezing-and-Thawing Effect**

An serious environmental threat to bridge structures with a poor quality of concrete is the freezing-and-thawing cycles. Research (ACI 201.2R-92) shows that cycles of freezing-and-thawing will damage the concrete and the damage is greatly accelerated by the use of deicing salts. Concrete is a permeable material. In addition, cracks usually

Table 6.1. Coefficient of Thermal Expansion of Various Materials
(Balazs and Borosnyoi, 2001)

Material	Coefficient of thermal expansion $*10^{-6}$ 1/K	
	Longitudinal	transverse
Carbon fiber	-0.9 to +0.7	8 to 18
Aramid fiber	-6.0 to -2.0	55 to 60
Glass fiber	5 to 15	5 to 15
Resin	60 to 140	
CFRP	-0.5 to 1.0	20 to 40
AFRP	-2.0 to -1.0	60 to 80
GFRP	7 to 12	9 to 20
Steel	12	
Concrete	6 to13	

exist throughout the service life of RC structures. Water or de-icing salt water could

potentially reach the interface between the rebars and concrete. Therefore, accumulated

damages may occur to the concrete and the FRP rebars as well as the interface by the

repeated freezing-and-thawing cycles. The structural behaviors will thus be adversely

affected. The effect of the freezing-and-thawing cycle on the hybrid system was

examined in this study.

- **Ultraviolet Radiation**

Polymeric materials can absorb the ultraviolet and, therefore, are susceptible to

reactions initiated by the absorption of ultraviolet energy. Generally, the effects of UV

exposure are confined to the top few microns of the surface. Thus, the degradation from

UV exposure may be a concern for the external application of FRP materials. However,

test results indicated that the mechanical properties of the FRP rebars were not

significantly affected even by direct exposure to the UV radiation (Tannous and

Saadatmanesh, 1998). For the application of FRP material in this project, FRP rebars were protected by concrete cover. Therefore, the degradation caused by UV radiation was expected to be negligible and was not investigated in this study.

- **De-icing Salt Solution**

De-icing salt used in cold climates, and associated chloride penetration, is a major cause of corrosion in steel reinforced highway structures. It may also affect the strength of the FRP materials. More than 20% tensile strength reduction was observed for E-glass/ vinylester immersed in de-icing salt solution for 180 days (Tannous and Saadatmanesh, 1998). As discussed previously, damage caused by the freezing-and-thawing cycles will be aggravated by the use of salt solution. The effect of a de-icing solution on this new hybrid system was simulated and investigated in this study.

- **Humidity Effect**

FRP rods are not waterproof. Moisture can diffuse into resin, leading to changes in mechanical characteristics as well as in physical appearance (increase of volume). As a consequence, the overall performance of the FRP/FRC hybrid system may be altered. Since the specimens in this study were in contact with salt water, the humidity effect on the FRP/FRC system was not investigated separately.

- **Alkaline Effect**

When in contact with alkaline media, FRP material will degrade due to the chemical reaction with an alkaline solution. For this hybrid FRP/FRC system, FRP rods were embedded in concrete, which is known to have a pH level as high as 13.5. This alkaline environment can damage glass fibers through the loss of toughness and strength. Several studies have been conducted out on the effect of alkaline on the FRP material.

However, in most of these studies, FRP rods were directly immersed into an alkaline solution to simulate the FRP rods in concrete, and significant degradation for GFRP rebars was reported (Uomoto and Nishimura, 1999). Direct immersion into an alkaline solution was thought to be much more severe than real conditions. Some researchers (Sekijima et al., 1999) conducted durability test in which prestressed concrete beams reinforced with GFRP grids were exposed outdoors for 7 years, where the annual average temperature was 60°F, and the annual precipitation amounted to 58 in.; an extremely small effect was observed. A similar observation was made by Tannous and Saadatmanesh (1998). Most likely, it is the mobility of the alkaline ions that greatly affects the test results. To accelerate the possible degradation effect from alkaline while not exaggerating it, FRP rods were embedded in concrete and the specimens were kept moist in this study.

In this study, a total of 36 bond specimens and 24 beam specimens were fabricated to study the effect of various environmental agents on the durability of the FRP/FRC system. To simulate the seasonal weather changes in the mid-west region of the US, specimens were subjected to combined environmental cycles, consisting of the freezing-and-thawing cycles and the high temperature cycles, while in contact with a salt solution. Then, bond behaviors and flexural beam behaviors were compared with unweathered specimens to investigate the durability of this new hybrid system.

6.3. TEST RESULTS AND DISCUSSIONS

6.3.1. Durability Effect on Bond. In the following sections, the environmental conditioning's effect on the specimen conditions and the bond behaviors are discussed.

Differences of the bond performances between the plain concrete specimens and the FRC specimens after being subjected to the environmental conditioning are also presented.

6.3.1.1. Appearance of specimen after environmental conditioning. After the environmental conditioning, the specimen conditions were changed.

- **Plain Concrete Specimens**

In addition to concrete scaling on the surface, most specimens also showed some damage on the concrete, especially at the corner areas. One DP4C specimen and one DP4G specimen were severely damaged and large portions of concrete were broken apart, as shown in Figure 6.1.
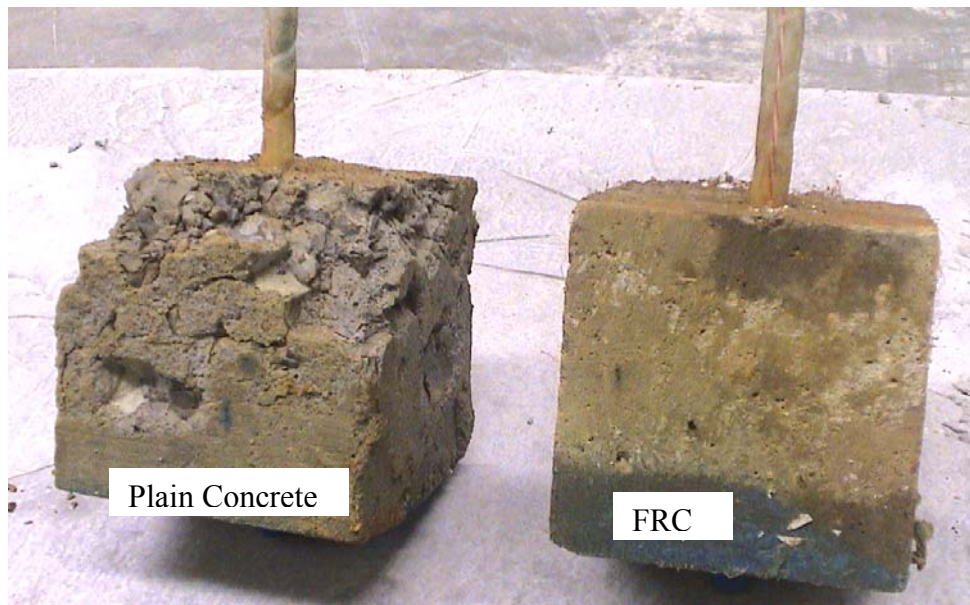
(a) #4 GFRP

Figure 6.1. Different in Appearance of Plain Concrete Specimen and FRC Specimen after Environmental Conditioning
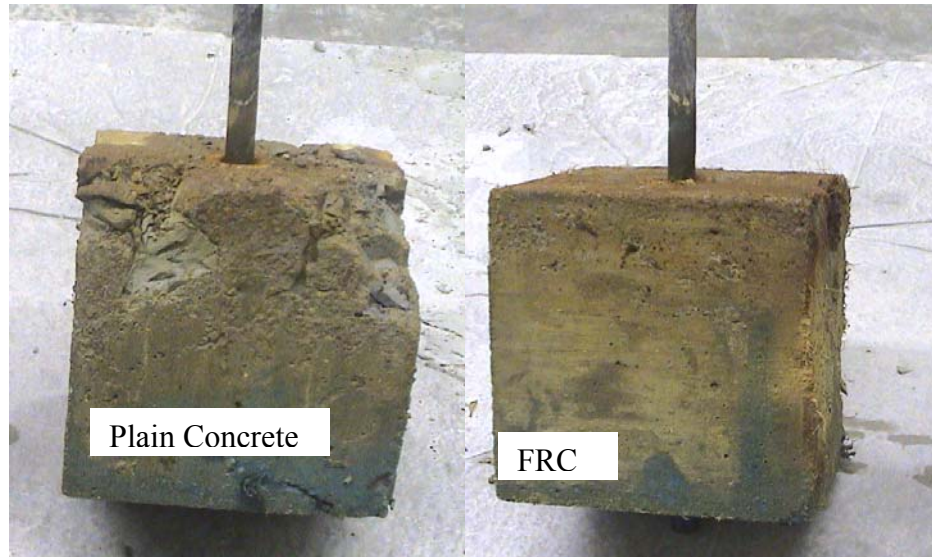
(b) #4 CFRP

Figure 6.1. Different in Appearance of Plain Concrete Specimen and FRC Specimen after Environmental Conditioning (Cont.)

- **FRC Specimens**

Damages were limited to the surfaces of the specimens. With the scaling of concrete at the surfaces, fibers could clearly be observed. However, all FRC specimens remained integrated, as shown in Figure 6.1. In comparison to plain concrete specimens, the FRC specimens were more immune to the attack of the environmental conditioning.

6.3.1.2. Environmental conditioning effect on bond behaviors. The test results are summarized in Table 6.2. The bond-slip responses at the loaded end and the free end are shown in Figures 6.2 to 6.13. Herein, the average bond strength was calculated as the pullout force over the embedded area of the rebar. The slip on the side of loading was calculated as the value of LVDT2 minus the elastic deformation of the FRP rebar between the bond zone and the location of LVDT2. Again, the deformation of the steel frame is ignored.

Table 6.2 Test Results of Durability Bond Tests

I.D.	Bond Strength (psi)		Loaded –End Slip (in.)		Design Bond Strength (psi)		Bond Stiffness (ksi/in.)		Mode +
VP4 C	1,269		0.03		1,273		637		P
	1,299	1,255	0.04	0.04	843	1,080	421	540	P
	1,198		0.04		1123		561		P
VP4 G	2,437		0.22		1034		517		S
	3,001	2,712	0.27	0.26	1706	1,322	853	661	S
	2,699		0.29		1226		613		S
VP8 G	2,759		0.34		1252		626		S
	2,538	2,682	0.34	0.33	1288	1,232	644	616	S
	2,748		0.32		1156		578		S
DP4 C	947		0.13		692		346		S
	805	970	0.06	0.08	782	813	391	406	P
	1,157		0.05		964		482		S
DP4 G	342		0.12		154		77		S
	1,803	1,185	0.15	0.13	1124	748	562	374	S
	1,400		0.13		967		484		S
DP8 G	2,598		0.50		935		468		S
	2,467	2,585	0.43	0.46	1162	1,101	581	551	S
	2,689		0.45		1207		603		S
VF4 C	1,243		0.04		1223		611		P
	930	1,035	0.04	0.04	922	1,026	461	513	P
	933		0.03		933		466		P
VF4 G	2,335		0.36		1716		858		S
	2,212	2,352	0.53	0.40	1139	1,293	569	647	P
	2,508		0.32		1025		513		S
VF8 G	1,768		0.57		795		397		P
	1,869	1,916	0.52	0.53	1036	959	518	480	P
	2,103		0.49		1047		524		P
DF4 C	979		0.06		888		444		P
	847	985	0.06	0.06	728	906	364	453	P
	1,130		0.07		1101		550		P
DF4 G	2,161		0.49		901		450		S
	2,012	2,005	0.37	0.47	967	1,081	484	540	S
	1,843		0.54		1375		687		P
DF8 G	1,835		0.85		876		438		P
	1,914	1,938	0.80	0.85	998	946	499	473	S
	2,064		0.90		963		482		P

Note: +P=Pullout failure; S=Splitting failure;

**Figure 6.2. Loaded-end Bond-Slip Relationship for #4 CFRP
Plain Concrete Specimens**

Figure 6.3. Loaded-end Bond-Slip Relationship for #4 CFRP FRC Specimens

Figure 6.4. Loaded-end Bond-Slip Relationship for #4 GFRP Plain Concrete Specimens

Figure 6.5. Loaded-end Bond-Slip Relationship for #4 GFRP FRC Specimens

Figure 6.6. Loaded-end Bond-Slip Relationship for #8 GFRP Plain Concrete Specimens
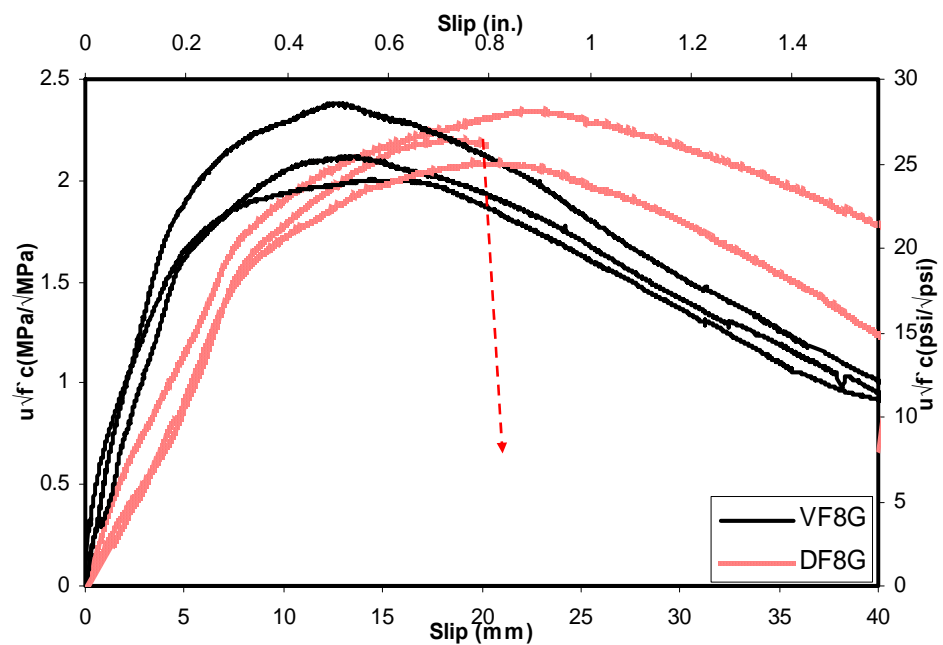
Figure 6.7. Loaded-end Bond-Slip Relationship for #8 GFRP FRC Specimens
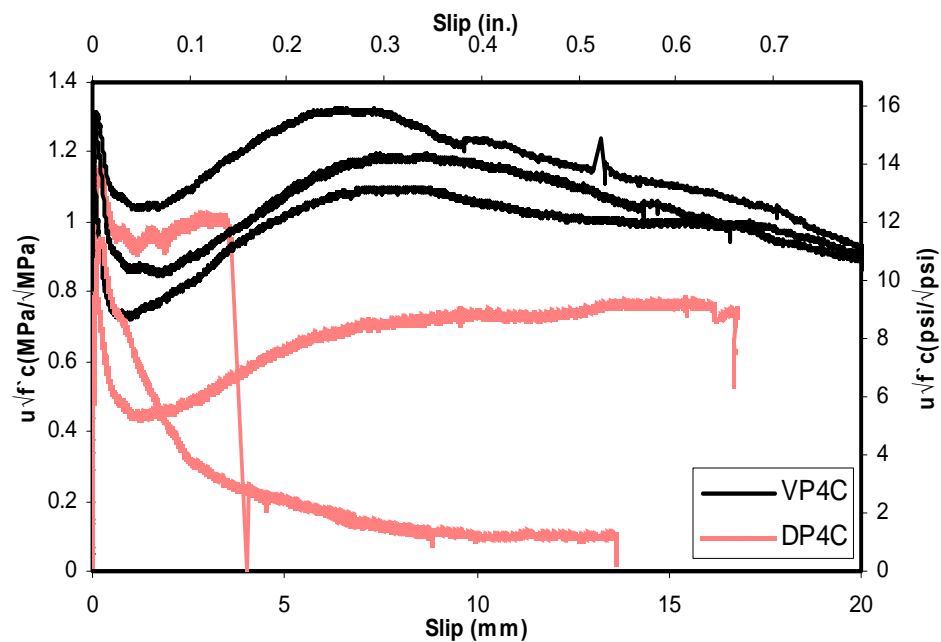
Figure 6.8. Free-end Bond-Slip Relationship for #4 CFRP Plain Concrete Specimens
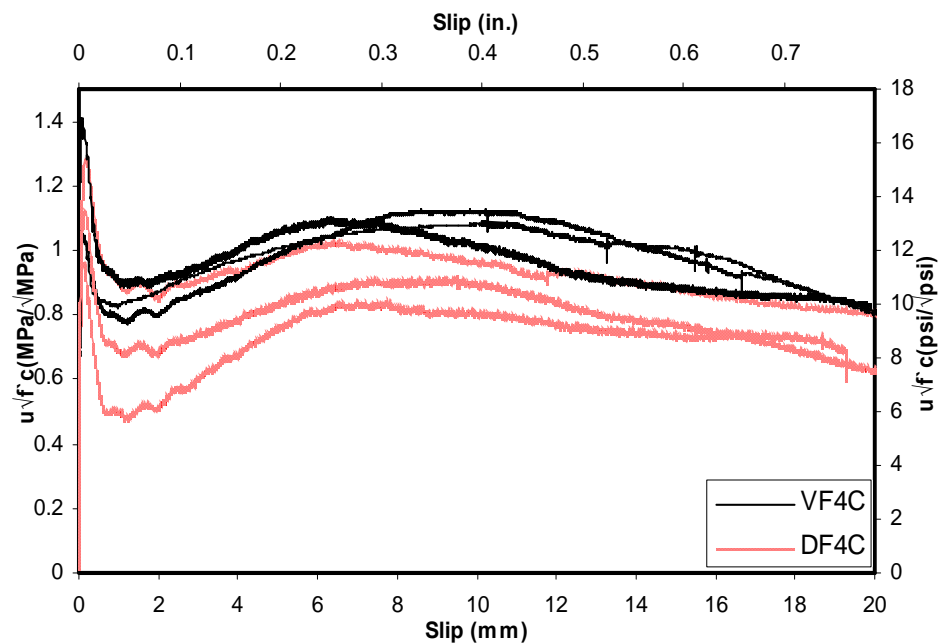
Figure 6.9. Free-end Bond-Slip Relationship for #4 CFRP FRC Specimens
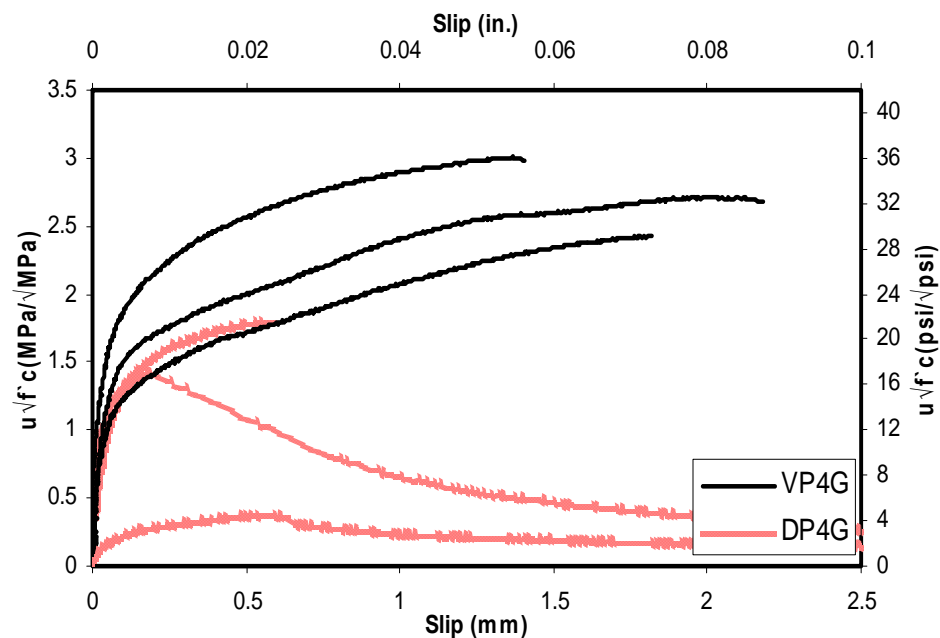
Figure 6.10. Free-end Bond-Slip Relationship for #4 GFRP Plain Concrete Specimens
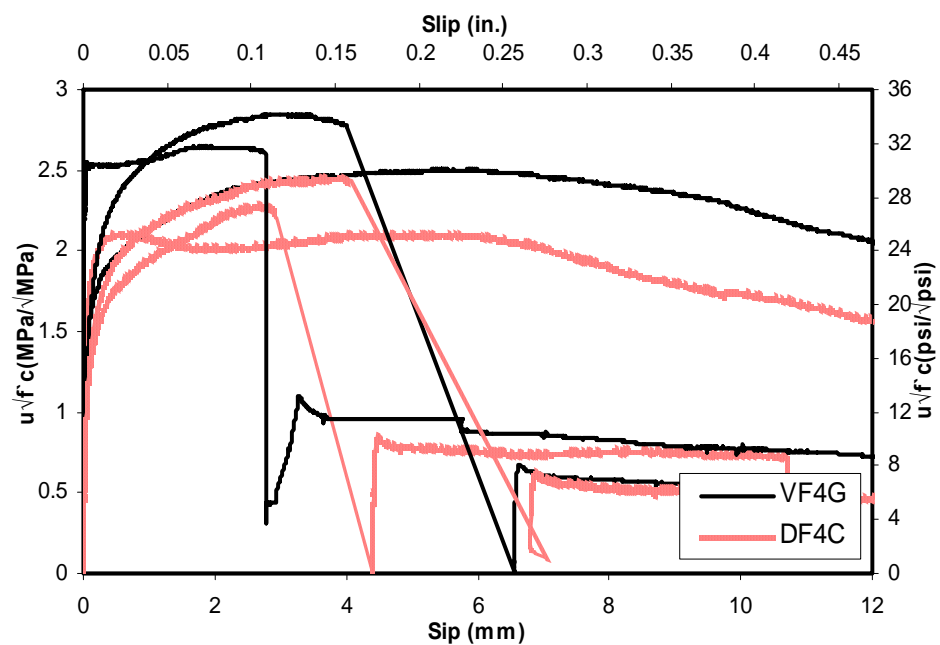
Figure 6.11. Free-end Bond-Slip Relationship for #4 GFRP FRC Specimens
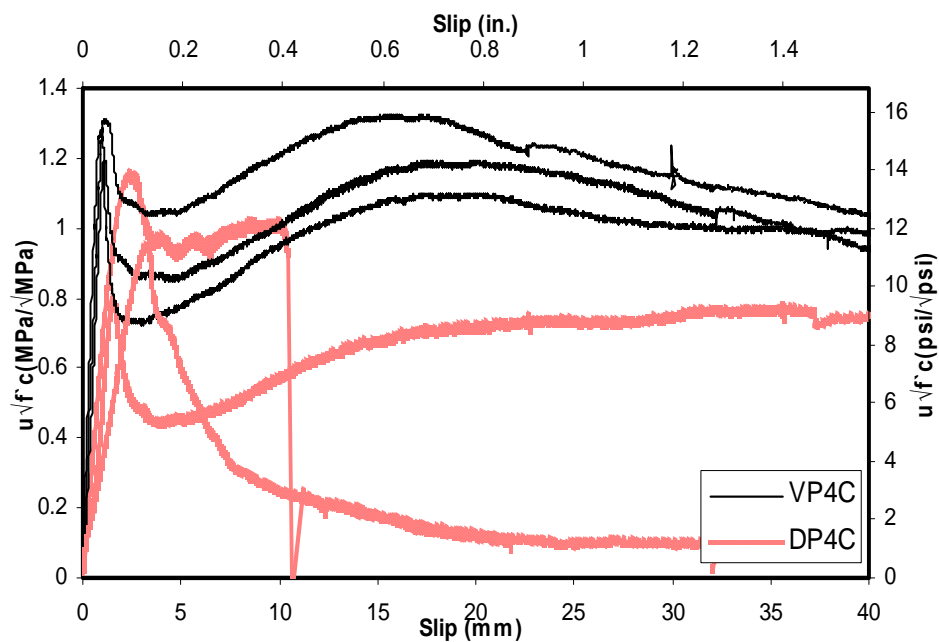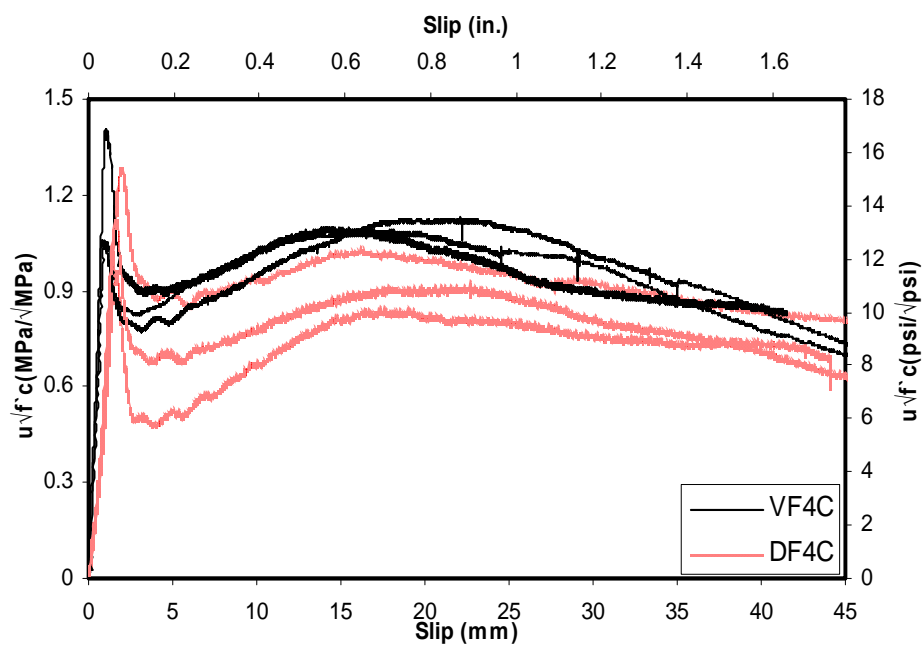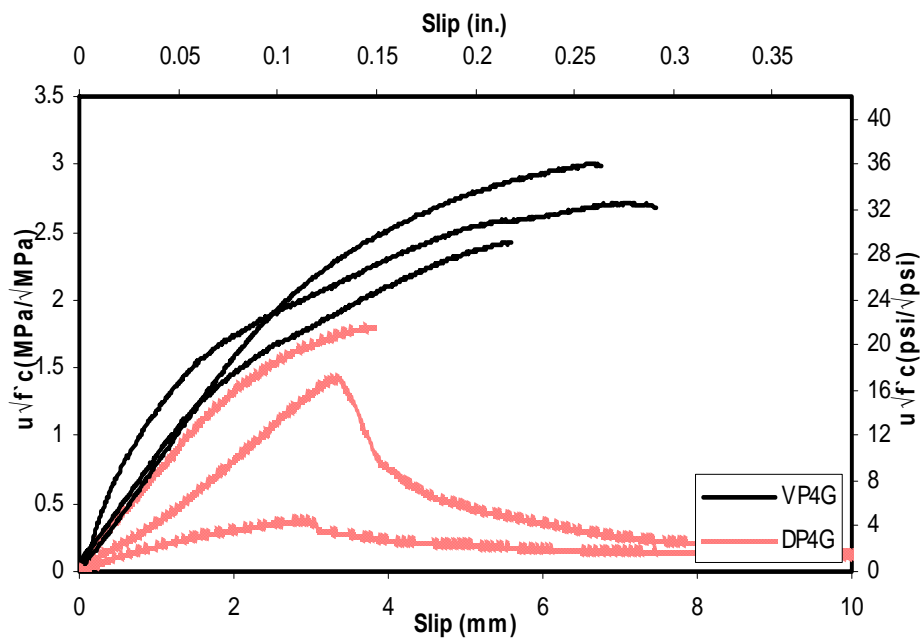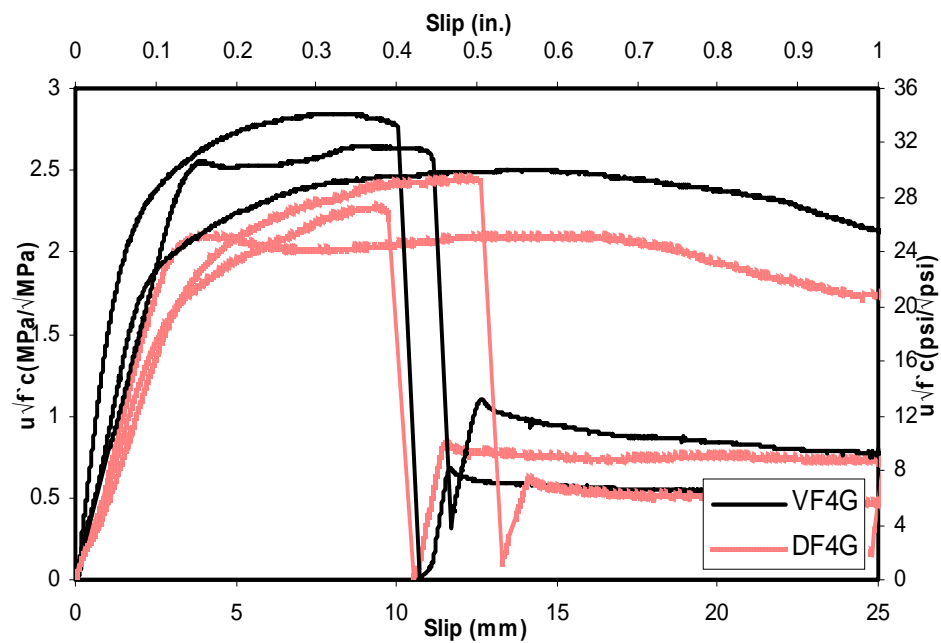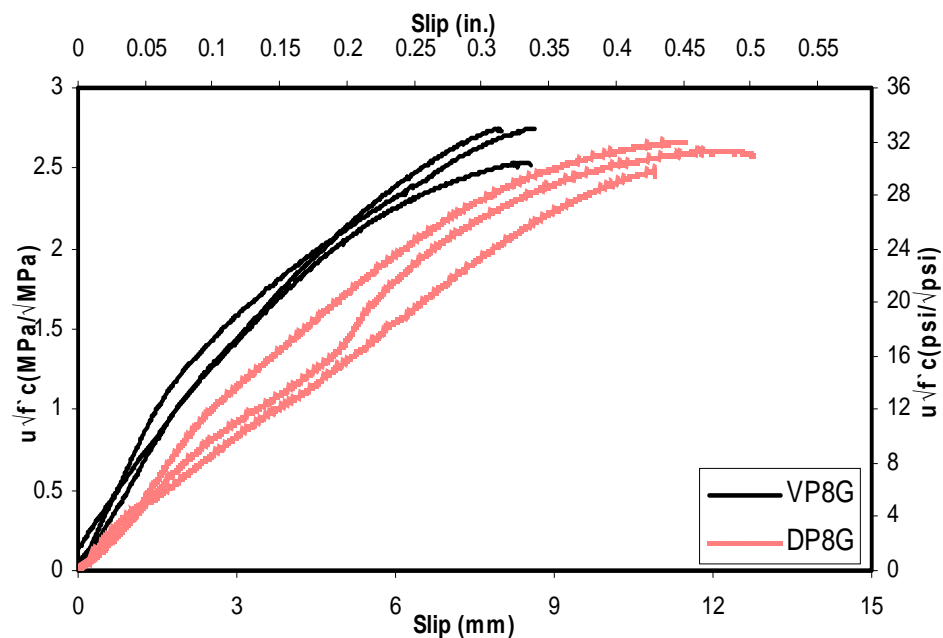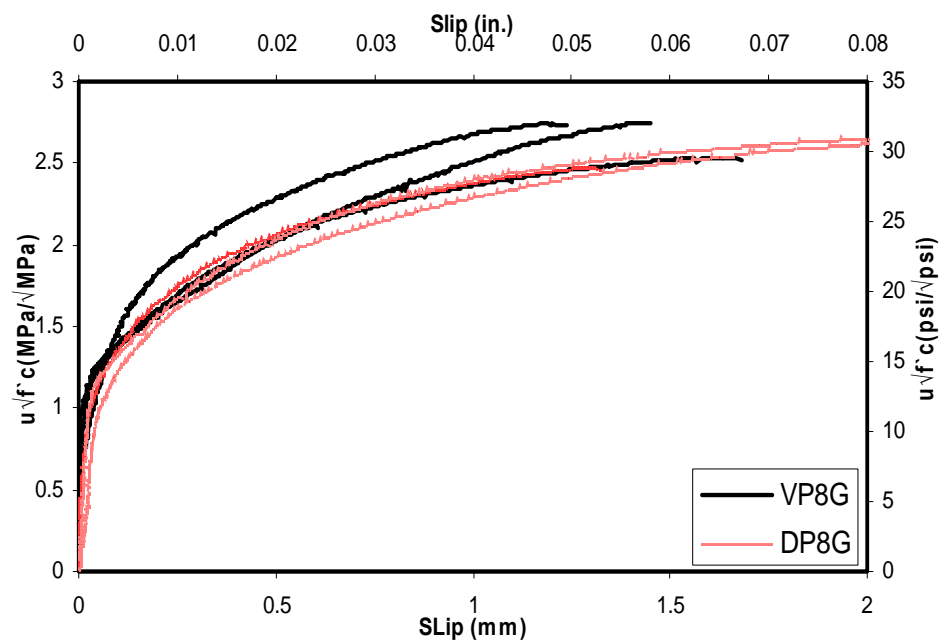
Figure 6.12. Free-end Bond-Slip Relationship for #8 GFRP Plain Concrete Specimens
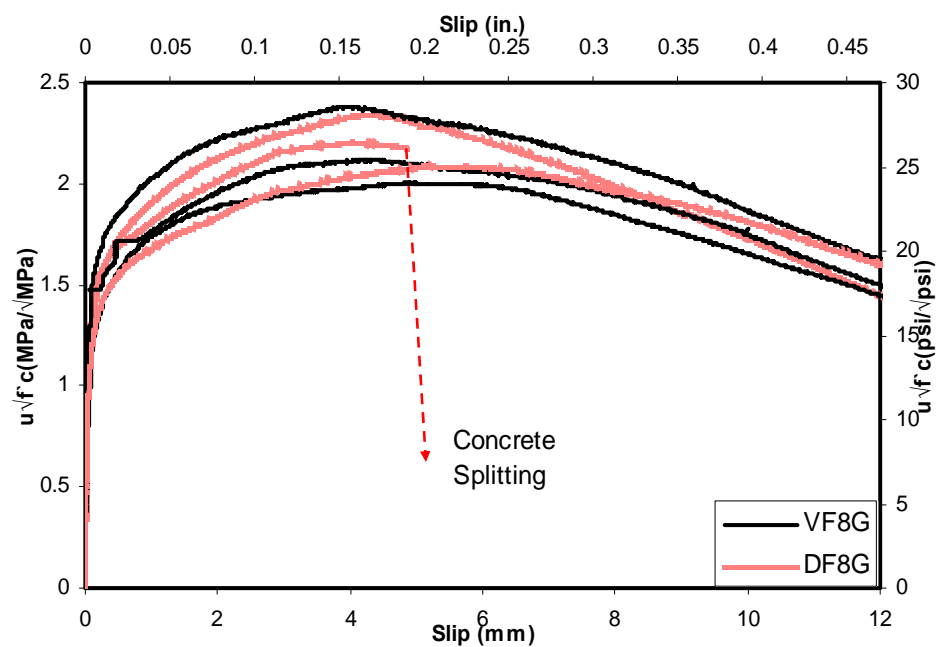
Figure 6.13. Free-end Bond-Slip Relationship for #8 GFRP FRC Specimens

6.3.1.2.1. <u>Plain concrete specimens.</u> As shown in Figures 6.2 to 6.13, in comparison to the unweathered specimens, the bond-slip response was significantly altered after being subjected to the environmental conditioning.

- **Bond-Slip Response**

Unweathered specimens showed fairly consistent test results with the same testing parameters. However, test results for specimens after being subjected to environmental conditioning were inconsistent. The inconsistent behavior may be due to the random nature of the development of the degradation (Bank et al., 1998). Different levels of damage on the specimens were observed visually. In general, specimens with more severely damaged concrete showed lower bond strength. In other words, the bond strength was strongly dependent on the condition of the concrete. Figure 6.1 showed the most severely damaged specimens (DP4C and DP4G). These specimens had large amounts of concrete broken apart and thus showed very low bond strengths.

After specimens had been subjected to the environmental conditions have their bond-slip curves softened. The slopes of the pre-peak curves were decreased and the shapes of the curves were even changed in some specimens. As discussed in Chapter 4, bond between the CFRP rebar and the concrete initially consisted of chemical adhesion and friction. With the increase of the relative slip between the rebar and the concrete, chemical adhesion was broken and the pullout load was then resisted by friction force only. Therefore, two peak bond strengths have been observed. One occurred when the chemical bond reached its ultimate; the other occurred when the friction force reached its maximum. As shown in Figure 6.3, only one peak was observed in one DP4C specimen

after environmental conditioning, which may be due to the serious damage to the chemical bond.

- **Failure Modes**

Most of the specimens had the same failure modes as the unweathered specimens. However, the failure modes were changed in the DP4C specimens. All three unweathered specimens, VP4C, failed in the rebar pullout. However, two of the three DP4C specimens failed in concrete splitting; the other one failed in rebar pullout. This was caused by the damage of concrete. Some portions of the concrete were broken apart; thus a smaller amount of concrete could resist the splitting force caused by the rebar.

- **Ultimate Bond Strength**

Ultimate bond strengths of all the specimens were reduced and this effect was more significant in specimens with small dimensions (#4 rebar specimens). As shown in Figure 6.14, 23%, 56 %, and 4% reductions were observed in ultimate bond strength for DP4C, DP4G, and DP8G specimens, respectively.

- **Bond Stiffness**

Because the bond stiffness gives a relationship between load and deformation, this value has an important effect on the width of flexural cracks in reinforced concrete and on the deflection of beams and slab (Katz, et al., 1999). Its value can be computed by the slope of the bond-slip curve at the loaded end or at the free end. As mentioned previously, after being subjected to environmental conditioning, the surfaces of most of the specimens were severely damaged. Some amounts of concrete at the surface were broken apart. Concrete may have become less compacted than before. During the pullout bond tests, the concrete at the loaded end was under compression, and the loose concrete would
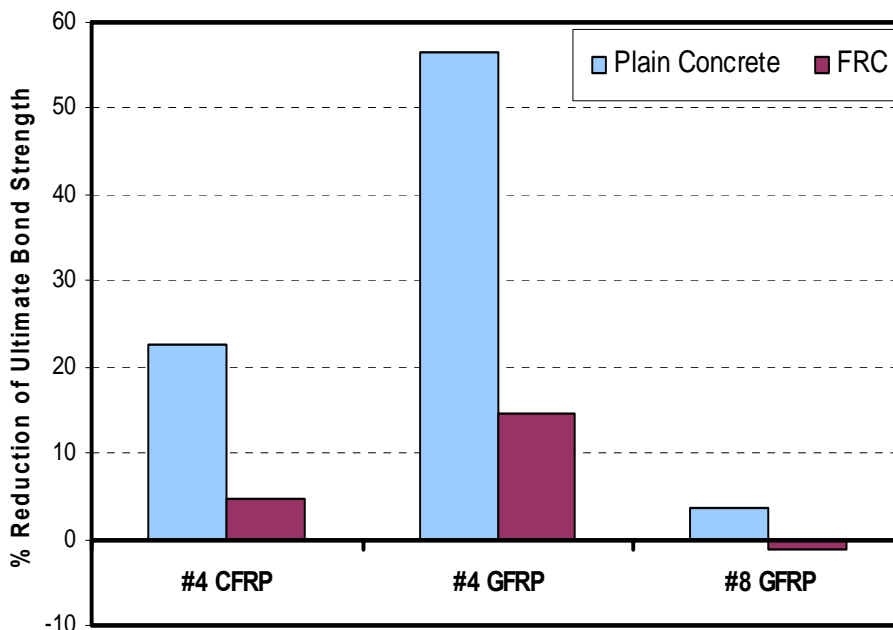
Figure 6.14. Reductions in Ultimate Bond Strength

be compacted. Thus, the measured loaded end slip would be enlarged. However, the slip

measured from the free-end slip did not have this influence. As shown in Figures 6.2 to

6.13, the slopes of the curves at the free end did not show as much reduction as those at

the loaded end. Thus, the bond stiffness in this research was computed by the slope of the

bond-slip curve at the free end. On the other hand, bond behavior at the service stage is of

more significance since bond failure rarely controls the design of the structural members.

It is more related to the serviceability. In this study, bond stiffness is defined as the slope

of the secant modulus corresponding to the slip of 0.002 in. at the free end. The value of

0.002 in. was used because this value is often selected as the criteria for the design

strength of bond. Some more explanation can be found in the later paragraphs.

As shown in Figure 6.15, 25%, 43%, and 11% reductions were observed in the

bond stiffness for DP4C, DP4G, and DP8G specimens, respectively.

Figure 6.15. Reductions in Design Bond Strength or Bond Stiffness

- **Design Bond Strength**

The application of the ultimate bond strength data to real design is not appropriate

because of the excessive slip occurring in these specimens at large loads. Too much slip

will result in untolerated crack width. From a designer's point of view, Mathey and

Watstein (1961) suggested that bond stress corresponding to 0.01 in. slippage of loaded

end or 0.002 in. of free end for steel reinforced structures can be defined as the critical

bond stress. The criterion of 0.01 in. slippage at the loaded-end was decided based on half

of the crack width limitation (Mathey and Watstein, 1961). Ferguson et al. (1966) pointed

out that the loaded-end slip of the pullout specimens was larger than that of the beam

specimens because flexural cracks in beam specimens tended to distribute the slip in

several places along the beam. Also, since there is relatively low elastic modulus of FRP

materials (GFRP is about 1/5 that of steel, CFRP is about 2/3 that of steel), greater elongation along the embedded rebar will be produced and will lead to a larger loaded-end slip. Thus, 0.01 in. slippage at the loaded-end of the pullout specimens as design criterion is not appropriate. To keep it comparable to limits imposed on the steel rebar, bond strength corresponding to 0.002 in. slippage at the free-end was adopted as the designing bond strength.

Based on the definition of the bond stiffness and the design bond strength in this study, the reduction rates of the design bond strengths were the same as those of the bond stiffness.

6.3.1.2.2. FRC specimens. In the following sections, test results regarding the FRC specimens are presented.

- **Bond-Slip Response**

In general, the test results of the FRC specimens showed good consistency. The behavior of the specimens in the same testing group was similar. Like the plain concrete specimens, all the bond-slip curves were softened after being subjected to the environmental cycles.

- **Failure Modes**

Like the plain concrete specimens, most of the FRC specimens had the same failure modes as the unweathered specimens. However, the failure mode of one of the three DF8G specimens was changed from rebar pullout to concrete splitting.

- **Ultimate Bond Strength**

Reductions of the bond strength in the FRC specimens were observed as in the plain concrete specimens. As shown in Figure 6.14, 5%, 15%, and -1% reductions were

observed in the ultimate bond strength for DF4C, DF4G, and DF8G specimens, respectively.

- **Bond Stiffness**

Like the plain concrete specimens, reductions of the bond stiffness were observed in the FRC specimens. As shown in Figure 6.15, 12%, 16%, and 1% reductions were observed in the bond stiffness for DF4C, DF4G, and DF8G specimens, respectively.
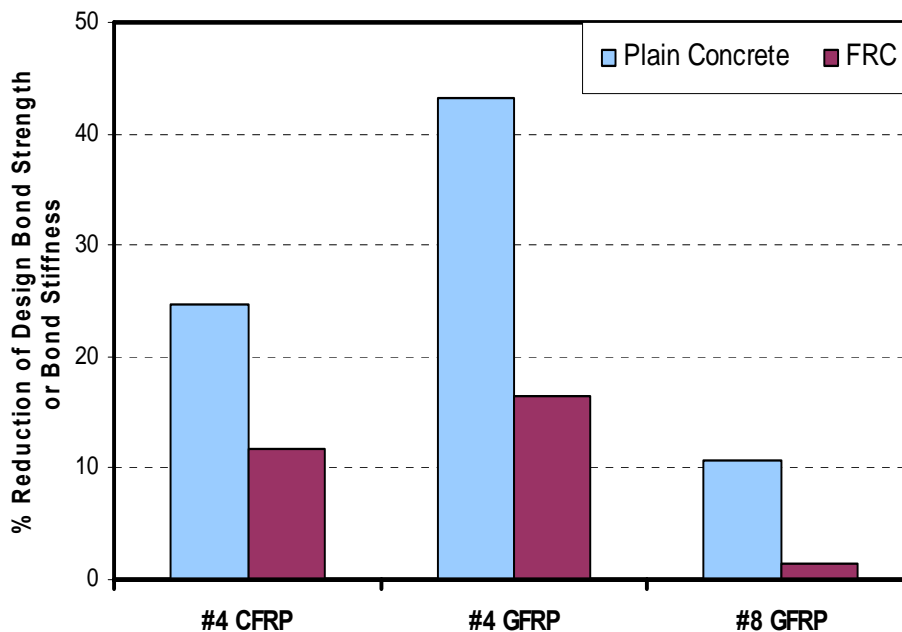
- **Design Bond Strength**

The reduction rates of design bond strength were the same as the rates of the bond stiffness, which are 12%, 16%, and 1% for DF4C, DF4G, and DF8G specimens, respectively.

6.3.1.3. Discussions on the durability effect on bond. After being subjected to the environmental conditioning, both the plain concrete specimens and the FRC specimens showed bond degradations. Bond is determined by the properties of its constitutions (concrete and rebar) and the interaction between the constitutions. Three possible reasons are provided to explain the bond degradation as follows:

1. Microvoids between the rebar and the concrete exist at the time of the specimen fabrication; i.e., rebar is not in full contact with the concrete (Gylltoft, et al., 1982). When specimens are submerged in the solution, the solution will permeate into the interface between the rebar and concrete. Later, the microvoids will be filled with solutions. The volume of water will expand about 10% when frozen. Microcracks will thus be induced if the stresses, f_c, are larger than the tensile strength of the concrete, f_t'. With the subsequent freezing-and-thawing cycles, damage will build up and more and bigger microcracks will be created.

2. As shown in Table 6.1, the FRP rebar has a higher CTE than the concrete. When the temperature increases, the expansion rate of the FRP rebar is larger than that of the concrete. Radial busting force will be imposed on the concrete surface at the interface, and the structure at the interface will be disrupted. When the stress in the concrete, f_c, is larger than the tensile strength, f_t', cracks will develop. When the temperature reduces, the contraction rate of the FRP rebar is bigger than that of the concrete, micro-gaps will form along the interface.

The above two mechanisms function together and degrade the bond mainly by disturbing the structures at the interface. Bond degradation may also come from the degradation of the rebar itself.

3. FRP rods are not waterproof. Moisture may diffuse into the polymer resin to a certain degree (Micelli and Nanni, 2004). Studies also show that some deterioration of the polymer resins may occur since water molecules can act as resin plasticizers, thereby disputing van der Waals bonds in polymer chains (Bank and Gentry, 1995). Furthermore, during the freezing-and-thawing cycles, water will expand and lead to the cracking of the resin. Resin damage will speed up the process by which moisture is transported inside the composite, thereby allowing the deteriorations to be accelerated. The surface area is most vulnerable to be attacked; thus, the surface is expected to be the most seriously deteriorated. Consequently, the rebar and concrete will not be contacted as tightly as before. Bond thus is degraded.

All three mechanisms play a certain role in the bond degradation and the combined effects are likely to be even more detrimental to the bond. As mentioned previously, all specimens showed bond degradation to some extent after environmental

conditioning. However, the degradation magnitude differed among the different specimens.

 6.3.1.3.1. **Specimen dimension effect on bond degradation.** Compared to the large (#8) specimens, the small specimens (#4) showed greater degradation effect. This was so in both the plain concrete specimens and the FRC specimens. As shown in Figure 6.14, the ultimate bond strengths reduced 56% for DP4G specimens, while only 4% reduction was observed in DP8G specimens. Similarly, the ultimate bond strengths reduced 15% for DF4G specimens; while DF8G specimens showed 1% increase. In design bond strength or bond stiffness, the small specimens also showed a much more serious reduction, as shown in Figure 6.15. Specimen dimensions effect on the bond durability can be explained by ways that the salt solution attacks the bond behavior. There are two ways in which the salt solution can reach the interface between the rebar and concrete, as shown in Figure 6.16. One is through the loaded-end of the specimens, since the free-end was coated with water-proof epoxy, and it was assumed that no solution can permeate the epoxy, as shown in Figure 6.16. The other way is through the concrete cover, as shown in Figure 6.16. In the large specimens, there were relatively smaller portions of the bonded area that could be immediately attacked by the solution. In this study, the loaded end of the specimen was directly exposed to the solutions, and the solutions could easily access the interface near the loaded end. Since the depth of the specimen that was immediately accessible to the solution was independent of the size of the specimens, the absolute depths that were affected were the same. On the other hand, the bigger specimens had a bigger embedment length; thus, the ratio of affected area to the whole bonded area was smaller in the case of the large specimens. Another reason

may be due to the larger cover depth of the large specimens. The #4 specimens had 2.5"

embedment length and dimensions of 5 in. × 5 in. × 5 in., which meant a 2.25 in. concrete

clear cover. The #8 specimens had 5" embedment length and dimensions of 10 in. × 10 in.

× 10 in., which meant a 4.5 in. concrete clear cover. The concrete cover played a

significant role in decreasing the rate of the ingress of the solution. Potter and Ho (1987)

found that the depth of water penetration was a function of square root of time, which

meant it would take three times longer for water to reach the rebar if double the cover

depth. Since the cover of the large specimens was twice as thick as the small specimens,

the interface between the rebar and concrete was better protected.
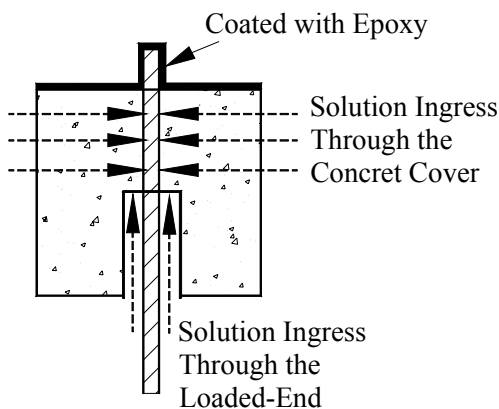
Figure 6.16. Two Ways of Solution Ingress

6.3.1.3.2. <u>Fiber effect on bond degradation.</u> With the addition of fibers, the

degradation rate of bond was significantly reduced. As shown in Figure 6.14, an average

reduction of 28% of bond strength was observed in the plain concrete specimens, while

only 6% reduction was observed in the FRC specimens. In the design bond strength, an

average reduction of 26% was observed in the plain concrete specimens, while only 10% reduction was observed in the FRC specimens, as shown in Figure 6.15. It can be concluded that fibers can effectively alleviate the bond deteriorations caused by environmental conditioning. As discussed earlier, cracks or voids were created during the environmental conditioning. Although the addition of fibers would not increase the first cracking load, the fibers would restrict the further development of the cracks due to the expansion of the water or the rebar. Hence, the deteriorations would not be accumulated, or this would happen at a much more moderate rate.

It should also be noted that the fact that there was less bond degradation for the FRC specimens could also be partly attributed to the fact that there was less damage of the concrete after the environmental conditioning. It was clear from the difference in appearance between the plain concrete specimens and the FRC specimens, after being subjected to environmental conditioning, the fibers could effectively alleviate the damage to the concrete caused by the freezing-and-thawing cycles. During the freezing cycles, the water entrained in the concrete microvoids would expand and induce microcracks. Microcracks were increased by the subsequent freezing-and-thawing cycles. In the worse cases, this cumulative effect resulted in the collapse of the concrete, as shown in the Figure 6.1. With the addition of fibers, the progress of the microcracks was restricted and the concrete was held integrated by the fibers. Also, the air content of the plain concrete used in this study was lower that that of FRC, which may also be responsible for the more severe damage of the plain concrete specimens.

6.3.1.3.3. Difference of GFRP vs. CFRP. The bond degradation rate of the GFRP specimens was more severe than that of the CFRP specimens. As shown in Figure

6.14, the bond reduced by 23% in the DP4C specimens and 56% in the DP4G specimens. Similarly, the bond reduced 5% in the DF4C specimens and 15% in the DF4G specimens. In the design bond strength or bond stiffness, the reductions were also observed to be larger in the GFRP specimens, as shown in Figure 6.15.

As discussed previously, the degradation of the rebar may partly be attributed to the bond degradation. Due to the attack by the salt water, the rebar, especially the outer surface, was damaged. Thus, less contact area may result. Research has shown that the CFRP rebar has superior durability characteristics compared to the GFRP rebar. Thus, less damage was expected in the case of the CFRP rebar, and hence, the CFRP specimens showed better durability of bond.

6.3.2. Durability Effect on Flexural Behavior. In the following sections, the effect of the environmental conditioning on the beam, in terms of specimen condition, flexural behaviors, and ductility is discussed. Differences in the flexural performances between the plain concrete specimens and the FRC specimens after being subjected to environmental conditioning are also reported.

6.3.2.1. Appearance of specimen after environmental conditioning. After the environmental cycles were completed, the appearance of the specimens was examined. Some observations were made as follows:

1. Concrete scaling on the surface of the beams was observed, as shown in Figure 6.17. Concrete scaling was limited to the top surface, and no concrete was broken apart. It can be concluded that the deterioration to the beam's flexural behavior due to the concrete scaling is negligible, if any. The most obvious concrete scaling occurred at the places where rebar chairs were placed. This is expected since the CTE of the plastic rebar

chairs is different from that of the concrete. Overall, the damage was much less severe compared to the damage in bond specimens. In real bridge decks, the exposure condition is expected to be similar to that of beam specimens in this study, thus, the concrete damage due to the environmental conditioning for bridge deck is expected to be small.
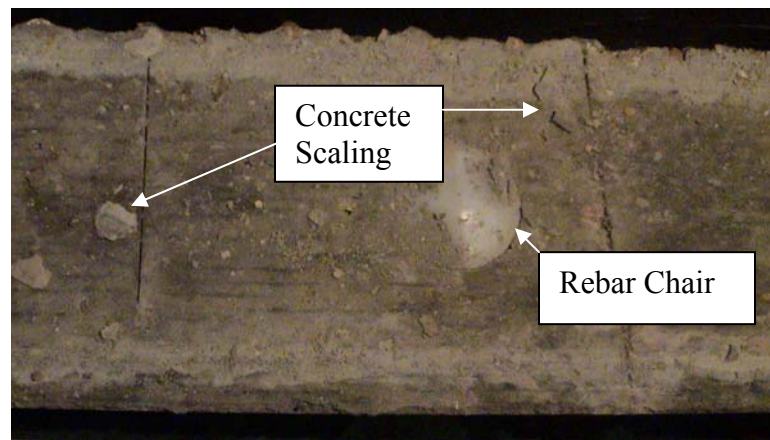
Figure 6.17. Concrete Scaling on the Beam Surface

2. Traces of steel rust can be found on the beam surface, as shown in Figure 6.18, indicating steel stirrups have already corroded to a certain degree. On the other hand, the corrosion of steel stirrups revealed that the environmental conditionings of this study are very critical for the steel reinforced structures.

6.3.2.2. Flexural response after environmental conditioning. In this section, the effect of the environmental conditioning on the overall flexural behavior, in terms of failure modes, flexural stiffness, and flexural strength is presented.

- **Failure Mode.** After being subjected to the environmental conditioning, the failure modes for the beams did not change. That is, all the beams still failed in concrete

crushing. No slips between the rebar and concrete were measured during the tests, which meant that the development length was long enough for the required stresses in the rebars to develop.
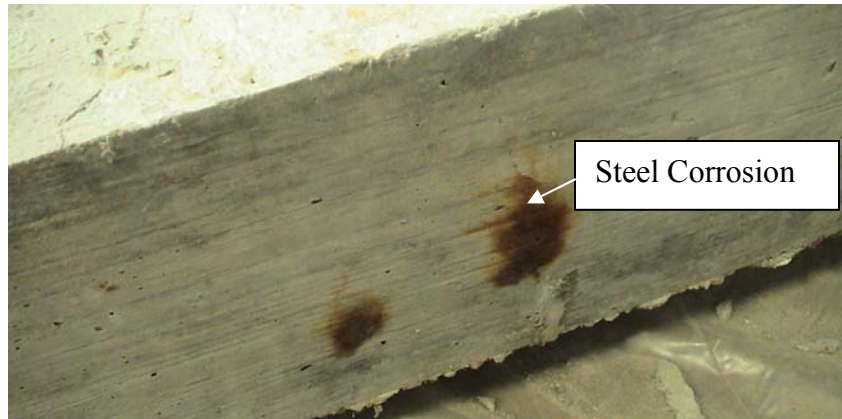
Figure 6.18. Photo Showing Steel Stirrups Corroded

- **Flexural Stiffness.** Figures 6.19 to 6.24 show the moment-deflection response of the beams before and after the environmental conditioning. Following the initial cracking, the flexural stiffness decreased but still remained approximately the same value for beams before and after the environmental conditioning. Flexural stiffness is determined by E_cI_m, and it is assumed that E_c has not changed after the environmental conditioning. Thereby, I_m is expected to remain the same before and after environmental conditioning. According to current ACI code, I_m is determined by M_{cr}, I_g, and I_{cr} at a certain load level. M_{cr} remained constant, which was verified by the moment-deflection curves. I_g was not expected to have any change, since concrete scaling induced by the environmental conditioning was limited to the top surface and no concrete
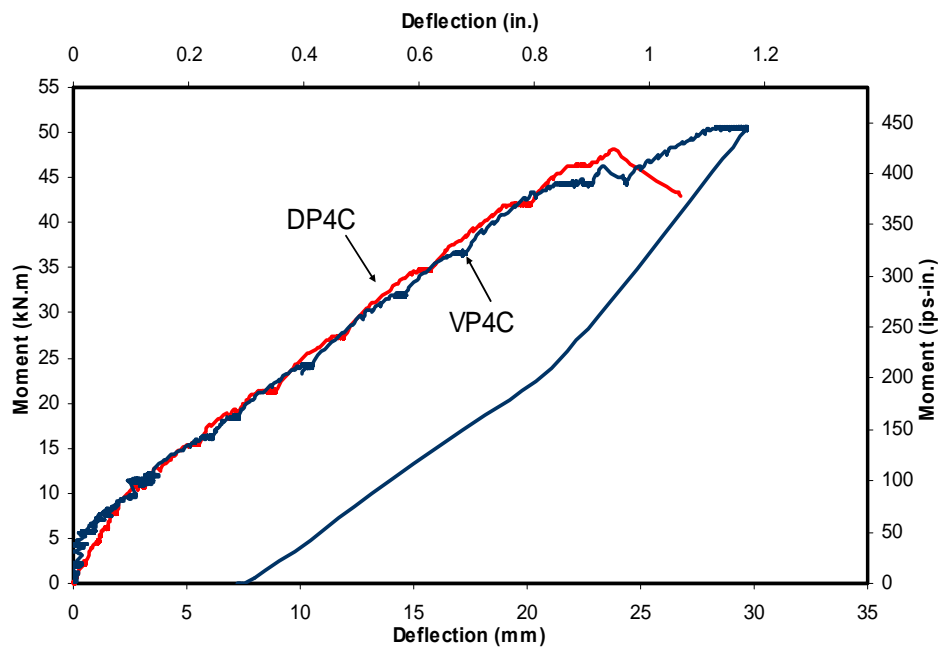
Figure 6.19. Moment-Deflection Relationship for #4 CFRP Plain Concrete Specimens
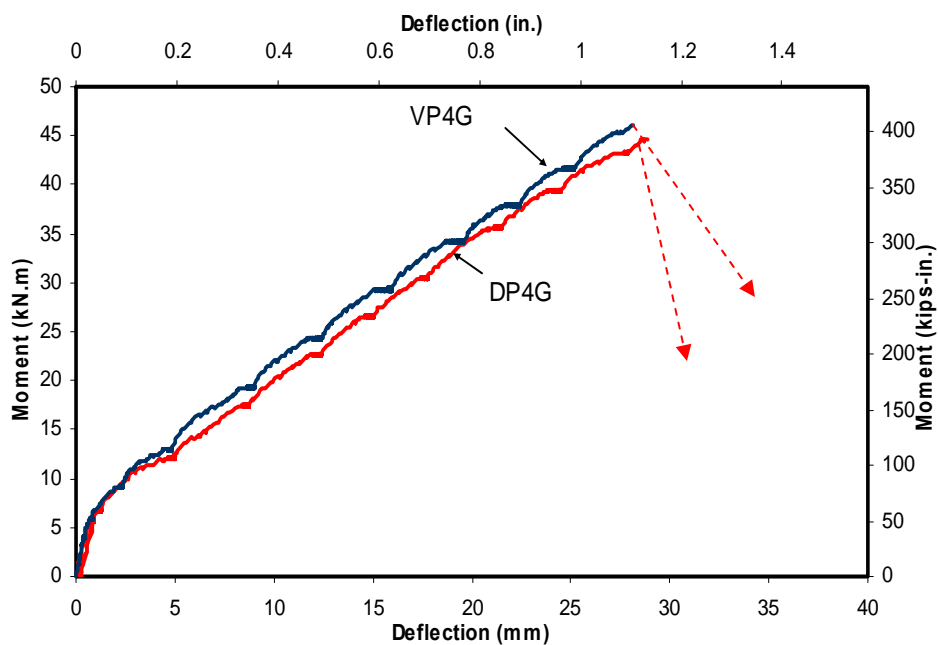
Figure 6.20. Moment-Deflection Relationship for #4 GFRP Plain Concrete Specimens
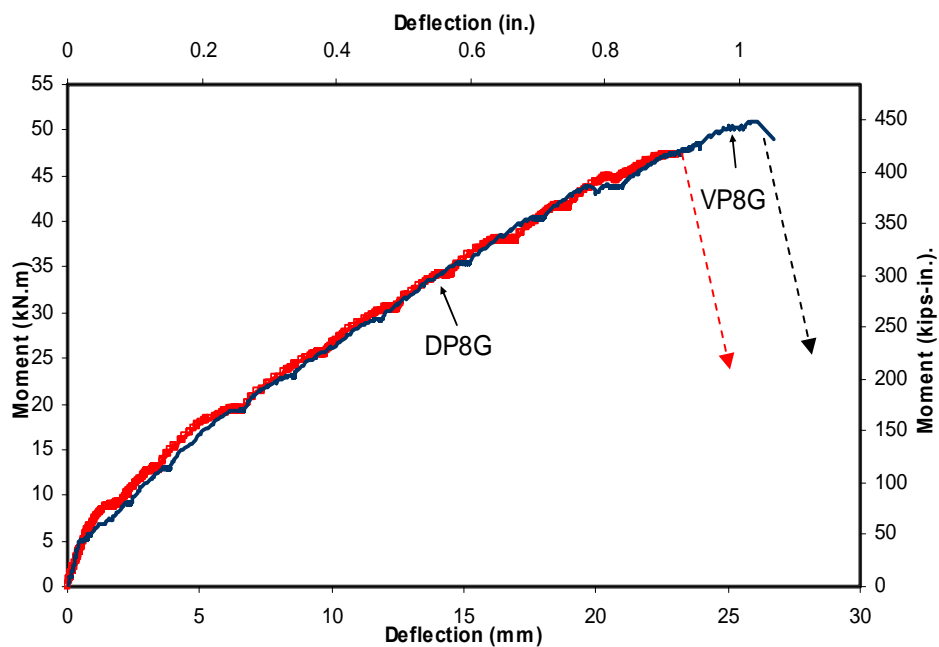
Figure 6.21. Moment-Deflection Relationship for #4 GFRP Plain Concrete Specimens
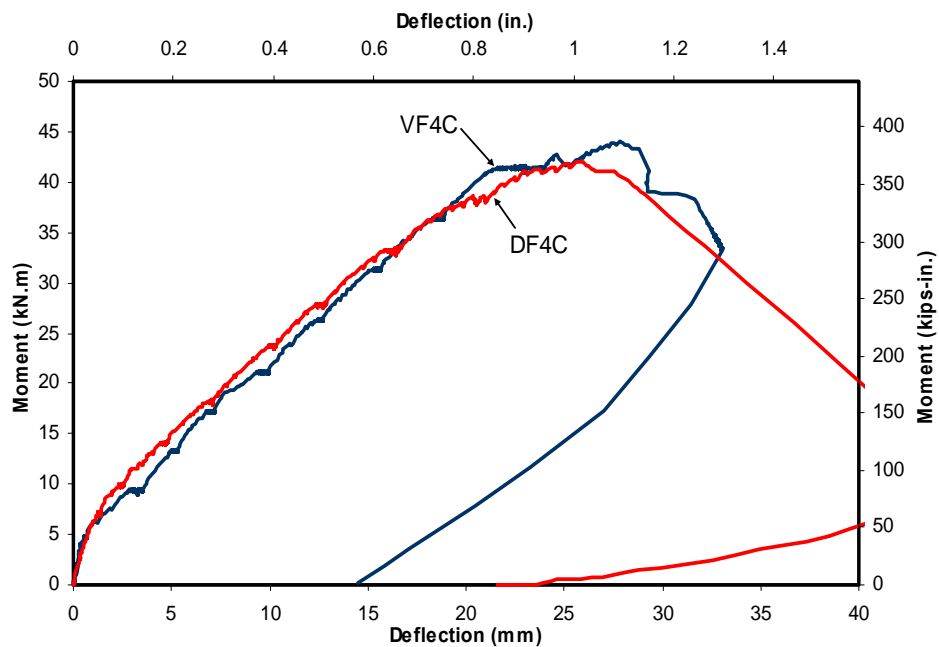
Figure 6.22. Moment-Deflection Relationship for #4 CFRP FRC Specimens
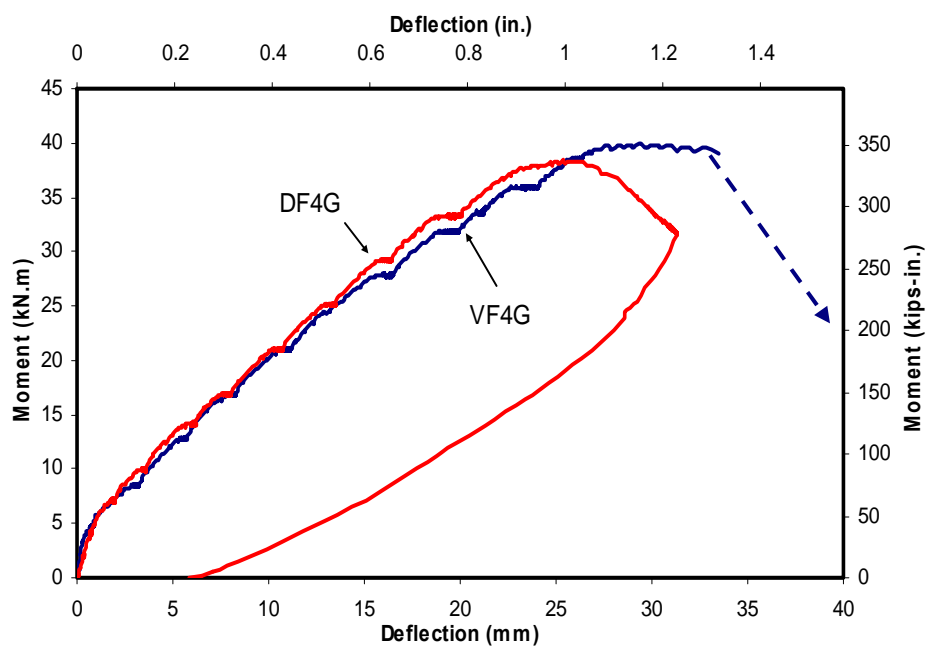
Figure 6.23. Moment-Deflection Relationship for #4 GFRP FRC Specimens
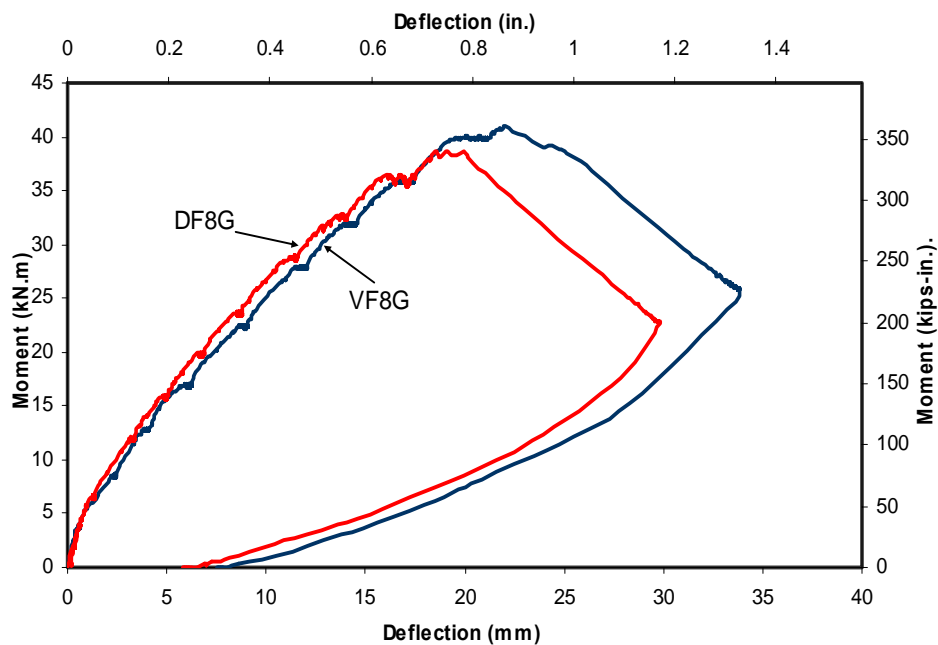
Figure 6.24. Moment-Deflection Relationship for #8 GFRP FRC Specimens

disintegration occurred. Thus, it was indicated that the I_{cr} did not change. The value of I_{cr}

is strongly dependent on the rebar properties, including its elastic modulus and rebar area.

Therefore, it can be concluded that the rebar properties, in the elastic modulus, E_f, and

rebar effective area, A_f, did not significantly change after being subjected to

environmental conditioning. Similar findings were made by Giernacky et al. (2002).

- **Flexural Strength.** Tables 6.3 and 6.4 summarize the flexural strengths and

ultimate deflections for all the plain concrete beams and the FRC beams before and after

the environmental conditioning. Generally, the beams showed insignificant changes in

both the flexural strength and the ultimate deflection. In the flexural strength, reductions

ranged from 4% to 16% for the plain concrete beams and from 4% to 8% for the FRC

beams. In ultimate deflection, reduction ranged from -6% to 17% for the plain concrete

beams and from 3% to 18% for the FRC beams.

Table 6.3. Durability Beam Test Results for Plain Concrete Beams

Specimen I.D.	Ultimate Moment M_V (kips-in.)		Specimen I.D.	Ultimate Moment M_D (kips-in.)		$\dfrac{M_D}{M_V}$
VP4C-1	457	450	DP4C-1	423	420	0.93
VP4C-2	442		DP4C-2	417		
VP4G-1	405	413	DP4G-1	393	397	0.96
VP4G-2	420		DP4G-2	401		
VP8G-1	448	449	DP8G-1	339	378	0.84
VP8G-2	449		DP8G-2	416		
Specimen I.D.	Ultimate Deflection Δ_V (in.)		Specimen I.D.	Ultimate Deflection Δ_D (in.)		$\dfrac{\Delta_D}{\Delta_V}$
VP4C-1	1.19	1.18	DP4C-1	0.84	0.98	0.83
VP4C-2	1.17		DP4C-2	1.12		
VP4G-1	1.03	1.03	DP4G-1	1.14	1.09	1.06
VP4G-2	1.02		DP4G-2	1.04		
VP8G-1	0.96	0.96	DP8G-1	0.83	0.87	0.91
VP8G-2	0.95		DP8G-2	0.91		

Table 6.4. Durability Beam Test Results for FRC Beams

Specimen I.D.	Ultimate Moment M_V (kips-in.)		I.D.	Ultimate Moment M_D (kips-in.)		$\dfrac{M_D}{M_V}$
VF4C-1	415	402	DF4C-1	370	388	0.96
VF4C-2	388		DF4C-2	405		
VF4G-1	350	356	DF4G-1	326	332	0.93
VF4G-2	362		DF4G-2	338		
VF8G-1	371	366	DF8G-1	341	335	0.92
VF8G-2	361		DF8G-2	328		
Specimen I.D.	Ultimate Deflection Δ_V (in.)		I.D.	Ultimate Deflection Δ_D (in.)		$\dfrac{\Delta_D}{\Delta_V}$
VF4C-1	1.20	1.15	DF4C-1	1.01	1.11	0.97
VF4C-2	1.10		DF4C-2	1.21		
VF4G-1	1.19	1.19	DF4G-1	0.98	1.00	0.82
VF4G-2	1.19		DF4G-2	1.01		
VF8G-1	0.95	0.91	DF8G-1	0.78	0.77	0.84
VF8G-2	0.87		DF8G-2	0.76		

According to the current theory, the flexural strength controlled by the concrete crushing is determined by the rebar and the concrete. As discussed previously, the mechanical properties of the rebars were not significantly changed. Thus, the most plausible reason for the reduction of flexural strength was the degradation of concrete. The strains in the concrete at the ultimate were decreased slightly after the environmental conditioning. In the plain concrete beams, the average ultimate concrete strains decreased from 2,950 microstrains to 2,660 microstrains. In the FRC beams, the average ultimate concrete strains decreased from 4,500 microstrains to 3,800 microstrains, as shown in Figures 6.25 to 6.30.

In the previous study, it was found that the flexural strengths predicted by assuming ε_{cu} equal to 0.0035 for the FRC beams have a comparable safety factor as $\varepsilon_{cu} =$ 0.003 for the plain concrete beams. After the concrete beams were subjected to
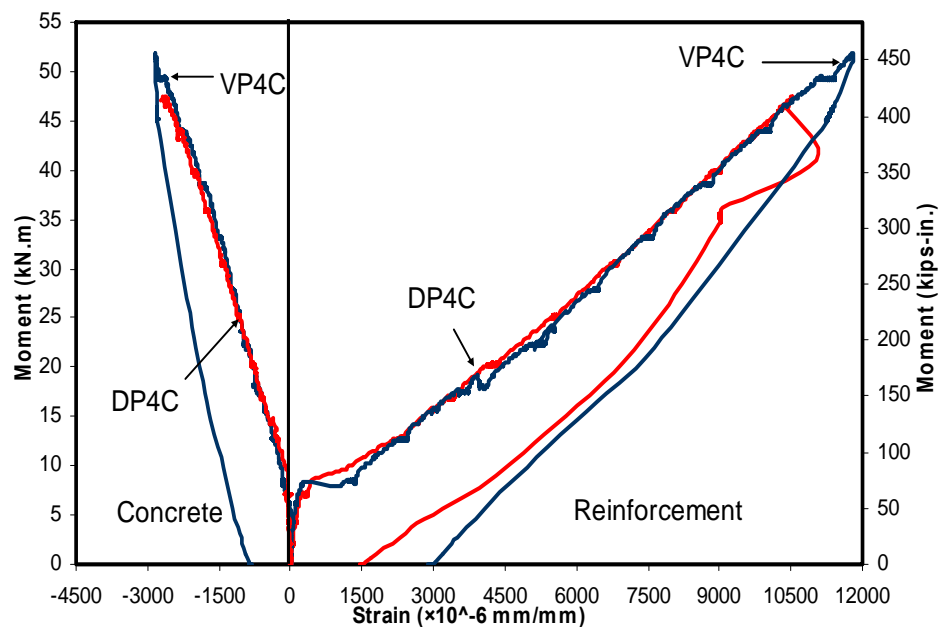
Figure 6.25. Strain Distributions of #4 CFRP Plain Concrete Specimens
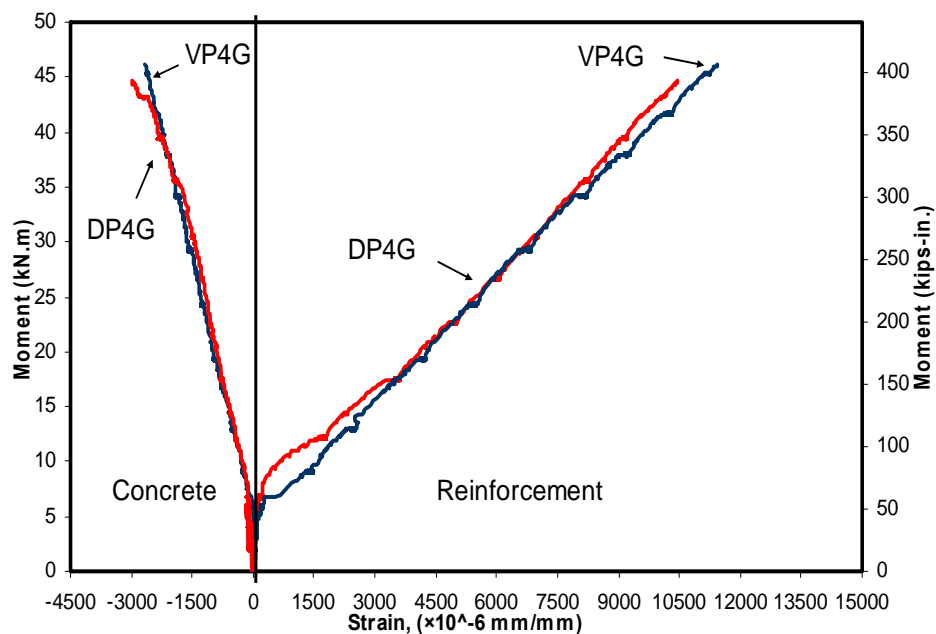
Figure 6.26. Strain Distributions of #4 GFRP Plain Concrete Specimens
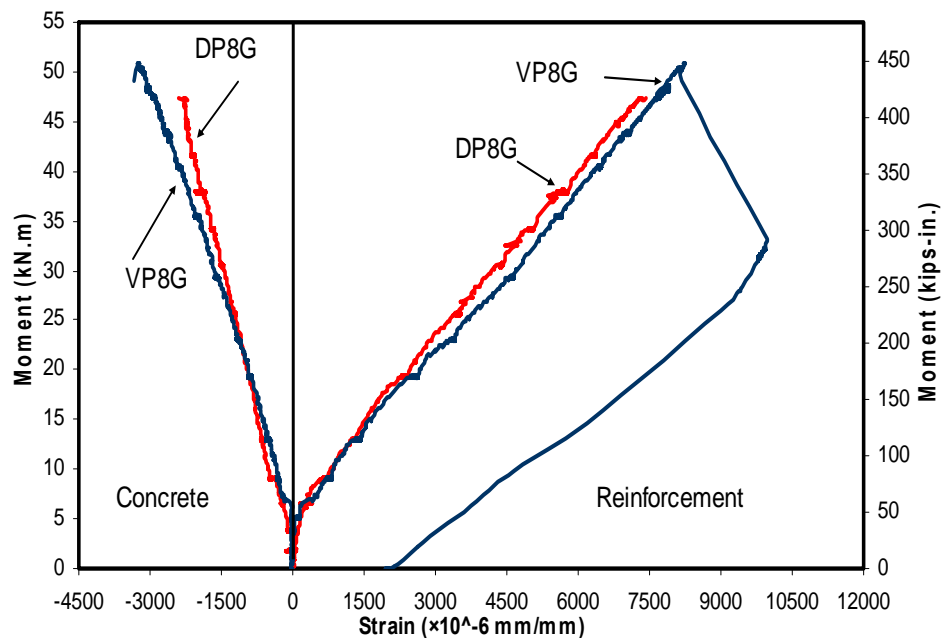
Figure 6.27. Strain Distributions of #8 GFRP Plain Concrete Specimens
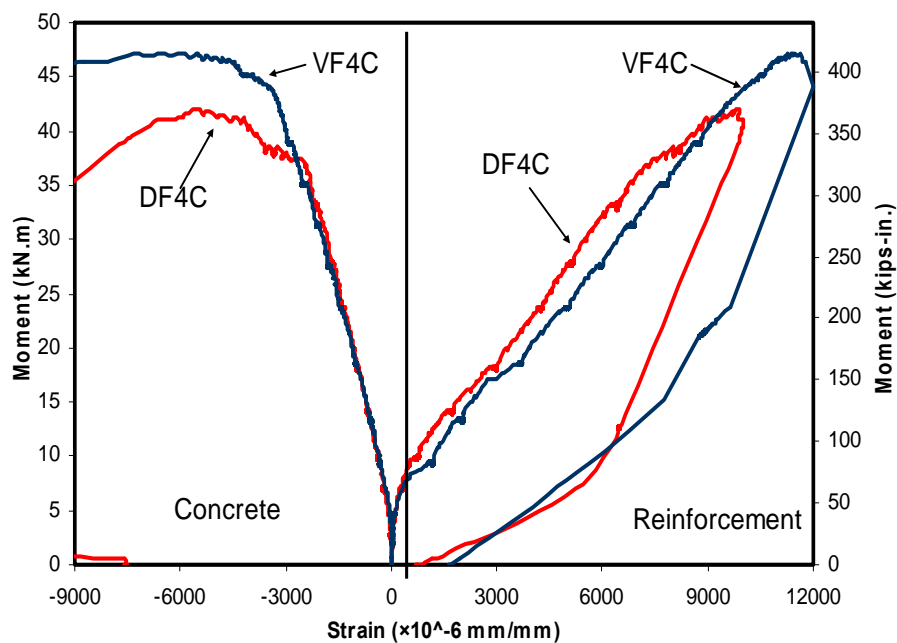
Figure 6.28. Strain Distributions of #4 CFRP FRC Specimens
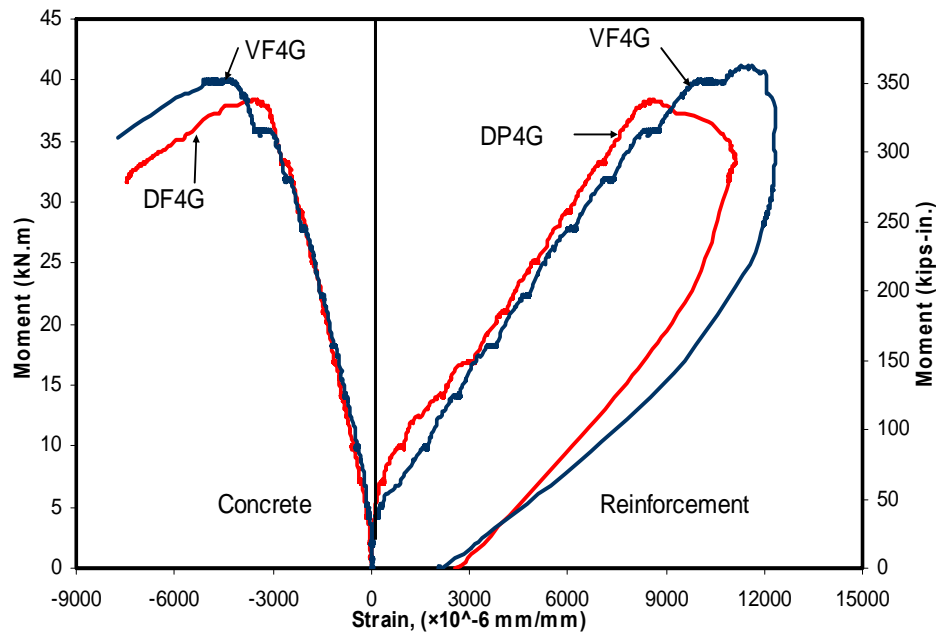
Figure 6.29. Strain Distributions of #4 GFRP FRC Specimens
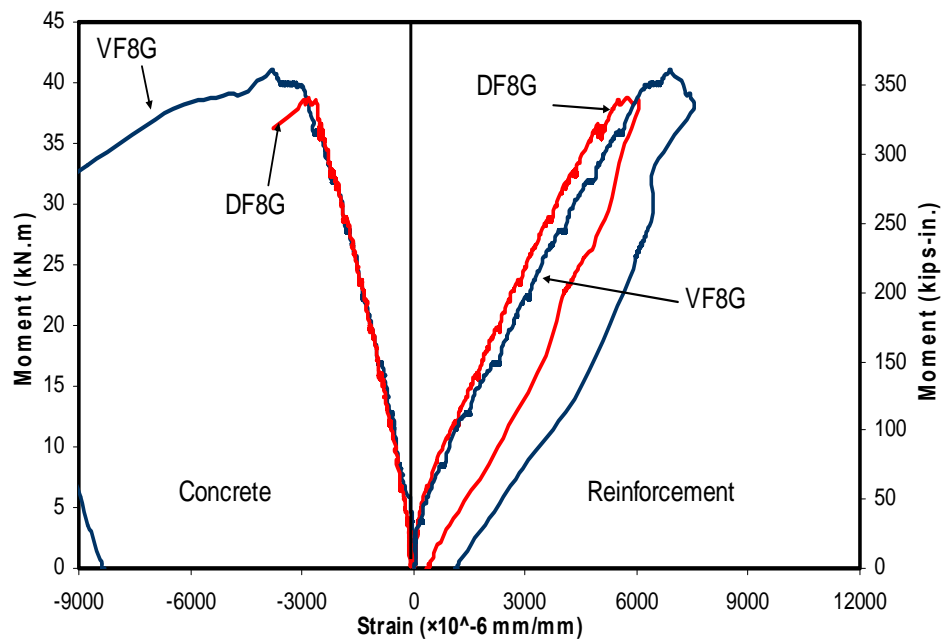
Figure 6.30. Strain Distributions of #8 GFRP FRC Specimens

environmental conditioning, the concrete became more brittle, as shown in Figure 6.31.

To reflect this effect in the design, 0.0025 and 0.003 were selected as the ultimate

concrete strains for the plain concrete beams and FRC beams after the environmental

conditioning. By using the new values of ultimate concrete strains, the beams after

environmental conditioning have a comparable safety factor as the unweathered beams,

as shown in Tables 6.5 and 6.6.
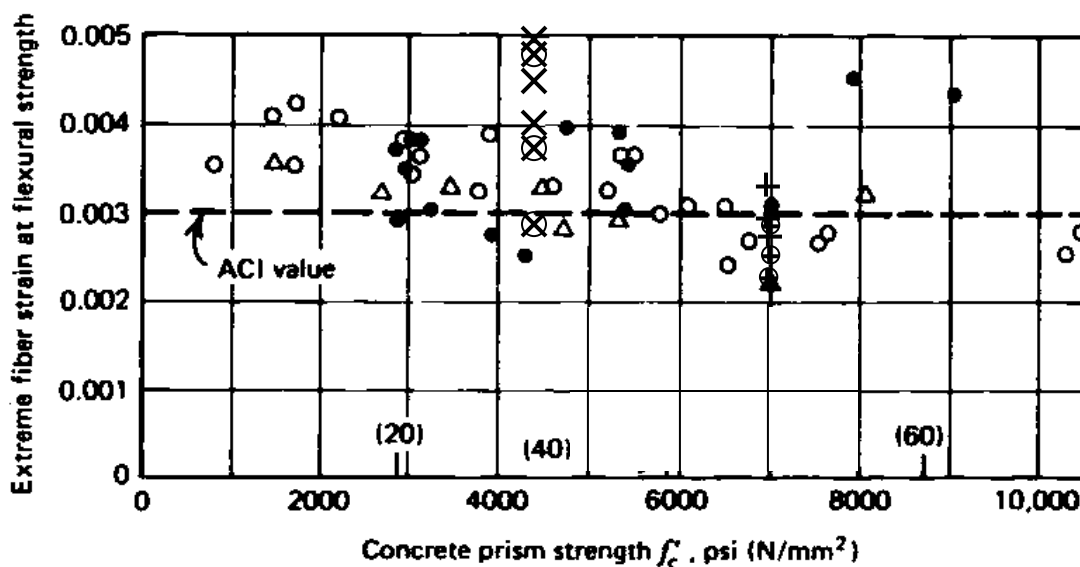
**Figure 6.31. Comparison of Ultimate Strain of Concrete of ACI Value and Test
Results in this Study (Courtesy of Park and Paulay)**
Note: × is the values of FRC measured in this study; + is the values of plain concrete
measured in this study.⊠ is the FRC measured after environmental conditioning;
and ⊕ is the plain concrete measured after environmental conditioning

6.3.2.3. Ductility. Since ductility is an important parameter in the civil structures,

it is of interest to study the effect of the environmental conditioning on the ductility of

beams. As discussed in Chapter 4, Jaeger's deformation based approach seems to be most

Table 6.5. Predictions of Ultimate Capacities for Plain Concrete Beams

I.D.	$M_{exp.}$ (kips-in.)		M_{ACI} (kips-in.)	$\frac{M_{ACI}}{M_{exp.}}$
VP4C-1	457	450	355	0.79
VP4C-2	442			
VP4G-1	405	413	367	0.89
VP4G-2	420			
VP8G-1	448	449	401	0.89
VP8G-2	449			
Average				**0.86**
DP4C-1	423	420	331	0.79
DP4C-2	417			
DP4G-1	393	397	341	0.86
DP4G-2	401			
DP8G-1	339	378	375	0.99
DP8G-2	416			
Average				**0.88**

Note: For the unweathered plain concrete beams, the above calculations were based on ε_{cu} =0.003; for the plain concrete beams after environmental conditioning, the above calculations were based on ε_{cu} =0.0025.

appropriate to evaluate the ductility characteristics for FRP reinforced concrete structures. This approach is adopted in this study.

After being subjected to the environmental conditioning, the ductility indices of the beams showed small reductions, as shown in Table 6.7. The reduction of the ductility index was mainly due to the degradation of concrete, which leaded to the reduction of the ultimate strength and the associated curvature, as shown in Figures 6.32 to 6.37. The reduction rate between the plain concrete beams and the FRC beams was similar. However, after environmental conditioning, the FRC beams still showed superior ductility compared to the plain concrete beams.

Table 6.6. Predictions of Ultimate Capacities for FRC Beams

I.D.	$M_{exp.}$ (kips-in.)		M_{ACI} (kips-in.)	$\dfrac{M_{ACI}}{M_{exp.}}$
VF4C-1	415	402	306	0.76
VF4C-2	388			
VF4G-1	350	356	314	0.88
VF4G-2	362			
VF8G-1	371	366	338	0.92
VF8G-2	361			
Average				0.86
DF4C-1	370	388	290	0.75
DF4C-2	405			
DF4G-1	326	332	298	0.90
DF4G-2	338			
DF8G-1	341	335	322	0.96
DF8G-2	328			
Average				0.87

Note: For the unweathered FRC beams, the above calculations were based on ε_{cu} =0.0035; for the FRC beams after environmental conditioning, the above calculations were based on ε_{cu} =0.003.

Table 6.7. Ductility Index by Deformation Based Method

I.D.	$M_{\varepsilon=0.001}$ (kips-in.)	$\psi_{\varepsilon=0.001}$ (1/in.)	M_{ult} (kips-in.)	ψ_{ult} (1/in.)	μ_E	$\dfrac{\mu_{ED}}{\mu_{EV}}$
VP4C	202	7.82×10^{-4}	450	19.46×10^{-4}	5.50	1
VP4G	177	6.66×10^{-4}	405	17.63×10^{-4}	6.05	1
VP8G	190	4.96×10^{-4}	449	14.73×10^{-4}	7.04	1
VF4C	163	6.15×10^{-4}	402	20.78×10^{-4}	8.35	1
VF4G	153	5.74×10^{-4}	356	22.10×10^{-4}	8.94	1
VF8G	157	4.45×10^{-4}	366	14.40×10^{-4}	7.56	1
DP4C	191	7.09×10^{-4}	420	17.07×10^{-4}	5.29	0.96
DP4G	180	6.53×10^{-4}	397	17.20×10^{-4}	5.80	0.96
DP8G	183	4.47×10^{-4}	378	12.88×10^{-4}	5.95	0.85
DF4C	166	5.44×10^{-4}	388	20.09×10^{-4}	8.62	1.03
DF4G	139	4.62×10^{-4}	332	16.13×10^{-4}	8.33	0.93
DF8G	158	4.14×10^{-4}	335	13.49×10^{-4}	6.89	0.91

Note: μ_{ED} is the ductility index after environmental conditioning;
μ_{EV} is the ductility of the unweathered beams;
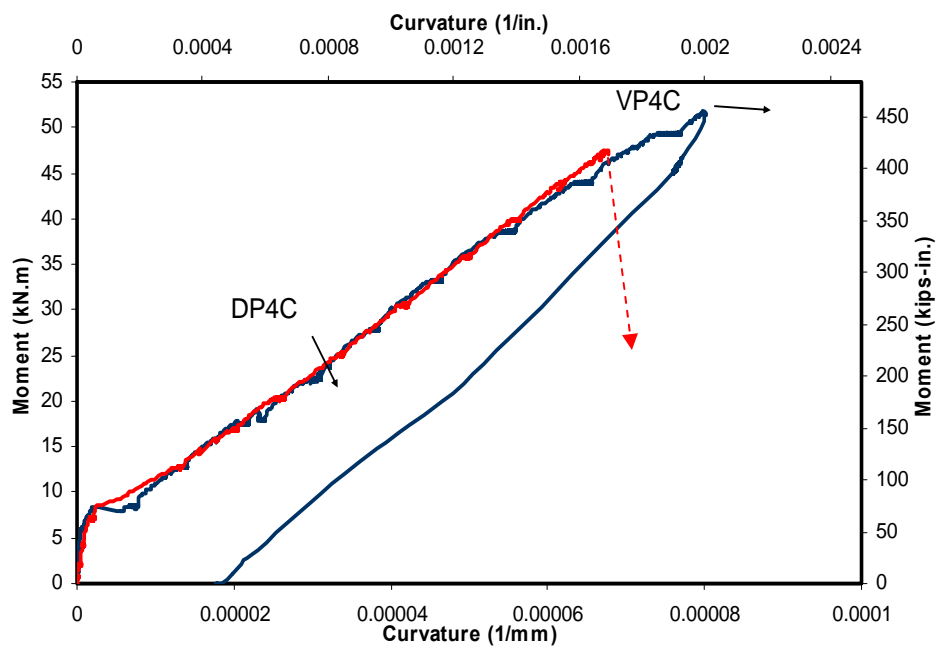
Figure 6.32. Typical Moment Curvature Relationship for #4 CFRP Plain Concrete Beams
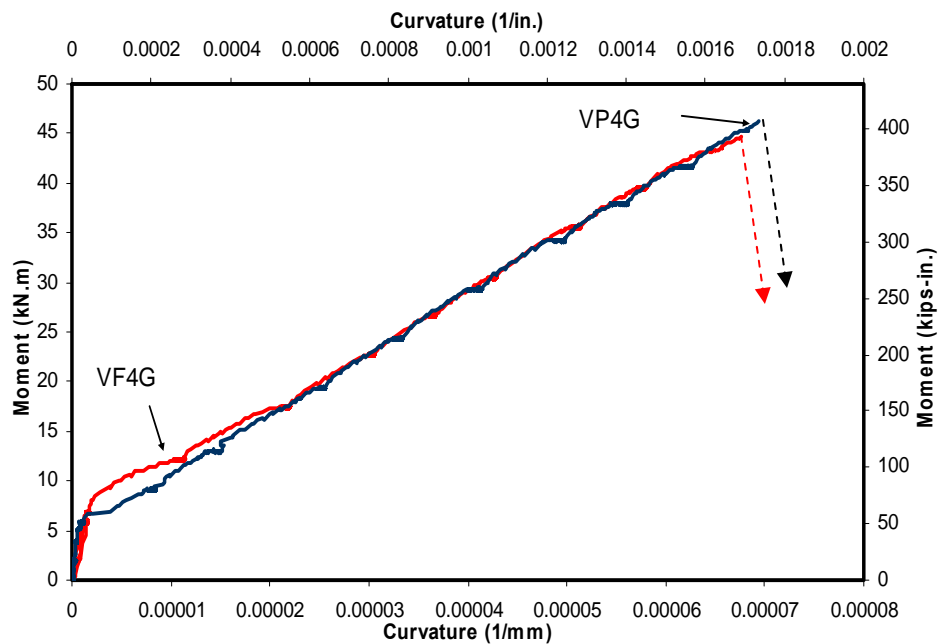
Figure 6.33. Typical Moment Curvature Relationship for #4 GFRP Plain Concrete Beams
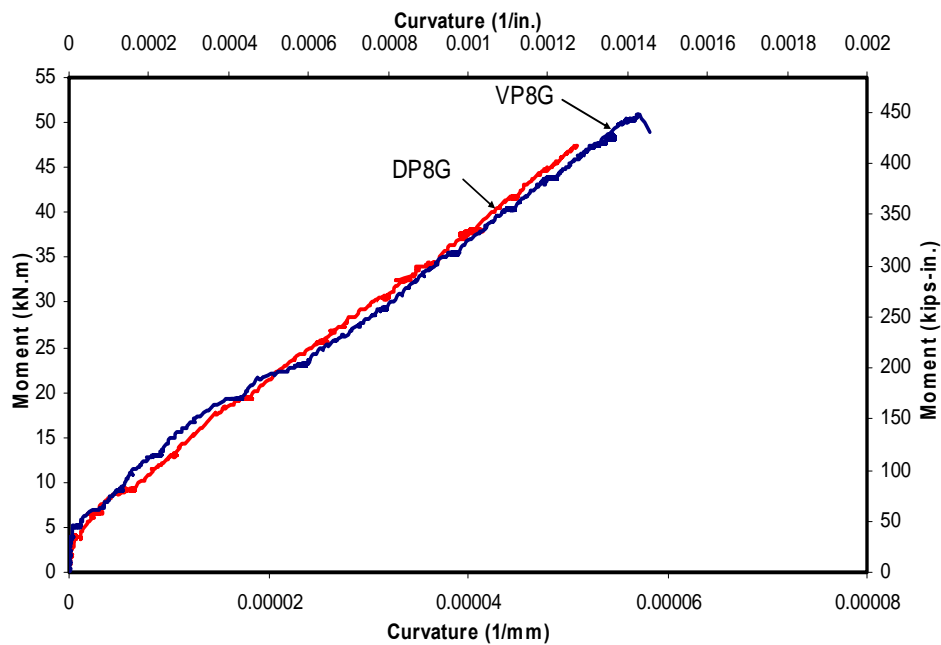
Figure 6.34. Typical Moment Curvature Relationship for #8 GFRP Plain Concrete Beams
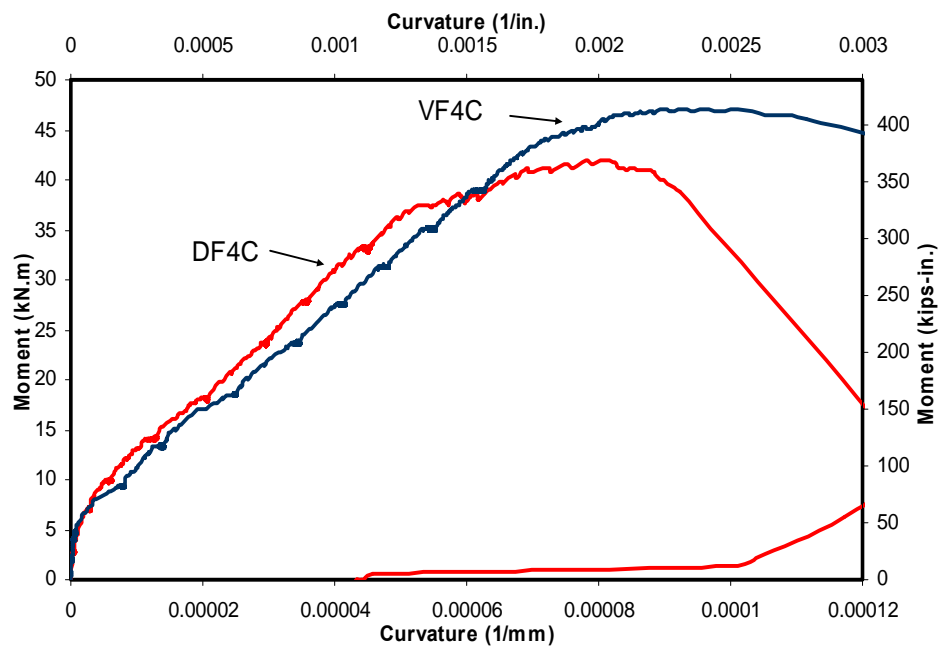
Figure 6.35. Typical Moment Curvature Relationship for #4 CFRP FRC Beams
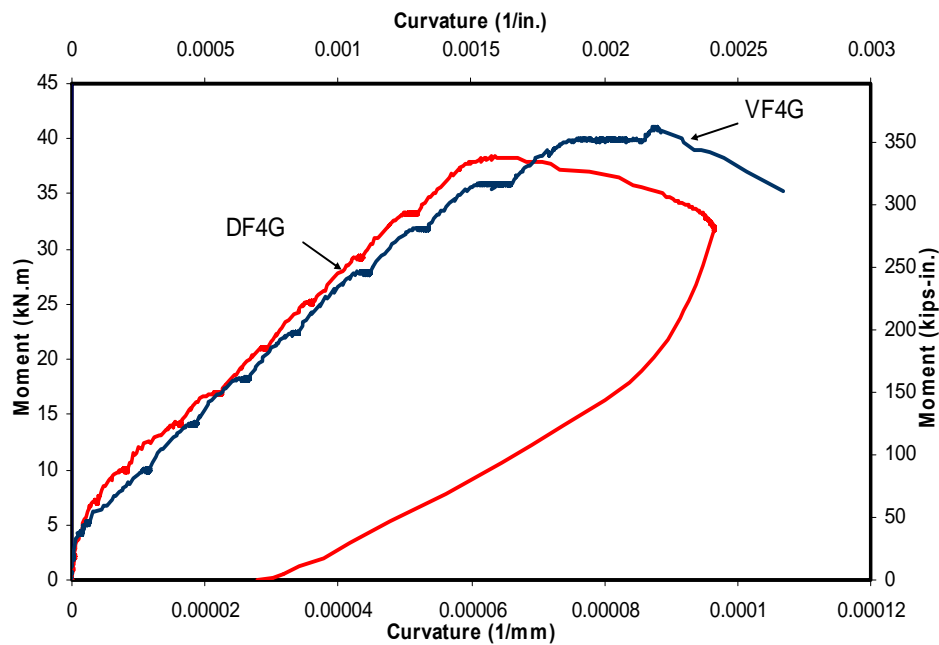
Figure 6.36. Typical Moment Curvature Relationship for #4 GFRP FRC Beams
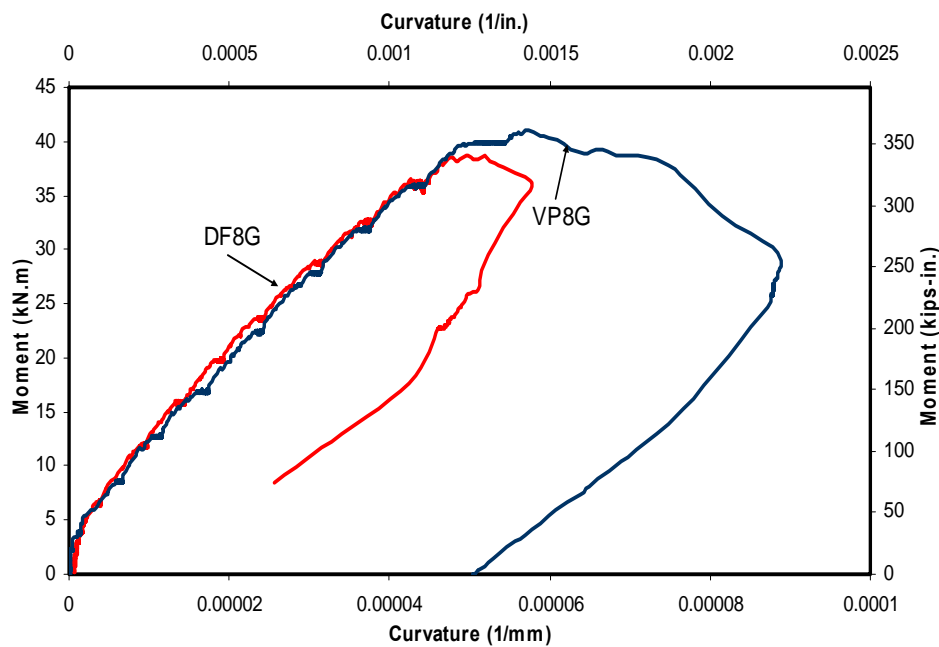
Figure 6.37. Typical Moment Curvature Relationship for #8 GFRP FRC Beams

Based on the criterion proposed by Jaeger et al. (1995) and the Canadian Highway Bridge Design Code, both the plain concrete beams and the FRC beams exceeded the ductility index limit of 4. Therefore all the beams in this study can be considered safe for design in terms of ductility requirement.

6.4. CONCLUDING REMARKS

Durability performances, in terms of bond and flexural behavior, between the FRP rebars and fiber-reinforced-concrete were investigated and compared to the performance of the FRP rebars in the plain concrete. The accelerated aging test was accomplished by placing specimens in contact with salt solutions and subjecting them to 10 combined environmental cycles, each of which consisted of 20 freezing-and-thawing cycles and 20 high temperature cycles. The following conclusions can be drawn from this study:

- Three reasons mainly contributed to the bond degradation: (1) expansion of solutions in the microvoids at the interface; (2) difference in CTE between the rebar and concrete; (3) damage of the rebar, especially on the surface. The first two mechanisms function together and degrade the bond mainly at the interface. The third reason is through damage of the rebar surface, resulting in separation between the rebar and concrete.

- With the addition of polypropylene fibers, the bond of weathered specimens significantly improved due to restriction of the development of cracks at the interface. The loss of the ultimate bond strength of the FRP rebars in the plain concrete due to weathering effects was found to be 28% on average, while only

6% reduction was observed in the FRC specimens. Similarly, bond stiffness exhibited a 26% average reduction in plain concrete specimens, while only 10% reduction was observed in the FRC specimens.

- The larger specimens with longer embedment length and relatively smaller exposed area to the solution of sodium chloride (NaCl) showed better performance.

- Under durability effect, the CFRP specimens exhibited superior bond performance as compared to the GFRP specimens. This may be attributed to the more durable characteristics of the CFRP rebar.

- Both plain concrete beams and FRC beams exhibited a small reduction in ultimate flexural strength and ductility in the durability test. The degradation of concrete was the main reason for the flexural degradation.

- Under environmental conditioning and weathering, all beams included in this study showed similar performance in terms of ductility requirement. Compared to the plain concrete beams, FRC beams showed approximately 40% increase in ductility index based on deformation based approach both before and after the environmental conditioning.

It should be noted that the above conclusions are drawn based on the tests conducted in this study, where bond specimens and beam specimens are unstressed. In the real conditions, the structures are under loading conditions, thus, the above conclusions may not be suitable. Also, different environmental conditionings may have different results, cautions should be used when applying the results into different situation.

7. DESIGN RECOMMENDATIONS

7.1. GENERAL

The design recommendations are based on the current design guidelines for the concrete members reinforced with FRP bars as proposed by ACI 440. Information not covered in this report, such as material properties, construction, shear design, etc., can be found in the ACI 440.3R-04 documents.

The reinforcing system proposed in this report consists of the FRP rebar (GFRP and CFRP) and polypropylene fiber reinforced concrete with a fiber volume fraction V_f of 0.5%. Thus, the design recommendations may not be applicable to other FRP rebar, fiber, or fiber volume fraction, V_f. Also, the design recommendations for the long-term performance of the FRP/FRC system are based on the test results obtained from the environmental conditioning used in this study. They may not be applicable in other situations.

7.2. DESIGN EQUATIONS

Many design theories and equations for the FRP/plain concrete system are still applicable to the FRP/FRC system. In the following sections, only the design equations that are not existent in, or are different from, the ACI 440, including flexural strength, development of reinforcement, and durability of the system are presented as follows:

- **Flexural Strength**

The concrete crushing failure mode is more desirable for the concrete member reinforced with the FRP bars. By experiencing concrete crushing, a flexural member does

exhibit some plastic behavior before failure (ACI 440, 2004), as demonstrated in this study. The same design philosophy is recommended for the FRP/FRC reinforcing system. The following equations can be used to predict the flexural strength:

$$M_n = \rho_f f_f \left(1 - 0.59 \frac{\rho_f f_f}{f_c'}\right) bd^2 \text{ kips-in.} \tag{7.1}$$

$$f_f = \left(\sqrt{\frac{(E_f \varepsilon_{cu})^2}{4} + \frac{0.85 \beta_1 f_c'}{\rho_f} E_f \varepsilon_{cu}} - 0.5 E_f \varepsilon_{cu}\right) \leq f_{fu} \text{ psi} \tag{7.2}$$

$$\rho_{bf} = 0.85 \beta_1 \frac{f_c'}{f_{fu}} \frac{\varepsilon_{cu}}{\varepsilon_{cu} + \varepsilon_{fu}} \tag{7.3}$$

Based on the current testing data, $\varepsilon_{cu} = 0.0035$ is suggested for FRC beams and ε_{cu} = 0.003 for plain concrete beams.

- **Crack Width**

With the addition of fibers, the crack width of the FRC beam is smaller than that of the plain concrete beams at the service stage, but this phenomenon is not pronounced at high load level due to the inadequate bond between the fibers and concrete. Thus, the contribution from fibers is ignored in the prediction of the crack width. Based on the test data, the following equation proposed by Salib and Abdel-Sayed (2004) is recommended for both the plain concrete beam and the FRC beam:

$$w = \left(\frac{2200}{E_f} \times (2/3) \sqrt{\frac{u_{b,s}}{u_{b,f}}}\right) \times \beta f_f \sqrt[3]{d_c A} \text{ in.} \tag{7.4}$$

where $u_{b,s} = 6.25 \sqrt{f_c'}$, and

$u_{b,f}$ is the design bond strength for the FRP rebars; and it is equal to $u_{b,s} = 9.25 \sqrt{f_c'}$ for the FRP rebars used in this study. If the data are unavailable, $u_{b,f}$ can be taken as $u_{b,s}$.

- **Development Length**

The bond behavior in the pre-peak region does not change with the addition of fibers. The contribution from the fibers is in the post-peak region. Since the development length is determined by the bond behavior in the pre-peak region, the same equation is used for both the plain concrete and the FRC. In this study, the bond strength corresponding to 0.002 in. slippage at the free-end or 0.01 in. at the loaded end is recommended as the designing bond strength. A statistical analysis with 95% confidence was performed on the design bond strength, and the following equation in the format of current AASHTO expressions is proposed to calculate the development length:

$$l_{db} = 0.056 \frac{A_f f_{fu}}{\sqrt{f_c'}} \text{ in.} \tag{7.5}$$

- **Durability**

In the current ACI 440 recommendations, the long-term environmental effect on the structural behaviors of the FRP reinforced members is reflected in the environmental reduction factor, C_E. However, the flexural strength of the FRP reinforced member is governed by the property of concrete rather than the property of the FRP rebar when the member fails by the concrete crushing. Furthermore, the environmental reduction factor, C_E, does not reflect the bond degradation due to the long-term weather exposure. Thus, new coefficients are needed to account for the long-term environmental effect on the structural behaviors of the FRP reinforced system.

(a) Long-term flexural strength. The flexural strengths of the FRP reinforced beams experienced reductions due to the environmental conditioning, which was most likely due to the degradation of concrete. By adjusting the ultimate concrete strain, the predictions were in good agreement with the test results. The ultimate concrete strain ε_{cu}

= 0.0030 for the FRC beams and ε_{cu} = 0.0025 for the plain concrete beams are suggested

to account for the more brittle behavior of the concrete after the environmental

conditioning. Again, different environmental conditionings may have different effects on

the ultimate concrete strain. The above values may not be appropriate for the other

conditionings.

(b) Long-term bond strength. Based on the tests of the durability effect on the

bond behavior, the bond degradation effect is closely related to the ratio between the

portions directly exposed to the solution to the whole embedment area. Based on the

ductility test results, the crack spacing was approximately 4 to 5 inches under service

conditions in the beam specimen. The #4 pullout bond specimen had 2.5 inches

embedment length, which was close to half of the crack spacing. Bond stress distribution

along half of the crack spacing in beam specimen is similar to that in pullout bond

specimen, as shown in Figure 3.6. Thus, the degradation rate is expected to be able to

represent the bond degradation in beam. Table 7.1 summarizes the residual design bond

strength for CFRP and GFRP specimens and more details can be found in Chapter 6.3.1.

Table 7.1. Residual Design Bond Strength Based on Experiment

	GFRP	CFRP
Plain Concrete	0.57	0.75
FRC	0.83	0.88

Byars et al. (2003) proposed a reduction coefficient for the bond strength for the

FRP/Plain concrete system as follows:

$$\eta_{env,b} = 1 - \Delta f_{fb,env} \cdot \eta_{mo} \cdot \eta_T \cdot \eta_{SL} \qquad (7.6)$$

where $\Delta f_{fb,env}$ is the standard reduction of bond strength due to environmental influence,

taken as 0.30; and η_{mo}, η_T, and η_{SL}, as proposed by Byars et al., are listed in Tables 7.2

to 7.4.

Table 7.2. Correction Factors for Moisture Condition in Concrete Member, η_{mo}
(Byars, 2003)

Dry (RH app. 50%)	Moist (Concrete not constantly in contact with water, RH app. 80%)	Moist saturated (Concrete constantly in contact with water, RH app. 100%)
0.65	1.0	1.5

Table 7.3. Correction Factors for Mean Annual Temperature, η_T
(Byars, 2003)

MAT <41^{0}F	41^{0}C< MAT <59^{0}F	59^{0}F< MAT <77^{0}F
0.85	1.0	1.15

Table 7.4. Correction Factors for Required Service Life, η_{SL}
(Byars, 2003)

Service life =50 years	Service life =100 years
0.85	1.0

The test data from this durability bond test are used to calibrate the Byars' model.

In the durability bond test, specimens were submerged into a solution. Thus, η_{mo}=1.5.

Average temperature was approximately 50^0F. Thus, $\eta_T = 1.0$. η_{SL} is taken as 1.0 to represent the 100 service life. Thus,

$$\eta_{env,b} = 1 - \Delta f_{fb,env} \cdot \eta_{mo} \cdot \eta_T \cdot \eta_{SL} = 1 - 0.3 \times 1.5 \times 1.0 \times 1.0 = 0.55 \qquad (7.7)$$

The Byars' model was developed to predict the FRP/Plain concrete system. The value 0.55, as predicted Equation 7.7, is very close to the test result for the GFRP/plain concrete specimens, which is equal to 0.57. However, the Byars' model does not consider the effect of the different rebar types on the bond degradation. As shown in the experiment, different rebars had different effects on the bond degradation. Also, the contribution of the fibers to the bond degradation was not reflected in Byars' model. Following the same methodology proposed by Byars, some modifications are suggested:

$$\eta_{env,b} = 1 - \Delta f_{fb,env} \cdot \eta_{mo} \cdot \eta_T \cdot \eta_{SL} \cdot \eta_{bar} \qquad (7.8)$$

where the correction factors η_T and η_{SL} are the same as the Byars' model. Other factors are listed in Table 7.5 and Table 7.6.

Table 7.5. Correction Factors for Standard Reduction of Bond Strength, $\Delta f_{fb,env}$

Plain Concrete	FRC
0.3	0.15

Table 7.6. Correction Factors for Rebar Type, η_{bar}

GFRP	CFRP
1.0	0.70

According to Equation 7.8, the reduction coefficients for GFRP and CFRP embedded in plain concrete and FRC are computed as the followings:

GFRP in Plain concrete:

$$\eta_{env,b} = 1 - \Delta f_{fb,env} \cdot \eta_{mo} \cdot \eta_T \cdot \eta_{SL} \cdot \eta_{bar} = 1 - 0.3 \times 1.5 \times 1.0 \times 1.0 = 0.55$$

CFRP in Plain concrete:

$$\eta_{env,b} = 1 - \Delta f_{fb,env} \cdot \eta_{mo} \cdot \eta_T \cdot \eta_{SL} \cdot \eta_{bar} = 1 - 0.3 \times 1.5 \times 1.0 \times 0.7 = 0.69$$

GFRP in FRC:

$$\eta_{env,b} = 1 - \Delta f_{fb,env} \cdot \eta_{mo} \cdot \eta_T \cdot \eta_{SL} \cdot \eta_{bar} = 1 - 0.15 \times 1.5 \times 1.0 \times 1.0 = 0.78$$

CFRP in FRC:

$$\eta_{env,b} = 1 - \Delta f_{fb,env} \cdot \eta_{mo} \cdot \eta_T \cdot \eta_{SL} \cdot \eta_{bar} = 1 - 0.15 \times 1.5 \times 1.0 \times 0.7 = 0.84$$

As shown in Table 7.7, the degradation rates computed by Equation 7.8 are very close and are conservative compared to the test data. Since the bond degradation rate will be affected by different environmental conditionings, Cautions should be used when the environmental conditionings are different with that used in this study.

Table 7.7. Comparison of Test Results and Predictions

	GFRP			CFRP		
	Experiment	Prediction	$\frac{Prediction}{Experiment}$	Experiment	Prediction	$\frac{Prediction}{Experiment}$
Plain Concrete	0.57	0.55	0.96	0.75	0.69	0.92
FRC	0.84	0.78	0.93	0.88	0.84	0.95

The degradation of the bond results in the necessity to modify the development length. Thus, Equation 7.5 becomes

$$l_{db} = 0.056 \frac{A_f f_{fu}}{\eta_{env,b} \sqrt{f_c'}} \quad \text{in.} \tag{7.9}$$

where $\eta_{env,b}$ is the reduction coefficient of bond strength due to the long-term environmental conditioning.

8. CONCLUSIONS

Through this research program on the structural performances of the "steel-free FRP/FRC hybrid reinforcing system," a greater understanding of the bond characteristics, flexural behavior, and durability performance has been achieved.

8.1. BOND TESTS. Based on the bond study, including pullout bond tests and splitting bond tests, the following conclusions can be made:

- With the addition of fibers, the bond-slip relationship significantly improved in the post-peak region, while little change was observed for the pre-peak behavior. The FRC specimens failed in a more ductile fashion with a smooth descending portion. A large portion of the load could be held, even at large slip. The plain concrete specimens failed in a very brittle fashion. Once it reached the peak value, the load dropped suddenly to zero.

- Different bond mechanisms were observed for the CFRP and the GFRP specimens due to their different surface treatments. Bond strength of the GFRP specimen was about twice as much as that of the CFRP. The GFRP specimen failed by concrete splitting; while the bond failure of the CFRP specimen initiated by the rebar pullout, providing more ductile behavior;

- Fatigue loading, within a working stress range, was shown to increase the bond stiffness and the bond strength, while causing the bond behavior to be more brittle and often change the failure mode from rebar pullout to concrete splitting.

- The large amount of slip between the rebar and concrete has occurred during the fatigue loading. Therefore, the total slip, including the residual slip due to fatigue

loading, could be regarded as an inherent property for bond behavior between the rebar and the concrete, and it has little relationship with the loading history.

- Polypropylene fibers can effectively decrease the rate of bond degradation due to the fatigue loading.

- Based on analytical derivation and experimental calibration, an equation was proposed to predict the bond strength for the FRP bars embedded in FRC failed by concrete splitting.

- Bond value corresponding to 0.002 in. at the free-end slip or 0.01 in. at the loaded end was recommended as the designing bond strength in previous studies (Mathey and Watstein, 1961). Based on this criteria, an equation for the basic development length of the FRP rebar in the FRC was proposed.

8.2. FLEXURAL BEAM TESTS. Based on the flexural ductility study, the following conclusions can be made:

- The deflection predicted by the current ACI 440 guidelines yield results consistent with experimental results, especially at the service load stage, and could be used for both the plain concrete beams and the FRC beams.

- The model proposed by Salib et al. (2004) yields reasonable predictions of the crack width for both the plain concrete beams and the FRC beams. The predictions by the ACI 440 were found to be conservative.

- The addition of fibers reduced the crack widths at the service load in the case of FRC beams as compared to plain concrete beams.

- The compression concrete strain measured at the compression fiber of the FRC beams was larger than that of the plain concrete beams. It ranged from 4,000

microstrains to 5,500 microstrains, with an average of 4,500 microstrains for the FRC beams, while concrete strains, ranging from 2,700 microstrains to 3,300 microstrains, with an average of 2,950 microstrains, were measured for the plain concrete beams.

- With the addition of polypropylene fibers, the ductility indices increased by approximately 40% based on deformation based approach, which takes into account the strength effect as well as the deflection (or curvature) effect on determining the ductility. In addition, both plain concrete beams and FRC beams provided an adequate deformability level, as described by Jaeger. Moreover, FRC made it slightly more ductile, based on the new definition of ductility for the FRP reinforced beam.

8.3. DURABILITY TESTS. Based on the accelerated durability study, and investigating the bond and flexural test of weathered specimens, the following conclusions can be drawn:

- Three reasons mainly contributed to the bond degradation: (1) expansion of solutions in the microvoids at the interface; (2) difference in CTE between the rebar and concrete; (3) damage of the rebar, especially on the surface. The first two mechanisms function together and degrade the bond mainly at the interface. The third reason is through damage of the rebar surface, resulting in separation between the rebar and concrete.

- With the addition of polypropylene fibers, the bond of weathered specimens significantly improved due to restriction of the development of cracks at the interface. The loss of the ultimate bond strength of the FRP rebars in the plain

concrete due to weathering effects was found to be 28% on average, while only 6% reduction was observed in the FRC specimens. Similarly, bond stiffness exhibited a 26% average reduction in plain concrete specimens, while only 10% reduction was observed in the FRC specimens.

- The larger specimens with longer embedment length and relatively smaller exposed area to the solution of sodium chloride (NaCl) showed better performance.

- Under durability effect, the CFRP specimens exhibited superior bond performance as compared to the GFRP specimens. This may be attributed to the more durable characteristics of the CFRP rebar.

- Both plain concrete beams and FRC beams exhibited a small reduction in ultimate flexural strength and ductility in the durability test. The degradation of concrete was the main reason for the flexural degradation.

- Under environmental conditioning and weathering, all beams included in this study showed similar performance in terms of ductility requirement. Compared to the plain concrete beams, FRC beams showed approximately 40% increase in ductility index based on deformation based approach both before and after the environmental conditioning.

BIBLIOGRAPHY

AASHTO LRFD Bridge Design Specifications, American Association of State Highway and Transportation Officials, Washington, D.C., 1998, pp. 5-138.

ACI Committee 201, "*Guide to Durable Concrete,*" ACI 201.2R-92, American Concrete Institute, Farmington Hills, Michigan, 1992, 39 pp.

ACI Committee 318. *"Building Code Requirements for Structural Concrete (318-02) and Commentary (318R-02),"* American Concrete Institute, Farmington Hills, Michigan., 2002, 443 pp.

ACI Committee 408, "*State–of–the–Art Report on Bond under Cyclic Loads,*" ACI 408.2R-92 (Reapproved 1999), American Concrete Institute, Farmington Hills, Michigan, 1999, 32 pp.

ACI Committee 440, "*Guide for the Design and Construction of Concrete Reinforced with FRP Bars,*" ACI 440.3R-04, American Concrete Institute, Farmington Hills, Michigan, 2004, 40 pp.

ACI Committee 544, "*State–of–the–Art Report on Fiber Reinforced Concrete,*" ACI 544.1R-96, American Concrete Institute, Farmington Hills, Michigan, 1996, 66 pp.

Admi, M.R., Rahman, A.H. and Benmokrane, B., "New Method for Testing Fiber-Reinforced Polymer Rods under Fatigue," *Journal of Composites for Construction*, Vol. 4, No.4, November 2000, pp. 206-213.

Al-Dulaijan S.U., Al-Zahrani, M., Nanni, A., Bakis, C., and Boothby, E., "Effect of Environmental Pre-Conditioning on Bond of FRP Reinforcement to Concrete," *Journal of Reinforced Plastics and Composites*, Vol. 20, No.10, pp. 881-900.

Alsayed, S.H., and Alhozaimy, A.M., "Ductility of Concrete Beams Reinforced with FRP Bars and Steel Fibers," *Journal of Composite Materials*, Vol. 33, No. 19, 1999, pp. 1792-1806.

ASTM C 666-03, "Standard Test Method for Resistance of Concrete to Rapid Freezing and Thawing in Water," *Annual Book of Standards,* American Society for Testing and Materials, West Conshohocken, Pennsylvania, 2003.

ASTM A-944-99, "Standard Test Method for Comparing Bond Strength of Steel Reinforcing Bars to Concrete Using Beam-End Specimens," *Annual Book of Standards*, American Society for Testing and Materials, West Conshohocken, Pennsylvania, 1999.

ASTM C 1543-02, "Standard Test Method for Determining the Penetration of Chloride Ion into Concrete by Ponding," *Annual Book of Standards*, American Society for Testing and Materials, West Conshohocken, Pennsylvania, 2002.

Bakht, B., and Mufti, A., "FRC Deck Slabs without Tensile Reinforcement," *Concrete International*, Vol.18, No.2, February 1996, pp. 50-55.

Bakht, B., and Mufti, A., "Five Steel Bridge Deck Slabs in Canada," *Structural Engineering International*, Vol. 8, No.3, 1998, pp. 196-200.

Bakis, C.E., AL-Dulaijan, S.U., Nanni, A., Boothby, T.E., and Al-Zahrani, M.M., "Effect of Cyclic Loading on Bond Behavior of GFRP Rods Embedded in Concrete Beams," *Journal of Composites Technology & Research*, JCTRER, Vol. 20, No. 1, January 1998, pp. 29-37.

Balazs, G.L., and Borosnyoi, A., "Long-term behavior of FRP," *Composites in construction: a reality, Proceedings of the International Workshop*, July 20-21 2001 Capri, (Italy) by Edoardo Cosenza, Gaetano Manfredi, and Antonio Nanni.

Bank, L.C., and Gentry, T.R., "Accelerated Test Methods to Determine the Long-Term Behavior of FRP Composite Structures: Environmental Effects," *Journal of Reinforced Plastics and Composites*, Vol. 14, June 1995, pp. 559-587.

Bank, L.C., Puterman, M., and Katz, A., "The Effect of Material Degradation on Bond Properties of Fiber Reinforced Plastic Reinforcing Bars in Concrete," *ACI Materials Journal*, Vol. 95, No. 3, May-June 1998, pp. 232-243.

Barker, R.M., and Puckett, J.A., *Design of Highway Bridges*, A Wiley-Interscience Publication, 1997

Batchelor, B. deV., and Kwun, M., "Shear in RC Beams without Web Reinforcement," *Journal of the Structural Division,* ASCE*,* Vol. 107, No. 5, May 1981, pp. 907-921.

Belarbi, A., Chandrashekhara, C., and Watkins, S.E., "Performance Evaluation of Fiber Reinforced Polymer Reinforcing Bar Featuring Ductility and Health Monitoring Capability," *Fourth International Symposium on Fiber Reinforced Polymer for Reinforced Concrete Structures,* SP-188, American Concrete Institute, Farmington Hills, Michigan, 1999, pp. 1-12.

Belarbi, A., and Wang, H., "Bond-Slip Response of FRP Reinforcing Bars in Fiber Reinforced Concrete under Direct Pullout," *Proc. of ICFRC--International Conference on Fiber Composites, High Performance Concretes, and Smart Materials,* January 8-10, 2004, Chennai, India pp. 409-419, Ed. By V. S. Parameswaran

Belarbi, A., and Wang, H**.,** "Bond Splitting Behavior of FRP Reinforcing Bars Embedded in Fiber Reinforced Concrete," *Proceeding for the 84th Transportation Research Board Annual Meeting,* 2005, Washington D.C.

Benmokrane, B., Tighiouart, B., and Chaallal, O., "Bond Strength And Load Distribution of Composite GFRP Reinforcing Bars in Concrete," *ACI Materials Journal.* Vol. 93, No. 3, May-June 1996, pp. 246-253.

Berg, A.C., Bank, L.C., Oliva, M.G., and Russell, J.S., "Construction of FRP Reinforced Bridge Deck on US Highway 151 in Wisconsin," *Proceeding for the 84th Transportation Research Board Annual Meeting,* 2004, Washington D.C.

Bradberry, T.E., "Concrete Bridge Decks Reinforced with Fiber-Reinforced Polymer Bars," *Transportation Research Record 1770*, 2001, pp. 97-104.

Bresler, B., *Reinforced Concrete Engineering,* John Wiley & Son, 1974.

Byars, E.A., Waldron, P., Dejke, V., Demis, S., and Heddadin, S., "Durability of FRP in Concrete--Current Specifications and a New Approach," *International Journal of Materials and Product Technology,* Vol. 19, No. 1-2, 2003, pp. 40-52.

Cairns, J., and Abdullah, R., "An Evaluation of Bond Pullout Tests and Their Relevance to Structural Performance," *Structural Engineer,* Vol. 73, No. 11, June 1995, pp. 179-185.

Cairns, J., and Plizzari, G., "Towards a Harmonized European Bond Test," *Materials and Structures*, Vol. 36, October 2003, pp. 498-506.

Campbell, T. I., Chitnuyanondh, L., and Batchelor B. deV., " Rigid-Plastic Theory V. Truss Analogy Method for Calculating the Shear Strength of Reinforced Concrete Beams," *Magazine of Concrete Research.* Vol. 32, No. 110, March 1980, pp. 39-44.

CAN/CSA-S6-00, 2000, "Canadian Highway Bridge Design Code," Canadian Standard Association, Rexdale, Ontario, Canada, 190 pp.

Carrasquillo, R.L., Nilson, A.H., and Slate, F.O., "Properties of High Strength Concrete Subject to Short-Term Loads," *ACI Journal*, Vol. 78, No. 3, May-June 1981, pp. 171-178.

CEB-FIP, *Model Code for Concrete Structures: CEB-FIP International Recommendations,* 3rd ed., Comité Euro-International du Béton, Paris, 1978, 348 pp.

Chaallal, O., and Benmokrane, B., "Pullout and Bond Glass-Fiber Rods Embedded in Concrete And Cement Grout," *Materials & Structures.* Vol. 26, No. 157, April 1993, pp. 167-175.

Chen, Wai-Fah and Duan, Lian, *Bridge Engineering Handbook*, CRC Press, 1999

Chinn, J., Ferguson, P.M., and Thompson, J.N., "Lapped splices in reinforced concrete beams," ACI *Journal*, Vol. 52, No.10, 1955, pp. 201-213.

Choi, O.C., and Lee, W.S., "Interfacial Bond Analysis of Deformed Bars to Concrete," *ACI Structural Journal*, Vol.99 No.6, November-December 2002, pp. 750-756.

Clark, C.R., and Johnston, D.W., "Early Loading Effects on Bond Strength," ACI Journal, Vol. 80, No. 6, November-December 1983, pp. 532-539.

Collins, M.P., and Mitchell, D., *Prestressed Concrete Structures,* Prentice-Hall, Inc., 1991, 753 pp.

Cosenza, E., Manfredi, G., and Realfonzo, R. "Behavior and Modeling of Bond of FRP Rebars to Concrete," *Journal of Composites for Construction*, Vol. 1, No.2, May 1997, pp. 40-51.

Demers, C.E., "Tension-Tension Axial Fatigue of E-Glass Fiber-Reinforced Polymeric Composites: Fatigue Life Diagram," *Construction and Building Materials*, Vol. 12, No.1, 1998, pp. 303-310.

Demers, C.E., "Fatigue Strength Degradation of E-Glass FRP Composites and Carbon FRP Composites," *Construction and Building Materials*, Vol. 12, No. 5, July 1998, pp. 311-318.

Ehsani, M.R., Saadatmanesh, H., and Tao, S. "Bond Behavior of Deformed GFRP Rebars," *Journal of Composite Materials*, Vol. 31, No. 14, 1997, pp. 1413-1430.

El-Salakawy, E. and Benmokrane, A., "Serviceability of Concrete Bridge Deck Slabs Reinforced with Fiber-Reinforced Polymer Composite Bars," *ACI Structural Journal*, Vol. 101, No. 5, September-October 2004, pp. 727-736.

Federal Highway Administration, "Deficient Bridges by State and Highway System," http://www.fhwa.dot.gov/bridge/deficient.htm, Accessed in February 2005

Federal Highway Administration, "Innovative Bridge Research and Construction (IBRC) Program," http://ibrc.fhwa.dot.gov, Accessed in February 2005.

Ferguson, P. M., Breen, J.E., and Thompson, J.N., "Pullout Tests on High Strength Reinforcing Bars," *ACI Journal*, Vol. 62, No. 8, August 1965, pp. 933-950.

Ferguson, P. M., and Thompson, J. N., "Development Length of High Strength Reinforcing Bars in Bond," *ACI Journal,* Vol. 59, No. 1, January 1962, pp. 887-922.

Gao, D., Benmokrane, B., and Masmoudi, R., "A Calculating Method of Flexural Properties of FRP-Reinforced Concrete Beam: Part 1: Crack Width and Deflection," *Technical Report*, Department of Civil Engineering, University of Sherbrooke, Sherbrooke, Quebec, Canada, 24 pp.

Gergely, P., and Lutz, L.A., "Maximum Crack Width in Reinforced Concrete Flexural Members," *Causes, Mechanism, and Control of Cracking in Concrete*, SP-20, American Concrete Institute, Farmington Hills, Michigan, 1999, pp. 87-117.

Giernacky, R.G., Bakis, C.E., Mostoller, J.D., Boothby, T.E., and Mukherjee, A., "Evaluation of Concrete Beams Reinforced With Internal GFRP Bars: A Long-Term Durability Study," *Second International Conference on Durability of Fiber Reinforced Polymer (FRP) Composites for Construction*, Ed. Benmokrane, B., and El-Salakawy, E., 2002, Canada, pp. 39-50.

Gopalararatnam, V.S., and Meyer, J.W., "Fatigue Response of Flexural Bond in FRP Reinforced Concrete," *Proceeding of ICFRC International Conference*, 8-10 January 2004, Chennai, India, pp. 363-373.

Goto, Y, "Cracks Formed in Concrete Around Deformed Tension Bars," *Journal of the American Concrete Institute*, Vol. 68, No. 4, April 1971, pp. 244-251.

Gupta, S.D., *Bridge Manual*, Missouri Department of Transportation, 12/19/2001.

Gylltoft, K., Cederwall, K., Elfgren, L., and Nilsson., L., "Bond Failure in Reinforcement Concrete Under Monotonic and Cyclic Loading: A Fracture Mechanics Approach," *Fatigue of Concrete Structures, SP-75,* American Concrete Institute, Detroit, 1982, pp. 269-287.

Hamad, B.S., "Comparative Bond Strength of Coated and Uncoated Bars with Different Rib Geometries," *ACI Material Journal,* Vol. 92, No. 6, November-December 1995, pp. 579-591.

Harris, H.G., Somboonsong, W., and Ko, F. K., "New Ductile Hybrid FRP Reinforcing Bar for Concrete Structures," *Journal of Composites for Construction*, Vol. 2, No. 1, February 1998, pp. 28-37.

Laboubi, K., El-Salakawy, E., Pigron, M., and Benmokrane, B., "Behavior of Concrete Beams Reinforced With GFRP under Sustained Load and Freeze/Thaw Cycles," *Second International Conference on Durability of Fiber Reinforced Polymer (FRP) Composites for Construction*, Ed. Benmokrane, B., and El-Salakawy, E., 2002, Canada, pp. 453-464.

Jaeger, G.L., Tadros, G., and Mufti, A.A., "Balanced Section, Ductility and Deformability in Concrete with FRP Reinforcement," *Research Report* No. 2-1995, Industry Center for Computer-Aided Engineering, Technical University of Nova Scotia, Halifax, Nova Scotia, Canada, 1995, 29 pp.

Katz, A., "Bond to Concrete of FRP Rebars after Cyclic Loading," *Journal of Composites for Construction*, Vol. 4, No. 3, August 2000, pp. 137-144.

Katz, A., "Bond Mechanism of FRP Rebars to Concrete," *Materials and Structures,* Vol. 32, December 1999, pp. 761-768.

Katz, A., Berman, N., and Bank, L., "Effect of high temperature on bond strength of FRP rebars," *Journal of Composites for Construction*, Vol. 3, No. 2, May 1999, pp. 73-81.

Keesler, R.J., and Power, R.G., "Corrosion of Epoxy Coated Rebars--Keys Segmental Bridge-Monroe County," *Report No. 88-8A*, Florida Dept. of Transportation, Materials Office, Corrosion Research Laboratories, Gainesville, Fl, 1988.

Kemp, E.L., "Bond in Reinforced Concrete: Behavior and Design Criteria," *ACI Journal*, Vol. 83, No. 1, January-February 1986, pp. 50-57.

Li, V.C., and Wang, S., "Flexural Behaviors of Glass Fiber-Reinforced Polymer (GFRP) Reinforced Engineered Cementitious Composite Beams," *ACI Materials Journal*, Vol. 99, No. 1, January-February 2002, pp. 11-21.

Malvar, L.J., Cox, J.V., and Cochran, K.B., "Bond between Carbon Fiber Reinforced Polymer Bars and Concrete. 1: Experimental Study," *Journal of Composites for Construction*, Vol. 7, No.2, May 2003, pp. 154-163.

Mashima, M., and Iwamoto, K., "Bond characteristics of FRP rod and concrete after freezing and thawing deterioration," *Fiber-Reinforced-Plastic Reinforcement for Concrete Structures - International Symposium*, SP 138, American Concrete Institute, Detroit, 1993, pp. 51-70.

Mathey, R., Wastein, D., "Investigation of Bond in Beam and Pull-Out Specimens with High-Yield-Strength Deformed Bars," *ACI Journal*, Vol. 57, No. 3, March 1961, pp. 1071-1090.

Mays, G.C., and Tilly, G.P., "Long Endurance Fatigue Performance of Bonded Structural Joints," *International Journal of Adhesion and Adhesives*, Vol. 2, No. 2, April 1982, pp. 109-113.

Micelli, F., and Nanni, A., "Durability of FRP Rods for Concrete Structures," *Construction and Building Materials*, Vol. 18, 2004, pp. 491-503.

Naaman, A.E., and Jeong, S.M. "Structural Ductility of Concrete Beams Prestressed with FRP Tendons," *Proc., 2nd Int. RILEM Symp. (FRPRXS-2), Non-Metric (FRP) Reinforcement for Concrete Structures*, RILEM, Bagneux, France, 1995, pp. 379-386.

Nanni, A., Al-Zaharani, M.M., Al-Dulaijan, S.U., Bakis, C.E., and Boothby, T.E., "Bond of FRP Reinforcement to Concrete-Experimental Results," *Proceedings of the Second Int. RILEM Symp. (FRPRCS-2),* L. Taerwe, ed., 1995, pp. 135-145.

Park, R., and Paulay, T., *Reinforced Concrete Structures*, John Wiley & Sons, 1976, 769 pp.

Potter, R., and Ho, D., "Quality of Cover Concrete and Its Influence on Durability," *Concrete Durability, Katharine and Bryant Mather, International Conference, SP100,* American Concrete Institute, Detroit, 1987.

Rasheeduzzafar, A., Dakhil, F., Basa, M., and Khan, M., "Performance of Corrosion-Resisting Steels in Chloride-Bearing Concrete," *ACI Materials Journal*, Vol. 89, No. 5, September-October 1992, pp. 439-448.

Rehm, G., and Eligehausen, R., "Bond of Ribbed Bars under High Cycle Repeated Loads," *ACI Journal*, Vol. 76, No. 2, February 1979, pp. 297-309.

RILEM 7-II-128 (Réunion Internationale des Laboratoires et Experts des Matériaux, Systèmes de Constructions et Ouvrages), "RC6: Bond Test for Reinforcing Steel. 1. Pull-Out Test," *RILEM Technical Recommendations for the Testing and Use of Construction Materials*, E & FN Spon, U.K. 1994, pp.102-105.

Salib, S.R., and Abdel-Sayed, G., "Prediction of Crack Width for Fiber-Reinforced Polymer-Reinforced Concrete Beams," *ACI Structural Journal*, Vol. 101, No. 4, July-August 2004, pp. 532-536.

Schutte, C.L., "Environmental Durability of Glass-Fiber Composites," *Materials Science and Engineering*, Vol. 13, No.7, 1994, pp. 265-324.

Sekijima, K., Otsuka, Y., and Konno, T., "Durability of Fiber Reinforced Polymer Reinforcement Embedded in Concrete," *Fourth International Symposium on Fiber Reinforced Polymer Reinforced Concrete Structures,* SP-188, American Concrete Institute, Farmington Hills, Michigan, 1999, pp. 501-513.

Sen, R., Mariscal, D., and Shahawy, M., "Durability of Fiberglass Prestensioned Beams," *ACI Structural Journal*, Vol. 90, No. 5, September-October 1993, pp. 525-533.

Sen, R., Shahawy, M., Sukumar, S., and Rosas, J., "Durability of Carbon Fiber Reinforced Polymer (CFRP) Pretensioned Elements under Tidal/Thermal Cycles," *ACI Structural Journal*, Vol. 96, No. 3, May-June 1999, pp. 450-457.

Standard Specifications for Highway Bridges, 16th *ed.,* American Association of State Highway and Transportation Officials, Washington, D.C., 1996.

Status of the Nation's Highways, Bridges, and Transit: 2002 Conditions and Performance Report. http://www.fhwa.dot.gov/policy/2002cpr/highlights.htm. Accessed July, 2004.

Tannous, F.E., and Saadatmanesh, H., "Environmental Effects on the Mechanical Properties of E-Glass FRP Rebars," *ACI Materials Journal*, Vol. 95, No.2, March-April 1998, pp. 87-100.

Theriault, M., and Benmokrane, B., "Effects of FRP Reinforcement Ratio and Concrete Strength on Flexural Behavior of Concrete Beams," *Journal of Composites for Construction,* Vol. 2, No. 1, February 1998, pp. 7-16.

Thorenfeldt, E., Tomaszewicz, A., and Jensen, J.J., "Mechanical Properties of High-Strength Concrete and Application in Design," *Proceedings of the Symposium "Utilization of High Strength Concrete,"* Stavanger, Norway, June 1987, Tapir, Trondheim, pp. 149-159.

Tighiouart, B., Benmokrane, B., and Gao, D., "Investigation of Bond in Concrete Member With Fiber Reinforced Polymer (FRP) Bars," *Construction and Building Materials*, Vol. 12, No. 8, December 1998, pp. 453-462.

Toutanji, H. A., and Saafi, M., "Flexural Behavior of Concrete Beams Reinforced with Glass Fiber-Reinforced Polymer (GFRP) Bars," *ACI Structural Journal*, Vol. 97, No. 5, September-October 2000, pp. 712-719.

Uomoto, T., and Nishimura, T., "Deterioration of Aramid, Glass, and Carbon Fibers Due to Alkali, Acid, and Water in Different Temperatures," *Fourth International Symposium on Fiber Reinforced Polymer for Reinforced Concrete Structures,* SP-188, American Concrete Institute, Farmington Hills, Michigan, 1999, pp. 515-522.

Vijay, P.V., and GangaRao, H.V.S., "Bending Behavior and Deformability of Glass-Fiber-Reinforced Polymer Reinforced Concrete Members," *ACI Structural Journal*, Vol. 98, No. 6, November-December 2002, pp. 834-842.